Crystal-chemistry and reactivity of fibrous amphiboles of environmental and health interest

Alessandro Pacella

To cite this version:

Alessandro Pacella. Crystal-chemistry and reactivity of fibrous amphiboles of environmental and health interest. Material chemistry. Université Pierre et Marie Curie - Paris VI; Università di Roma "La Sapienza", 2009. English. NNT : 2009PA066208 . tel-00814192

HAL Id: tel-00814192
https://theses.hal.science/tel-00814192
Submitted on 16 Apr 2013

Università di Roma "La Sapienza"
Dipartimento di Scienze della Terra

Université Pierre et Marie Curie
Laboratoire de Rèactivité de Surface
UMR CNRS 7197

Tesi di Dottorato in Cotutela
Thèse de Doctorat en Cotutelle

Spécialité :

Physique et Chimie des Matériaux – ED 397 **Scienze della Terra - Mineralogia**

Sujet de la these :

Crystal-chemistry and reactivity of fibrous amphiboles of environmental and health interest

Cristallochimie et réactivité de surface d'amphiboles fibreuses d'intérêt environnemental et sanitaire

- Dr. Alessandro Pacella -

Date de la soutenance : 30 juin 2009

Composition du Jury :

M. Antonio Gianfagna - Directeur de Thèse

M. Mickey E. Gunther, Alessandro Gualtieri - Rapporteurs

M. Jean-François Lambert, Mme Jeanine Fournier - Examinateurs

TABLE OF CONTENTS

1 THE AMPHIBOLES

2 GEOLOGICAL FRAMEWORK OF THE AREAS OF THE EXAMINED SAMPLES

3 CRYSTAL-CHEMICAL AND STRUCTURAL CHARACTERIZATION OF TREMOLITES OF ENVIRONMENTAL AND HEALTH INTEREST

4 A MICRO-ANALYTICAL SEM-EDS METHOD APPLIED TO THE QUANTITATIVE CHEMICAL COMPOSITIONS OF FIBROUS AMPHIBOLES

5 CHEMICAL AND STRUCTURAL CHARACTERIZATION OF A SUITE OF FIBROUS AMPHIBOLES FROM BIANCAVILLA (SICILY, ITALY)

6 CHEMICAL AND STRUCTURAL CHARACTERIZATION OF A SAMPLE OF FIBROUS AMPHIBOLE FROM LIBBY (MONTANA,USA)

7 INVESTIGATION OF FIBROUS AMPHIBOLES BY X-RAY PHOTOELECTRON SPECTROSCOPY

8 STUDY OF THE REACTIVITY OF THE FIBROUS AMPHIBOLES BY ELECTRON PARAMAGNETIC RESONANCE (EPR) SPECTROSCOPY

9 STUDY OF THE LIPID PEROXIDATION IN PRESENCE OF HYDROGEN PEROXIDE ON VARIOUS FIBROUS AMPHIBOLES

INTRODUCTION

The origin of the word “asbestos” comes from the two Greek words αμιαντος and ασβεστος. The Greek word αμιαντος (transliterated as “amiantos”), when used as a noun is synonymous with the English word asbestos, and when used as an adjective can mean pure or undefiled. The Greek word ασβεστος (transliterated as “asvestos”-not “asbestos”), when used as a noun means lime, quicklime, and when used as an adjective, can mean not extinguishable or unquenchable (Ross and Nolan, 2003). Historically asbestos is a generic commercial industial term used to describe a group of hydrate silicate minerals with fibrous morphology and combined to form bundles. The high tensile strenght, flexibility, electrical and termal resistence of asbestos led to use it in several mechanical and commercial applications such as thermal insulation, building materials, fire- and bulletproof materials, texile products, and many more. Tipically the minerals designated as asbestos are six: chrysotile, tremolite, actinolite, anthophyllite, grunerite, and riebeckite asbestos. Chrysotile asbestos, the only fibrous member of the serpentine mineral group, has the ideal chemical formula $Mg_3Si_2O_5(OH)_4$. The remaing asbestos are amphibole asbestos: anthophyllite asbestos, ideally $(Mg,Fe^{2+})_7Si_8O_{22}(OH)_2$; tremolite-actinolite asbestos, ideally $Ca_2(Mg,Fe^{2+})_5Si_8O_{22}(OH)_2$; grunerite asbestos, ideally $(Fe^{2+},Mg)_7Si_8O_{22}(OH)_2$, usually referred to colloquially as “amosite” (from the acronym AMOS, representing Asbestos Mines of South Africa); riebeckite asbestos, ideally $Na_2(Fe^{2+},Mg)_3Fe_2^{3+}Si_8O_{22}(OH)_2$, usually referred to colloquially as “crocidolite”. Notably, five of the six designated minerals can also occur in a non-fibrous form.

Exposure to asbestos have been linked to numerous health problems and respiratory diseases. The earliest reports of asbestos-related disease were from France and the United Kingdom in 1906 (Murray, 1990). In 1927, the terms “asbestosis” and “asbestos bodies” were used for the first time in English (Cooke, 1927) and in 1950 the relationship between exposure to asbestos and lung cancer and mesothelioma became known (Wagner et al.,1960; Sleggs et al., 1961). Today three principal diseases linked to asbestos exposure are commonly well kown: asbestosis, lung cancer, and mesothelioma. (1) *Asbestosis* is a non-malignant diffuse interstitial fibrosis of the lung tissue. High asbestos exposure can cause scarring of the lung tissue (fibrosis), causing it to become stiff, resulting in a restriction in pulmonary function and reduction in the lung's ability to exchange carbon dioxide for oxygen. (2) *Lung cancers* related to asbestos exposure are bronchogenic carcinomas, which include squamous cell carcinomas, small- and large-cell carcinoma, and adenocarcinomas. Cancers that arise in other parts of the lung, such as alveolar carcinomas and sarcomas, are rare and are not known to be caused by asbestos. (3) *Mesothelioma* is a cancer which mainly develops in the pleura (outer lining of the lungs and internal chest wall), but it may also occur in the pericardium and peritoneum, lining of heart and abdominal cavities, respectively. The pleural mesothelial cells occur almost as a monolayer surrounding the outer lining of the lung and the internal chest wall. The main features of such tumors are: long latency, difficult diagnosis, exposure to amphibole asbestos only (Constantopoulos et al. 1987), and capability of appearing even after the inhalation of an extremely low asbestos concentration, known as triggering dose (U.S. National Research Council 1985; Piolatto 1996).

The mechanism through which asbestos fibers may give rise to disease is not yet completely clear. Many authors agree in attributing to mineral fibers the formation of Reactive Oxygen Species (ROS) that determine a strong release of $^{\bullet}OH$ free radicals by partially dissolving into biological fluids parteciping in Fenton chemistry (Kane et al. 1996; Fubini and Otero Aréan 1999; Kamp and Weitzman, 1999; Robledo and Mossman, 1999). Toxicological studies evidenced that interactions between fibrous material and biological environment are strongly dependent on both the geometry and the crystal chemistry of mineral fibers (Stanton et al. 1981; Fubini 1993, 1996; Gilmour et al. 1997). In particular, the presence and the bioavailability of Fe received considerable attention by the biomedical community. It was proposed that both the presence and structural coordination of Fe are important factors in the toxicity of asbestos (Fubini et al. 2001) and, furthermore, that only the Fe exposed on the fiber surface is relevant in the ROS production (Gazzano et al. 2005; Favero-Longo et al. 2005).

The investigations on the relationships between asbestos exposure and relate diseases have been mainly focused on working exposures so far. However asbestos are also occurring as accessory minerals in some rocks. In the most abundant of these rocks, the ophiolite complexes, chrysotile, tremolite and actinolite asbestos are frequently found. The term ophiolite indicates fragments of oceanic lithosphere obducted onto the edges of continental plates. The idealized ophiolite sequence, from bottom to top, includes: (1) ultramafic multilayered cumulates and residual mantle sequence comprising tectonized dunites, lherzolites, and harzburgites; (2) a plutonic complex of layered mafic-ultramafic cumulates at the base, grading upward to massive gabbros; (3) diabase sheeted dikes; (4) basaltic pillow lavas and breccias; and (5) deep-sea sediments. Ophiolte rocks are used as building and ornamental materials, because of their exceptional physical and mechanical qualities such as strength, durability, variety in appearance and color. Natural asbestos (both chrysotile and amphibole) occurence represents an environmental problem due to the potenzial exposure that may resutl if the asbestos-bearing rocks are disturbed by weathering processes and/or human activities. Epidemiological studies show that low to moderate exposure to chrysotile asbestos presents a very low health risk, and this is presumably due to its solubility in the body. On the contrary, the bio-solubility was observed to be very low in the case of amphibole asbestos (Van Oss et al., 1999). Epidemiological studies showed an unusually large occurrence of mesothelioma cases in small villages in Turkey, Greece, Cyprus, Corsica, and New Caledonia. All these villages lie within or near to ophiolite complexes, and the residents have been exposed to tremolite and actinolite asbestos quarried from the local rock formations and used as an ingredient for stucco and whitewash (Ross and Nolan, 2003). In addition, fibrous tremolite and actinolite asbestos are also occurring in the ophiolite complexes of Virginia, Maryland and Pennsylvania (USA), and El Dorado County, California (USA). Due to the possible health effects that the mineral dust may have on the local residents, an asbestos exposure control plan has been instiued (Ross and Nolan, 2003).

In the Italian peninsula, especially in the Alps and the Apennines (Fig. 1), there is a massive presence of ophiolitic outcrops rich in serpentine (chrysotile) and amphibole fibers (tremolite-actinolite and anthophyllite). The Piedmont region (NW Italy) has the largest number of such outcrops such as: the Lanzo Valley and in particular the ex-mine of Balangero, in which chrysotile was mined. Environmental concern was recently caused by the excavations of the Susa Valley railway tunnel (Ballirano et al. 2008). In fact, some high-speed railway lines such as Turin-Lyon and Genoa-Milan involve tunnel excavations occurring in metamorphic formations, such as serpentinites, in which zones containing fibrous tremolite may be found. These excavations give rise to worker health and public environmental issues (Piolatto et al. 1990; Astolfi et al. 1991). Ophiolites hosting fibers of tremolite also outcrop in various localities in the central and southern part of Italy: quarries of ophiolite, widely used in the past, are present in Calabria (Punturo et al., 2004) and Latium (Burragato et al., 2001), but their presence has not been associated with health problems so far. However, in Basilicata, the presence of fibrous tremolite in the soils of Lauria and Castelluccio Superiore Towns (Potenza) was related to some pleural mesothelioma cases occurred in these rural communities (Burragato et al. 2004, Pasetto et al. 2004).

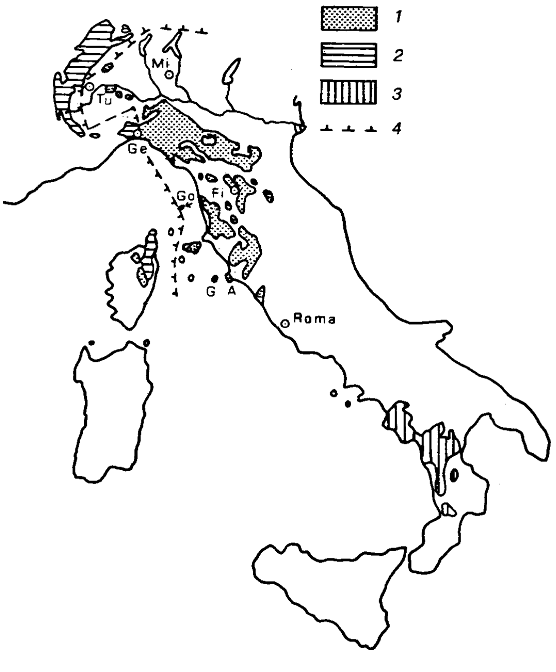

Figure 1 - Map showing the ophiolitic outcrops between the western Alps and southern Appennins. (Abbate et al., 1980, modified after Dal Piaz, 1974). 1: Liguridi 2: Schists lustres of Piedmont, Corsica, Gorgogna (Go), Giglio Island (G) and Argentario (A); 3: Units of ophiolites of the southern Appennins; 4: Limit of Alpine orogenetic metamorphism.

Recently, epidemiological studies revealed cases of environmental contamination of fibrous amphiboles not regulated. A study on the mortality from malignant pleural mesothelioma in Italy evidenced a high and unusual presence of cluster of malignant mesothelioma cases among people living in Biancavilla, a town located on the southwestern side of Etnean volcanic area in Sicily (Di Paola et al., 1996). Environmental and mineralogical surveys in Biancavilla showed no asbestos exposure either from occupational activities or from the use of manufactured products (Paoletti et al., 2000). However, some sites in the nearby resulted to be the sources of environmental diffusion of amphibole minerals with fibrous habit (Paoletti et al., 2000; Gianfagna et al., 2003). The fibrous amphiboles were characterized and the new end-member fluoro-edenite was recognised. On the basis of these results Comba et al. (2003) suggested that the unusual cluster of mesothelioma in Biancavilla could be caused by the exposure to such new fibrous amphiboles. From the toxicological point of view, these amphibole fibers showed high carcirogenicity in the previous intraperitoneal injection experiments with rats (Soffritti et al., 2004). In addition, recent *in vitro* studies revealed that their toxicity is strongly related to the chemical composition, with particular relevance of the Fe content and its oxidation state (Cardile et al., 2004; Pugnaloni et al., 2007). Another well known case of not regulated amphibole fiber occurence is that of Libby (Montana, USA). In this area, an elevated incidence of lung cancer and mesothelioma cases was found in the local miners and millers (Mc. Donald et al 1986, 2001). The local vermiculite mine operated from 1923 to 1990 for the building local industry. First Wilye & Verkouteren (2000) and later Gunter et al. (2001, 2003) demonstrated the presence of fibrous amphiboles, with composition dominantly ranging from winchite to richterite, in the vermiculitic deposits. The environmental survey finally related the diseases to the fibrous amphiboles (Gunter et al., 2003). The above mentioned environmental diseas are related to both regulated and not regulated amphiboles fibers make the study of these minerals a topic of great interest. Although in the scientific literature the crystal-chemistry of the various amphibole prismatic varieties has been described in thousands of works, that of the corresponding fibrous variety has been well characterized just in few cases (Sokolova et al., 2000, 2003, Gunter et al., 2003; Gianfagna et al., 2003, 2007; Ballirano et al. , 2008).

The present study is devoted to the investigation of amphibole fibers by means of a well tested multi-analitical approach. The studied speciments are tremolite fibers coming from ophiolitic outcrops at different italian localities such as (from north to south): 1) Ala di Stura (Lanzo Valley, Piedmont); 2) Mt. Rufeno (Acquapendente, Latium); 3) Castelluccio Superiore (Potenza, Basilicata); 4) S. Mango (Catanzaro, Calabria). A sample of fibrous tremolite from the ophiolite complex outcropping in Montgomery County, Maryland (USA) was also studied. In addition, the not regulated fibrous amphiboles coming from Biancavilla (Catania, Sicily) and Libby (Montana, USA) are studied for comparison. The detailed crystal chemical characterization was carried out by combining Inductively Coupled Plasma-Mass (ICP-MS) spectrometry, Electron Microprobe Analysis (EMPA) , Scanning Electron Microscopy (SEM) with microanalysis system, parallel-beam X-Ray Powder Diffraction (XRPD), ^{57}Fe Mössbauer spectroscopy (MS) and Fourier-Trasform Infra-Red (FT-IR) spectroscopy. Beside the mineralogical characterization, the surface chemistry and surface reactivity of some samples have been also investigated. The surface chemistry of the fibers was studied by X-Ray Photoemission Spectroscopy (XPS) with specific attention to the surface iron content and its oxidation state. The Electron Paramagnetic Resonance (EPR) Spectroscopy was used to characterize the HO° hydroxyl radicals and the measurement of their absolute concentration. In addition, tests of lipid peroxidation in presence of hydrogen peroxide were performed to identify and distinguish their reactivity, and the degradation of linolenic acid in conditions similar to those found in pulmonary alveoli was monitored. The products of degradation of linolenic acid were studied by UV-visible spectroscopy. The surface chemistry and the reactivity of a sample of crocidolite UICC (Union Internationale contre le Cancer, Johannesburg, South Africa) and a sample of calcite (Iceland spar variety) were also investigated as positive and negative references, respectively. Finally, fibrous amphiboles full characterization (morphology, crystal chemistry, crystal structure, cation site partitioning, Fe^{3+}/Fe_{tot} ratio of the bulk and surface, surface chemistry and reactivity) were coupled with cytotoxicity tests *in vitro* (MTT test on A 559 and MeT-5A cells) performed on the same samples. The aim is to understand the relationships between mineralogical features and biological activity in order to shed new light on the chemical, molecular and toxic-chemical processes in the interaction between fiber and organic environment. The multidisciplinary approach of this work required the presence of several experiences, complementary with each other, ranging from the mineralogy to the chemistry and biology. Therefore, the collaboration between the Sapienza University of Rome and the University of Pierre et Marie Curie of Paris VI was the underlying framework of such a challenging and interdisciplinary work.

1

THE AMPHIBOLES

INTRODUCTION

This chapter is a crystal-chemical and structural description of the amphiboles; for deepenings we recommend consulting Hawthorne (1981, 1983) and Hawthorne et al. (2007).

CHYSTAL-CHEMICAL FORMULA

The general chemical formula of the amphiboles can be written as

$$A\ B_2\ C_5\ T_8\ O_{22}\ W_2$$

where:

A = □, Na, K, CA, Li;

B = Na, Li, Ca, Mn^{2+}, Fe^{2+}, Mg;

C= Mg, Fe^{2+}, Mn^{2+}, Al, Fe^{3+}, Mn^{3+}, Ti^{4+}, Li;

T = Si, Al , Ti^{4+};

W = (OH), F, Cl, O^{2-}.

Minor elements such as Zn, Ni^{2+}, Co^{2+}, V^{3+}, Sc, Cr^{3+} and Zr are also observed as C cations.

The calculation of the crystal-chemical formula of the amphibole can be done assuming a content of anions of 24 apfu or 23 atoms per unit formula (apfu). In both cases we assume (OH, F, Cl) = 2 apfu; the calculation based on the content of anions of 24 apfu requires to determine H_2O, F and Cl content and it allows a complete evaluation of the chemical composition (sum of wt% of all oxides). More complicated is when an amount of O^{2-} , replacing OH^-, is present at O(3); in this case we have (OH, F, Cl) < 2 apfu and particular substitutions such as ${}^{M(1)}Ti^{4+}$ replacing ${}^{M(1)}(Mg, Fe^{2+})$ occur in the structure. The formula is still normalized on 24 cations, but the (OH, F, Cl) content is $= 2 - 2\ X\ {}^{M(1)}Ti^{4+}$.

CRYSTAL STUCTURE

The amphibole stucture consists of two principal elements: a double chain of corner-sharing tetraedra and a strip of edge-sharing octahedra, both of which estend in the *c*-direction (fig. 6).

Both the tetrahedrally sites are denoted by T, while octaedra are denoted by M. There are two distinct tetrahedra designated T(1) and T(2) and three distinct types of octahedra designated M(1), M(2) and M(3). The double chain of tetrahedra and the strip of octahedra are linked by the M(4) site, and beelow the hexagonal ring of tetrahedra there is the A site, at the center of a large cavity (Fig. 1).

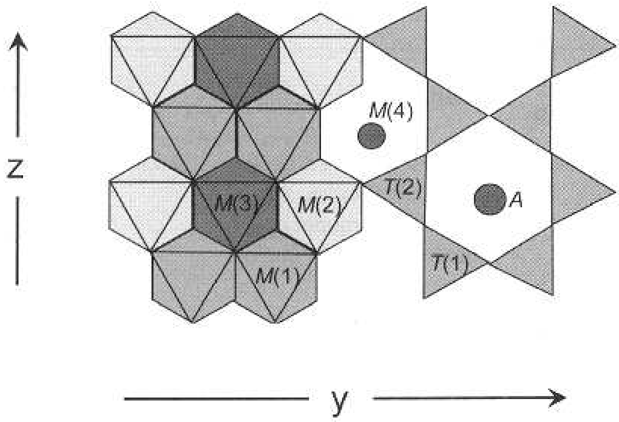

Figure 1 - Model of amphibole structure showing the chain of tetrahedra, the strip of octahedra and M(4) and A sites (Hawthorne et al, 2007).

There are currently six known structural variants of amphibole: (1) those that involve different stacking sequences along the *a*-direction (C2/*m*, P*nma* e P*nmn*) and those derived from (1), but with differences in coordination ($P2_1/m$) and/or in topochemistry (P 2/*a*, C $\bar{1}$). The structure C $\bar{1}$ is known only for a little common composition of a synthetic amphibole. In this work only monoclinic amphiboles of C2/*m* structure have been studied, and therefore only this structural variant will be dealt below. The structure of a monoclin C2/*m* amphibole is shown in Figure 2. For more details we still reccomend Hawthorne et al. (2007).

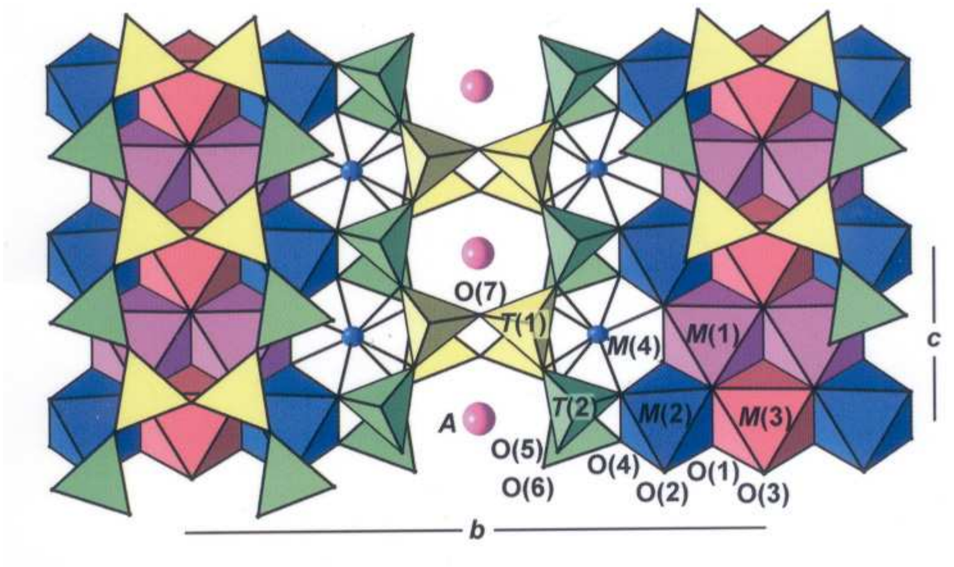

Figure 2 - Structure of a C 2/*m* amphibole projected onto (100) (from Hawthorne et al, 2007).

The structure is characterized by two different sites T(1) and T(2), occupied by T-cations, tetrahedrally coordinated and linked together forming a double chain of tetrahedra. The T(1) site is coordinated by the O(1), O(5), O(6) and O(7) oxygens, and the T(2) sites is coordinated by O(2), O(4) O(5) and O(6); the two adjacent T(1) and T(2) tetrahedra are linked by O(5) and O(6) bridging oxygens and O(7) links two adjacent T(1) tetrahedra. As mentioned before, there are three sites of M-octaedra occupied by C-cations. The M(1) site is coordinated by two O(1) oxygen atoms, two O(2) oxygen atoms and two O(3) W anions (OH, F, Cl, O2-). The site M(2) is instead coordinated by two O(1) oxygen atoms, two O(2) oxygen atoms and two O(4) oxygen atoms. The M(3) site is coordinated by four O(1) oxygen atoms and two O(3) W anions. The double chain of tetrahedra links adjacent stirps of octahedra along the *b*-direction through the T (2)-M (2) linkage *via* the common O(4) oxygen and along the *a*-direction through the O(1) and O(2) oxygens. The M(4) site is located at the perifery of the strip of octahedra and is occupied by B-cations. It is surrounded by eight oxygens arranged as a square antiprism: O(2) x 2, O(4) x 2, O(5) x 2 and O(6) x 2. Note that the cation occupancy of M(4) is the primary characteristic on which the major groups of amphiboles are classified and is also related with the space-group variations. The A-site is located at the center of a large cavity between the back-to-back double chains of tetrahedra. The center of the cavity has point symmetry 2/m, but the A cations occupy the point symmetry 2 or *m* [respectively A(2) and A(*m*)]. This site is surrounded by twelve oxygens: O(5) x 4, O(6) x 4 and O(7) x 4.

The double chain of tetrahedra

Many works (Hawtorne 1981, 1983, Oberti et al. 1995) treated the relations between the content of tetrahedrically-coordinated Al and the variation of the <<T-O>> distance. The variation of <<T-O>> bondlength with the $^{[4]}$Al content is shown in the diagrams of Figure 3. We note scattered data below ~ 0.50 $^{[4]}$Al apfu, but a well-developed linear relation above ~ 0.50 $^{[4]}$Al apfu (Fig. 3a). Such linear relation is better shown in Figure 3b; the regression coefficient (0.989) suggests that the variation of <<T-O>> distance is only a function of the total $^{[4]}$Al content for $^{[4]}$Al > 0.50 apfu. Such simple model does not perfectly work for small amonuts of $^{[4]}$Al content (<0.50 apfu) because of the influence on <<T-O>> distance of other factors such as $<<r^{M(4)}>$, $r^{M(1,2,3)}$ and $<r^{O(3)}>$. The observed and calculated values of <<T-O>> are compared in Figure 3c.

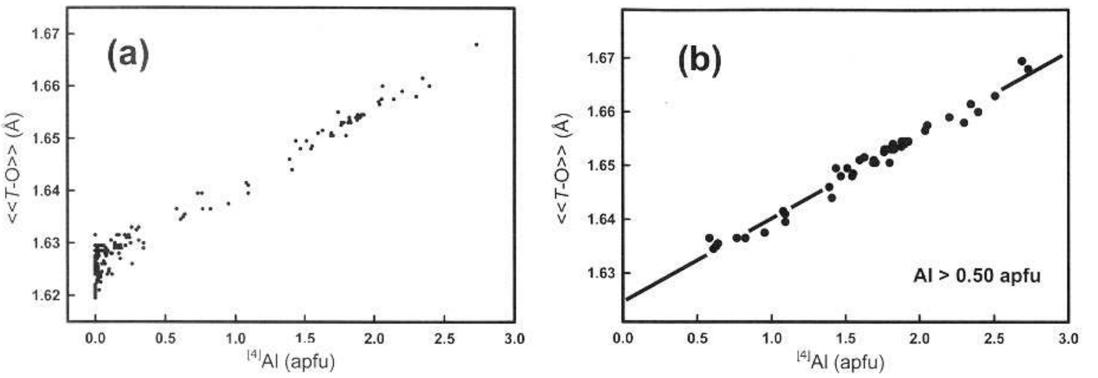

Figure 3 - a) Relation between the <<T-O>> distance and $^{[4]}$Al content (all data), b) <<T-O>> as a function of $^{[4]}$Al content, where $^{[4]}$Al > 0.50 apfu c) observed *versus* calculated values of <<T-O>> for all amphiboles with $^{[4]}$Al <0.50 apfu (from Hawthorne et al, 2007).

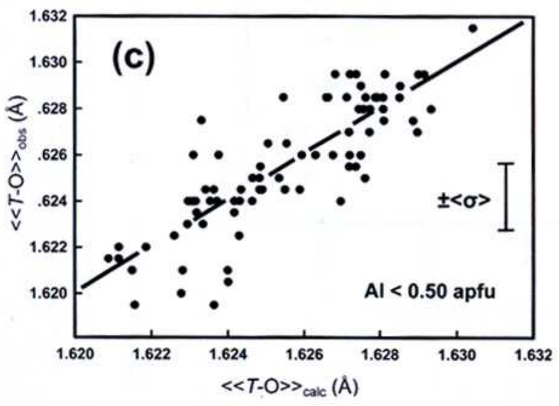

In Figure 4 the <T(1)-O> and <T(2)-O> variations as a function of $^{[4]}$Al content are showed. Note that there are two distinct regimes of behavior of the tetrahedra. Below Al content of 0.40 apfu the data are very densely clustered, with a variation of lengthbond from 1.640 to 1.614 Å for Al content of 0 apfu; this variation decreases with increasing Al content up to 0.40 apfu. Above 0.50 apfu the behavior of the tetrahedra drastically changes, since <T(1)-O> increases very strongly with increasing $^{[4]}$Al content, whereas <T(2)-O> increases less strongly.

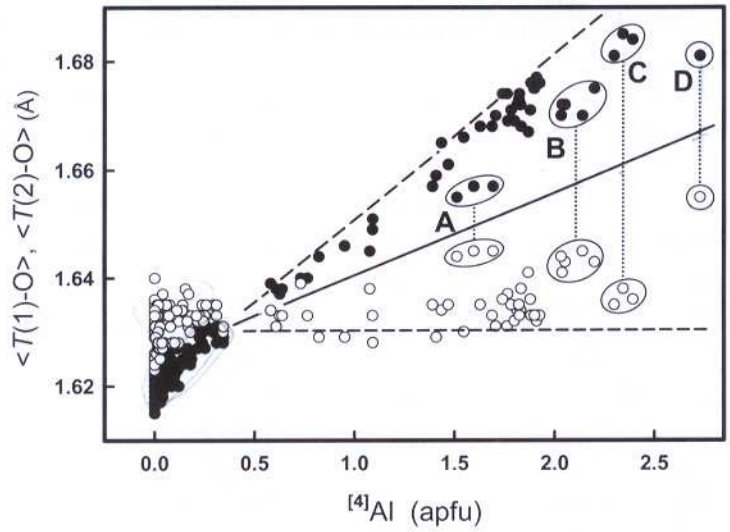

Figure 4 - <T(1)-O> (black circles) and <T(2)-O> (white circles) variation as a function of $^{[4]}$Al for the C2/*m* amphiboles. The circles denoted by A, B, C and D represent amphiboles with with $^{[4]}$Al disorder over T(1) and T(2) (by Hawthorne et al, 2007).

The strip of the octahedra

The variation of <M(1,2,3)-O> distance is a function of the radius of cations costituent the octahedra and is also affected by the size of the anions occupying the O(3) site, as their ionic radii are very different: OH^- (r = 1.34 Å), F (r = 1.30 Å) and O (r = 1.36 Å). <M(1,2,3)-O> bondlength can be also affected by $<r^{M(4)}>$, the mean radius of cations at M(4) site. Considering all these factors, a linear relation for <M(1,2,3)-O> distance was found, with a correlation coefficient of 0.990 (Fig. 5).

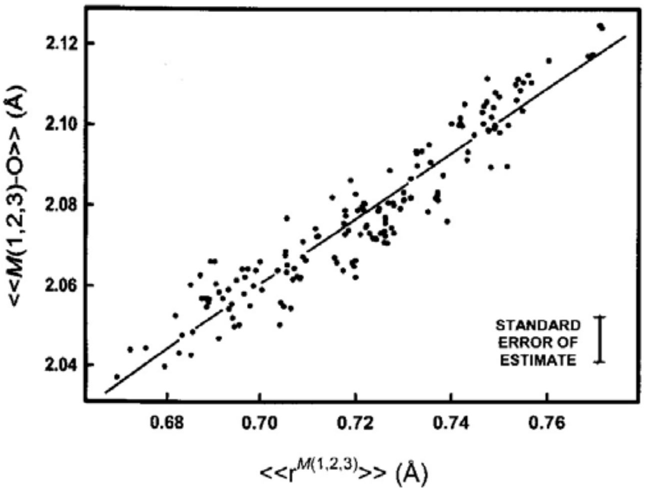

Figure 5 - Variation in <<M(1, 2, 3)>> distance as function of the mean aggregate radius of the M(1, 2, 3) for the C2/*m* amphiboles. (from Hawthorne et al, 2007).

Figure 6 shows the variation of <M(2)-O> distance as a function of the aggreagate size of the constituent cations, $<r^{M(2)}>$; a well-developed linear relation can be observed and points out that the mean radii at M (1,3), M(4) and O(3) do not significantly affect the <M(2)-O> distance.

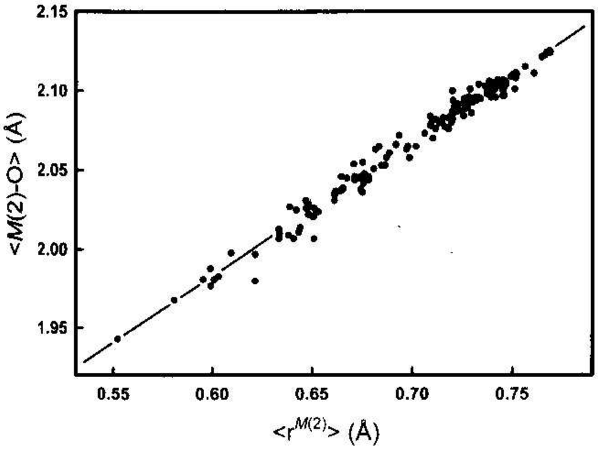

Figure 6 - Variation in <M(2)-O> distance as function of the aggreagate size of the constituent cations $<r^{M(2)}>$ in C2/*m* amphiboles (from Hawthorne et al, 2007).

The situation for <M(1,3)-O> distances is more complicated, as M(1) and M(3) are coordinated by O(3) site hosting cations with different ionic radii (OH^- = 1.34 Å), F = 1.30 Å and O = 1.36 Å); in fact a lot of scattering in the <M(1,3)-O> variations as a function of only $<r^{M(1,3)}>$ was observed

(Fig. 7). Therefore, <M(1)-O> and <M(3)-O> distances are significantly affected by $<r^{M(1,3)}>$ and $<r^{O(3)}>$, but inductively, by $<r^{M(4)}>$ and tetrahedrally-coordinated Al content.

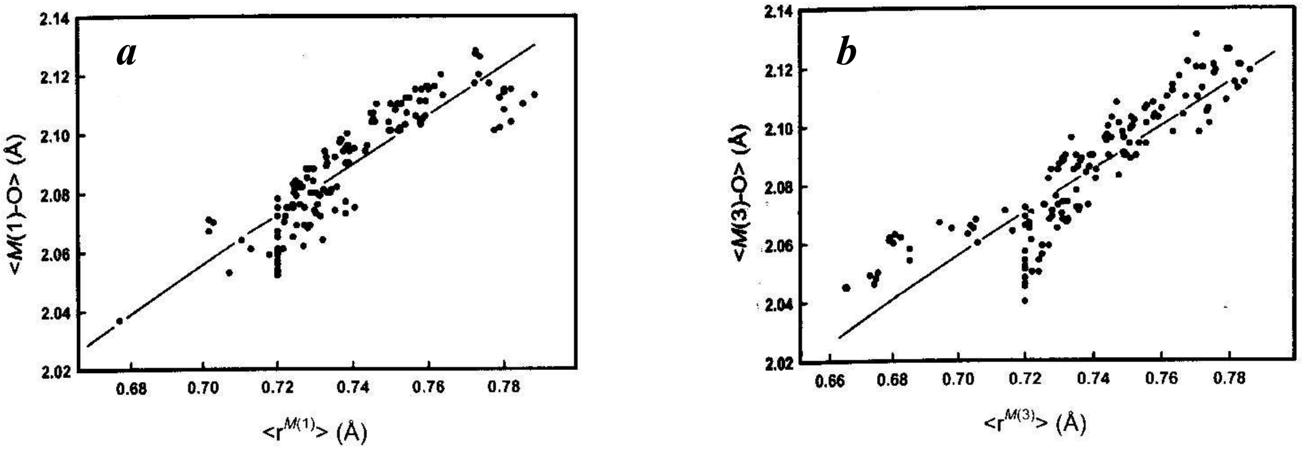

Figure 7 - Variation in <M(1)-O> (a) e <M(3)-O> (b) distance as function of the mean aggregate radius for the C2/*m* amphiboles. (from Hawthorne et al, 2007).

The M(4) site

The M(4) site occurs at the junction of the strip octahedra and the double-chain of tetrahedra. It is occupied by B cations (Na, Li, Ca, Mn^{2+}, Fe^{2+}, Mg), affecting the β angle value and hence the periodicity of the structure along a^* ($a \sin \beta$); in fact, there is a linear relation between $<r^{M(4)}>$ and β angle, which also involves the formal charge, Z, of the M(4) cations, the aggregate size M(1,2,3) cations and the tetrahedrally-coordinated Al content. In calcic, calcic-sodic and sodic amphiboles the site M(4) has point symmetry 2 and occupies the position 0 ~0.28 0.5, but if small cations (Mn^{2+}, Fe^{2+}, Mg) are present, they occupy the M(4') site of position 0 ~0.26 0.5. The M(4) polyhedron size increases with the Na-Ca vicariance at M(4) (from Ca_2 to Na_2), but is also affected by the M(2) size, increasing with increasing <M(2)-O> distance for a fixed size of M(4) cation. Other factors affecting the <M(4)-O> distance are the size of O(3) cation, the mean aggregate radius of M(1) and M(3), and the tetrahedrally-coordinated Al content.

The A site

Figure 8 shows the arrangement of cations occupying the A site. Note the cations do not occupy the central position of the site (0, 0.5 0) with point symmetry 2/m, but the adjacent A(*m*) and A(2) sites, depending on the nature of the cation. If the A cation is K, the electronic density is concentrated at the A(*m*) site, along the mirror plane and elongated in the direction of O(7) oxygen; if the A cation is Na, the situation is more complicated because Na can occupy both the A(2) and A(m) positions.

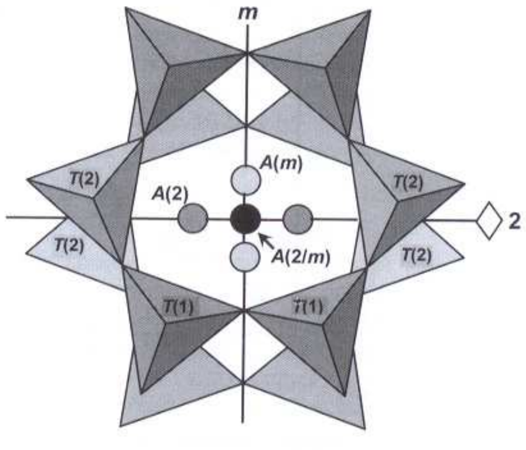

Figure 8 - The arrangemet of polyhedra around the A cavity and the A site in the C 2/*m* amphibole structure. (from Hawthorne et al, 2007).

The O(3) site

The location of the site O(3) within the structure of a C2/*m* amphibole is shown in Figure 9. It was seen by polarized infrared spectroscopy when is occupied by OH, the O-H bond is orthogonal to (100), and the H atom hydrogen-bonds only to oxygen O(7). Where O(3) = F the hidrogen-bond is not present and, as a consequence, there is a slightly shorter <T(1)-O(7)> distance, according to the valence-sum rule. Where O(3) = Cl, the site is significantly diaplaced with reference to the strip of M(1,2,3) octaedra relative to where O(3) = OH, F. In the special case where the O(3) = O, the strip of octahedra is occupated by high charge cations high as Ti^{4+} and Mn^{3+}, in order to satisfy the local bond-valence requirements.

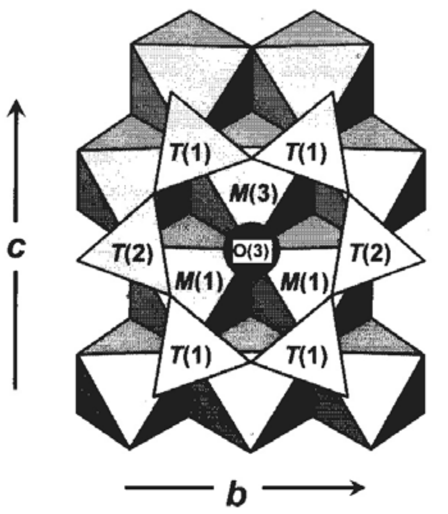

Figure 9 - The O(3) in the C 2/*m* amphiboles (from Hawthorne et al, 2007).

CLASSIFICATION OF THE AMPHIBOLES

The classification of amphibole is a topic of great interest because of the chemical and structural complexity of this group. As a result, the classification of the amphole is still work in progress in order to satisfy the different needs of crystallographers, mineralogists, petrologist and geochemists. The current classification scheme was proposed by Leake (1997) and it is shown in Figure 10.

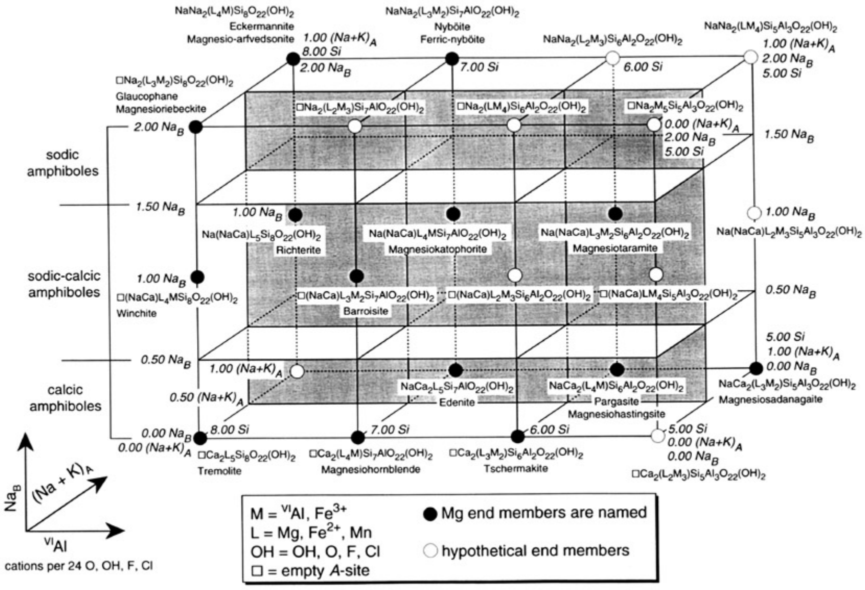

Figure 10 - General classification of the amphiboles, escluding the Mg-Fe-Mn-Li amphiboles (from Leake et al., 1997).

Hawthorne and Oberti (2006), after new amphibole compositions discoveries (Oberti 2000, 2003, 2004), proposed a new classification based not more on the chemistry but on the cystal-chemical basis, considering the role of OH, F, Cl, Li and Fe^{3+}.

The current classification scheme (Leake et al. 1997, 2003)

The general formula of amphibole, as previously mentioned, can be written as $A\ B_2\ C_5\ T_8\ O_{22}\ W_2$, where:

A = □, Na, K, CA, Li;

B = Na, Li, Ca, Mn^{2+}, Fe^{2+}, Mg;

C= Mg, Fe^{2+}, Mn^{2+}, Al, Fe^{3+}, Mn^{3+}, Ti^{4+}, Li;

T = Si, Al , Ti^{4+};

W = (OH), F, Cl, O^{2-}.

In structure, and in particular at C site, minor elements such as Zn, Ni^{2+}, Co^{2+}, V^{3+}, Sc, Cr^{3+} e Zr can be present.

The primary classification of the amphiboles is based on the identity and the amount of B cations:

Group 1: magnesium-iron-manganese-lithium group, where ^{B}(Mg, Fe, Mn, Li) ≥ 1.5 apfu .

Group 2: calcic amphiboles, where ^{B}(Mg, Fe, Mn, Li) ≤ 0.5 apfu and ^{B}(Ca, Na) ≥ 1.5 apfu.

Group 3: sodic-calcic amphiboles, where ^{B}(Mg, Fe, Mn, Li) ≤ 0.5 apfu, ^{B}(Ca, Na) $\geq 1,5$ apfu e $0.5 < {}^{B}Na < 1.5$ apfu.

Group 4: sodic amphiboles, where ^{B}(Mg, Fe, Mn, Li) ≤ 0.5 apfu e $^{B}Na \geq 1.5$ apfu.

Group 5: sodium-calcium-magnesium-iron-manganese-lithium amphiboles, where $0.5 <$ ^{B}(Mg, Fe, Mn, Li) < 1.5 apfu e $0.5 \leq$ ^{B}(Ca, Na) <1.5 apfu.

Within each group a mineral has a specific name refered to a composition with a suitable two-dimensional diagram. These are divided on the basis of the Si contents and the $Mg/(Mg + Fe^{2+})$ or $Mg/(Mg + Mn^{2+})$ ratio. The iron-magnesium amphiboles can be orthorhombic or monoclinc amphiboles (P*nma* or *Pnmn*) ($C\ 2/m$, $P\ 2_1/m$); the classification is shown in figure 11 and the end-member compositions are listed in Table 1. The calcic, sodis-calcic an sodic amphiboles are all monoclinic amphiboles; the classifications and the end-member composition, are shown, respectively, in Figures 12, 13, 14 and in Tables 2, 3, 4.

Table 1 - End-member composition of Mg-Fe-Mn-Li amphiboles (Leake et al. 1997, 2003).

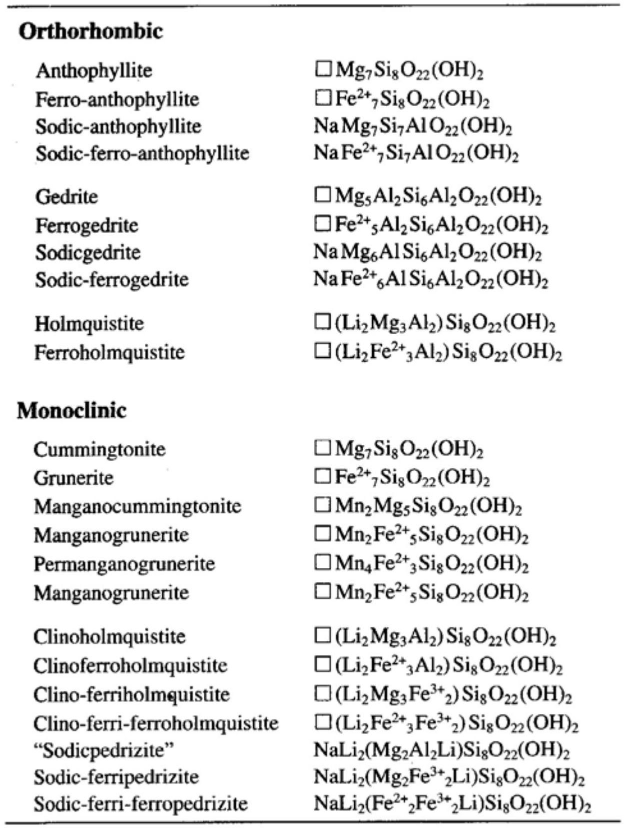

Orthorhombic	
Anthophyllite	$\square Mg_7Si_8O_{22}(OH)_2$
Ferro-anthophyllite	$\square Fe^{2+}{}_7Si_8O_{22}(OH)_2$
Sodic-anthophyllite	$NaMg_7Si_7AlO_{22}(OH)_2$
Sodic-ferro-anthophyllite	$NaFe^{2+}{}_7Si_7AlO_{22}(OH)_2$
Gedrite	$\square Mg_5Al_2Si_6Al_2O_{22}(OH)_2$
Ferrogedrite	$\square Fe^{2+}{}_5Al_2Si_6Al_2O_{22}(OH)_2$
Sodicgedrite	$NaMg_6AlSi_6Al_2O_{22}(OH)_2$
Sodic-ferrogedrite	$NaFe^{2+}{}_6AlSi_6Al_2O_{22}(OH)_2$
Holmquistite	$\square (Li_2Mg_3Al_2)Si_8O_{22}(OH)_2$
Ferroholmquistite	$\square (Li_2Fe^{2+}{}_3Al_2)Si_8O_{22}(OH)_2$
Monoclinic	
Cummingtonite	$\square Mg_7Si_8O_{22}(OH)_2$
Grunerite	$\square Fe^{2+}{}_7Si_8O_{22}(OH)_2$
Manganocummingtonite	$\square Mn_2Mg_5Si_8O_{22}(OH)_2$
Manganogrunerite	$\square Mn_2Fe^{2+}{}_5Si_8O_{22}(OH)_2$
Permanganogrunerite	$\square Mn_4Fe^{2+}{}_3Si_8O_{22}(OH)_2$
Manganogrunerite	$\square Mn_2Fe^{2+}{}_5Si_8O_{22}(OH)_2$
Clinoholmquistite	$\square (Li_2Mg_3Al_2)Si_8O_{22}(OH)_2$
Clinoferroholmquistite	$\square (Li_2Fe^{2+}{}_3Al_2)Si_8O_{22}(OH)_2$
Clino-ferriholmquistite	$\square (Li_2Mg_3Fe^{3+}{}_2)Si_8O_{22}(OH)_2$
Clino-ferri-ferroholmquistite	$\square (Li_2Fe^{2+}{}_3Fe^{3+}{}_2)Si_8O_{22}(OH)_2$
"Sodicpedrizite"	$NaLi_2(Mg_2Al_2Li)Si_8O_{22}(OH)_2$
Sodic-ferripedrizite	$NaLi_2(Mg_2Fe^{3+}{}_2Li)Si_8O_{22}(OH)_2$
Sodic-ferri-ferropedrizite	$NaLi_2(Fe^{2+}{}_2Fe^{3+}{}_2Li)Si_8O_{22}(OH)_2$

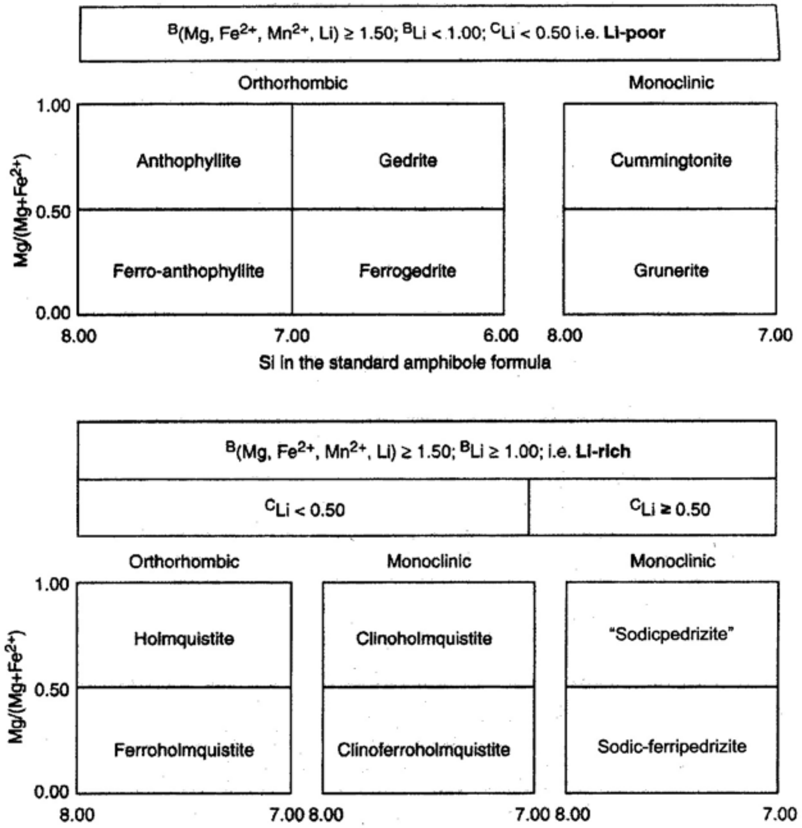

Figure 11 - Classification of iron-magnesium amphiboles; atoms in apfu. (Leake et al 1997, 2003).

⬚ : end member location.

Table 2 - End-member composition of Ca amphiboles (Leake et al. 1997, 2003).

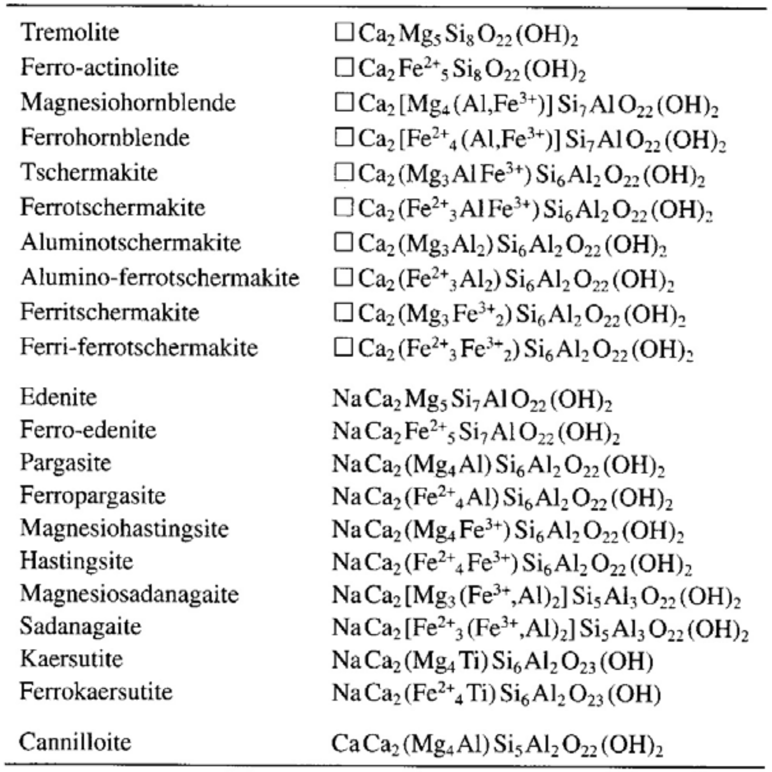

Tremolite	$\square Ca_2Mg_5Si_8O_{22}(OH)_2$
Ferro-actinolite	$\square Ca_2Fe^{2+}{}_5Si_8O_{22}(OH)_2$
Magnesiohornblende	$\square Ca_2[Mg_4(Al,Fe^{3+})]Si_7AlO_{22}(OH)_2$
Ferrohornblende	$\square Ca_2[Fe^{2+}{}_4(Al,Fe^{3+})]Si_7AlO_{22}(OH)_2$
Tschermakite	$\square Ca_2(Mg_3AlFe^{3+})Si_6Al_2O_{22}(OH)_2$
Ferrotschermakite	$\square Ca_2(Fe^{2+}{}_3AlFe^{3+})Si_6Al_2O_{22}(OH)_2$
Aluminotschermakite	$\square Ca_2(Mg_3Al_2)Si_6Al_2O_{22}(OH)_2$
Alumino-ferrotschermakite	$\square Ca_2(Fe^{2+}{}_3Al_2)Si_6Al_2O_{22}(OH)_2$
Ferritschermakite	$\square Ca_2(Mg_3Fe^{3+}{}_2)Si_6Al_2O_{22}(OH)_2$
Ferri-ferrotschermakite	$\square Ca_2(Fe^{2+}{}_3Fe^{3+}{}_2)Si_6Al_2O_{22}(OH)_2$
Edenite	$NaCa_2Mg_5Si_7AlO_{22}(OH)_2$
Ferro-edenite	$NaCa_2Fe^{2+}{}_5Si_7AlO_{22}(OH)_2$
Pargasite	$NaCa_2(Mg_4Al)Si_6Al_2O_{22}(OH)_2$
Ferropargasite	$NaCa_2(Fe^{2+}{}_4Al)Si_6Al_2O_{22}(OH)_2$
Magnesiohastingsite	$NaCa_2(Mg_4Fe^{3+})Si_6Al_2O_{22}(OH)_2$
Hastingsite	$NaCa_2(Fe^{2+}{}_4Fe^{3+})Si_6Al_2O_{22}(OH)_2$
Magnesiosadanagaite	$NaCa_2[Mg_3(Fe^{3+},Al)_2]Si_5Al_3O_{22}(OH)_2$
Sadanagaite	$NaCa_2[Fe^{2+}{}_3(Fe^{3+},Al)_2]Si_5Al_3O_{22}(OH)_2$
Kaersutite	$NaCa_2(Mg_4Ti)Si_6Al_2O_{23}(OH)$
Ferrokaersutite	$NaCa_2(Fe^{2+}{}_4Ti)Si_6Al_2O_{23}(OH)$
Cannilloite	$CaCa_2(Mg_4Al)Si_5Al_2O_{22}(OH)_2$

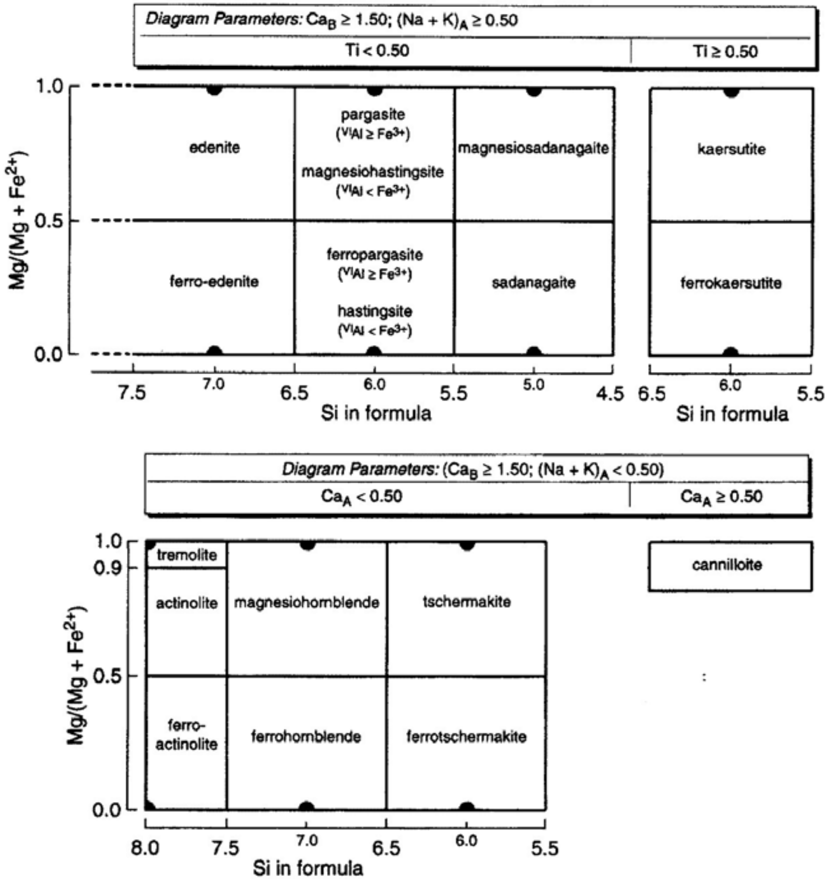

Figure 12 - Classification of calcic amphiboles; atoms in apfu. (Leake et al 1997, 2003).

● : end member location.

Table 3 - End-member composition of Ca-Na amphiboles (Leake et al. 1997, 2003).

Richterite	$Na(CaNa)Mg_5Si_8O_{22}(OH)_2$
Ferrorichterite	$Na(CaNa)Fe^{2+}{}_5Si_8O_{22}(OH)_2$
Winchite	$\square(CaNa)Mg_4(Al,Fe^{3+})Si_8O_{22}(OH)_2$
Ferrowinchite	$\square(CaNa)Fe^{2+}{}_4(Al,Fe^{3+})Si_8O_{22}(OH)_2$
Barroisite	$\square(CaNa)Mg_3AlFe^{3+}Si_7AlO_{22}(OH)_2$
Ferrobarroisite	$\square(CaNa)Fe^{2+}{}_3AlFe^{3+}Si_7AlO_{22}(OH)_2$
Aluminobarroisite	$\square(CaNa)Mg_3Al_2Si_7AlO_{22}(OH)_2$
Alumino-ferrobarroisite	$\square(CaNa)Fe^{2+}{}_3Al_2Si_7AlO_{22}(OH)_2$
Ferribarroisite	$\square(CaNa)Mg_3Fe^{3+}{}_2Si_7AlO_{22}(OH)_2$
Ferri-ferrobarroisite	$\square(CaNa)Fe^{2+}{}_3Fe^{3+}{}_2Si_7AlO_{22}(OH)_2$
Magnesiokatophorite	$Na(CaNa)Mg_4(Al,Fe^{3+})Si_7AlO_{22}(OH)_2$
Katophorite	$Na(CaNa)Fe^{2+}{}_4(Al,Fe^{3+})Si_7AlO_{22}(OH)_2$
Magnesiotaramite	$Na(CaNa)Mg_3AlFe^{3+}Si_6Al_2O_{22}(OH)$
Taramite	$Na(CaNa)Fe^{2+}{}_3AlFe^{3+}Si_6Al_2O_{22}(OH)$
Alumino-magnesiotaramite	$Na(CaNa)Mg_3Al_2Si_6Al_2O_{22}(OH)_2$
Aluminotaramite	$Na(CaNa)Fe^{2+}{}_3Al_2Si_6Al_2O_{22}(OH)_2$
Ferri-magnesiotaramite	$Na(CaNa)Mg_3Fe^{3+}{}_2Si_6Al_2O_{22}(OH)_2$
Ferritaramite	$Na(CaNa)Fe^{2+}{}_3Fe^{3+}{}_2Si_6Al_2O_{22}(OH)_2$

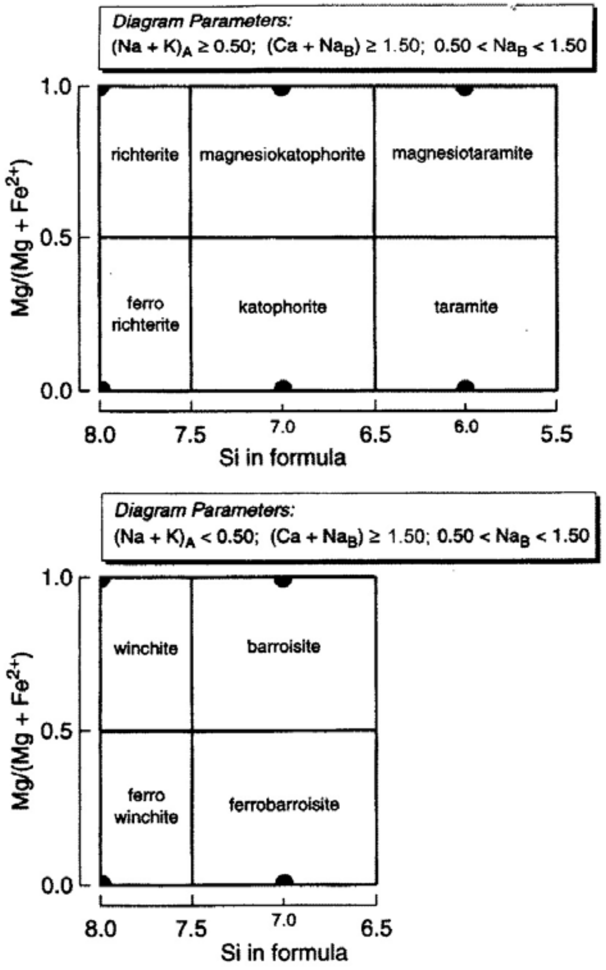

Figure 13 - Classification sodic-calcic amphiboles:atoms in apfu. (Leake et al 1997, 2003).

● : end member location.

Table 4 – End-member composition of Na amphiboles (Leake et al. 1997, 2003).

Glaucophane	$\square Na_2(Mg_3Al_2)Si_8O_{22}(OH)_2$
Ferroglaucophane	$\square Na_2(Fe^{2+}{}_3Al_2)Si_8O_{22}(OH)_2$
Magnesioriebeckite	$\square Na_2(Mg_3Fe^{3+}{}_2)Si_8O_{22}(OH)_2$
Riebeckite	$\square Na_2(Fe^{2+}{}_3Fe^{3+}{}_2)Si_8O_{22}(OH)_2$
Eckermannite	$NaNa_2(Mg_4Al)Si_8O_{22}(OH)_2$
Ferro-eckermannite	$NaNa_2(Fe^{2+}{}_4Al)Si_8O_{22}(OH)_2$
Magnesio-arfvedsonite	$NaNa_2(Mg_4Fe^{3+})Si_8O_{22}(OH)_2$
Arfvedsonite	$NaNa_2(Fe^{2+}{}_4Fe^{3+})Si_8O_{22}(OH)_2$
Kozulite	$NaNa_2Mn^{2+}{}_4(Fe^{3+},Al)Si_8O_{22}(OH)_2$
Nyböite	$NaNa_2(Mg_3Al_2)Si_7AlO_{22}(OH)_2$
Ferronyböite	$NaNa_2(Fe^{2+}{}_3Al_2)Si_7AlO_{22}(OH)_2$
Ferric-nyböite	$NaNa_2(Mg_3Fe^{3+}{}_2)Si_7AlO_{22}(OH)_2$
Ferric-ferronyböite	$NaNa_2(Fe^{2+}{}_3Fe^{3+}{}_2)Si_7AlO_{22}(OH)_2$
Leakeite	$NaNa_2(Mg_2Fe^{3+}{}_2Li)Si_8O_{22}(OH)_2$
Ferroleakeite	$NaNa_2(Fe^{2+}{}_2Fe^{3+}{}_2Li)Si_8O_{22}(OH)_2$
Kornite*	$KNa_2(Mg_2Mn^{3+}{}_2Li)Si_8O_{22}(OH)_2$
Ungarettiite	$NaNa_2(Mn^{2+}{}_2Mn^{3+}{}_2)Si_8O_{22}O_2$

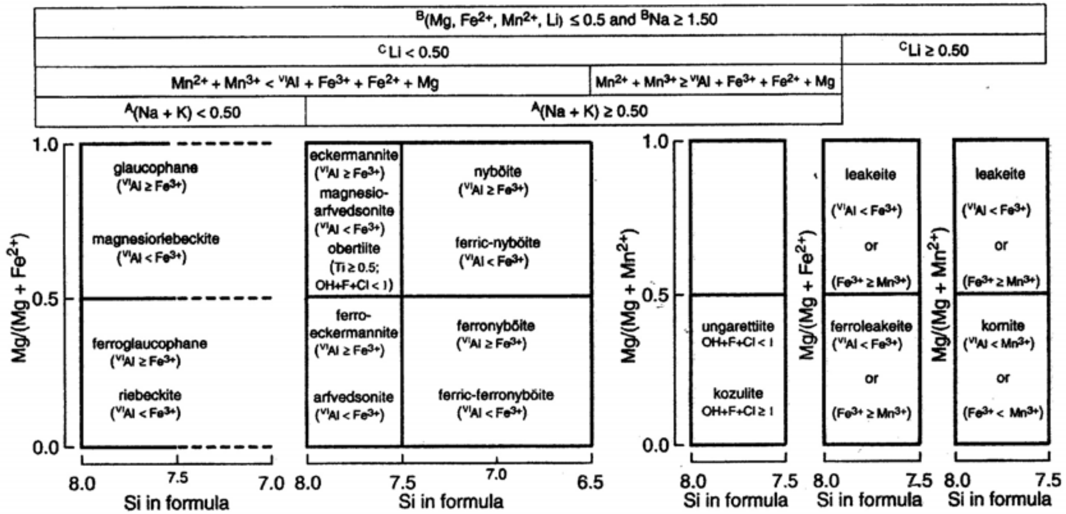

Figure 14 - Classification of sodic amphiboles; atoms in apfu. (Leake et al. 1997, 2003). - - - : end member location

The new classication scheme

In the new classification scheme of amphiboles the criterion to identify the different groups accords to the dominant B cation, and therefore an amphibole is classified as calcic if ^{B}Ca is dominant on ΣMg, ^{B}Na and ^{B}Li. Furthermore, since the different chemical behavior of ^{B}Li, previously considered by Leake et al. (1997, 2003) with $^{B}(Mg, Fe, Mn)$, ^{B}Ca e ^{B}Na, in the iron-lithium-sodium-calcium-manganese-magnesium amphibole group, it was decided to disclose the dominant ^{B}Li amphiboles as a distinct group. Another new distinct group is that of the amphiboles with O^{2-} as dominant W cation; these amphiboles contain high charge cations in C. The new scheme of classification considers the A, B, C cations as the most appropriate for the classification and not more the A, B, T cations as previously determined by Leake et al. (1997, 2003). The use of C cations can be implemented considering the content of high charge cations $^{C}M^{3+}$. The names of the groups were also redefined: it is proposed to use, not more the adjectives (for eg. calcic, sodic amphiboles), but the name of the dominant cation (eg. Ca-amphiboles or calcium amphiboles, Na- amphiboles or sodium amphiboles).

In the new scheme the amphiboles are divided into two classes according to the dominant cations in W:

1) amphiboles with $^{W}(OH, F, Cl)$-dominant.
2) amphiboles with $^{W}(O)$-dominant.

The amphiboles with $^{W}(OH, F, Cl)$-dominant are then divided, according to B dominant cations, in:

Magnesium-iron-manganese amphiboles, where$\Sigma^{B}(Mg + Fe^{2+}+Mn)$ is dominant in respect to $\Sigma^{B}(Na+Ca)$ a ^{B}Li.

Calcium amphiboles, where $\Sigma^{B}(Ca+Na)$ is dominant in respect with $\Sigma^{B}(Mg + Fe^{2+}+Mn)$ and ^{B}Li and $^{B}Ca/\Sigma^{B}(Ca+Na) \geq 0.75$.

Sodium-calcium amphiboles, where $^{B}(Ca+Na)$ is dominant in respect with $\Sigma^{B}(Mg + Fe^{2+}+Mn)$ and ^{B}Li and $0.25 < {}^{B}Ca/\Sigma^{B}(Ca+Na) < 0.75$.

Sodium amphiboles, where ^{B}(Ca+Na) is dominant in respect with Σ^{B}(Mg + Fe^{2+}+Mn) and ^{B}Li and ^{B}Ca/Σ^{B}(Ca+Na) $\leq$ 0.25.

Litium amphiboles, where ^{B}Li is dominant in respect with Σ^{B}(Mg + Fe^{2+}+Mn) and Σ^{B}(Ca+Na).

2

GEOLOGICAL FRAMEWORK OF THE AREAS OF THE EXAMINED SAMPLES

THE PIEMONTE ZONE (WESTERN ALPS)

The Piemonte Zone (Fig. 1) extends approximately for 200 km in the Western Alps, between Italy, France and Switzerland. It derives from the Mesozoic Ligurian-Piemontese Ocean and it mainly consists of Calcschists with intercalations of ophiolitic bodies. It is bounded by the Briançonnais Zone on the west and by the Internal Crystalline Massif on the east, both representing the thinned european paleo-margin. Within the Piemonte Zone, according to the litological and genetic differences, and to the metamorphic grade, the *Lanzo Ultramafic Massif*, the *Internal Piemonte Zone* and the *External Piemonte Zone* can be recognized (Fig. 1). The *Lanzo Ultramafic Massif* mainly consists of partially converted to serpentine peridotites, representing a portion of sub-continental mantle that reached, during the Alpine orogenesis, the eclogite facies (high pressure) (Piccardo et al., 2004). The *Internal Piemonte Zone* mainly consists of Calcschists deriving from the sediments of the Tetidian Ocean, with intercalations of ophiolites (serpentinites, meta-gabbros, meta-basalts). During the alpine metamorphism, the *Internal Piemonte Zone* reached the metamorphic peak of eclogite facies. The *External Piemonte Zone* is similar to *Internal Piemonte Zone*, but characterized by a metamorphic peak of blue-schist facies.

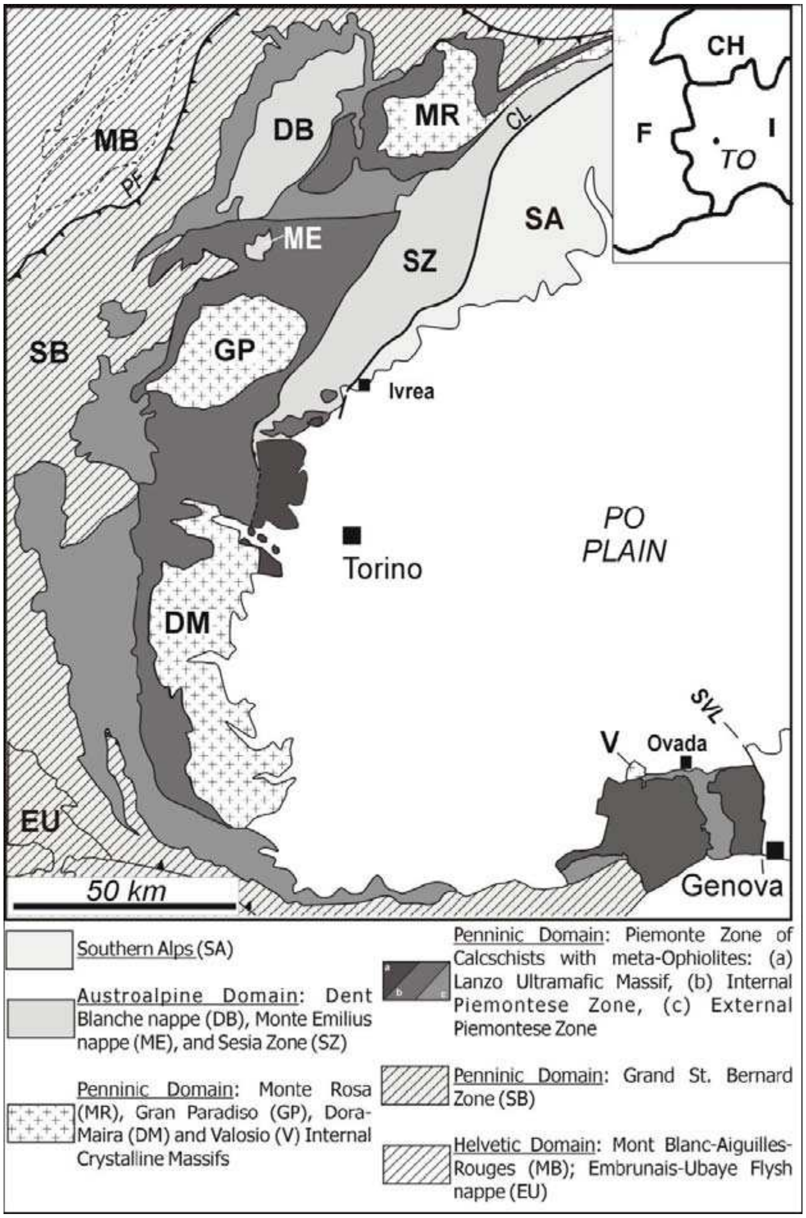

Figure 1 - Simplified tectonic sketch-map of the Italian Western Alps. Helvetic Domain: Mont Blanc-Aiguilles-Rouges (MB); Penninic Domain: Grand St. Bernard Zone (SB), and Monte Rosa (MR), Gran Paradiso (GP), Dora-Maira (DM) and Valosio (V) Internal Crystalline Massifs; Austroalpine Domain: Dent Blanche nappe (DB), Monte Emilius nappe (ME), and Sesia Zone (SZ); Southern Alps (SA); Embrunais-Ubaye Flysch nappe (EU); Voltri Massif (VM); Canavese line (CL); Sestri-Voltaggio line (SVL); Piemonte Zone of Calcschists with meta-Ophiolites (in the three grey scale) (from Grendon, 2005).

.

The Lanzo UltraMafic Massif

The Lanzo UltraMafic Massif is part of the innermost portion of the Piemonte Zone, surrounded by the Sesia Zone on the north and Dora-Maira Massif on the south, by the Po Valley on the east and the Internal Piemonte Zone on the west (Fig. 1). The Lanzo UltraMafic Massif is a large body of fresh tectonitic spinel-plagioclase lherzolite, subordinate harzburgite and rare dunites, partially converted to antigorite-serpentinite along the shear zones (Compagnoni et al., 1980; Pognante et al., 1985). According to Compagnoni et al. (1980), the serpentinization process mainly occurred during the first stage of the alpine metamorphism, causing the formation of antigorite. The alpine metamorphic evolution is well preserved in the serpentinitic portions of the Massif. It consists of a first ocean stage, followed by a peak of eclogite facies. The metamorphic conditions of the peak were: temperature 500-550°C and pressure 15-16 kbar (Compagnoni et al., 1980; Pognante, 1991). Within the serpentinite, the paragenesis of the eclogite-facies is characterized by antigorite, olivine, Ti-clinohumite, magnetite and diopside. Subsequently, the Lanzo Massif underwent a process of exhumation associated with a decreasing of both temperature and pressure, with transition from eclogite to greenschists facies (Compagnoni et al., 1980; Pognante, 1991).The conditions ranged T = 300-400°C and P = 3-4 kbar (Castelli, 1995).

Internal Piemonte Zone

The Internal Piemonte Zone is characterized by parageneses typical of the ecloglite facies. Within the Internal Piemonte Zone a metamorphic zoning between the central-southern and the northern portion can be differentiated. The central and southern portion are characterized by the presence of paragonite-eclogites and zoisite and conditions of T = 500-550°C and P = 15-16 kbar; the north portion is characterized by eclogites locally containing kyantite and conditions of T = 600-650°C and P = 20 kbar (Pognante, 1991). During the subsequent exhumation, the Piedmont International Zone was characterized by a decreasing of temperature (T = ca. 450°C) and pression (P = 11-12 kbar) (Reinecke, 1995).

External Piemonte Zone

The External Piemonte Zone is characterized by a mineralogical associations typical of blueschists facies. A metamorphic zoning between the inner (eastern) and external (western) portions can be recognized, with the presence of lawsonite and epidote, respectively.The high pressure event in the lawsonite-zone caused the formation of quartz, fengite, paragonite, chlorite, lawsonite, chloritoide, glaucofane and rutile in the meta-pelites, and glaucofane, lawsonite, fengite and paragonite parageneses in the metabasites. The presence of lawsonite suggests a temperature below ca. 400°C. Moreover, Pognante (1991) on the basis of the coexistence of glaucofane and paragonite in the metabasites, reported conditions of metamorphic peak of T = 330-350°C and P = 11-12 kbar. The high pressure event in epidote blue-schist facies zone caused the formation of quartz, fengite, paragonite, chlorite, glaucofane, chloritoide, rutile and zoisite in the metapelites and glaucofane, fengite, garnet, quartz, rutile and zoisite parageneses in the metabasites. The presence of epidote indicates a temperature above 400°C. The high pressure event is followed by a decompressional event both in the internal and the external zone. Pognante (1991) suggested that the decompressional event was almost isotherm; on the contrary Agard et al. (2000) suggested a significant decreasing of temperature from T = 350-400°C and P = 14-15 kbar to T = 300°C and P = ~5 kbar.

THE LIGURIDE UNITS ON THE CALABRIAN-LUCANIAN BORDERLINE (SOUTHERN APPENNIN)

The Liguride complex, outcropping on the Calabrian-lucanian borderline (Fig.1), consists of two ophiolitic units. The unit on the top is the *Frido Unit* (Upper Oligocene), and the unit on the bottom is the C*alabrian-lucanian Flysch Unit*. On the latter unit, turbiditic sequences as the *Formazione del Saraceno* and the *Albidonia Flysch* deposited.

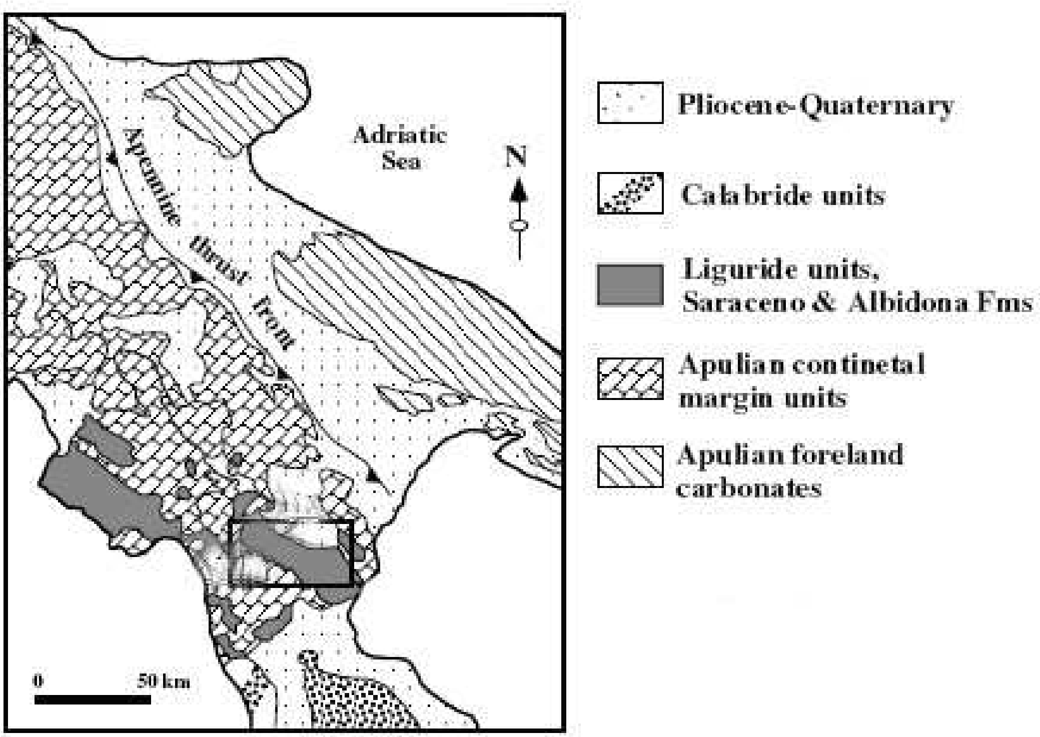

Figure 1 - Simplified geology scheme of southern Appennin (modified from Mazzoli, 1998), showing the Liguride complex outcropping on the Calabrian-lucanian borderline (in the box).

The *Frido Unit* consists of a succession of metamorphic rocks of Cretaceous-Late Oligocenic age, with ophiolitic blocks (Vezzani, 1969); within this unit two tectonic overlapping sub-units were detected. The lower unit mainly consists of argillaceous schists with intercalated meta-arenites, metasiltites and quarzites; the upper unit mainly consists of calcschists (Spadea, 1976). The ophiolitic rocks mainly consist of black-green cataclasitic serpentinite, including blocks of crystalline rocks (gneiss, amphibolite). The rocks of Frido Unity were involved in a metamorphic event of high pressure/low temperature (pressure 8-10 Kb and temperature about 400-450°C), recordered by the presence of the glaucofane-lawsonite association in the metabasalts and by the presence of aragonite in the calcschists (Monaco et al., 1993). This event was followed by a green schist facies metamorphic event (temperature around 300-350°C and pressures below the 4 Kb). The *Calabrian-lucanian Flysch Unit* is a not metamorphic succession (Monaco et al. 1993), constitued by an alternation of clay interspersed with quartz sandstone, and calcarenites including ophiolitic sequences with Upper Jurassic-Late Cretaceous sedimentary cover, Cretaceous-Eocene deep-sea sediments and Upper Oligocenic vulcanoclastic deposits. Several autors (Vezzani, 1968, Ogniben, 1969, Lanzafame et al., 1978, Spadea 1982) consider the Calabrian-Lucanian ophiolites as a strip of the original crust of the Jurassic Tetide ocean. The sequences are composed of brecciate serpentinites, gabbros and pillow's lavas, with pelagic radiolarites, limestone and red clays. On the Calabrian-Lucanian Flysch the turbiditic Oligo-Miocenic successions as the *Formazione del Saraceno* and the *Albidona flysch* are in discrepancy. The *Formazione del Saraceno* consists of an alternating of calcarenites and calclutites with lists of black flint; on the top a gradual reduction of the lists of flint and an increase of intercalated silicoclastic arenites occur. The *Albidona flysch* consists of alternated arenaceous and pelitic layers, with levels of limestone and conglomerates. On the bottom whole Bouma's sequences are present; on the contrary in the middle part and on the top only cut Bouma's sequence are present.

GEOLOGICAL SETTING OF THE CALABRIAN-PELORITANIAN ARC

The mountain chain connecting the southern Apennines with the Sicilian Maghrebides is known as Calabrian-Peloritanian Arc (Fig. 1). The Calabrian-Peloritanian Arc is a fragment of the Alpine Arc consisting of penninic, liguride and austroalpine covers, entirely thrusted during the low-Miocene on the more internal units of the future neogenic Apennine chain. In fact, close to Sangineto's line, the units of Appennines immerse under the Calabrian covers and outcrop as tectonic window between Bonifati and Catanzaro. The Sangineto's line is interpreted as a binary of left movement that allowed the chain to penetrate deeply in the Ionic Arc through a tectonic activity lasted until Tortonian. A similar role is played on the south by the Taormina's line having a right moviment.

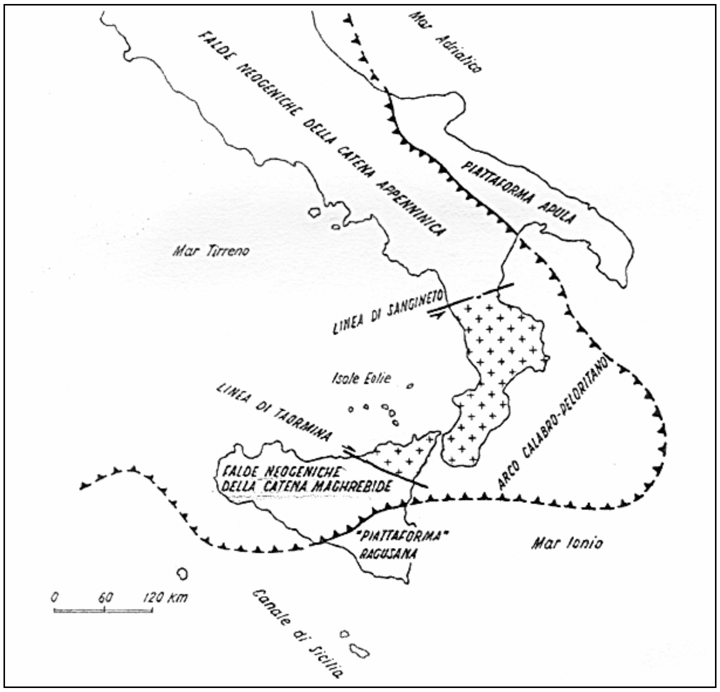

Figure 1 - Outline of the Maghrebide-Appenin system. From Amodio-Morelli et al. (1976)

The bending of the Arc, which is reflected in the calabrian physiography, was interpreted by Scandone (1975) and by-Amodio Morelli (1976) as an inheritance of the form of the African continental margin in this area. The Calabrian-Peloritanian Arc was previously considered as an unitary structure with a single evolutionary history. According to the absence of an alpine metamorphism of high P and low T on the northern area and the absence of ophiolites on the southern area, it was splitted into two areas. The first-one northern and second-one southern, separated by the tectonic line of Catanzaro. On the north area there are two mountain chains: the Costiera Chain and the reliefs of Sila separated each other by the Crati Valley (Fig. 2), where an elongated depression bounded by normal faults with NS direction has developed since the late Pleistocene onwards.

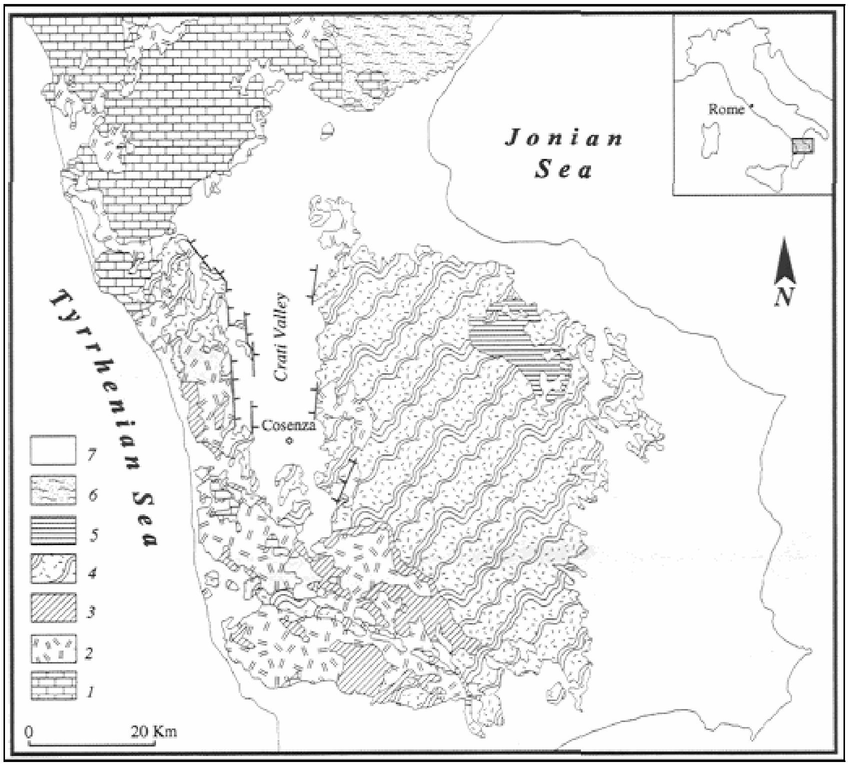

Figure 2 - Geology of northern Calabrian-Peloritanian Arc (from Piluso, 1997).

In the Calabrian-Peloritanian Arc area a sequence of thrusts consisting of apennines mesozoic sequences, ophiolitic mesozoic sequences, pre-Ercinic and Ercinic rocks of crystalline basement with intrusion of ercinian plutinic rocks outcrop. The rocks of the crystalline basement represent the remaining continental crust which underwent a long and complex evolution from the pre-Alpine to the Alpine orogenesis. During the Alpine orogenesis a portion of the continental crust separated from the southern part of the Iberian plate and thrusted on the Adriatic plate from the late Oligocene onwards (Piluso et al., 2000). Amodio-Morelli et al. (1976) divided the Calabrian-Peloritanian Arc system into three complex, which are (from the bottom to the top): the Apennine Unit Complex, the Liguride Complex, the Calabride Complex, all divided into several units (Table 1). Neogenic-Quaternary deposits discontinuously cover the Complex.

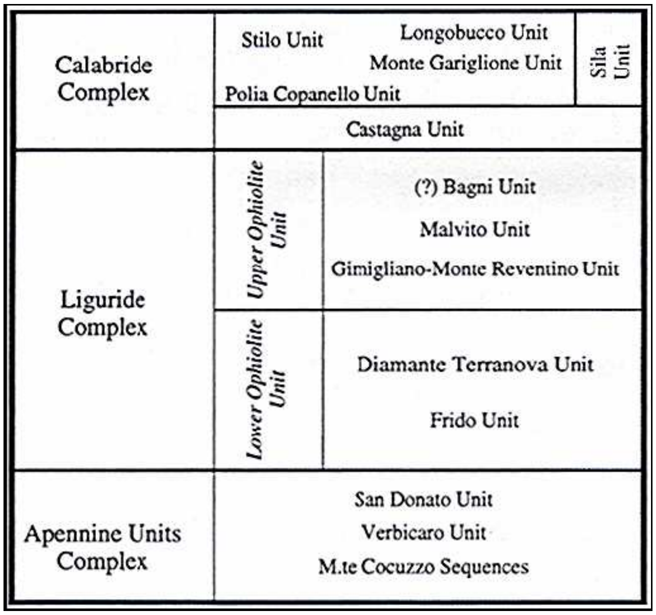

Calabride Complex	Stilo Unit Longobucco Unit Monte Gariglione Unit Polia Copanello Unit	Sila Unit
	Castagna Unit	
Liguride Complex	Upper Ophiolite Unit	(?) Bagni Unit Malvito Unit Gimigliano-Monte Reventino Unit
	Lower Ophiolite Unit	Diamante Terranova Unit Frido Unit
Apennine Units Complex	San Donato Unit Verbicaro Unit M.te Cocuzzo Sequences	

Table 1 - Breakdown of complex forming the northern Calabrian-Peloritanian Arc (Piluso et al., 2000).

The Apennines Units Complex consists of a paleozoic crystalline basement at low metamorphic grade (Ietto and Ietto, 1998) and a cover of mesozoic carbonate deposits; the Liguride Complex consists of two mesozoic ophiolitic units, considered as the remaining Tetide ocean. In agreement with the stratigraphic and structural data, these units record subduction processes and continent-continent collision associated with a subduction in E-NE direction during the pre-Lutetian (Cello et al., 1990). The Calabride Complex consists of a late-Ercinic continental crust covered by mesozoic sediments.

Gimigliano-Reventino Unit

Within the Liguride Complex there is the Gimigliano-Reventino Unit, consisting of serpentines, metabasalts and metagabbros/metadolerites, while marble, calcschists, quartzites and phyllade-quartzites representing the metamorphic terms of the original sedimentary cover. There is not yet an agreement on the age attributable to this unit: Amodio-Morelli et al. (1976) placed it in the Upper Jurassic-Cretaceous, and Vai (1992), on the basis of the correlations between basic volcanism of Gimigliano and the southern Alpine magmatism, suggests a middle-Triassic age. The unit widely outcrpos both in Costiera Chain and in Sila Piccola, from the Sangineto's line to the Nicastro-Gimigliano alignment and it is divided into two sequences: the *Fuscaldo-Rose sequence* and *Gimigliano-Reventino sequence*. The *Fuscaldo-Rose sequence* is on the Frido Unit and is tectonicly covered by the Malvito Unit on the north and by the Bagni-Fondachelli Unit on the south; it consists of green and purple metabasalts with large crystals of feldspars, meta-pillow lavas, and metabrecce with on the top rare serpentinites covered by an alternation of phyllades and meta-limestones (Amodio-Morelli et al., 1976). The *Gimigliano-Reventino sequence* overtops the Frido Unity and is covered by Bagni-Fondachelli Unit. It mainly consists of serpentinites and metabasites covered by meta-limestones and phyllades. The metabasites, mainly outcropping in the Reventino area and around the Gimigliano town, seem to derive from the metabasaltic and metadoleritic protolites; frequent veins of calcite cut the rock contributing to the its olive green color. The rocks have a grano-lepido-nematoblastic texiture due to the alternance of layers of epidotes, actinolite and chlorite with thin levels of quartz and albite.

There are also K-micas and accessories phases such as iron and titanium oxides (Piluso et al., 2000). The serpenites occur as massive bodies and are mainly composed of serpentine, rare relics of pyroxene, opaque minerals, and veins of fibrous tremolite. The serpentine is present both with laminated and fibrous morphology. In some cases relics of olivine and portions of bastites (producted by the alteration of the ortho-rombic pyroxene) can be reconized. The petrography of the serpentinites is quite similar to those of the calabrian-lucanian serpentinites (Punturo et al., 2002). Lanzafame et al. (1979) supposed that the growth of asbestiform mineral was promoted, in the ductile and brittle cutting zones, by the retrograde metamorphism (from bluschist- to that of greenschist-facies).

GEOLOGICAL SETTING OF MONTE RUFENO (ACQUAPENDENTE, VT)

The geology of the Monte Rufeno (Fig. 1) consists of two overlapping tectonic units, which were originally two different and contiguous paleo-geographical domains: the *Ligurian Domain* and *Internal Austroalpine Domain* (Buonasorte et al., 1988).

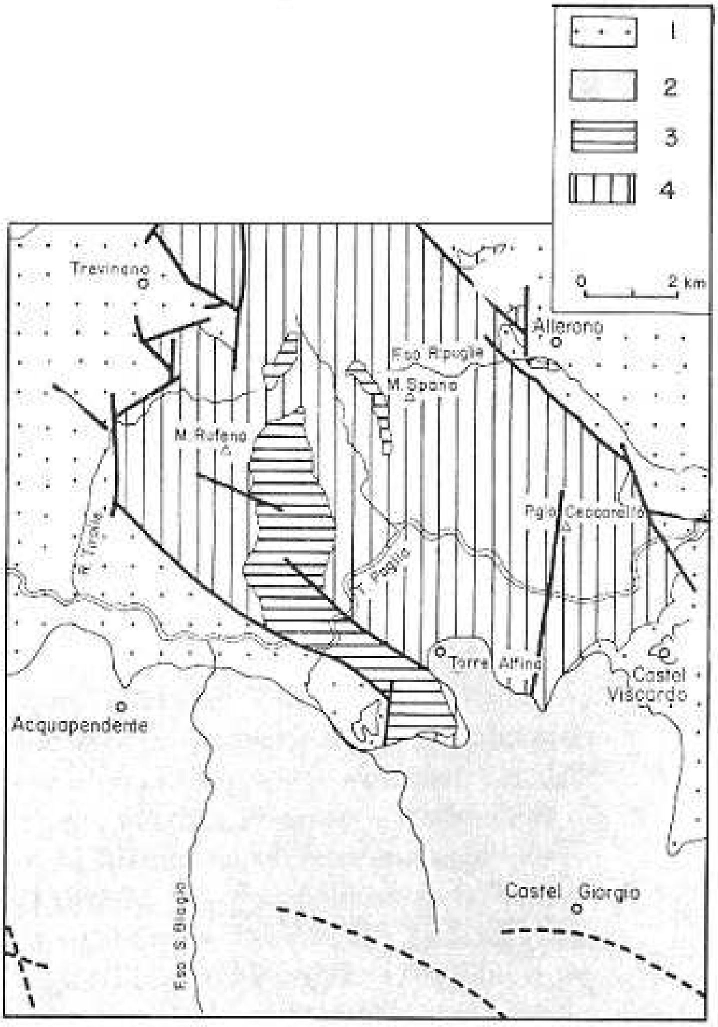

Figure 1 - Geological outline of the area of Mt. Rufeno. 1: Terrigen and marine Unit, Pliocen-Pleistocen; 2: Volcanic Unit of idromagmatic facies, middle-upper Pleistocen; 3: Formation of clays with palombini limestones and ophiolites, lower-Cretaceous; 4: Santa Fiora Formation, upper-Cretaceous-Eocene (modified from Buonasorte et al. 1988).

The units are the *Santa Fiora Unit* and the ophiolitic Unit of «*clays with palombini limestones* ». The *Santa Fiora Unit* consists of four formations that, from the most recent, are: S. Pietro Acquaeortus Formation, Poggio Belvedere Formation, Santa Fiora Formation, Villa la Selva

Formation. Villa la Selva Formation.is characterized by a turbiditic succession of calcarenites, siltites, quarz-siltites and limestones, associated with clay levels and irregularly, layers of Calpionelle limestones. Upwards the succession gradually changes to an alternation of clay, silt and siliceous limestones «palombino» type. The presence of Calpionelle suggests an age of lower Cretaceous (from the Berriasian to the Valangin-Barremiano). The transition with the S. Fiora Formation, although has never been observed directly, seems to be stratigraphic (Buonasorte et al., 1988). This formation aged between Aptian-Albiano and lower-Createaceous, consists of turbiditic arenaceous-pelitic or calcarenitic-lutitic sequences, with a green gray or red argillitic portion, (Buonasorte et al., 1988). In the formation lenticular quartz-carbonate sandstone (member of sandstone of Mount Rufeno) are also interspersed and are associated with portions of polygenic conglomerates of metamorphic (quartzite, schist filladici, schists, limestone and dolomia), volcanic (mainly rhyolite and andesite) and sedimentary (mainly carbonate) rocks. In the S. Fiora Formation olistostrome levels of the ophiolitic Unit and limestone blocks scattered in a clay matrix are present; in addition breccias and conglomerates in an ophiolitic-arenaceous matrix are also present (Buonasorte et al., 1988). The Poggio Belvedere Formation consists of turbiditic sequences, with higher amount of carbonate terms than the underlying formation. Globigerine, Gumbeline and rare Globorotalie, suggesting the lower-Paleocene age, are present (Buonasorte et al., 1988). The St. Pietro Acquaeortus Formation mainly consists of gray-nut-brown limestones and limestones with low content of clay, arenaceous rocks and argillites. Globigerine and Globoratalie Nummulites, Echinoderms, Briozoi and fragments of molluscs occur.The age was the Upper-Paleocene and the Midlle-Upper-Eocene. The ophiolitic Unit of «clays with palombini limestones» is discordant on the S. Fiora and S. Pietro Acquaeortus Formations. It is represented by a chaotic clay mass with dark gray limestone blocks and green rocks. The observed microfauna in siliceous limestone mainly consists of Radiolari and rare Calpionelle of lower Cretaceous.

GEOLOGY OF THE OPHIOLITES OF CENTRAL APPALACHIANS

The Central Appalachian Ophiolitic Complex extends from Virginia to Pennsylvania, crossing the Maryland State (USA, fig. 1). It is composed by mafic and ultra-mafic rocks (Proterozoic-early Paleozoic) such as pillow lavas, peridotites, serpentinites, gabbros and actinolitic shists. The rocks show a degree of metamorphism increasing from north to south (Drake and Morgan, 1981).

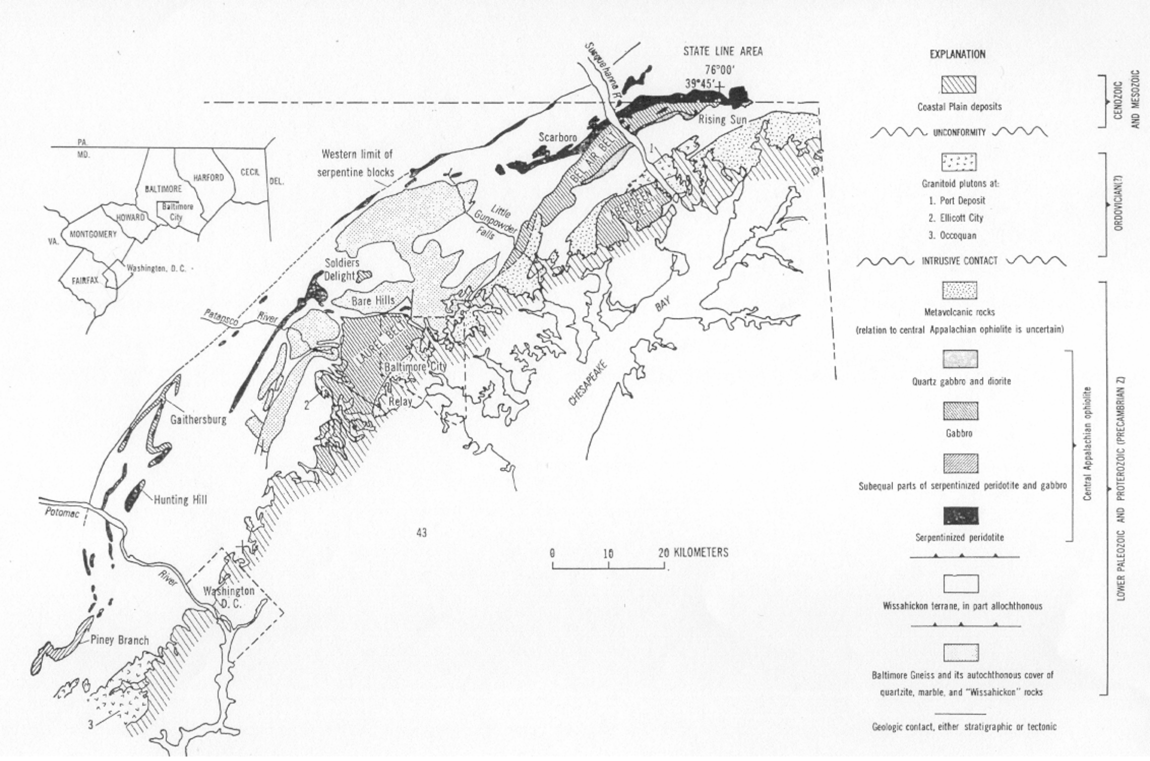

Figure 1 - Geological Map of Maryland and northern Virginia showing the distribution of the fragments appalachian ophiolites (from Drake and Morgan, 1981).

The outcropping rocks near the State Line and Maryland are the least altereted; in the serpentines relics of olivina are common and pyroxenes of ultra-mafic cumulites and gabbros are often preserved. In the most altered rocks of Baltimore Complex (Virginia), there are rare relics of olivine and the pyroxenes are partially converted to amphiboles (Hopson, 1964). The Piney Branch Complex (Virginia), located in the southern part of the Appalachian Ophiolitic Complex, shows no relic minerals because intensely metamorphosed. The samples showed a trend with a strong enrichment in iron and alkali and an impoverishment in MgO (Drake, 1981), as well as a high ratio CaO/Na_2O and low TiO_2 content. Further information on the chemistry and mineralogy of these rocks with their stratigraphic relations are reported by Morgan (1977). Drake (1986) examined the Piney Branch Complex and found fibrous actinolite confined in the anticlinal folds within actinolitic schists; Ross and Nolan (2003) revealed the presence of veins of fibrous tremolite in the serpentinitic body outcropping in Montgomery County (Maryland).

GEOLOGY OF ETNEAN AREA

The Etna, the most exstensive active volcano of Europe, stands along the northeast coast of Sicily (Fig. 1) up to 3345 meters above sea level (Fig. 2). Several authors (Rittmann, 1973; Romano, 1982; Branca et al., 2004) worked on the eruption history of this volcano. Geological studies mainly conducted in the Bove Valley allowed Rittmann (1973) to divide the history of the volcano in five main phases, later reduced to four by Romano (1982), on the basis of new geological and structural data. The first activity described by Romano (1982) was called " Subalkaline basal lavas." In this period the oldest sub-submarine and subaerial products, (about 580-460 ka) were erupted; the products outcrop in Acicastello, Acitrezza and Ficarazzi areas. The lava flows are subaerial tholeiitic basalts with transitional affinity (about 250-320 ka), and they outcrop along the south-western sector of the volcano (Valcorrente, S. Maria di Licodia, Biancavilla, Adrano). The second phase was identified with the ancient alkali eruptive centres such as the “primitive shield volcano”, Mount Po, Colonna and Trifoglietto I (between 200 and 100 Ka). The erupted products are hawaites and phonolitic tephrites, few differentiated terms of alkaline series. During this phase there was a change in eruptive style from fissural to central. The third phase, called Trifoglietto s.l., began about 100 Ka with a differentiared alcaline activity (benmoreites and mugearites) and the formation of the stratovolcano (Trifoglietto Unit) occured. The last phase is identified as Mongibello s.l., a strato-volcano, 30 Ka aged and located between the old shiled volcano on the west and south, and the Trifoglietto products on the east. This period was divided into Old Mongibello (consisting of two eruptive centres as Ellittico and Leone), and Recent Mongibello (consisting of less differentiated products). Recently, Branca et al. (2004) proposed various stages of the history of Etna based on stratigraphic and structural criteria (not more on lithological, petrochemical and stratigraphic criteria). They identified the first phase as Basal Tholeiitic phase, including products erupted between 580 and 260 Ka. The second phase, called Timpa, is characterized by a fissural activities and a shield volcano with alkaline magma. The third phase, Bove Valley, leads to the formation of small polygenic centers such as Rocche and Tarderia. After this phase there is the formation of the

Trifoglietto volcano. The most recent phase is called Stratovolcano, with the formation of the Ellittic volcano whose activity ends 15,000 years ago, after four plinian eruptions and the formation of a caldera. During the Olocene there is the Mongibello phase with a period of considerable strombolian activity.

Figure 1 - Map of Sicily, with the location of Etna.

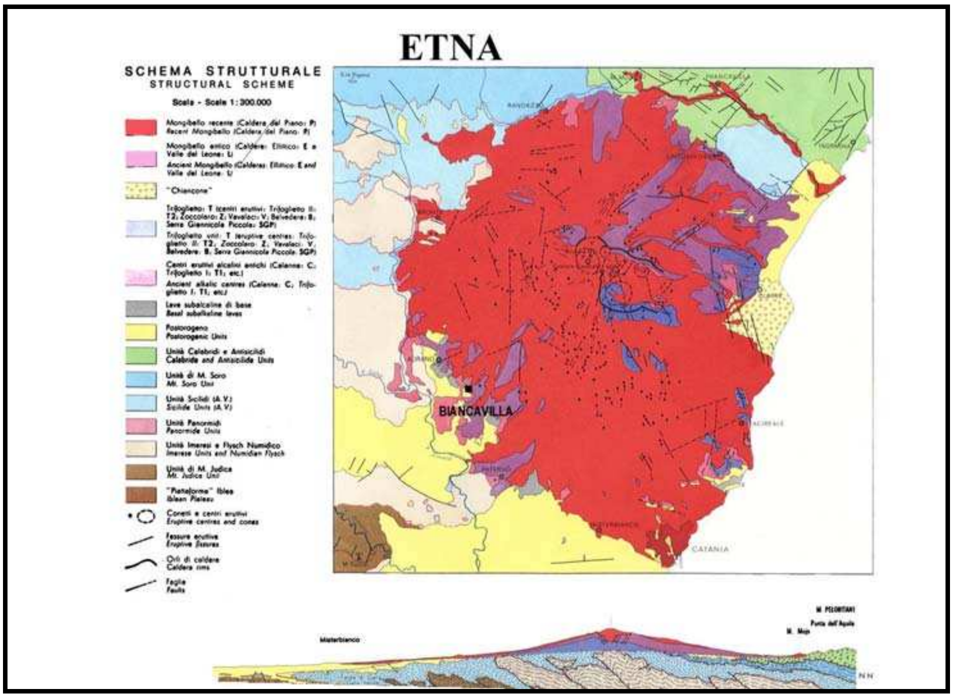

Figure 2 - Etna geological structural map (from Romano, 1982). Location of Biancavilla town.

Geology of the Biancavilla area

The town of Biancavilla is located on the south-west of the volcano Etna (Fig. 2). The outcropping products in this area concern the Old Mongibello phase and are identified into two phases: the Ellittico phase and Leone phase (Romano, 1982). The products of Ellittico phase are present on the south-western, northern and eastern flanks of the volcano; they consist of lava flows not well preserved. The products, belonging to the Ellittico phase, consist of several endogenous doma aligned in the NE-SW direction, and located in a large area between Biancavilla, Santa Maria di Licodia and Ragalna towns (Fig.3). The intrusion of such doma was attributed to an intense fissural activity of highly viscous lava. (Romano et al. 1979). In Biancavilla is present "Il Calvario" (Fig. 4), which is a benmoreitic doma locally metasomatized, associated with autocalastic breccia and mineralizations of hematite and subordinate tridimite. After this phase there was a strong explosive event (15 Ka years ago), in which the Ignimbrite of Biancavilla was erupted causing the formation of the caldera of Ellittico. The deposits outcrop around Biancavilla, in the Vallone San Filippo and in the Vallone Licodia. Romano and Sturiale (1981) examined the pyroclastic deposits of Vallone San Filippo and they divided them into four pyroclastic units. The deposits consist of volcanic material, lava blocks, pumice and sand scattered in a fine ash matrix of benmoreitic composition. In Biancavilla the deposit has a thickness ranging from 2 to 15 meters. In this area two units, probably belonging to the same eruptive event, can be distinguished. The lower unit was interpreted as a lahar deposit (Duncan, 1976), with a heterogeneous distribution of the products. The upper unit, more homogeneous, has characteristics of a pyroclastic flow. Kieffer (1979a, b) and Romano and Sturiale (1981), using ^{14}C method, carried out on this unit an age of 14 ± 26 ka BP.

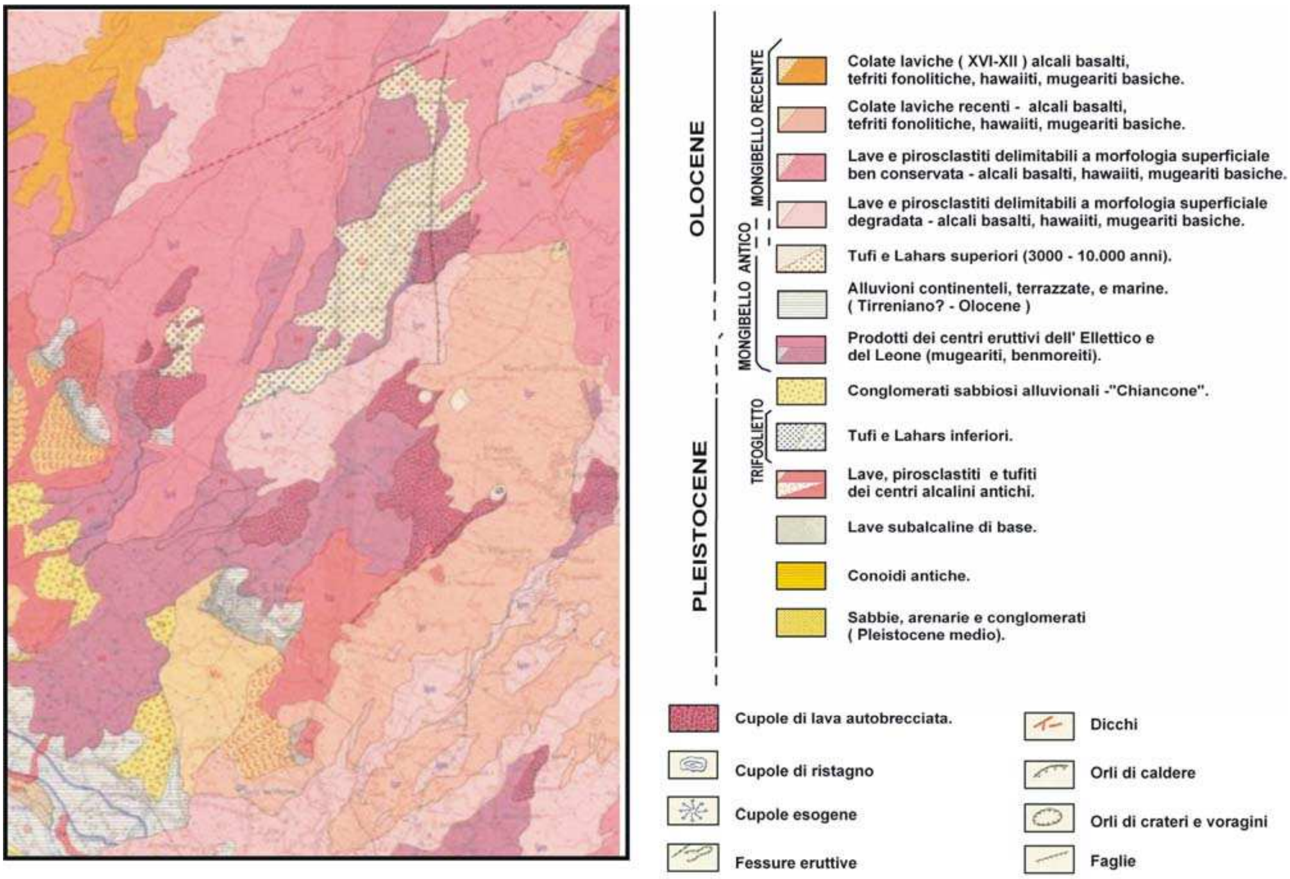

Figure 3 - Geological map of the south-western part of the Etna volcano showing the three aligned doma of brecciated lava present in Biancavilla, Santa Licodia and Ragalna (from Mazziotti-Talliani, 2007).

Figure 4 - Aerial image showing the locality “Il Calvario” (from Mazziotti-Talliani, 2007).

GEOLOGICAL SETTING OF LIBBY MONTANA (USA)

The Rainy Creek Complex

The alkaline-ultramafic Rainy Creek Complex (Fig. 1) represents an intrusion of Cretaceous age in precambrian metamorphic rocks (Belt Series) in the northwest of Montana. The pluton consists of a core of biotitite surrounded by a ring of biotite pyroxenite, in turn surrounded by a magnetite pyroxenite (Boettcher 1967).

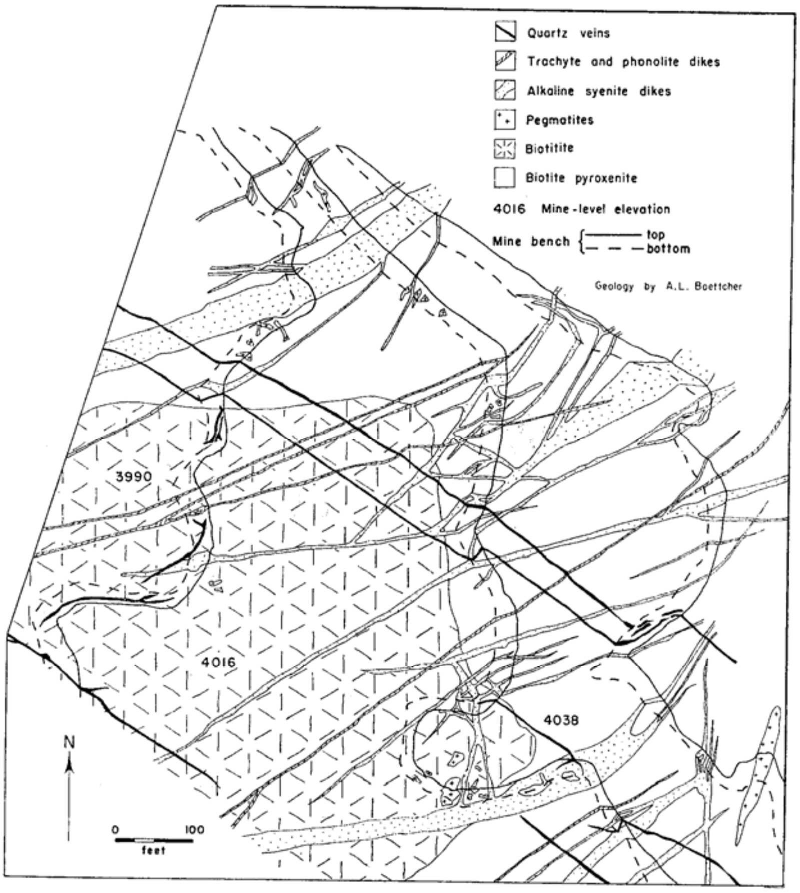

Figure 1 - Geological map of Rainy Creek Complex (from Boettcher 1966).

The mineralogical data suggested a crystallization from an alkaline magma under condition of high T, P_{H_2O}, and f_{O_2}. In the south-western sector a sienitic body, associated with dikes cutting the pyroxenite, outcrops. In the northern area a small fenitic body was identified, suggesting the presence of carbonatitic bodies in deep (Boettcher 1967). The biotite present in the pyroxenite was altered to vermiculite by a processes low-temperature weathering, and the pyroxenes were alerated in amphiboles under higher-temperature hydrotermal process (Boettcher 1966). Both pirossenitic and sienitic bodies are cut by dikes of alkaline pegmatite, alkaline granites and quartzite veins; in the in the fractures and cavities created by the dikes, prismatic and fibrous amphiboles are present. In the alterated zone the amphiboles reach concentrations from 50 to 75%. Accessory phases such as calcite, K-feldspar, talc, titanium, pyrite, limonite, quartz and albite are also present.

3

CRYSTAL-CHEMICAL AND STRUCTURAL CHARACTERIZATION OF TREMOLITES OF ENVIRONMENTAL AND HEALTH INTEREST

INTRODUCTION

Tremolite is a monoclinic (C2/m), calcic amphibole with ideal formula $\square Ca_2Mg_5Si_8O_{22}(OH)_2$. Natural tremolite samples usually contain small amounts of Fe and therefore belong to the tremolite – actinolite – ferro-actinolite series. In addition to the prismatic variety, the fibrous variety is very common and belongs to the regulated asbestos minerals, together with crocidolite, amosite, antophyllite and crysotile. When inhaled, asbestos fibers may give rise to either non-tumor diseases or malignant tumors in lungs (Martuzzi et al. 1999) and/or pleura (Mastrantonio et al. 2002). Particular attention should be paid to the role of asbestos on the rise of pleural mesothelioma (Bignon et al. 1996). The main features of such tumors are: long latency, difficult diagnosis, exposure to amphibole asbestos only (Constantopoulos et al. 1987), sensitivity to the "triggering" effect of extremely low amounts of fibers (U.S. National Research Council 1985; Piolatto 1996). Mineral fibers may promote the formation of Reactive Oxygen Species (ROS) by partially dissolving into biological fluids; toxicological studies evidenced that interactions between fibrous material and biological environment are strongly dependent on both the geometry and the crystal chemistry of mineral fibers (Stanton et al. 1981; Fubini 1993, 1996; Gilmour et al. 1997). In particular, the presence and bioavailability of Fe received considerable attention by the biomedical community. It was proposed that both the presence and structural coordination of Fe are important factors in the toxicity of asbestos (Fubini et al. 2001) and, furthermore, that only the Fe exposed on the fiber surface is relevant in the ROS production (Gazzano et al. 2005; Favero-Longo et al. 2005).

Fibers of Fe-bearing tremolite from Lanzo Valley (Piedmont, Italy) were used in an intraperitoneal injection experiment with Wistar rats, and high carcinogenicity and late timing of the mesothelioma appearance was observed (Davis et al. 1991, Addison and McConnel, 2005). However, cytotoxicity of this tremolite was later proved to be very low when compared with that of Fe-bearing tremolite fibers coming from the near Susa and Ossola Valleys (Gazzano et al., 2007; Turci et al., 2007).

Besides the mineralogical interest for the amphiboles, therefore, the crystal-chemical characterization of their fibrous varieties results particularly relevant for environmental and health aspects. The investigation on this issue has been mainly focused on working exposures so far. However, mesothelioma mortality associated with non-working exposure to amphibole fibers was observed in the Mediterranean area, such as in Greece (Langer et al. 1987) and Italy (Paoletti et al. 2000). In nature the presence of rocks containing fibrous amphiboles (and others fibrous minerals) as accessory phases is well known. The ophiolites, the most abundant of these rocks, are widely used as building and ornamental materials, because of their exceptional physical and mechanical qualities such as strength, durability, variety in appearance and color. In the Italian peninsula, especially in the Alps and the Apennines, there is a massive presence of ophiolitic outcrops rich in serpentine (chrysotile) and amphibole fibers (tremolite-actinolite and anthophyllite). The Piedmont region (NW Italy) has the largest number of such outcrops, and environmental concern was recently caused by tunnel excavations trough metamorphic rocks containing fibrous tremolite (Ballirano et al. 2008). Ophiolites hosting fibers of tremolite also outcrop in various localities in the central and southern part of Italy, such as Calabria (Punturo et al., 2004), Latium (Burragato et al., 2001). In addition, in Lauria and Castelluccio Superiore Towns, in Basilicata, the presence of fibrous tremolite was associated with health problems (Burragato et al. 2004).

In the present work, tremolite fibers sampled from such localities are investigated by means of a well tested multi-analitical approach. The localities (from north to south) are: 1) Ala di Stura (Lanzo Valley, Piedmont); 2) S. Mango (Catanzaro, Calabria); 3) Castelluccio Superiore (Potenza, Basilicata); 4) Mt. Rufeno, (Acquapendente, Latium). In addition, a sample of tremolite fibers from the Appalachian ophiolites of Maryland was also studied for comparison.

ANALYTICAL METHODS

Scanning Electron Microscopy (SEM), Electron MicroProbe Analysis (EMPA) and Inductively Coupled Plasma-Mass Spectrometry (ICP-MS)

Scanning electron microscopy (SEM) was performed using a ZEISS DSM 940A equipped with a LINK EDS system and a Philips XL30 equipped with EDAX system for EDS microanalysis. Images were obtained from a fragment of the hand specimen mounted on a sample stub and carbon coated. Analytical conditions were: 15 kV accelerating voltage and 3.4 μA beam current. Electron micrographs at different magnifications are reported in Figure 1 and show acicular morphology and fiber bundles. The chemical compostion of tremolite fibers was determined using a Cameca SX-50 electron microprobe equipped with five wavelenght-dispersive spectrometers at the following conditions: excitation voltage 15 kV acceleration , speciment current 15nA, beam diameter 5 μm, 20 s counting time (peak), 10 s counting time (background). The following standards were used: wollastonite (Si Kα, Ca Kα), rutile (Ti Kα), corundum (Al Kα), magnetite (Fe Kα), metallic Mn (Mn Kα), periclase (Mg Kα), ortoclase (K Kα), jadeite (Na Kα), metallic Cr (Cr Kα) fuorophlogopite (F Kα) and sylvite (Cl Kα). Table 1 shows the average chemical composition, while crystal-chemical formula, normalized on the basis of 24 (O+F+Cl), are reported in table 2. Cations are reporded in atoms per formula unit (apfu) and were assigned, following Hawthorne (1981), to the four A, B, C and T group sites, filled according to the order recommended by Leake et al. (1997). Table 1 also shows the results of the ICP-MS analyses used as a reference of bulk chemical composition. Cations are reporded in atoms per formula unit (apfu) and were assigned, following Hawthorne (1981), to the four A, B, C and T group sites, filled according to the order recommended by Leake et al. (1997).

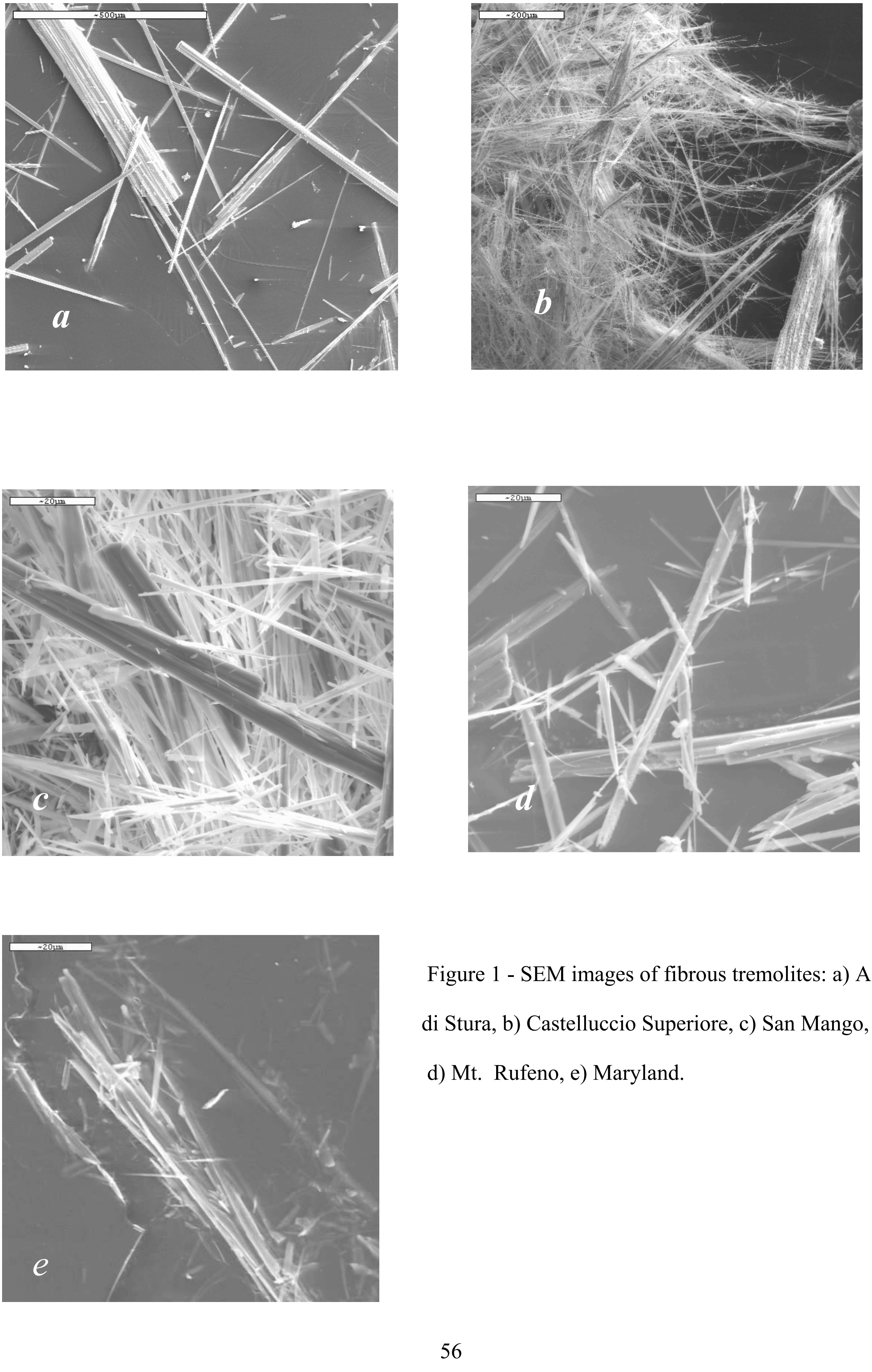

Figure 1 - SEM images of fibrous tremolites: a) Ala di Stura, b) Castelluccio Superiore, c) San Mango, d) Mt. Rufeno, e) Maryland.

Table 1 - Average chemical compositions obtained by EMP and ICP-MS analysis for the fibrous tremolites. Estimated standard deviations in brackets.

	Ala di Stura		Castelluccio		San Mango		Mt. Rufeno		Maryland	
Oxides	**EMP**	**ICP**	**EMP**	**ICP**	**EMP**	**ICP**	**EMP**	**ICP**	**EMP**	**ICP**
SiO_2	57.50(36)	-	58.04(47)	-	58.53(64)	-	56.75(42)	-	57.42(36)	-
TiO_2	0.02(2)	0.02	0.02(2)	0.03	0.01(1)	0.01	0.03(2)	0.02	0.03(2)	0.04
Al_2O_3	0.05(1)	0.04	0.16(4)	0.30	0.07(7)	0.50	0.55(7)	0.02	0.09(4)	0.15
Cr_2O_3	0.01(1)	-	0.01(2)	-	0.01(2)	-	0.03(2)	-	-	-
MgO	22.64(22)	28.01	23.36(22)	24.09	22.81(31)	21.71	22.13(28)	24.00	21.71(58)	21.28
CaO	13.14(13)	15.79	12.67(24)	12.84	13.43(28)	15.46	12.23(13)	9.41	13.45(19)	14.06
MnO	0.26(5)	0.19	0.13(4)	0.10	0.08(3)	0.09	0.10(4)	0.12	0.13(5)	0.11
FeO_{tot}	2.42(25)	2.27	2.06(16)	2.02	2.97(9)	2.94	2.23(8)	2.90	4.50(77)	4.18
Na_2O	0.06(2)	0.03	0.23(3)	0.22	0.06(2)	0.11	0.37(4)	0.11	0.02(1)	0.04
K_2O	0.03(1)	0.02	0.06(2)	0.05	0.02(1)	0.01	0.02(1)	0.03	0.01(1)	0.04
F	0.04(5)	-	0.04(6)	-	0.04(5)	-	0.05(5)	-	0.03(5)	-
Cl	0.01(1)	-	0.01(1)	-	0.01(1)	-	0.02(1)	-	0.00(1)	-
H_2O*	2.13		2.14		2.16		2.10		2.14	
	98.3		98.94		100.2		96.61		99.54	
F,Cl=O	0.02		0.02		0.02		0.02		0.01	
Total	98.28		98.92		100.18		96.59		99.53	
****Fe_2O_3**	0.32		0.48		0.20		0.60		0.80	
****FeO**	2.13		1.63		2.80		1.70		3.78	

Note: * estimated from stoichiometry.

** measured by Mössbauer spectroscopy.

Table 2 - Average crystal chemical formulas of the fibrous tremolites

Siti	**Ala di Stura**	**Castelluccio**	**San Mango**	**M.te Rufeno**	**Maryland**
Si	7.992	7.989	8.000	7.988	7.953
^{IV}Al	0.008	0.011	0.000	0.012	0.015
$\sum \boldsymbol{T}$	8.000	8.000	8.000	8.000	7.968
^{VI}Al	0.000	0.015	0.011	0.079	0.000
Ti	0.002	0.002	0.001	0.003	0.003
Cr	0.001	0.001	0.001	0.003	0.000
Fe^{3+}	0.033	0.050	0.021	0.064	0.083
Mg	4.691	4.793	4.648	4.643	4.482
Fe^{2+}	0.248	0.188	0.320	0.200	0.438
Mn	0.031	0.015	0.009	0.012	0.015
$\sum \boldsymbol{C}$	5.005	5.064	5.011	5.005	5.022
$\boldsymbol{\Delta C}$	0.005	0.064	0.011	0.005	0.022
Ca	1.957	1.869	1.967	1.845	1.996
Na	0.015	0.061	0.016	0.101	0.005
K	0.005	0.011	0.003	0.004	0.002
$\sum \boldsymbol{B}$	1.983	2.005	1.997	1.954	2.025
OH	1.977	1.967	1.971	1.974	1.974
F	0.018	0.017	0.017	0.022	0.013
Cl	0.002	0.002	0.002	0.005	0.000
$\sum \boldsymbol{O_3}$	1.996	1.986	1.991	2.001	1.987
Ca/∑M*	0.39	0.37	0.39	0.37	0.40
X_{FeA}(%)**	5.6	4.1	6.6	4.4	9.2

Note: * M = Mg + Fe^{2+} + Mn + Ni + Ti + $^{VI}Fe^{3+}$ + $^{VI}Cr^{3+}$ + ^{VI}Al

** X_{FeA}= (Fe^{2+}+Mn)/(Fe^{2+}+Mn+Mg).

Infrared spectroscopy in a Fourier transform (FT-IR)

FT-IR data were collected on a Nicolet MAGNA 760 over the range 4000-400 cm^{-1}: 32 scans at a nominal resolution of 4 cm^{-1} were averaged. The instrument was equipped with a KBr beamsplitter and a TGS detector. The powdered samples were mixed in a 2:100 ratio with 200 mg of KBr in order to obtain transparent pellets. Measurements were done in air at room temperature.

All the spectra (Fig. 2) were fitted using the PEAKFIT program (Jandel Corporation); the background was modeled with a linear function and the peaks with symmetrical Voight. Constraints were not used. Table 3 lists the values of the calculated frequencies, the width (FWHM) and intensity of the peaks.

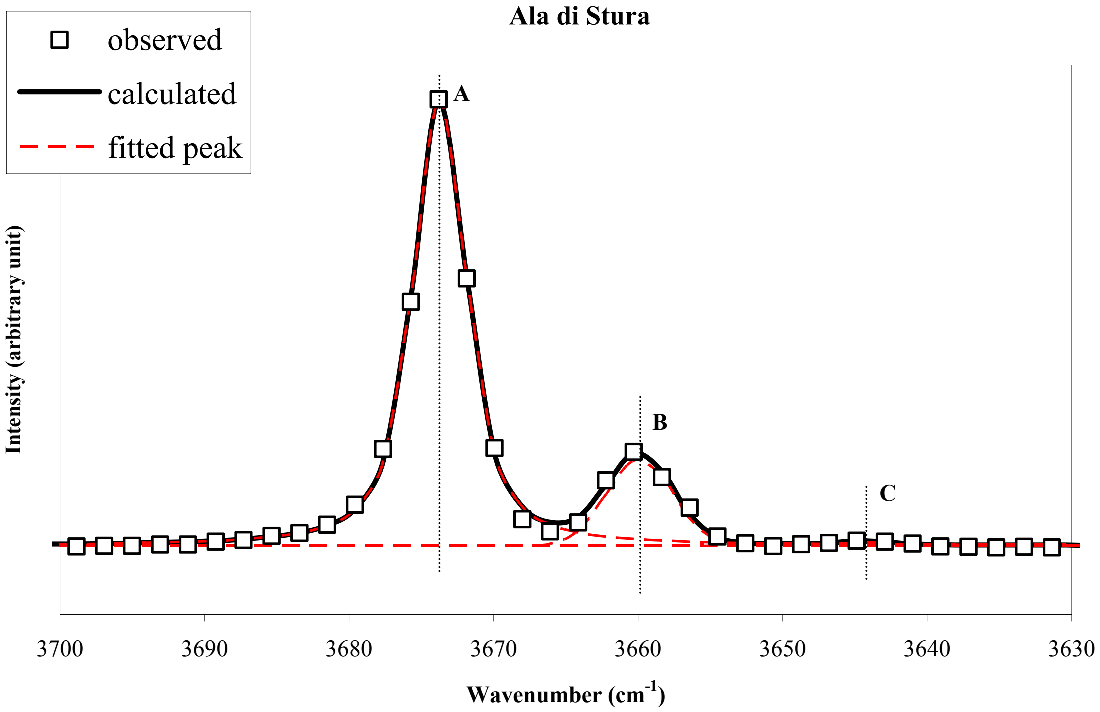
Ala di Stura
observed
calculated
fitted peak
A
B
C
Intensity (arbitrary unit)
3700
3690
3680
3670
3660
3650
3640
3630
Wavenumber (cm-1)

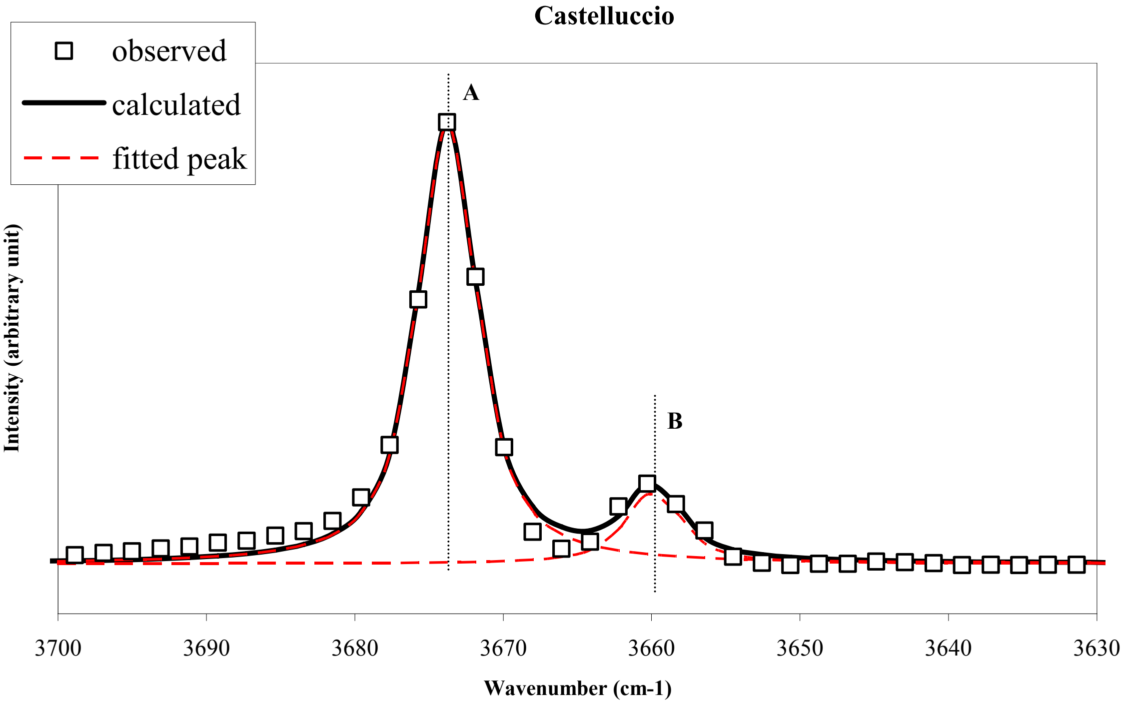
Castelluccio
observed
calculated
fitted peak
A
B
Intensity (arbitrary unit)
3700
3690
3680
3670
3660
3650
3640
3630
Wavenumber (cm-1)

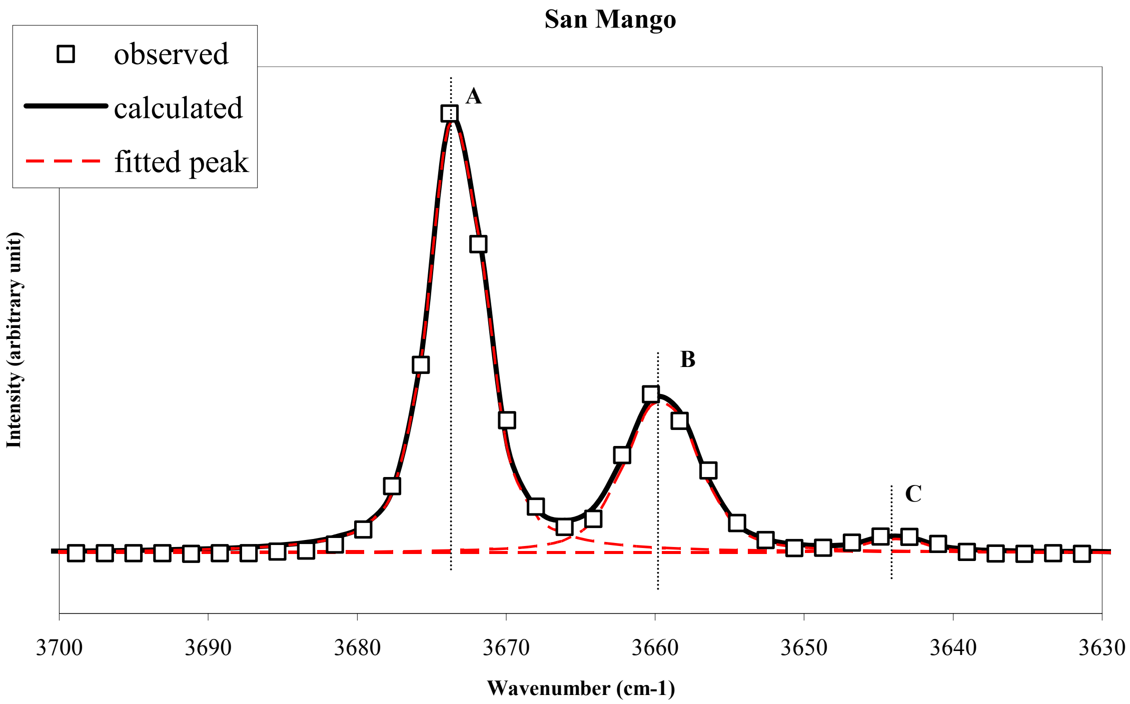
San Mango
observed
calculated
fitted peak
Intensity (arbitrary unit)
A
B
C
3700
3690
3680
3670
3660
3650
3640
3630
Wavenumber (cm-1)

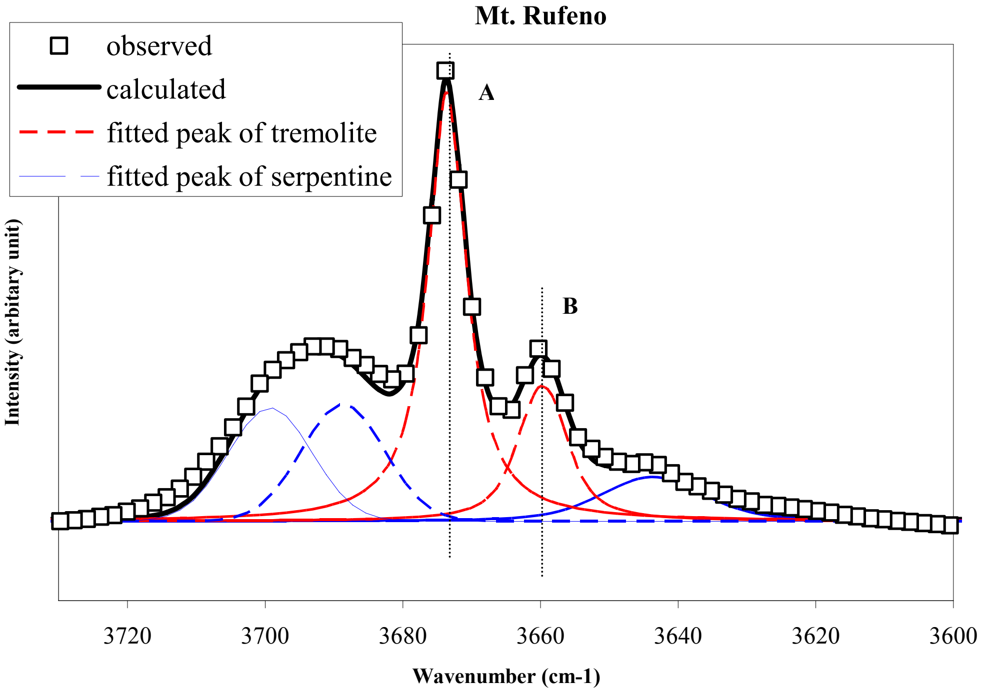
Mt. Rufeno
observed
calculated
fitted peak of tremolite
fitted peak of serpentine
Intensity (arbitary unit)
A
B
3720
3700
3680
3660
3640
3620
3600
Wavenumber (cm-1)

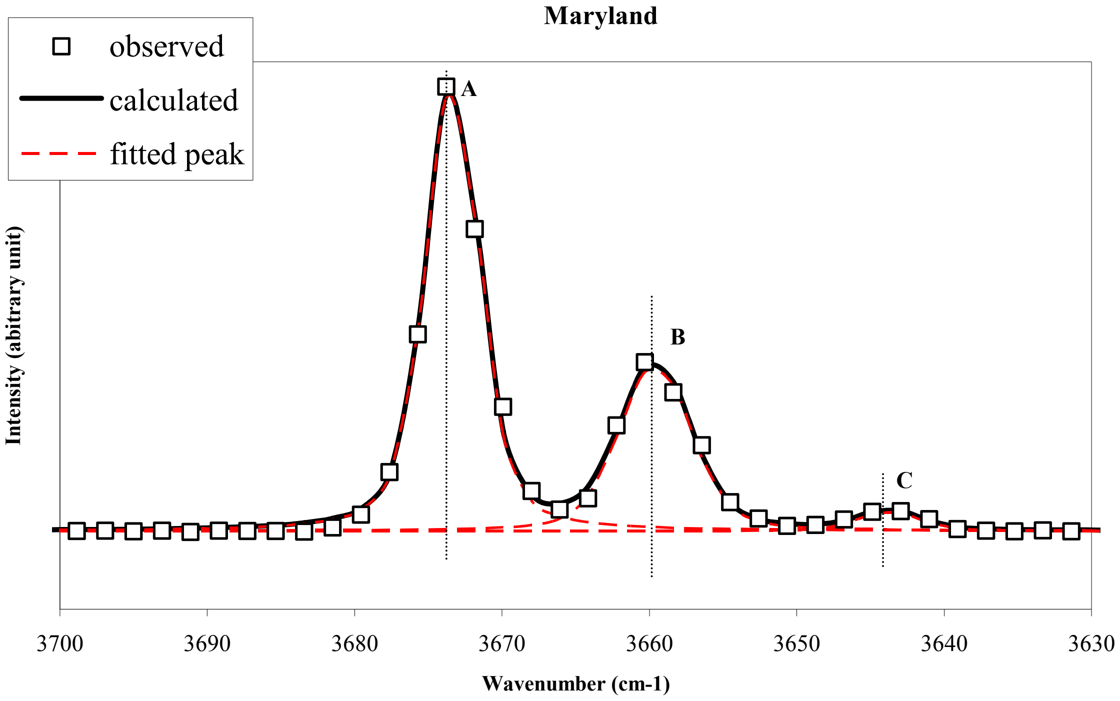

Figure 2 - FT-IR spectra in the 3700-3600 cm^{-1} range of the fibrous tremolites

Table 3- Fitted and calculated FT-IR data.

	Position	Width	Intensity	FT-IR		Mössbauer-EMP	
	(cm^{-1})	(cm^{-1})	(%)	${}^{M(1)+M(3)}Mg$	${}^{M(1)+M(3)}Fe^{2+}$	${}^{M(1)+M(3)}Mg$	${}^{M(1)+M(3)}Fe^{2+}$
		Ala di Stura		2.84	0.16	2.83	0.14
A	3674	4	84				
B	3660	5	15				
C	3644	4	1				
		Castelluccio		2.86	0.14	2.88	0.12
A	3674	5	86				
B	3660	5	14				
		San Mango		2.67	0.33	2.81	0.19
A	3673	4	68				
B	3660	6	30				
C	3644	4	2				
		Mt. Rufeno		2.74	0.26	2.88	0.12
A	3673	7	74*				
B	3660	8	26*				
		Maryland		2.60	0.40	2.74	0.27
A	3673	4	66				
B	3660	6	31				
C	3644	5	3				

Note: The intensities are correct by the correction factor (K=2.2) of Hawthorne (1997).

* normalized to 100

^{57}Fe Mössbauer Spectroscopy

The amphibole fibers were gently ground in an agate mortar with acetone and mixed with a powdered acrylic resin to avoid (or reduce) preferred orientations. About 100 mg of sample were availalble, so that the absorber was within the limits for the thin absorber thickness described by Long et al. (1983). Data were collected at room temperature, using a conventional spectrometer system operated in constant acceleration mode, with a ^{57}Co source of nominal strength of 50 mCi in rhodium matrix, and recorded in a multichannel analyzer using 512 channels for the velocity range -4 to 4 mm/s. After velocity calibration against a spectrum of high-purity α-iron foil (25 μm thick), the raw data were folded to 256 channels. The spectrum was fitted using Recoil 1.04 fitting program (Lagarec and Rancourt 1988). A first cycle of refinement was performed by fitting pure Lorentzian line-shapes (Fig. 3, Tab. 4), but the Lorentian line-shapes showed wide line-widths widths (see Γ values in Table 4). Therefore,a second cycle of refinement was carried out by fitting quadrupole-splitting distributions (QSD), following the approach of Gunter et al., 2003 and Gianfagna et al., 2007. A number of fitting models with unconstrained parameters [isomer shift(δ_0), coupling parameter (δ_1), center of Gaussian component (Δ_0), Gaussian width (σ_Δ), and absorption area(A)] were tried in order to obtain the best fit. A model based on two sites ($1Fe^{2+}$ + $1Fe^{3+}$) each with two each components was finally chosen. The increasing of the number of Gaussian components did not change the resulting distribution resulting significantly. The uncertainties have been calculated using the covariance matrix and errors were estimated no less than ±3% for both Fe^{2+} and Fe^{3+} absorption areas (Fig. 4, Table 5).

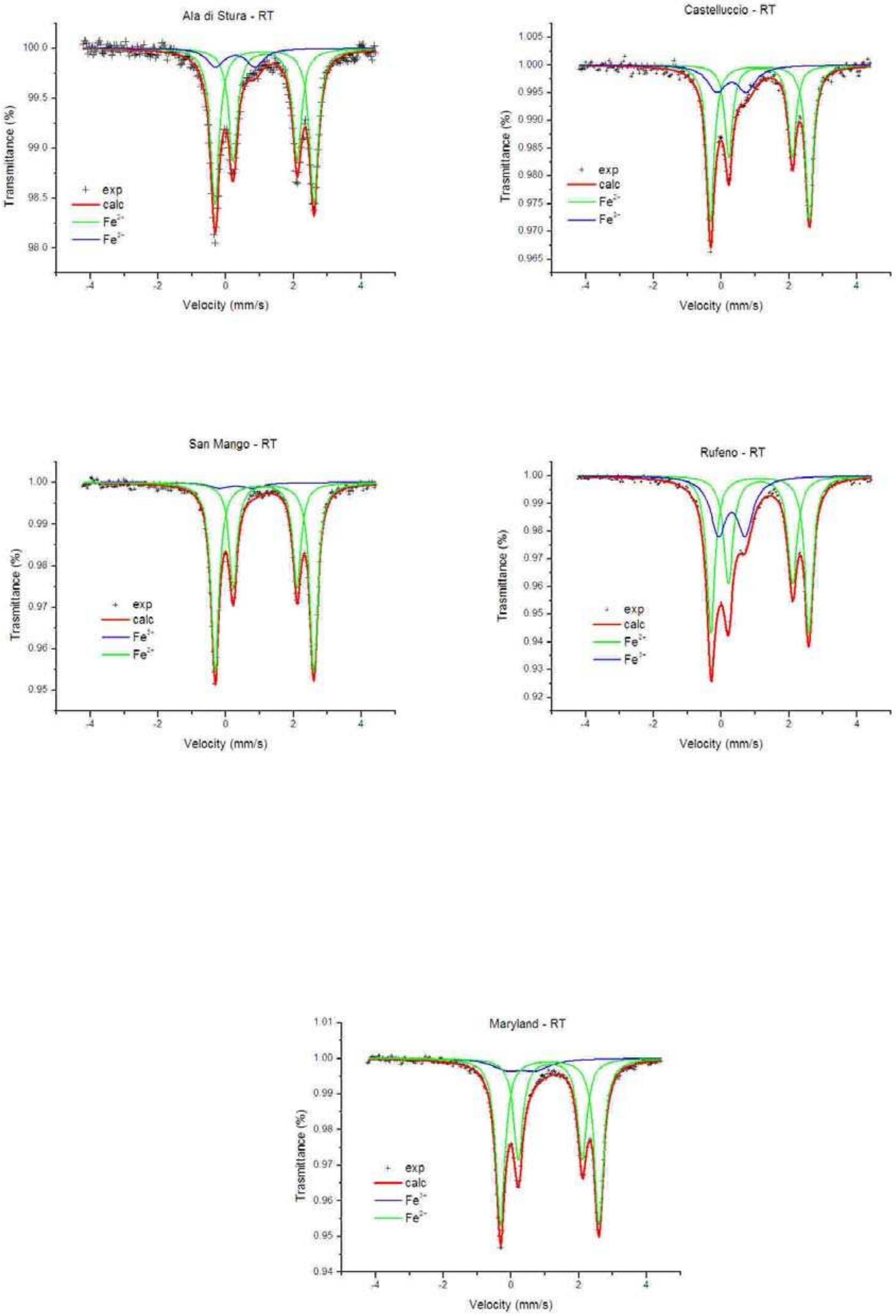

Figure 3 - Room temperature ^{57}Fe Mössbauer spectra of the fibrous tremolites.

Table 4 - Room temperature Mössbauer parameters of the fibrous tremolites. Lorentzian fitting model.

Sample	χ^2	Fe^{2+}				Fe^{3+}			
		ΔE_Q (mm/s)	Γ (mm/s)	δ (mm/s)	Area (%)	ΔE_Q (mm/s)	Γ (mm/s)	δ (mm/s)	Area (%)
Ala di Stura	0.71	1.89	0.32	1.16	38	1.17	0.60	0.28	11
		2.92	0.32	1.14	51				
Castelluccio	0.81	1.88	0.28	1.16	31	0.88	0.66	0.30*	19
		2.92	0.26	1.14	50				
San Mango	0.93	1.89	0.28	1.16	35	0.99	0.72	0.30*	4
		2.92	0.28	1.14	61				
Mt. Rufeno	0.86	1.89	0.34	1.16	32	0.79	0.56	0.31	27
		2.89	0.28	1.14	41				
Maryland	0.80	1.89	0.32	1.16	34	0.82	1.04	0.30*	11
		2.91	0.32	1.14	55				

Note: δ = centre shift (with respect to α iron); ΔE_Q = quadrupole splitting; Γ = full width half maximum.

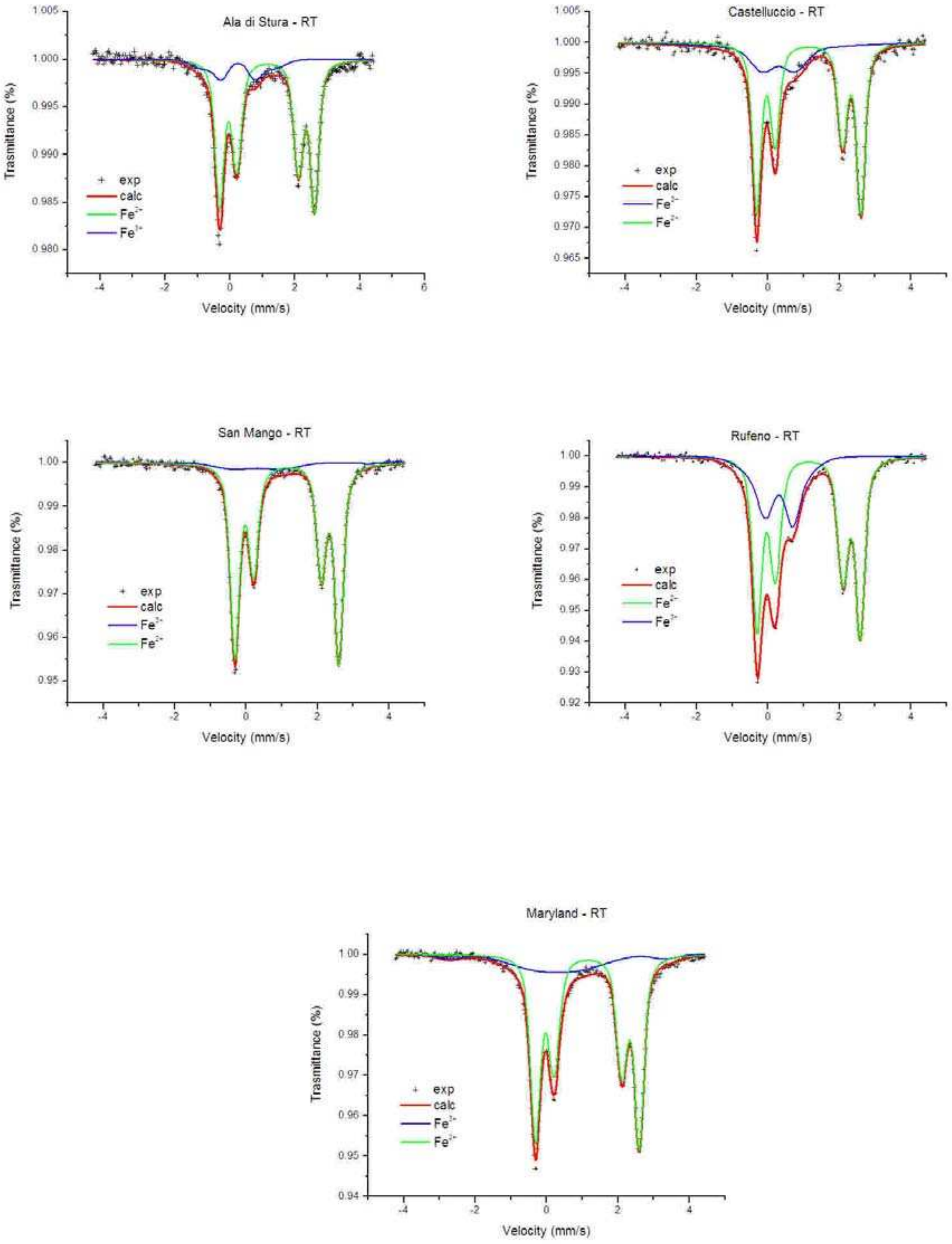

Figure 4 - Room temperature ^{57}Fe Mössbauer spectrum of the fibrous tremolites. Fitting by QSD.

Table 5 - ^{57}Fe Mössbauer hyperfine parameters at *RT* for fibrous tremolites. QSD fitting model.

Sample	χ^2	Fe^{2+}				Fe^{3+}				Fe^{3+}_{raw}	Fe^{3+}_{corr}
		Δ_0 (mm/s)	σ_Δ (mm/s)	δ_0 (mm/s)	Area (%)	Δ_0 (mm/s)	σ_Δ (mm/s)	δ_0 (mm/s)	Area (%)	(% Fe_{tot})	(% Fe_{tot})
Ala di Stura	0.79	1.89	0.20	1.19	45	1.02	0.32	0.25	56	15	12
		2.92	0.17	1.19	55	2.16	0.62	0.25	44		
Castelluccio	0.94	1.89	0.16	1.14	40	0.90	0.57	0.30*	60	24	21
		2.92	0.13	1.14	60	2.00	3.00	0.30*	40		
San Mango	0.83	1.89	0.17	1.19	63	1.32	0.97	0.30*	94	7	6
		2.91	0.15	1.19	37	6.06	0.00	0.30*	6		
Mt. Rufeno	0.65	1.89	0.21	1.18	45	0.76	0.31	0.35	51	28	24
		2.89	0.16	1.18	55	1.07	0.86	0.35	49		
Maryland	1.46	1.90	0.18	1.19	40	1.30	1.46	0.30*	85	18	16
		2.90	0.17	1.19	60	6.06	0.61	0.30*	15		

Notes: Fitting approach: Symbols according to Rancourt and Ping (1991). Quadrupole Splitting Distributions (QSD). Isomer shift (δ_0) with respect to α-iron; δ_1 always lower than 0.05; $\gamma = 0.194$ mm/s; $h_+/h_- = 1$. The Fe^{3+}_{raw} is obtained from the area of absorption peaks assigned to Fe^{3+}. The Fe^{3+}_{corr} is obtained from the raw value by applying the correction factor C = 1.22 (Dyar et al. 1993). Estimated uncertainties are about 0.02 mm/s for hyperfine parameters, and no less than 3% for absorption areas.

*:kept fixed throghout the refinement.

X-ray Powder Diffraction

Powder diffraction data were collected on a fully automated parallel-beam Bruker AXS D8Advance diffractometer, operating in trasmission mode, equipped with a Position Sensitive Detector (PSD) VÅNTEC-1. Fibers were ground under ethanol in an agate mortar and subsequently charged in a 0.7 mm diameter borosilicate glass capillary. Preliminary evaluation of the diffraction pattern indicated the presence of serpentine (a reflection at 12.5° removed from the refinement) in Ala di Stura and Rufeno samples, in addition to 10% wt of calcite (included in the refinement) in S. Mango sample. Rietveld refinement was carried out by the GSAS crystallographic suite of programs (Larson and Von Dreele 1985) using the EXPGUI grafical user interface (Toby 2001).

The background was fitted with a Chebyshev polynomial (from 25 to 36-terms) of the first kind to model the amorphous contribution arising from the capillary. Peak-shape was fitted with the TCH pseudo-Voight function (Thompson et. al 1987) modified for asymmetry (Finger et. al 1994).

Refined variables were GW (angle-independent) Gaussian parameter, LX, LY (1/cosθ and tanθ dependent) Lorenzian parameters, and S/L and H/L asymmetry parameters (constrained to be equal in magnitude). For S. Mango sample the refinement of two independent scale-factors for amphibole and calcite allowed a quantitative analysis of the mixture. Starting structural data for the fibres were those Yang and Evans (1996), whereas for the calcite were those of Sitepu e O'Connor (2005). Isotropic displacement parameters were kept fixed throughout the refinement to the reference values. Cell parameters, fractional coordinates for all the atoms, and site scattering for M(1), M(2), M(3), M(4) and M(4') were refined for the fibers. Only the cell parameters were refined for the calcite. The geometry of the system was partly restrained under the following conditions: T-O x 8 =1.625(25) Å, O-O x 12 = 2.655(40) Å, M(1)-O x 6 = 2.08(1) Å, M(2)-O x 6 = 2.08(5) Å, M(3)-O x 6 = 2.07(1) Å, M(4)-O x 8 = 2.51(15) Å, M(4')-O x 8 = 2.55(35) Å with an initial weight on the constraints of 1000. The weight associated with those observations was progressly reduced to 2 at the last stages of the refinement. However, the attempts to refine the M(4') site failed because the *y* fractional coordinate of M4' moved toward M(4) with a corresponding reduction of the occupancy to zero, indicating a nonsplit M(4) site. The presence of electron density at the A site was investigated but without any success (as further confirmed by EMP data). Attempts to model the presence of preferred orientation by means of the generalized spherical harmonics descriptions of Von Dreele (1997) produced a small improvement of the fit as a result of a J texture index very close to 1. Convergences were reached with the agreement factors reported in Table 6; fractional coordinates and isotropic displacement parameters are instead reported in Table 7, cell parameters in Table 8, selected bond distances in Table 9. The experimental and calculated patterns with the relative differences are shown in Figure 5.

Table 6 - Experimental details of the X-ray diffraction data collection and miscellaneous data of the refinement. Statistical descripotor ad defined by Young (1993).

Ala di Stura	
Instrument	Siemens D8 Advance
X-ray tube	CuKα at 40 kV and 40 mA
Incident beam optic	Multilayer X-ray mirrors
Sample mount	Rotating capillary (60 rpm)
Soller slits	2 (2.3° divergence + radial)
Divergence and antidivergence slits	0.6 mm
Detector	Position Sensitive Detector (PSD) VÅNTEC-1 opening window 6° 2θ.
2θ range (°)	5-140
Step size (°)	0.02
Counting time (s)	10
R_p (%); R_{wp} (%); R_F^2 (%)	2.19; 3.49; 6.02
Reduced $\chi 2$	14.91
Restraints contribution to $\chi 2$	76.7
Refined parameters	87
Peak-cut-off (%)	0.05
J	1.042
GW	18.9(3)
LX, LY	0.7(1), 9.0(2)
S/L=H/L	0.0273(3)

Table 6 - continue

Castelluccio	
Instrument	Siemens D8 Advance
X-ray tube	CuKα at 40 kV and 40 mA
Incident beam optic	Multilayer X-ray mirrors
Sample mount	Rotating capillary (60 rpm)
Soller slits	2 (2.3° divergence + radial)
Divergence and antidivergence slits	0.6 mm
Detector	Position Sensitive Detector (PSD) VÅNTEC-1 opening window 6° 2θ.
2θ range (°)	5-140
Step size (°)	0.02
Counting time (s)	10
R_p (%); R_{wp} (%); R_F (%)	1.51; 2.21; 2,55
Reduced χ2	6.06
Restraints contribution to χ2	84.5
Refined parameters	87
Peak-cut-off (%)	0.05
J	1.001
GW	22.1(5)
LX, LY	6.2(1), 6.6(1)
S/L=H/L	0.0233(2)

Table 6 - continue

S. Mango	
Instrument	Siemens D8 Advance
X-ray tube	CuKα at 40 kV and 40 mA
Incident beam optic	Multilayer X-ray mirrors
Sample mount	Rotating capillary (60 rpm)
Soller slits	2 (2.3° divergence + radial)
Divergence and antidivergence slits	0.6 mm
Detector	Position Sensitive Detector (PSD) VÅNTEC-1 opening window 6° 2θ.
2θ range (°)	5-140
Step size (°)	0.02
Counting time (s)	10
R_p (%); R_{wp} (%); R_F (%)	1.68; 2.48; 3,72
Reduced $\chi2$	8.19
Restraints contribution to $\chi2$	85.0
Refined parameters	89
Peak-cut-off (%)	0.2
J	1.030
GW	17.8(4)
LX, LY	2.4(1), 8.3(2)
S/L=H/L	0.0271(3)
Amphibole; calcite (wt %)	90.1(4); 9.90(5)

Table 6 - continue

Mt. Rufeno	
Instrument	Siemens D8 Advance
X-ray tube	CuKα at 40 kV and 40 mA
Incident beam optic	Multilayer X-ray mirrors
Sample mount	Rotating capillary (60 rpm)
Soller slits	2 (2.3° divergence + radial)
Divergence and antidivergence slits	0.6 mm
Detector	Position Sensitive Detector (PSD) VÅNTEC-1 opening window 6° 2θ.
2θ range (°)	5-140
Step size (°)	0.02
Counting time (s)	10
R_p (%); R_{wp} (%); R_F (%)	6.11; 7.88; 5.87
Reduced $\chi2$	2.95
Restraints contribution to $\chi2$	104.3
Refined parameters	84
Peak-cut-off (%)	0.5
J	1.012
GU, GV, GW	316(29), -181(18), 67(4)
LX, LY	4.2(1), 19(2)
S/L=H/L	0.0290(6)

Table 6 - continue

Maryland	
Instrument	Siemens D8 Advance
X-ray tube	CuKα at 40 kV and 40 mA
Incident beam optic	Multilayer X-ray mirrors
Sample mount	Rotating capillary (60 rpm)
Soller slits	2 (2.3° divergence + radial)
Divergence and antidivergence slits	0.6 mm
Detector	Position Sensitive Detector (PSD) VÅNTEC-1 opening window 6° 2θ.
2θ range (°)	5-145
Step size (°)	0.02
Counting time (s)	10
R_p (%); R_{wp} (%); R_F^2 (%)	2.41; 3.14; 4.34
Reduced $\chi 2$	1.89
Restraints contribution to $\chi 2$	91.5
Refined parameters	77
Peak-cut-off (%)	0.02
J	1.026
GW	19.2(3)
LY	14.5(2)
S/L=H/L	0.0246(3)

Table 7 - Fractional coordinates and isotropic displacement parameters (not refined) for the fibrous tremolites.

Ala di Stura

Site	*x*	*y*	*z*	U_{iso} (Å^2)
O(1)	0.1161(6)	0.08577(29)	0.2190(14)	0.008
O(2)	0.1180(7)	0.17225(33)	0.7233(14)	0.008
O(3)	0.1086(7)	0	0.7144(19)	0.008
O(4)	0.3648(6)	0.24733(27)	0.7863(17)	0.008
O(5)	0.3431(7)	0.13367(29)	0.0944(15)	0.008
O(6)	0.3460(7)	0.11632(25)	0.5980(16)	0.008
O(7)	0.3426(7)	0	0.2929(20)	0.008
T(1)	0.28274(33)	0.08374(15)	0.2978(8)	0.005
T(2)	0.2886(4)	0.17043(14)	0.8018(8)	0.005
M(1)	0	0.08811(23)	0.5	0.006
M(2)	0	0.17708(23)	0	0.006
M(3)	0	0	0	0.006
M(4)	0	0.27735(15)	0.5	0.008
H	0.206*	0*	0.771*	0.030

Note: * Kept fixed throghout the refinement.

Table 7 - continue

Castelluccio				
Site	*x*	*y*	*z*	U_{iso} (Å^2)
O(1)	0.1140(4)	0.08624(18)	0.2197(7)	0.008
O(2)	0.1149(4)	0.17200(20)	0.7245(7)	0.008
O(3)	0.1077(4)	0	0.7140(9)	0.008
O(4)	0.3635(4)	0.24785(16)	0.7929(8)	0.008
O(5)	0.3466(5)	0.13301(17)	0.0955(7)	0.008
O(6)	0.3438(5)	0.11717(16)	0.5925(8)	0.008
O(7)	0.3383(5)	0	0.2873(10)	0.008
T(1)	0.28019(21)	0.08397(9)	0.2973(4)	0.005
T(2)	0.28784(24)	0.17060(9)	0.8039(4)	0.005
M(1)	0	0.08708(14)	0.5	0.006
M(2)	0	0.17642(15)	0	0.006
M(3)	0	0	0	0.006
M(4)	0	0.27767(9)	0.5	0.008
H	0.206*	0*	0.771*	0.030

Note: * Kept fixed throghout the refinement.

Table 7 - continue

San Mango

Site	*x*	*y*	*z*	U_{iso} (Å^2)
O(1)	0.1148(5)	0.08622(22)	0.2184(8)	0.008
O(2)	0.1171(6)	0.17190(24)	0.7234(8)	0.008
O(3)	0.1092(6)	0	0.7131(11)	0.008
O(4)	0.3653(5)	0.24752(20)	0.7931(9)	0.008
O(5)	0.3469(6)	0.13368(21)	0.0992(9)	0.008
O(6)	0.3461(6)	0.11656(19)	0.5951(10)	0.008
O(7)	0.3405(7)	0	0.2888(12)	0.008
T(1)	0.28035(27)	0,08382(11)	0.2971(5)	0.005
T(2)	0.28812(29)	0.17086(10)	0.8040(5)	0.005
M(1)	0	0.08723(17)	0.5	0.006
M(2)	0	0.17687(18)	0	0.006
M(3)	0	0	0	0.006
M(4)	0	0.27745(11)	0.5	0.008
H	0.206*	0*	0.771*	0.030

Note: * Kept fixed throghout the refinement.

Table 7 - continue

Mt. Rufeno

Site	*x*	*y*	*z*	U_{iso} (Å^2)
O(1)	0.1120(8)	0.0873(4)	0.2209(16)	0.008
O(2)	0.1172(9)	0.1712(4)	0.7246(19)	0.008
O(3)	0.1098(10)	0	0.7175(20)	0.008
O(4)	0.3659(9)	0.2472(4)	0.7939(21)	0.008
O(5)	0.3482(11)	0.1334(4)	0.0955(18)	0.008
O(6)	0.3404(10)	0.1165(4)	0.5909(20)	0.008
O(7)	0.3344(12)	0	0.2748(26)	0.008
T(1)	0.2784(4)	0,08589(23)	0.2949(10)	0.005
T(2)	0.2897(5)	0.16999(21)	0.8080(11)	0.005
M(1)	0	0.08733(35)	0.5	0.006
M(2)	0	0.1740(4)	0	0.006
M(3)	0	0	0	0.006
M(4)	0	0.27527(23)	0.5	0.008
H	0.206*	0*	0.771*	0.030

Note: * Kept fixed throghout the refinement.

Table 7 - continue

Maryland

Site	*x*	*y*	*z*	U_{iso} (Å^2)
O(1)	0.1137(6)	0.08582(28)	0.2190(10)	0.008
O(2)	0.1178(7)	0.17158(30)	0.7260(11)	0.008
O(3)	0.1071(7)	0	0.7122(12)	0.008
O(4)	0.3652(8)	0.24714(25)	0.7943(12)	0.008
O(5)	0.3463(8)	0.13447(27)	0.0976(11)	0.008
O(6)	0.3443(8)	0.11826(25)	0.5923(12)	0.008
O(7)	0.3354(10)	0	0.2903(16)	0.008
T(1)	0.2793(4)	0.08406(15)	0.2964(6)	0.005
T(2)	0.2873(4)	0.17117(15)	0.8032(6)	0.005
M(1)	0	0.08830(22)	0.5	0.006
M(2)	0	0.17651(23)	0	0.006
M(3)	0	0	0	0.006
M(4)	0	0.27751(15)	0.5	0.008
H	0.206*	0*	0.771*	0.030

Note: * Kept fixed throghout the refinement.

Table 8 - Unit-cell parameters of the fibrous tremolites. Reference data of Yang ed Evans, 1996 (Y&E96) are also shown for comparison.

	***a* (*Å*)**	***b* (*Å*)**	***c* (*Å*)**	***β*(°)**	***V* (*Å*^{3})**
Ala di Stura	9.8424(1)	18.0712(2)	5.28354(7)	104.680(1)	909.07(2)
Castelluccio	9.8477(1)	18.0623(2)	5.28086(4)	104.742(1)	908.40(2)
San Mango	9.8474(1)	18.0753(2)	5.28246(4)	104.758(1)	909.23(1)
Mt. Rufeno	9.8354(3)	18.0567(6)	5.2775(2)	104.664(3)	906.72(6)
Maryland	9.8538(2)	18.0709(2)	5.27903(6)	104.738(1)	909.09(2)
Y&E96	9.8356(12)	18.0557(22)	5.2785(6)	104.782(9)	906.4(2)

Table 9 - Selected bond distances (Å) and polyhedral distortion ($\Delta \times 10^4$) for the fibrous tremolites. Reference data of Yang and Evans 1996 (Y&E96) from single-crystal are reported for comparison. Polyhedral distortion Δ as defined by Brown and Shannon (1973): $\Delta = (1/n)\Sigma[(R_i-R)/R]^2$ where n is the number of ligands. R is the average bond lenght and R_i an individual bond lenght.

Sample	**Ala**	**Castell.**	**S.Mango**	**Rufeno**	**Maryland**	**Y&E96**	**Sample**	**Ala**	**Castell.**	**S.Mango**	**Rufeno**	**Maryland**	**Y&E96**
T(1)-O(1)	1.587(5)	1.583(3)	1.577(4)	1.583(8)	1.587(6)	1.600(1)	**T(2)-O(4)**	1.591(5)	1.590(3)	1.588(4)	1.594(7)	1.579(5)	1.587(1)
T(1)-O(7)	1.627(3)	1.627(2)	1.632(3)	1.658(5)	1.620(4)	1.619(1)	**T(2)-O(2)**	1.624(5)	1.648(4)	1.629(5)	1.641(8)	1.615(6)	1.612(1)
T(1)-O(5)	1.627(6)	1.644(3)	1.638(4)	1.637(8)	1.650(5)	1.633(2)	**T(2)-O(6)**	1.656(7)	1.672(4)	1.682(4)	1.669(9)	1.669(5)	1.676(1)
T(1)-O(6)	1.658(8)	1.638(4)	1.652(5)	1.623(10)	1.650(6)	1.630(2)	**T(2)-O(5)**	1.643(8)	1.647(4)	1.661(5)	1.621(10)	1.653(5)	1.656(2)
<T(1)-O>	1.625	1.623	1.625	1.625	1.627	1.620	**<T(2)-O>**	1.629	1.639	1.640	1.631	1.629	1.633
Δ	2.4	2.2	3.1	2.8	2.6	0.6	**Δ**	2.3	3.4	4.7	2.8	4.6	4.6
M(1)-O(3) x 2	2.085(5)	2.066(3)	2.072(4)	2.084(7)	2.077(4)	2.087(1)	**M(2)-O(4) x 2**	2.037(7)	2.031(4)	2.021(5)	2.055(10)	2.028(7)	2.019(1)
M(1)-O(1) x 2	2.091(7)	2.074(4)	2.085(5)	2.050(8)	2.074(5)	2.067(1)	**M(2)-O(2) x 2**	2.087(6)	2.059(3)	2.081(4)	2.072(9)	2.074(6)	2.088(1)
M(1)-O(2) x 2	2.088(6)	2.087(4)	2.091(5)	2.082(8)	2.081(5)	2.081(1)	**M(2)-O(1) x 2**	2.167(6)	2.144(4)	2.151(4)	2.092(9)	2.149(6)	2.134(1)
<M(1)-O>	2.088	2.076	2.083	2.072	2.077	2.078	**<M(2)-O>**	2.097	2.078	2.084	2.073	2.084	2.080
Δ	0.0	0.2	0.1	0.6	0.0	0.2	**Δ**	6.5	5.3	6.5	0.5	5.7	5.2
M(3)-O(3) x 2	2.058(9)	2.055(4)	2.069(5)	2.050(9)	2.059(6)	2.062(2)	**M(4)-O(4) x 2**	2.297(7)	2.339(4)	2.325(4)	2.312(9)	2.329(6)	2.327(1)
M(3)-O(1) x 4	2.092(6)	2.090(4)	2.091(4)	2.099(7)	2.083(5)	2.073(1)	**M(4)-O(2) x 2**	2.378(7)	2.376(4)	2.381(5)	2.361(9)	2.394(6)	2.405(1)
<M(3)-O>	2.081	2.078	2.079	2.083	2.075	2.069	**M(4)-O(6) x 2**	2.580(6)	2.570(3)	2.571(4)	2.626(8)	2.553(6)	2.535(2)
Δ	0.6	0.6	0.2	1.2	0.3	0.1	**M(4)-O(5) x 2**	2.808(7)	2.794(4)	2.777(5)	2.809(9)	2.775(6)	2.766(1)
							<M(4)-O>	2.516	2.520	2.520	2.527	2.513	2.508
T1-O5-T2	139.4(5)	136.5(3)	136.4(4)	135.1(7)	135.8(5)		**Δ**	62	52	46	64	47	44
T1-O6-T2	136.4(5)	135.3(3)	135.9(4)	138.8(7)	136.9(5)								
T1-O7-T1	137.0(6)	137.6(4)	136.4(5)	138.6(8)	139.4(7)								

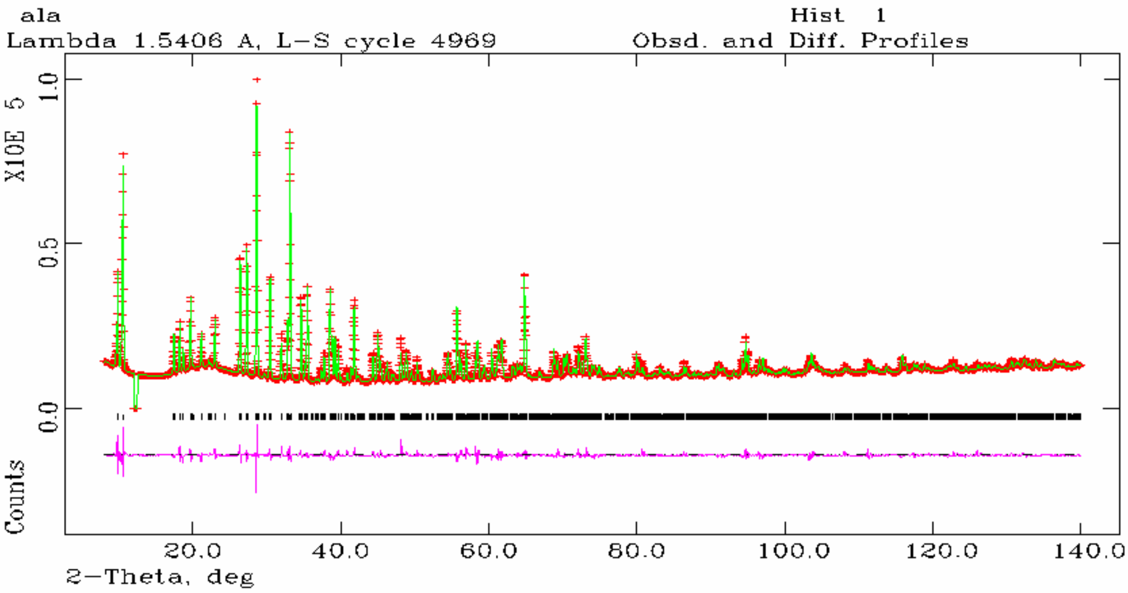
ala
Hist 1
Lambda 1.5406 A, L-S cycle 4969
Obsd. and Diff. Profiles
Counts
X10E 5
0.0
0.5
1.0
20.0
40.0
60.0
80.0
100.0
120.0
140.0
2-Theta, deg

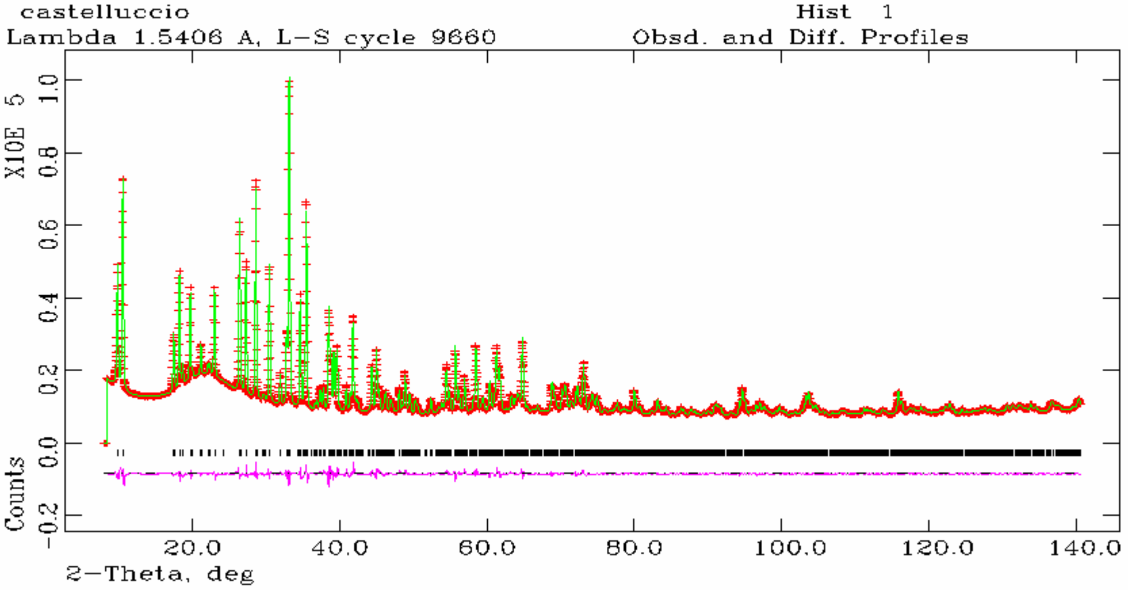
castelluccio
Hist 1
Lambda 1.5406 A, L-S cycle 9660
Obsd. and Diff. Profiles
Counts
X10E 5
-0.2
0.0
0.2
0.4
0.6
0.8
1.0
20.0
40.0
60.0
80.0
100.0
120.0
140.0
2-Theta, deg

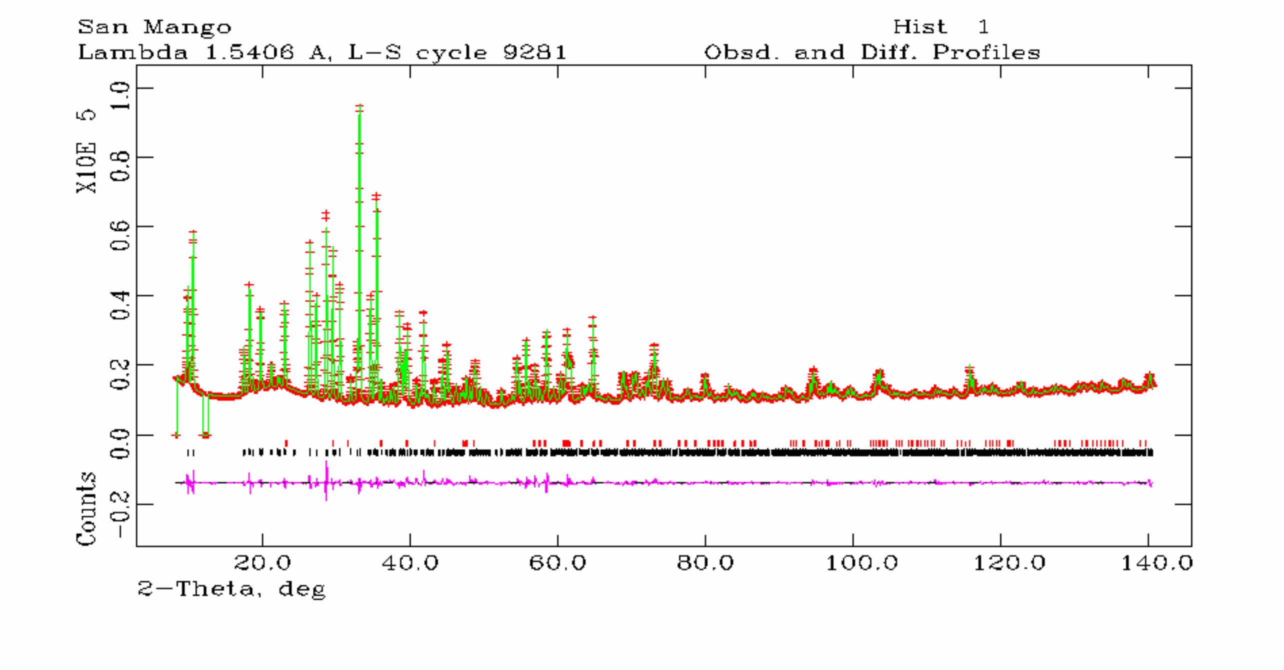
San Mango
Hist 1
Lambda 1.5406 A, L-S cycle 9281
Obsd. and Diff. Profiles
X10E 5
Counts
1.0
0.8
0.6
0.4
0.2
0.0
-0.2
20.0
40.0
60.0
80.0
100.0
120.0
140.0
2-Theta, deg

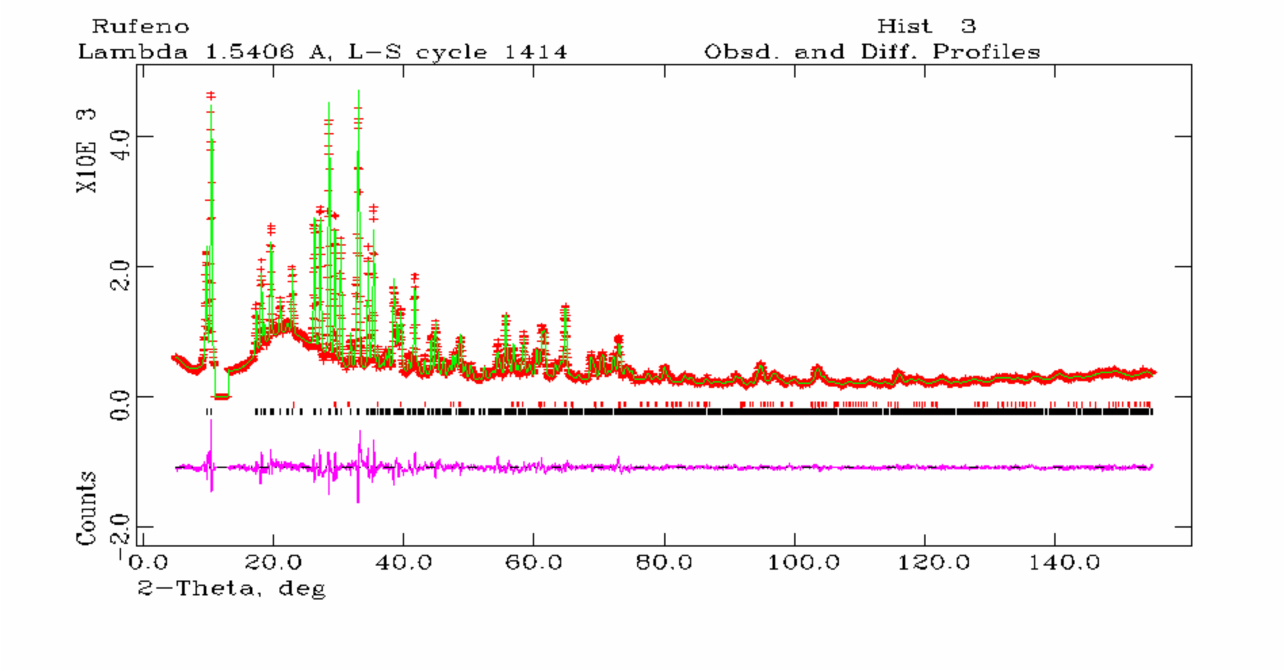
Rufeno
Hist 3
Lambda 1.5406 A, L-S cycle 1414
Obsd. and Diff. Profiles
X10E 3
Counts
4.0
2.0
0.0
-2.0
0.0
20.0
40.0
60.0
80.0
100.0
120.0
140.0
2-Theta, deg

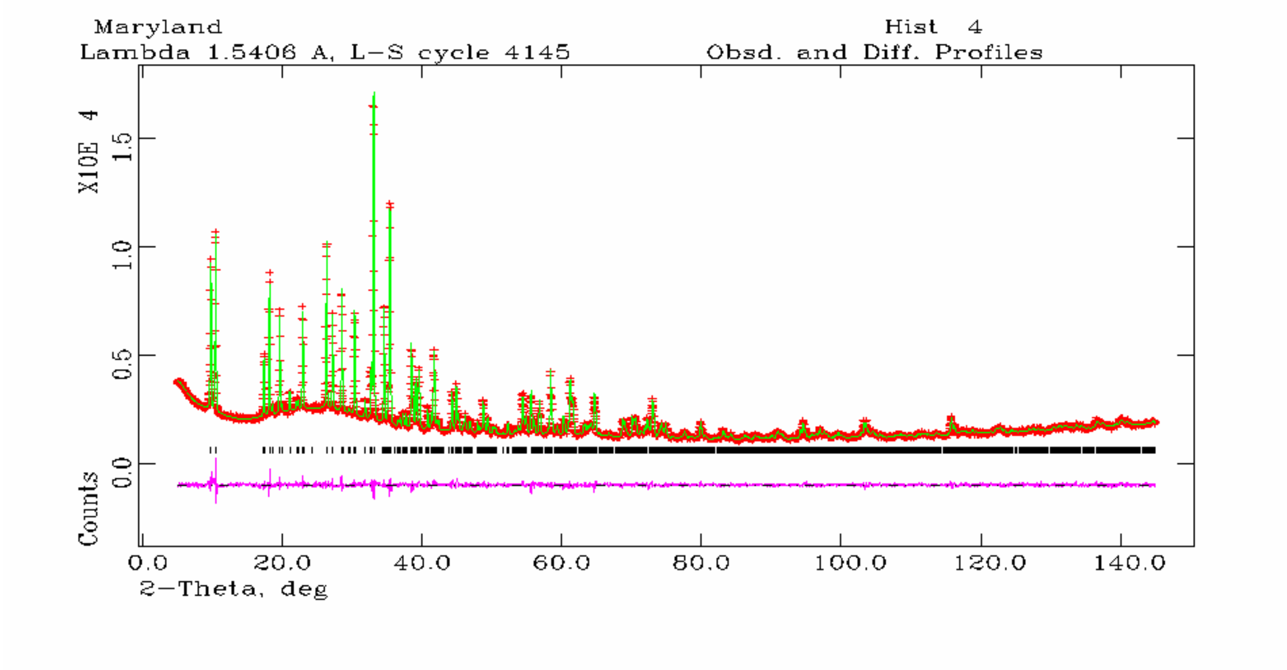

Figure 5 - Experimental (dots) anc calculated (continous line) Rietveld plots for the fibrous tremolites. The difference profile is shown at the bottom of the figure. Vertical markers refer to the position of the calculated Bragg reflections for amphibole (in black) and calcite (in red).

RESULTS AND DISCUSSIONS

The comparison between bulk (ICP-MS) and punctual (EMP) chemical results (Table 1) reveals for some samples (Ala di Stura, San Mango and Monte Rufeno) differences for MgO and CaO, which are far larger than standard deviations. However, these differences are not due to chemical inhomogeneities, but are related to the presence of serpentine and calcite in the hand sample, as further confirmed by XRPD. The EMP analyses suggest a substantial chemical homogeneity of each sample. In fact, the variations observed for SiO_2, MgO e CaO are very small (ca. 1 - 3 % relative) and, as an exception, the variations observed for FeO_{tot} reach values up to 20% relative. Comparing the various samples each other, the differences between major (SiO_2, MgO and CaO) and minor (Al_2O_3, MnO and Na_2O) oxides are still lower. The most important difference is recorded for FeO_{tot}, because the Maryland sample shows a content almost double than the Italian ones (Table 1). All sample showed a Ca/ΣM ratio (Table 2) very close to the ideal tremolite (Ca/ΣM=0.40).

The Mössbauer spectra of fibrous tremolites (Figs. 3-4) is typical of a paramagnetic material and is composed of two contributions. The first one is due to two Fe^{2+} components with δ_0 of 1.1 mm/s (both in the Lorentzian and in the QSD fits) and two quadruple splitting distributions centred at Δ_0 of 1.9 and 2.9 mm/s in both fits. The second contribution, due to Fe^{3+}, is made of several components with δ_0 of 0.30 mm/s and a very large quadrupole splitting distribution (Tables 4 and 5). The Fe^{3+}/Fe_{tot} ratio was quantified from QSD fits on the basis of spectral areal measurement (Fe^{3+}_{raw}). To account for the temperature effect, the empirical factor of Dyar et al. (1993) was applied, and the corrected Fe^{3+} ratios (Fe^{3+}_{corr}) were obtained (values from 6 to 24% Fe_{tot}, Table 5). Notably, the Fe^{3+} ratios obtained by QSD analysis are closely comparable with those retrieved by Lorentzian site analysis (table 4). In the series of the tremolite-actinolite, Burns and Greaves (1971) attribued the Fe^{2+} doublets with QS of 1.7-1.9 mm/s and 2.8-2.9 mm/s to the presence of $^{M(2)}Fe^{2+}$ and $^{M(1)}Fe^{2+}$, respectively. More recently, many authors agreed to assign the doublet with the lowest QS to $^{M(2)}Fe^{2+}$, but different assignements were proposed for the doublets with the highest QS, often suggesting an irresolvable combination of $^{M(1)+M(3)}Fe^{2+}$ (Ballirano et al. 2008, Gunter et al. 2003). In the present work, according the refined area of Mössbauer absorbtion peaks, both analyses allocated about 40% of the total Fe^{2+} at M(2) (Δ_0 1.90 mm/s), and the remaining 60% at M(1)+M(3). Moreover, the Fe^{3+} was allocated at the M(2) site, as consistently reported by various authors for sodic amphiboles (Ernst and Wai 1970), strontian potassirichterite (Sokolova et al. 2000), ferrian winchite (Sokolova et al. 2001), winchite-richterite (Gunter et al. 2003), fluoro-edenite (Gianfagna et al. 2007) and tremolite (Ballirano et al. 2008).

The measured cell volume of the fibrous samples (table 8), except for Rufeno sample, is always higher than the values of 906.5 Å^3 (Gottschalk et al., 1999), 906.6 Å^3 (Verkouteren and Wylie, 2000), 907.0 Å^3 (Yang ed Evans, 1996) reported for pure tremolite and 907.37 Å^3 (Ballirano et al. 2008) reported for the fibrous tremolite of Susa Valley. The higher volumes take into account the presence of ferro-actinolite content ranging from 4 to 10% [Table 2, X_{FeA}= $(Fe^{2+}+Mn)/(Fe^{2+}+Mn+Mg)$]; in addition the reduced volume observed for Rufeno tremolite is in agreement with its highest amount of smaller high-charge cations (Al^{3+}, Fe^{3+}) at C sites. Rietveld refinements indicate the mean <T(1)-O> distances observed for all samples are comparable and always slightly smaller than <T(2)-O> as reported for C2/m amphiboles with no tetrahedrally-coordinated Al (Hawthorne 1981). Polyhedral distortion Δ shows comparable values for both T(1)- and T(2)-centered tetrahedra. Refined site scattering (s.s.) for M(1), M(2) and M(3) sites indicates the presence of a scatterer heavier than Mg, in agreement with both chemical data and the assignement of Mössbauer spectroscopy. A possible site partition is proposed in Table 10. Calculated site scattering (corresponding to the sum of electrons per formula unit) was derived from chemical data integrated by Mössbauer analysis. The agreement between s.s. derived from Rietveld refinement and those calculated from chemical data is quite satisfactory, with the largest difference being ca. 4% relative for Castelluccio and Maryland tremolites. Site assignament, beside the constraints indicated by Mössbauer spectroscopy, allocates for all samples ca. 67% of the ${}^{M(1)+M(3)}Fe^{2+}$ at M(1) and ca. 33% at M(3). Considering site multiplicity, a substantial equidistribution of Fe^{2+} may be observed over M(1), M(2) and M(3) (Table 10) in full agreement with the findings of Evans and Yang (1998) for tremolite—ferro-actinolite series and Ballirano et al. (2008) for tremolite from Susa Valley. Moreover, the presence of Fe^{2+} at M(1) and M(3) is also confirmed by the FT-IR spectrum (Fig. 2). In fact, except for the typical absorbtion band at 3673-3675 cm^{-1} assigned to the arrangement ${}^{M(1)}Mg{}^{M(1)}Mg{}^{M(3)}Mg$, a well developped band is observed at 3660 cm^{-1} and for Ala di Stura, San Mango and Maryland tremolites, a very weak band at 3645 cm^{-1}. Both were attributed to ${}^{M(1)+M(3)}Fe^{2+}$ environment according to results of Skogby and Rossman (1991) and Hawthorne and Della Ventura (2007). ${}^{M(1)+M(3)}Fe^{2+}$ occupancies calculated using the equations of Burns and Strens (1966) are shown in Table 3 and are in remarkably good agreement with those obtained combining Mössbauer and EMP data. Fe^{3+} was only assigned at M(2) according to the absence in FT-IR spectrum of absorbtion bands at Δ= -50 cm^{-1} from the tremolite reference band (Raudsepp et al., 1987), indicating the presence of ${}^{M(1)+M(3)}Fe^{3+}$. No correlation has been attempted for <M(1)-O> and <M(2)-O> distances because their differences are widely within two standard deviations of an individual bond distance. Moreover, the increase in <M(2)-O> distance observed for Ala di Stura tremolite with respect to Castelluccio, Rufeno and ideal tremolites (Yang ed Evans, 1996), is consistent with its higher Fe^{2+} content at M(2) site. With respect to the ideal tremolite (Yang ed Evans, 1996) the combined increase of both <M(3)-O> distance and Δ observed in all samples is consistent with the presence of low Fe^{2+} at M(3) site. The observed <M(4)-O> distances are comparable each other, except for Rufeno tremolite which showed a slightly larger <M(4)-O> distance, consistent with its highest $^{M(4)}$Na content.

Table 10 - Site scattering values (in electrons per formula unit) for the fibrous Ala di Stura tremolite obtained from the structure refinement. Possible site partition is the result of combining chemical. Mössbauer and Rietveld refinement data.

Ala di Stura	Refinement	Possible site partition	Chemical data
M(4)	39.08(20)		
B site sum	**39.08(20)**	$Ca_{1.96}$; $Na_{0.02}$	**39.42**
M(1)	24.86(17)	$Mg_{1.88}$; $Fe^{2+}_{0.09}$; $Mn_{0.03}$	25.65
M(2)	25.46(17)	$Mg_{1.86}$; $Fe^{3+}_{0.03}$; $Fe^{2+}_{0.11}$	25.96
M(3)	12.48(12)	$Mg_{0.95}$; $Fe^{2+}_{0.05}$	12.70
C site sum	**62.80(27)**		**64.31**

Castelluccio	Refinement	Possible site partition	Chemical data
M(4)	39.03(12)		
B site sum	**39.03(12)**	$Ca_{1.87}$; $Na_{0.06}$; $K_{0.01}$; $Mn_{0.01}$; $Mg_{0.05}$	**39.15**
M(1)	24.18(10)	$Mg_{1.92}$; $Fe^{2+}_{0.08}$	25.12
M(2)	24.17(10)	$Mg_{1.87}$; $Fe^{3+}_{0.05}$; $Fe^{2+}_{0.07}$; $Al_{0.01}$	25.69
M(3)	12.43(7)	$Mg_{0.96}$; $Fe^{2+}_{0.04}$	12.56
C site sum	**60.78(16)**		**63.37**

San Mango	Refinement	Possible site partition	Chemical data
M(4)	38.92(12)		
B site sum	**38.92(12)**	$Ca_{1.97}$; $Na_{0.02}$; $Mn_{0.01}$	**39.87**
M(1)	25.01(12)	$Mg_{1.87}$; $Fe^{2+}_{0.13}$	25.82
M(2)	24.48(12)	$Mg_{1.84}$; $Fe^{3+}_{0.02}$; $Fe^{2+}_{0.13}$ $Al_{0.01}$	26.11
M(3)	12.70(8)	$Mg_{0.94}$; $Fe^{2+}_{0.06}$	12.84
C site sum	**62.19(19)**		**64.31**

Mt. Rufeno	Refinement	Possible site partition	Chemical data
M(4)	39.24(28)		
B site sum	**39.24(28)**	$Ca_{1.84}$; $Na_{0.10}$; $Mn_{0.01}$	**38.15**
M(1)	24.38(26)	$Mg_{1.92}$; $Fe^{2+}_{0.08}$	25.12
M(2)	25.75(24)	$Mg_{1.76}$; $Fe^{3+}_{0.06}$; $Fe^{2+}_{0.08}$; $Al_{0.08}$	25.80
M(3)	13.46(18)	$Mg_{0.96}$; $Fe^{2+}_{0.04}$	12.56
C site sum	**63.59(40)**		**63.48**

Maryland	Refinement	Possible site partition	Chemical data
M(4)	39.36(16)		
B site sum	**39.36(16)**	$Ca_{1.99}Na_{0.01;}Mn_{0.02}$	**40.39**
M(1)	25.97(14)	$Mg_{1.82}$; $Fe^{2+}_{0.18}$	26.52
M(2)	25.49(14)	$Mg_{1.75}$; $Fe^{3+}_{0.08}$; $Fe^{2+}_{0.17}$	27.50
M(3)	13.27 (11)	$Mg_{0.91}$; $Fe^{2+}_{0.09}$	13.26
C site sum	**64.73(23)**		**67.28**

4

A MICRO-ANALYTICAL SEM-EDS METHOD APPLIED TO THE QUANTITATIVE CHEMICAL COMPOSITIONS OF FIBROUS AMPHIBOLES

INTRODUCTION

The determination of the chemical compositions in mineral fibers (asbestos and not) represents a real complex analytical problem that still today is not satisfactory resolved. For the quantitative determinations of the fibrous minerals there are various analytical techniques, presenting advantages and disadvantages as reported in the preliminar papers concerning this issue (Meeker et al., 2003; Gunter et al., 2003, 2007; Gianfagna et al., 2007). The analysis in Scanning Electron Microscopy (SEM) is an usefull method for the morphological study of mineral fibers, although the correct definition and mineralogical classification of mineral fibers is only possible through the X-rays spectra elaboration, obtained by the EDS microanalysis technique. The quantitative analysis of fibers and particles results to be not a banal investigation. In the analysis of larger particles, to calculate the matrix effects (i.e. ZAF method), both the sample and the standard are considered as infinitely thick in comparison with the penetration of the incident electron beam, assuming moreover that both have a smooth and often polished, regular surface (Goldstein et al. 1981; Scott et al. 1995). In quantitative analysis of particles or fibers, the size and shape of the sample can not be controlled, therefore two important effects can drastically change the intensity of the characteristic X-rays generated by the sample and invalidate the results obtained with routine correction procedures (Small, 2002).The first effect (the "absent mass effect") is related to the limited size of the analized particle and is strongly influenced by the average atomic number of the particle, which determines the probability of elastic scattering and the real volume of electron beam diffusion inner (or outside) the same particle. When a significant portion of the beam incident goes outside the particle, and no ionization events and X-ray emissions are generated, the intensity of characteristic spectrum lines can not be corrected by the factor Z that takes into consideration, in the ZAF procedure for massive sample, the difference in average atomic number. The second effect (the "reduced X-ray absorption effect ") is related to the geometric shape of the particle, and influences both the length of the the absorbtion path within the particle and the X-ray take off angle. Consequently, the A correction factor, which takes into account differences in X-ray absorption of the sample and standard, could be radically different from that calculated with the usual ZAF algorithms. The magnitude of this effect is particularly important in the case of "soft X-ray " producted by light elements like Al and Si, having energies lower than 2 keV. Many methods, both empirical and based on ideally-shaped particles, have been proposed to solve this problem with EDS microanalysis (Laskin & Cowin, 2001; Ro et al., 2003). However, these methods only obtain semi-quantitative results or they assume, for the analyzed particles, a specific geometry. Thus, for a general application they are only partially useful.

Analysis of the prismatic fluoro-edenite fragments and calculation of the correction factor

In the Biancavilla area, located at southwest slopes of the Mt. Etna volcano (Sicily, Italy), a new amphibole mineral species was recently found, *fluoro-edenite*, belonging to the amphibole calcic group of the edenite↔fluoro-edenite series (Gianfagna & Oberti 2001). The mineral presents two different morphological varieties - prismatic and fibrous (Fig. 1a,b), the latter with larger compositional variability, as already reported in the papers of Gianfagna et al. (2003), Bruni et al. (2006), and Gianfagna et al. (2007). For a quantitative evaluation of such chemical differences, fibrous fluoro-edenite samples were studied by means of Scanning Electron Microscopy (SEM) and X-rays Micro-analysis (EDS).

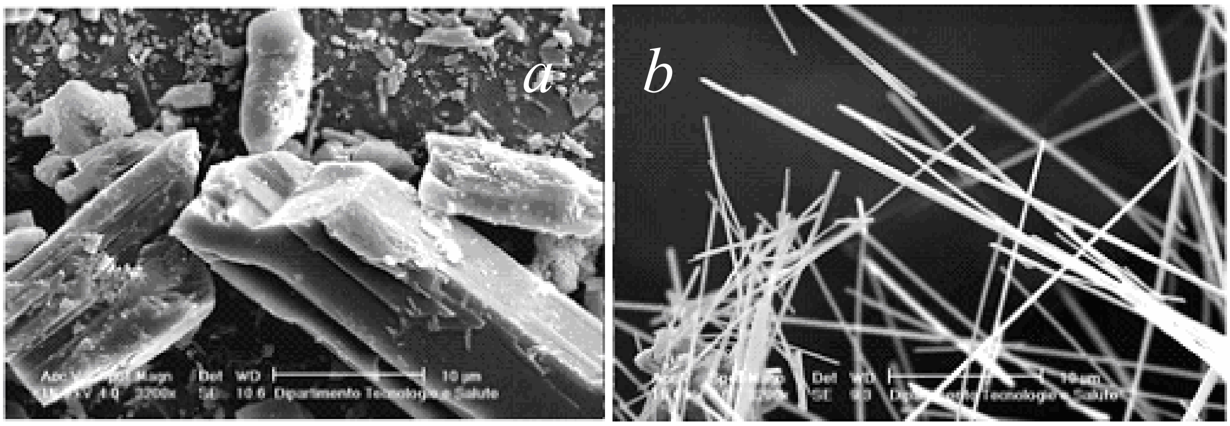

Figure 1- a) Prismatic fluoro-edenite; b) fibrous fluoro-edenite.

To obviate the problem of the small size of the fibers (averaged diameters of 0.30 and 0.70 µm), in SEM-EDS analysis, an empirical procedure was developed. This procedure, previously reported in Paoletti et al. 2008, is based on the assumption that both the "absent mass" and the "reduced absorption" effects will have, with good approximation, the same significance in the analysis of both the fibers and the fluoro-edenite crystal fragments with similar sizes (0.2 to 1 µm).Therefore, to evaluate these effects the X-ray spectra of fluoro-edenite fragments were collected and compared with a spectrum obtained by the same original crystal (Fig. 2), previously analized by Electron Microprobe Analyzer (EMPA). The "apparent" concentrations of the different elements of the fragments were calculated on the acquired spectra by the ordinary ZAF procedure.

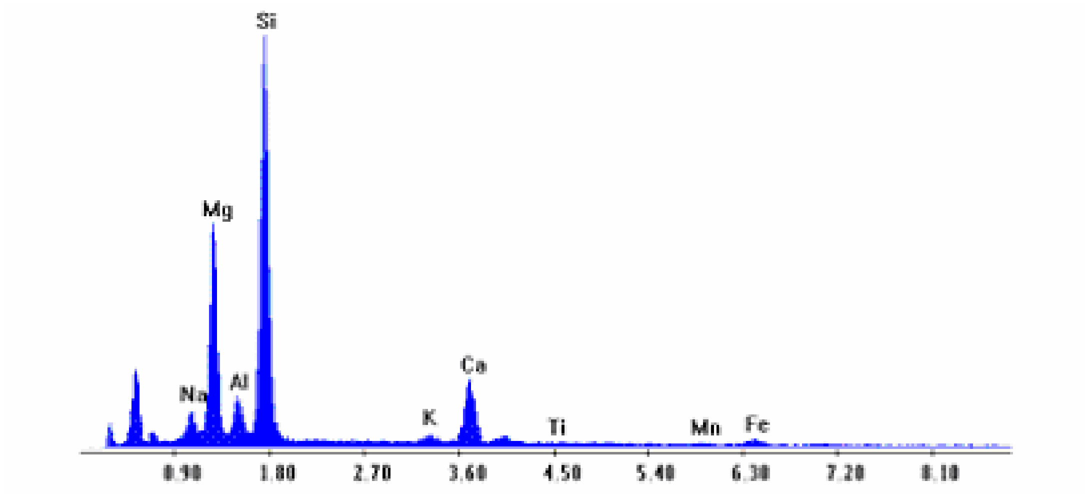

Figure 2 - EDS spectrum of a prismatic fluoro-edenite crystal (from Paoletti et al. 2008).

EXPERIMENTAL METHODS

Sample preparation and observation condition

Prismatic fluoro-edenite fragments were obtained by grinding the prismatic sample in agate mortar under acetone. During the analysis of both prismatic crystal and fragments, the instrumental operating conditions were kept fixed: 15 keV beam energy, 10 mm WD, tilt angle 0°, spot analysis mode. The size of the fragments were determined in the SEM; the error on the particle size was evaluated in the range of ±20 nm.

RESULTS

To determine the significance of the “absent mass” and “reduced absorption” effects, the "apparent" concentrations of the different chemical elements in the fragments were calculated on the acquired spectra by the ordinary ZAF procedure, adopting the bulk crystal as standard. Figure 3 shows the analytical results carried out on thirty-six fragments of prismatic fluoro-edenite, with dimensions between 0.2 and 1 µm. The concentrations of the most aboundant five elements (Na, Mg, Si, Ca, and Fe) The concentrations of the most abundant five elements (Na, Mg, Si, Ca, and Fe), as obtained by the ZAF procedure, are plotted versus the particle sizes without consideration of the "absent mass" and the "reduced absorption" effects. Moreover, the Figure 3 also shows for comparison the actual elemental values (known from the measures on the massive crystal) for each element. We did not select the type of the regression models to use (e.g., a linear regression), because the experimental results are caused by a combination of several different processes (absent mass, reduced absorption, fragment geometry), which do not show a linear dependence to the fragment size. We thus selected the empirical regression model which yielded the best fit with our data (polynomial, linear, power). Such models were considered the better estimation of the correlation between the apparent concentrations of the elements and the sizes of the fragments.

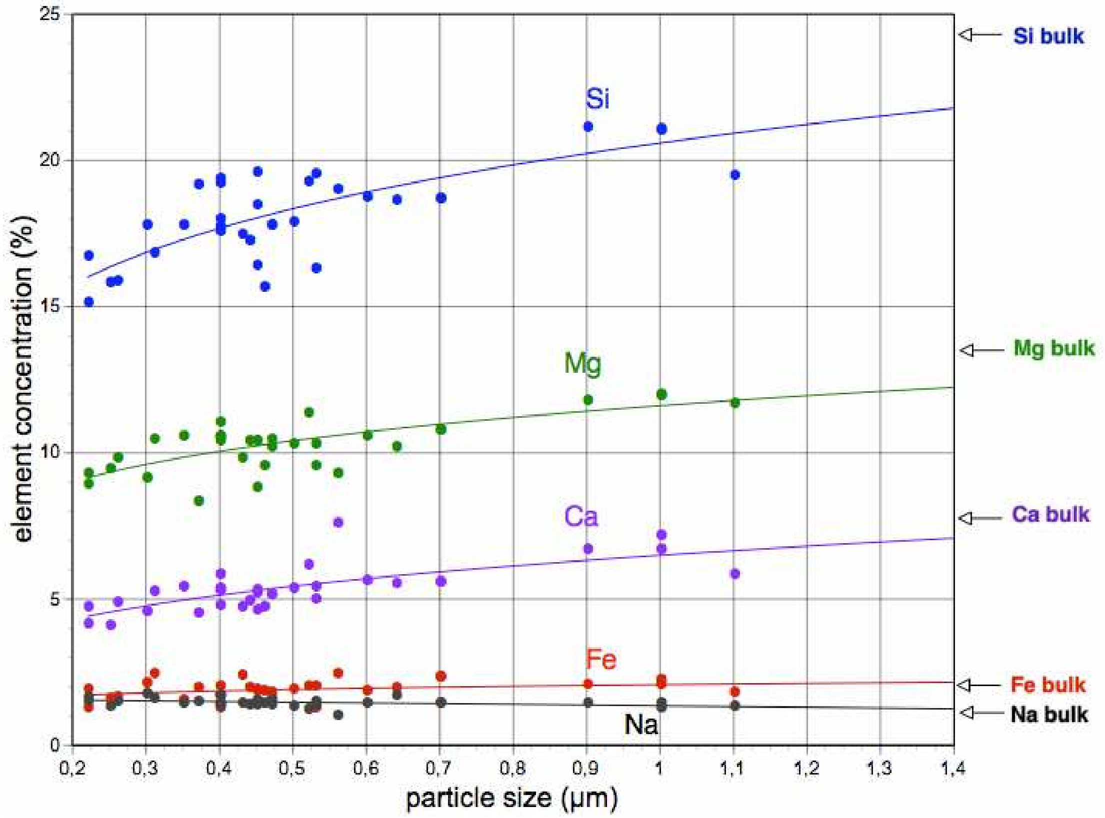

Figure 3 - Concentrations of the five more aboundant elements (Na, Mg, Si, Ca, and Fe) as a function of the particle sizes, using the ZAF procedure (from Paoletti et al., 2008).

In table 3 the correlation coefficients *R* of the regression curves are reported; moreover the widths of the residual distributions around the relative regression curves (estimated by the standard deviation σ) are listed.

Table 3 - Correlation coefficients, R of the regression curves, and residual distribution widths (estimated by the standard deviation around the curves).

	Na	**Mg**	**Si**	**Ca**	**Fe**
Correlation coefficients of the regression curves	0.52	0.76	0.81	0.79	0.37
Standard deviation of residuals around the regression curves (σ)	0.135	0.628	1.028	0.539	0.294
Data dispersion (σ) from 14 analyses on a fluoro-edenite bulk sample	0.040	0.135	0.165	0.107	0.085
Contribution of the fluoro-edenite compositional variability to the residual dispersions	30%	22%	16%	20%	29%
Contribution of measurement error on particle sizes to the residual dispersions	6%	19%	19%	18%	5%

The observed dispersions around the average trend (the regression curves) are basically due to two effects:

1. The geometry (shape and orientation) of the standard crystal shards: it causes a random take-off angle which affects the range of the X-ray photon in the sample, adding a random effect on the intensity of the peaks;
2. The compositional variability of the fluoro-edenite shards: the standard prismatic crystal is not compositionally homogeneous so the shards, because their very small size, will show a varying composition; this effect may be particularly evident for the element that presents the greatest substitution in the fluoro-edenite structure.

A third effect contributing to the observed spreading around the average trend is the measurement error on the fragment size; however, it is possible to assume a random distribution of this error with a virtually zero mean value and a width equal to ± the resolution (instrumental error) obtained in the instrumental operative conditions. Thus, the result of this effect on the data average trend (the regression curves) may be disregard. The result on the widths of the residual distributions may be evaluated (Table 1) taking into account the regression curve slope in the size range of interest (0.2 – 1.1 μm). An evaluation of the significance of the second effect was attempted in considering the compositional variability of the fragments comparable to the observed variability in the chemical analyses carried out through EPMA technique, on different zones of a prismatic fluoro-edenite crystal. In Table 1 the data dispersions (standard deviation σ) of fourteen EPMA analyses are reported. Both the contribution (as percentage values) of the fluoro-edenite compositional variability and the contribution of the measurement error on particle sizes to the residual dispersions are shown.

Correction factors for the "apparent" concentrations

The element correction factors were calculated comparing the regression curves of the "apparent" elemental concentrations of the fluoro-edenite fragments with the "true" elemental concentrations of the massive standard sample. In the graphs of Fig. 4 the factors for Si, Mg, Fe, and Na, are plotted as a function of the dimensions of the fragments. These were used to correct both the "absent mass" and the "reduced absorption" effects for the fibers. Also shown in Fig. 4 are the correction factor errors, which are assumed equal to the standard error ($\sigma/\sqrt{n}$) of the residual dispersion for each regression curve. These results show that the concentrations of all the elements, except for Na, are underestimated in the fragments analysis, and even more when the fragment size decreases, therefore, the "absent mass" effect is predominant, with the exception of the Na Kα line (1.041 KeV) for which the "reduced absorption" effect prevails. For the Fe Kα line, with relatively high energy (6.40 KeV), both the "absent mass" and the "reduced absorption" effects appear to cancel each other for particles whose widths are greater than about 0.6 μm. The validity of the calibration curves, which describe the correction factor magnitude, is limited to the dimensional range between 0.2 - 1 µm (i.e., the size ranges for the particles we analyzed).

To obtain the true composition of a fibrous sample, the correction factors, valued by the calibration curves, will be applied to the "apparent" composition obtained through the EDS spectra (true compositions = apparent compositions **x** correction factors).

The "true" composition of the fiber will be determined through a total relative error [Δ*C%*] corresponding to the sum between the correction factor relative error [Δ*F%*] and the relative error on the apparent fiber composition [Δ*apparentC%*]:

$$[\Delta C\%] = [\Delta apparentC\%] + [\Delta F\%]$$

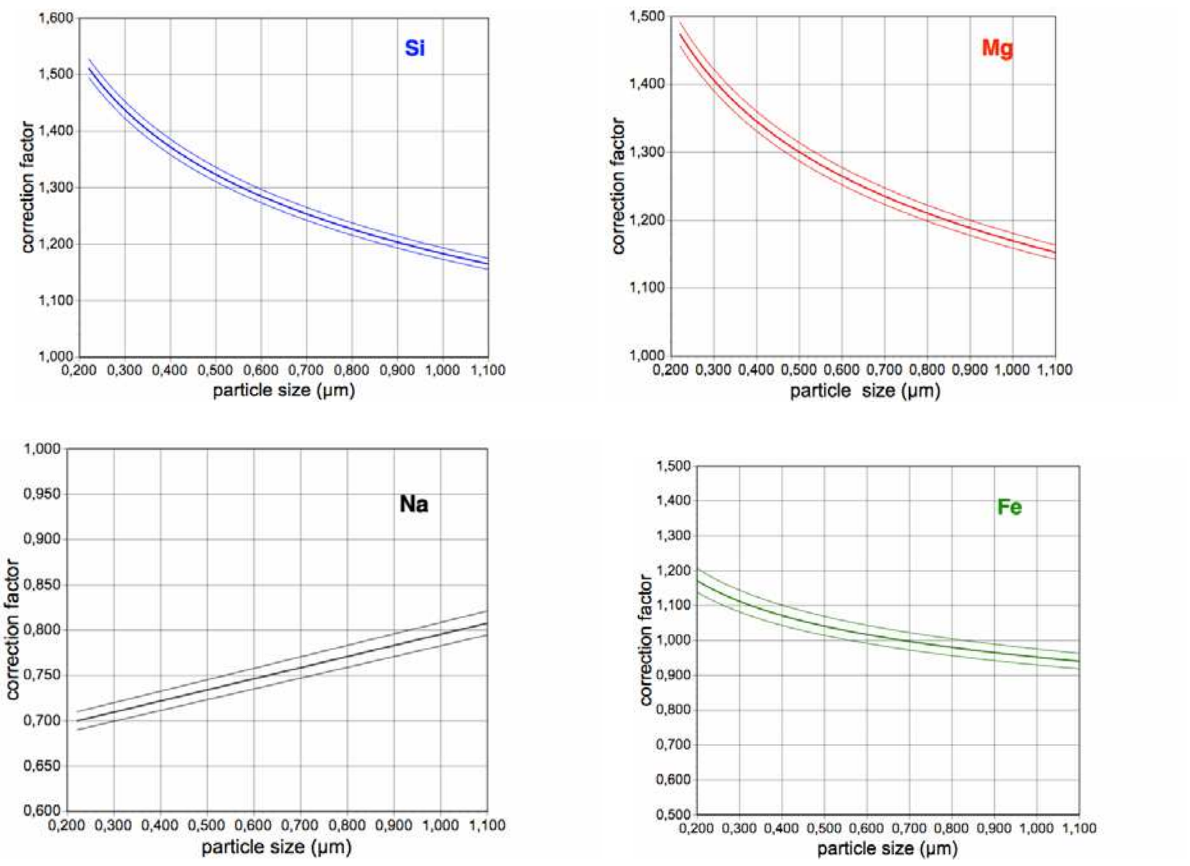

Figure 4 - Correction factors curves for Mg, Si, Na, and Fe, as a function of the fragment sizes. There are also reported the correction factor errors assumed equal to the standard error (σ/√n) of the residual dispersion for each regression curve.

Compositions of the fluoro-edenite fibers

Four fibrous fluoro-edenite samples were analyzed using the above described method. The analyzed fibers were collected in sites named 1, 2, 3, and 4, from the Biancavilla volcanic area, in which the prismatic fluoro-edenite crystals were first discovered. All fibers from the four sites have diameters in the range 0.2 to 1.0 µm. For each fiber sample (each site), al least forty fibers were analysed and the corresponding average compositions determined. The true compositions of each fiber sample, expressed as % of the element, are reported in Table 2, together with the experimental total errors [assumed equal to the standard error (σ/√n) of the data dispersion]. The absence of OH^- groups for both the prismatic and fiber samples was evaluated by Infra-red Spectroscopy; consequently, the fluorine and chlorine content was fixed to the value of the EMP analysis.

Table 2 - Average chemical composition of the four samples from Biancavilla; standard deviation in brackets. The correction factors calculated for each element are also reported.

Element	**Correction factor**	**1**	**2**	**3**	**4**
N. analyses		**52**	**40**	**42**	**58**
Si	1.34	25.30(52)	24.62(51)	25.00(42)	25.18(42)
Ti	0.23	0.02(1)	0.02(1)	0.01(1)	0.02(1)
Al	1.12	1.04(18)	1.54(18)	1.32(20)	1.22(20)
Mg	1.32	12.87(52)	12.37(40)	13.65(43)	13.23(43)
Ca	1.44	6.06(51)	7.29(40)	6.57(55)	6.14(48)
Mn	0.72	0.43(17)	0.35(9)	0.38(10)	0.34(13)
Fe	1.05	4.22(41)	4.65(44)	2.79(65)	3.91(52)
Na	0.74	2.30(28)	1.70(24)	2.28(32)	2.06(28)
K	1.04	0.44(20)	0.42(12)	0.46(14)	0.46(14)
F	1.00	4.40	4.40	4.40	4.40
Cl	1.00	0.06	0.06	0.06	0.06

AN OTHER EXEMPLE: FIBROUS RICHTERITE FROM LIBBY MONTANA (USA)

The same procedure used in the analysis of the fibrous fluoro-edenite from Biancavilla was adopted to analyze samples of richterite fibers from Libby, Montana, USA (Meeker et al. 2003; Gunter et al. 2003). The richterite amphibole can be found in prismatic as in the fibrous morphology, like the fluoro-edenite amphibole. The richterite fibers analyzed in this work occurred with a diameter range between 0.2 to 1 µm. Unlikely, in the Libby samples (fibrous and not fibrous material) there are not any prismatic crystals so large to use as a reference standard. Therefore, a prismatic richterite crystal from the Ontario, Canada, was obtained from the collection of the Mineralogical Museum of the Earth Sciences Department, “Sapienza Università di Roma”, Italy. The crystal, whose composition was previously and carefully determined by means of EPMA technique, was used as reference standard. On the basis of its composition, the massive crystal was defined as a fluor-richterite amphibole. The crystal was appropriately ground to obtain fragments with suitable sizes. The acquired EDS spectra of the fragments were utilized to calculate the "apparent" concentrations of the different elements, using the ZAF procedure. The calibration curves were utilized to correct both the "absent mass" and the "reduced absorption" effects. To test the validity of the method also when a reference standard is used with some chemical variabilities with respect to the fibrous variety, a bundle of richterite fibers were preparated in in thin section, embedded in resin, to simulate a massive sample, and were analyzed by EPMA tecnique. In Table 3, the average chemical compositions of the richterite fibers, based both on the EMPA (22 analythical points) and SEM-EDS analysis (on 22 fibers) are reported; it is also shown with the mean composition of the prismatic Ontario richterite (20 analyses) on EMPA and the calculated correction factors.

Table 3 - Averaged composition of prismatic richterite from Ontario (EMPA analysis)and fibrous richterite from Libby (EMPA and SEM analysis). Standard deviation in brackets. The correction factors calculated for each element are also reported.

Element	Correction factor	Ontario Richterite	EMPA fibers	SEM-EDS fibers
Si	1.29	26.53(10)	27.62(14)	27.40(29)
Ti	0.92	0.21(1)	0.05(2)	0.14(9)
Al	0.88	0.49(5)	0.07(3)	0.16(4)
Mg	1.24	14.10(14)	13.44(35)	13.90(31)
Ca	1.49	6.59(14)	5.22(48)	4.69(59)
Mn	0.66	0.15(3)	0.11(3)	0.08(3)
Fe	1.02	1.81(7)	3.26(80)	3.11(63)
Na	0.86	1.70(5)	1.87(12)	1.84(19)
K	1.23	0.56(2)	0.66(11)	0.77(16)

It is interesting to note that the composition of the massive Ontario richterite shows significant chemical differences with respect to the analyzed fibers of the same mineralogical species, while the fluoro-edenite fibers present minor compositional variability respect to the prismatic fluoro-edenite, utilized as reference standard. It is significant that a very strict agreement occurs between the composition of the bundled fibers, determined by EPMA, and the composition of the single fibers, determined by the SEM-EDS procedure.

DISCUSSION AND CONCLUSIONS

The characterization of fibrous materials is very difficult because of their small sizes (i.e., the fiber width). Careful analyses are frequently hindered and sometimes structural determinations are impossible. Therefore, in these particular cases it is important to develop innovative methods to characterize, identify, and correctly classify these materials. Quantitative micro-analyses of particles and/or fibers, and their subsequent interpretability, are very difficult to perform on samples with dimensions in the order of micron or sub-micron range, particularly in presence of low elemental concentrations. The experimental X-rays micro-analytical method here described overcomes the errors due to so-called "absent mass" and "reduced absorption" effects in the quantitative analysis of sub-micron mineral fibers. This new method was developed and applied on fibers with dimensional range between 0.2 and 1.0 μm, and a compositional reference “standard” was available from which small fragments, with size comparable to the fiber, was possible to obtain. The method was tested and applied for the first time on the new fluoro-edenite amphibole fibers from Biancavilla, Italy, and it was verified on fluor-richterite fibers from Libby, Montana, USA. The method can be also used for fibrous samples with slightly different elemental concentrations with respect to the massive standard crystal. Concerning the influence of the elemental abundances in the fibrous samples, the error (%)increases with the decrease of the relative contents (Fig. 5). This was verified in both the cases considered in the present study. With this methodological procedure a measured error not greater than 5% can be expected when the element is present in concentration not less than approximately 10%. The reliability of the procedure rapidly decreases when the abundance of the elements is below 3 to 4%.

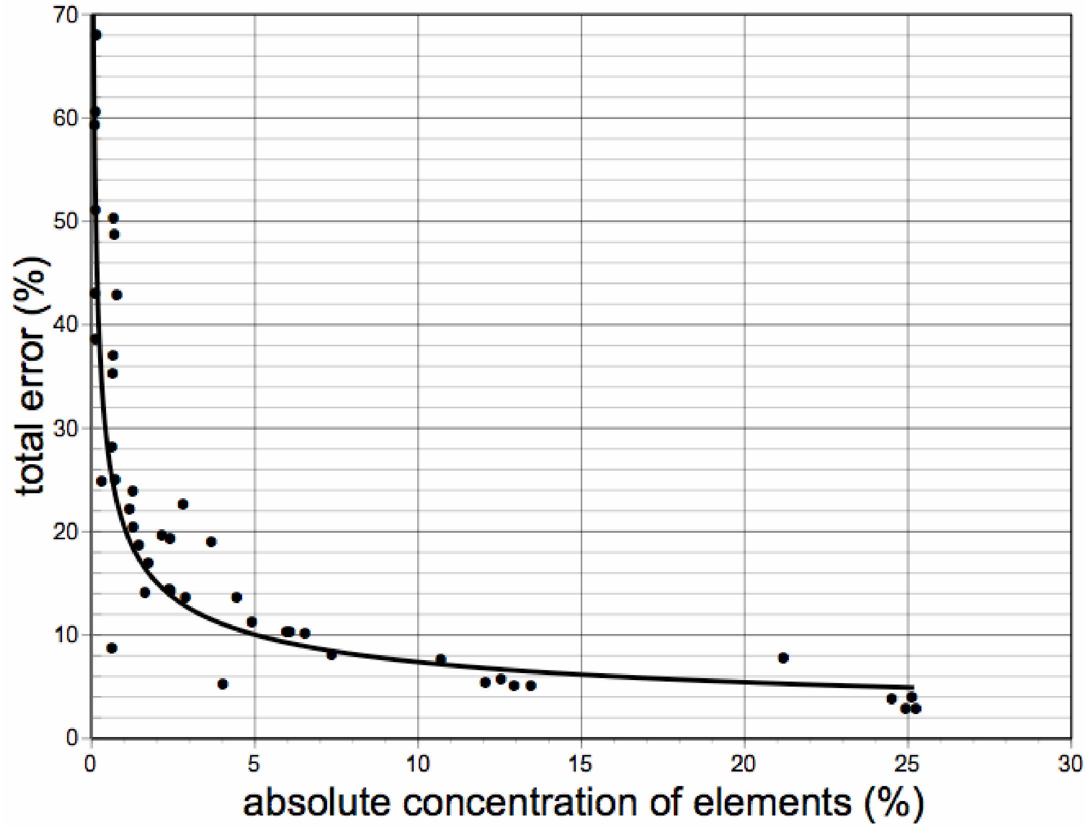

Figure 5 - Trend of the total error (%) as a function of the absolute concentration of the measured element in a fibrous sample.

5

CHEMICAL AND STRUCTURAL CHARACTERIZATION OF A SUITE OF FIBROUS AMPHIBOLES FROM BIANCAVILLA (SICILY, ITALY)

INTRODUCTION

The quantitative characterization of the mineral fibers, and in particular of the amphiboles fibers, is a topical subject due to environmental and health concerns. An interesting starting point in order to both clarify the classification of the mineral fibers (asbestos or not) and enhance our understanding of fiber-lung reactivity mechanisms is the case-study of Biancavilla (Sicily, Italy). In this area, in fact, the presence of some unexpected cases of pleural mesothelioma (Paoletti et al., 2000) was explained by the correlation between the widespread occurrence in amphibole fibers and the high incidence of this lung specific pathology (Comba et al., 2003; Burragato et al, 2005). Recent studies on the reactivity of these amphibole fibers in organic environment showed that their different toxicity is strongly related to differences in composition, in particular the content of Fe and its oxidation state (Soffritti et al., 2004; Cardile et al., 2004; Pugnaloni et al., 2007). The study of fibrous amphiboles from Biancavilla is therefore a topic of great interest from both strictly minero-petrographic and environmental point of view, since they represent a case of pollution from natural mineral fibers not previously ruled. The mineralogical literature reports few works dealing with quantitative chemistry of the fibrous minerals. Recently, Meeker et al. (2003), Gunter at al. (2003, 2007) and Ballirano et al. (2008) reported a good attempt to realize this goal for fibrous amphiboles (e.g., winchite, tremolite), using specific analytical procedures. Q*ualitative* chemical studies on Biancavilla loose fibers were reported in Gianfagna et al. (2003) and Bruni et al. (2006), displaying compositional differences of fibrous amphiboles as compared to the prismatic fluoro-edenite. A first attempt to obtain the full characterization of a sample of loose fibers from Biancavilla was reported in Gianfagna et al. (2007): the *semi-quantitative* chemical characterization of the sample (coming from Poggio Mottese locality) was realized exploiting a SEM-EDS "overlapping" analytical method. However, the method was further improved and tested on different types of fibrous amphiboles (see chapter 4). In this work a *quantitative* chemical characterization of a suite of four fibrous amphiboles coming from the same locality was obtained by the standardized SEM-EDS microanalysis method. The inclusive crystal-chemical characterization was obtained with a multi-analitical approach, combining the chemical investigation with X-ray powder diffraction (XRPD) and Mössbauer and FT-IR spectroscopies.

MATERIALS

Next to the eastern part of Biancavilla there is a quarry area called "Il Calvario", which was mined extensively for a sandy volcanic material for local buildings. After Romano (1982), this area was geologically reinterpreted as a series of domes and dikes associated with "autoclastic breccia", a fine grained material (Burragato et al., 2005). Previous mineralogical investigations identified in the area the new amphibole end-member *fluoro-edenite* (Gianfagna & Oberti, 2001), which displays prismatic, acicular, and fibrous morphologies. The discovery of the fibrous amphibole, recognized as the cause of the pathology in this area (Paoletti et al., 2000; Comba et al., 2003), made necessary further mineralogical and environmental studies. The volcanological and mineralogical investigations identified the presence of fibrous amphiboles inside and outside the quarry (Burragato et al., 2005). The fibrous morphology was found in the metasomatized benmoretic lava (sodian latite) both in the fractures and cavities in association with prismatic fluoro-edenite, and in the autoclastic breccia (Fig. 1). The aerial photograph of the Biancavilla area showing the location of the sampling points of the four samples is reported in Figure 2. The starting material utilized for this work was the autoclastic grained material, made of lava pieces scattered in a fine matrix, which contained the mineral assemblage of loose fibers, alkali-feldspars, clinopyroxenes, fluorapatite and

Fe-Ti oxides of micrometrical and sub-micrometrical dimensions (Fig. 1b). To avoid or at least reduce any influence of the other phases on the experimental data, samples enriched in amphibole fibers were prepared, according to the procedure reported in Gianfagna et al. (2007). Briefly, this method allows a fiber enrichment through a simple sedimentation in water, and a withdraw of the surnatant solution after 30 to 35 hours. In the SEM photographs of Figure 3 two examples of the fibrous amphiboles analyzed in the present work are displayed. These fluorine-rich fibrous amphiboles generally show a thickness lower than 1 μm (200 to 600 nm) and a variable length, until to 100-150 μm. In particular, sample 1, 2, and 3, are characterized by an acicular-fibrous morphology and shorter fibers (medium length ca. 50 μm), while sample 4 shows a more filamentous-asbestiform morphology with length up to 150 μm.

Figure 1 – a) Extractive front of the “Il Calvario” quarry, where the vertical fractures present superficial mineralization of prismatic yellow fluoro-edenite amphibole; b) fine grained volcanic material of the “autoclastic breccia” (fractured and crumbled benmoreite lava) containing the fibrous fluorine amphiboles.

Figure 2 - Aerial photograph of Biancavilla area, showing the "Il Calvario" quarry (central zone) and the related sampling points of the four samples of fibrous amphiboles. The red circle represents prismatic fluoro-edenite location. (Modified after Burragato et al., 2005).

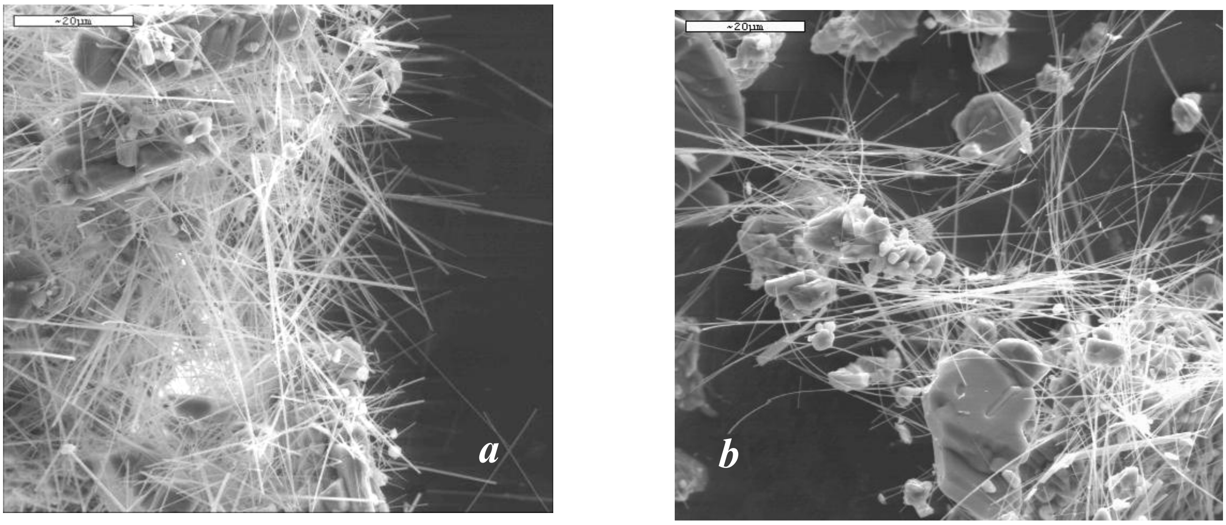

Figure 3 - SEM photographs of two examples of fibrous amphiboles from Biancavilla: sample 3 (a), and sample 4 (b). The other associated minerals prevalently are alkali-feldspars, clinopyroxenes, fluorapatite and Fe-Ti oxides.

ANALYTICAL METHODS

Scanning Electron Microscopy (SEM) with EDS micro-analysis

Because of the extremely reduced dimensions of the fibers, chemical analysis by Electron Microprobe (EMP) was not possible, therefore quantitative chemical analyses were obtained by utilizing the standardization procedure on SEM-EDS instrument, as previously reported. To address the problem of the small dimensions of the fibers, fragments of the prismatic fluoro-edenite, previously analysed by EMP, were utilized as a compositional reference. The operating conditions of the instrumental equipment were: 15 keV beam energy, 10 mm working distance, 0° tilt angle. A variable number of fibers (1–3 spots on about 40-60 fibers, with diameter between 0.2 and 0.9 μm) for each of the four samples were analyzed (Table 1). Notably, sample 2 is the same sample previously analyzed with the semi-quantitative approach in Gianfagna et al. (2007), and because of this it was reanalyzed. The contents of F and Cl were fixed at the values of 4.40% and 0.06%, respectively, previously obtained for the prismatic fluoro-edenite. The absence of OH^- was verified by FT-IR spectroscopy (Fig. 4). Table 2 shows the crystal-chemical formulas based on 24 (O + F + Cl). The cations are reported in atoms per formula unit (apfu) and were assigned according to Hawthorne (1981), with sites A, B, C and T filled in the order recommended by Leake et al. (1997).

Table 1 - Average chemical composition (wt.%) of the four amphibole fibrous samples from Biancavilla. Estimated standard deviations in brackets. The average analysis of prismatic fluoro-edenite (Gianfagna and Oberti 2001) is shown for comparison.

Sample	**1**[a]	**2**[b]	**3**[c]	**4**[d]	**F-edenite2001**[e]
SiO_2	54.12(112)	52.66(109)	53.49(90)	53.86(91)	51.52(99)
TiO_2	0.03(1)	0.03(1)	0.02(1)	0.03(1)	0.28(25)
Al_2O_3	1.95(34)	2.91(36)	2.51(39)	2.31(40)	3.81(66)
MgO	21.34(87)	20.50(66)	22.63(72)	21.94(71)	22.43(41)
CaO	8.48(71)	10.20(56)	9.19(76)	8.59(67)	10.70(28)
MnO	0.56(21)	0.45(12)	0.49(12)	0.44(17)	0.39(07)
FeO_{tot}	5.43(53)	5.98(57)	3.59(84)	5.03(67)	2.46(20)
Na_2O	3.10(39)	2.29(33)	3.08(44)	2.78(38)	3.05(09)
K_2O	0.53(24)	0.52(16)	0.55(17)	0.54(17)	0.88(11)
F	4.40	4.40	4.40	4.40	4.40
Cl	0.06	0.06	0.06	0.06	0.08
Total	100.00	100.00	100.00	100.00	100.00
$*Fe_2O_3$	3.26	4.45	3.67	5.25	2.54
***FeO**	2.50	1.97	0.29	0.30	0.17

Note: Average of a) 52 analyses, b) 40 analyses, c) 42 analyses, d) 58 analyses and e) 14 analyses.

* Fe^{3+}/Fe_{tot} measured by Mössbauer spectroscopy.

Table 2 - Average crystal-chemical formulas of the four amphibole fibrous samples from Biancavilla. Prismatic fluoro-edenite (Gianfagna and Oberti, 2001) is shown for comparison.

	1	**2**	**3**	**4**	**F-edenite2001**
Si	7.676	7.495	7.544	7.587	7.317
$^{\mathrm{IV}}\mathbf{Al}$	0.324	0.488	0.418	0.384	0.638
$\sum \boldsymbol{T}$	8.000	7.984	7.962	7.971	7.955
$^{\mathrm{VI}}\mathbf{Al}$	0.002	0.000	0.000	0.000	0.000
Ti	0.003	0.004	0.002	0.003	0.030
$\mathbf{Fe}^{3+}$	0.348	0.477	0.390	0.557	0.271
Mg	4.511	4.350	4.758	4.607	4.749
$\mathbf{Fe}^{2+}$	0.296	0.235	0.034	0.036	0.020
Mn	0.067	0.055	0.059	0.053	0.047
$\sum \boldsymbol{C}$	5.227	5.121	5.243	5.256	5.117
$\Delta \boldsymbol{C}$	0.227	0.121	0.243	0.256	0.117
Ca	1.289	1.555	1.389	1.297	1.627
Na	0.484	0.324	0.368	0.447	0.256
$\sum \boldsymbol{B}$	2.000	2.000	2.000	2.000	2.000
Na	0.368	0.307	0.474	0.312	0.584
K	0.096	0.094	0.099	0.097	0.159
$\sum \boldsymbol{A}$	0.462	0.401	0.573	0.409	0.743
F	1.974	1.981	1.963	1.961	1.977
Cl	0.014	0.014	0.014	0.014	0.019
$\sum \boldsymbol{O_3}$	1.988	1.995	1.977	1.975	1.996
$^{B}\mathbf{Na}$	0.484	0.325	0.368	0.447	0.257
$^{A}(\mathbf{Na+K})$	0.462	0.400	0.573	0.409	0.741

Fourier Transform Infrared (FT-IR) Spectroscopy

The FT-IR data were collected using a Perkin Elmer spectrometer (SYSTEM 2000) in the range 4000-400 cm^{-1}: 32 scans at a nominal resolution of 4 cm^{-1} were averaged. The instrument was equipped with a KBr beamsplitter and TGS detector. The samples were ground in the agate mortar and mixed in 2:100 ratio with 200 mg of KBR in order to obtain transparent pellets. Measurements were done in air at room temperature. All the spectra (Fig. 4) did not show any absorption bands in the OH-stretching region (3800-3600 cm^{-1}), as already verified for the prismatic fluoro-edenite (Gianfagna and Oberti, 2001).

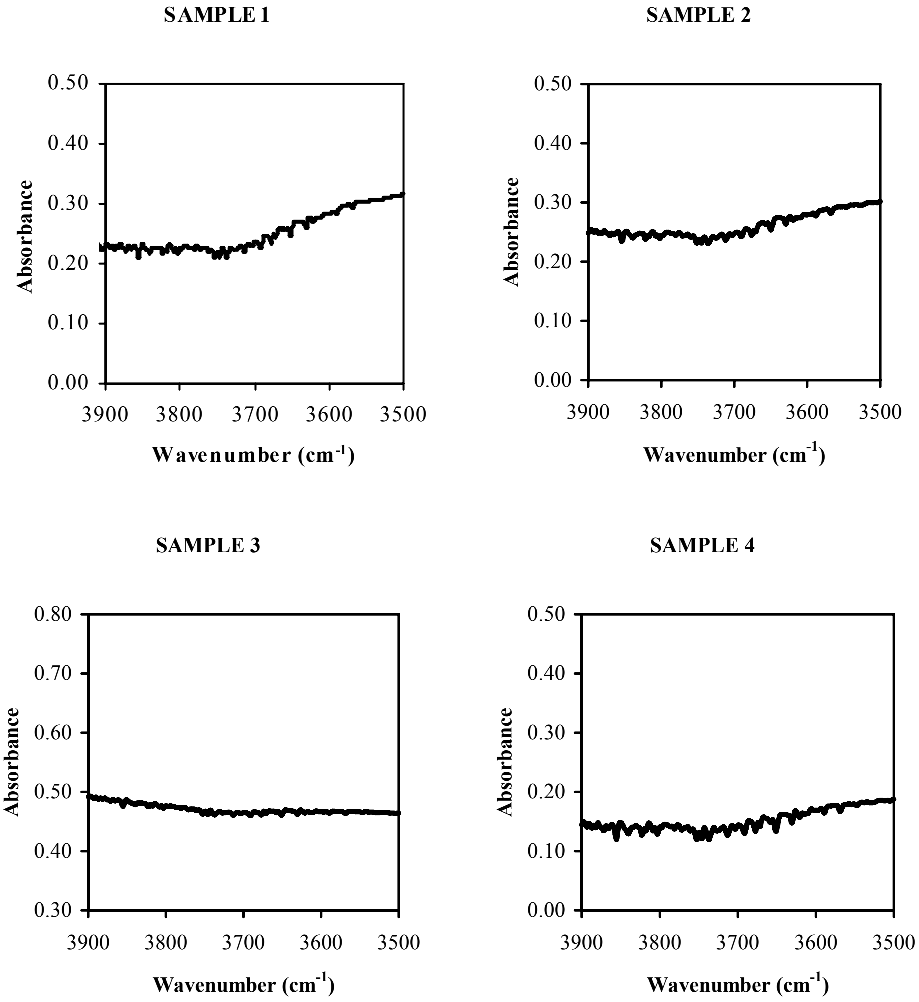

Figure 4 - FT-IR spectra in the 3900-3500 cm^{-1} range of the four amphibole fibrous samples from Biancavilla.

^{57}Fe Mössbauer spectroscopy

All samples were gently ground in an agate mortar with acetone and mixed with powdered acrylic resin to avoid (or reduce) preferred orientation. Depending on the availability of material, between 10 to 70 mg of sample were pressed to make an absorber in the limits of the thin absorber described by Long et al., 1983. The spectra were collected at room temperature using a conventional spectrometer operating in costant acceleration mode, with a ^{57}Co source of nominal strength of 50 mCi in a rhodium matrix. The data were recorded using a multichannel analyzer using 512 channels for the velocity range from -4 to 4 mm/s; to get a good statistical counting about 10^7 counts per channel were collected. After velocity calibration against a spectrum of high-purity α-iron (25 μm thick), the raw data were folded to 256 channels. The spectra were fitted using the Recoil 1.04 fitting program (Lagarec and Rancourt, 1998). A first cycle of refinement was performed by fitting three doublets, pure Lorentzian line-shapes (Table 3, Fig. 5) and the results obtained were quite satisfactory (χ^2 always <1), but the Lorentian line-shapes showed in some cases wide line-widths (Γ values up to 0.92 mm/s). Therefore, a second cycle of refinement was carried out by fitting quadrupole-splitting distributions(QSD), following the approach of Gunter et al. (2003) and Gianfagna et al. (2007a). A number of fitting models with unconstrained parameters [isomer shift(δ_0), coupling parameter (δ_1), center of Gaussian component (Δ_0), Gaussian width (σ_Δ), and absorption area (A)] were tried in order to obtain the best fit. A model based on two sites (1Fe^{2+} + 1Fe^{3+}) each with two components was finally chosen and the results were very satisfactory (Table 4, Fig. 6). The increasing of the number of Gaussian components did not change significantly the resulting distribution. Notably, the Fe^{3+} contents obtained by QSD analysis are closely comparable with those retrieved by Lorentzian site analysis (Tables 3 and 4). For sample 3, one component for both sites was sufficient, and this is related to the low resolution of the spectrum. The uncertainties were calculated using the covariance matrix and errors were estimated no less than ±3% for both Fe^{2+} and Fe^{3+} absorption areas.

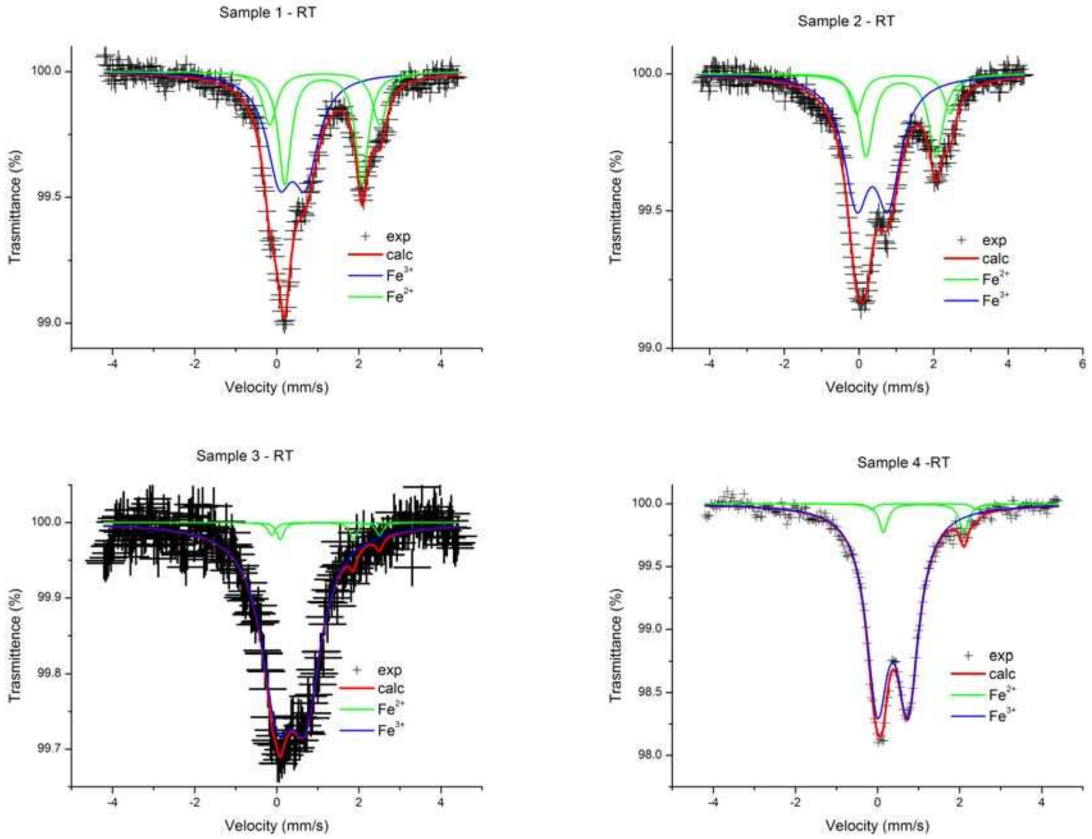

Figure 5 - Room temperature (RT) Mössbauer spectra with three-doublet Lorentzian fitting model of the four amphibole fibrous samples from Biancavilla.

Table 3 - ^{57}Fe Mössbauer hyperfine parameters at *RT* for the four amphibole fibrous samples from Biancavilla. Lorentzian fitting model.

Sample	χ^2	Fe^{2+}				Fe^{3+}				Fe^{3+}_{raw} (% Fe_{tot})	Fe^{3+}_{corr} (% Fe_{tot})
		ΔE_Q (mm/s)	Γ (mm/s)	δ (mm/s)	Area (%)	ΔE_Q (mm/s)	Γ (mm/s)	δ (mm/s)	Area (%)		
1	0.74	1.88	0.38	1.14	31.0	0.64	0.76	0.38	52.4		
		2.68	0.42	1.17	16.6					52	47
2	0.74	1.88	0.46	1.13	25.2	0.85	0.82	0.36	63.8	64	59
		2.52	0.42	1.19	11.0						
3	0.71	1.78	0.20	0.98	2.2	0.69	0.92	0.36	96.1		
		2.63	0.20	1.19	1.7					96	95
4	0.90	1.97	0.20	1.13	5.7	0.74	0.64	0.37	93.3	93	92
		2.55	0.26	1.13	0.9						

Note: δ = centre shift (with rispect to α-Fe); ΔE_Q = quadrupole splitting; Γ =full width half maximum; * = kept fixed during the refinement.

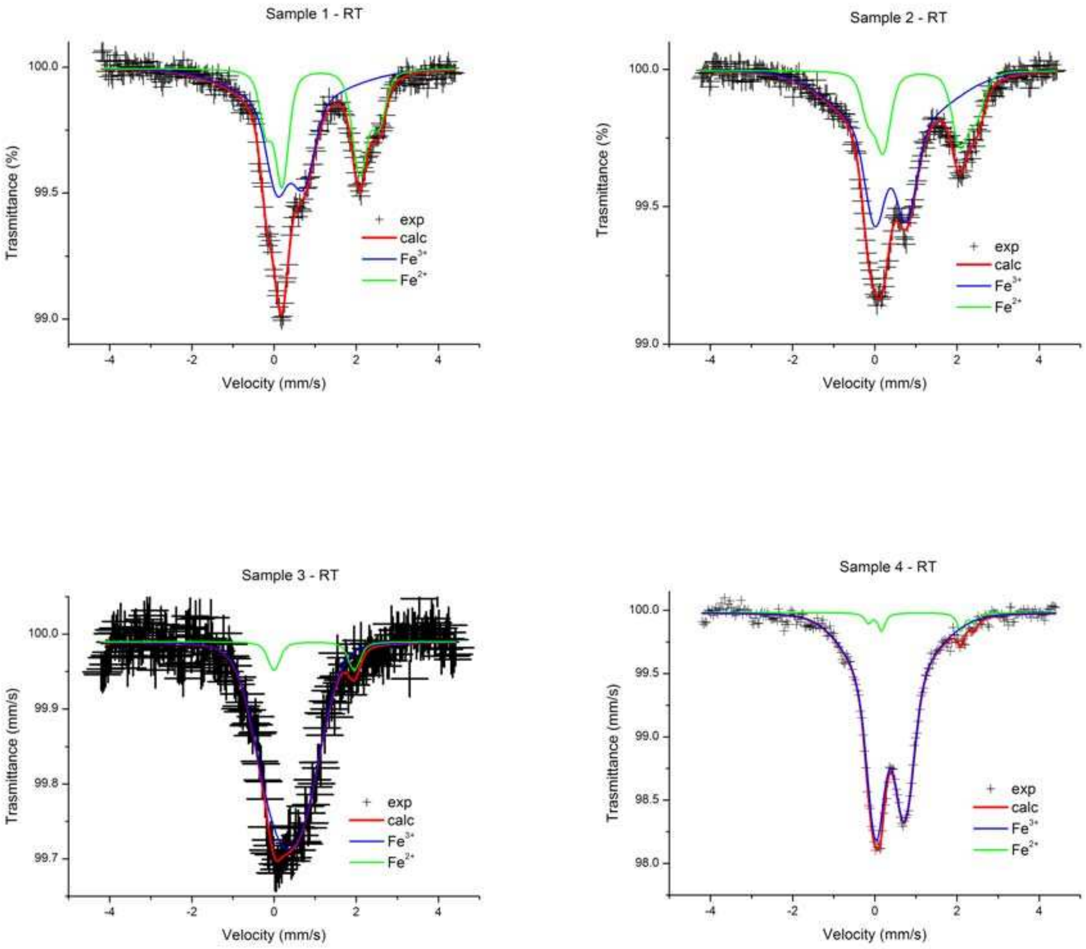

Figure 6 - Room temperature (RT) Mössbauer spectra with QSD fitting model of the four amphibole fibrous samples from Biancavilla.

Table 4 - ^{57}Fe Mössbauer hyperfine parameters at *RT* for the four amphibole fibrous samples from Biancavilla. QSD fitting model.

Sample	χ^2	Fe^{2+}				Fe^{3+}				Fe^{3+}_{raw}	Fe^{3+}_{corr}
		Δ_0 (mm/s)	σ_Δ (mm/s)	δ_0 (mm/s)	Area (%)	Δ_0 (mm/s)	σ_Δ (mm/s)	δ_0 (mm/s)	Area (%)	(% Fe_{tot})	(% Fe_{tot})
1	0.64	1.89	0.25	1.06	28.2	0.64	0.44	0.38	31.6	59	54
		2.75	0.23	1.06	13.2	1.1	2.2	0.38	27.0		
2*	0.58	1.87	0.28	1.09	18.9	0.77	0.41	0.38	31.4	71	67
		2.65	0.25	1.09	9.7	1.50	1.80	0.38	40.0		
3	0.74	1.96	0.20	0.98	6.9	0.74	0.87	0.35	93.1	93	92
4	0.74	1.93	0.03	1.13	3.1	0.70	0.36	0.35	55.3	95	94
		2.57	0.0	1.13	1.6	1.18	1.31	0.35	40.0		

Notes: Symbols according to Rancourt and Ping (1991). Fitting approach: Quadrupole Splitting Distributions (QSD). Isomer shift (δ_0) with respect to α-iron; δ_1 always lower than 0.05; $\gamma = 0.194$ mm/s; $h_+/h_- = 1$. The Fe^{3+}_{raw} is obtained from the area of absorption peaks assigned to Fe^{3+}. The Fe^{3+}_{corr} is obtained from the raw value by applying the correction factor C = 1.22 (Dyar et al. 1993). Estimated uncertainties are about 0.02 mm/s for hyperfine parameters, and no less than 3% for absorption areas.

*Data from Gianfagna et al. (2007).

X-ray Powder Diffraction

Powder diffraction data of samples 1 and 2 were collected on a parallel beam Siemens D5005 diffractometer, operating in transmission mode and equipped with a Peltier-cooled Si(Li) detector. Instead, powder diffraction data of samples 3 and 4 were collected on parallel-beam Bruker AXS D8 Advance diffractometer, operating in transmission mode and equipped with a Position Sensitive Detector (PSD) VÅNTEC-1. Samples were ground with ethanol in an agate mortar and the powders mounted in a 0.3 mm diameter borosilicate glass capillary. A reasonable compaction was obtained via an ultrasonic cleaner. Preliminary evaluations of diffraction patterns indicated for samples 1 and 2 the presence of albite and for samples 3 and 4 albite and sanidine. Minor phases were present in small amounts for samples 1, 2 and 3 (about 10 wt % of albite for samples 1 and 2, about 5 wt % of albite and 5 wt % of sanidine for sample 3), whereas their amount was found to be much higher for sample 4 (20 wt % of albite and 10 wt % of sanidine). Rietveld refinements were carried out with the GSAS suite of programs (Larson and Von Dreele 1985) coupled with EXPGUI graphical interface (Toby 2001). The background was fitted with a 36-term Chebyshev polynomial of the first kind to properly fit the amorphous component from the capillary. Peak-shapes were fitted using the TCH pseudo-Voigt (Thompson et al. 1987) modified for asymmetry (Finger et al. 1994). Refined variables were GV and GW (respectively tanθ-dependent andangle-independent) Gaussian parameters, LY (tanθ dependent) Lorentzian parameter and S/L and H/L asymmetry parameters (constrained to be equal in magnitude). Refinement of the scale-factors allowed a quantitative analysis of the mixture. Starting structural data of the amphibolic fibers were those of the prismatic fluoro-edenite of Gianfagna and Oberti (2001), whereas those of Meneghinello et al. (1999) and Gualtieri (2000) were respectively chosen for the albite and sanidine. Cell parameters, fractional coordinates for all atoms and site scattering for M(1), M(2), M(3), M(4) , A and A(m) were also refined for the fibers. Moreover, cell parameters were refined for albite and sanidine. Attempts to distribute the electron density at the A(2) site failed, possibly because of correlation with the neighbouring A site. Therefore, the simplification of a single site A (special position 0, 0.5, 0) was considered during the refinement. Moreover, for samples 2 and 4 refinement of a two A and A(*m*) sites model also failed. Isotropic displacement parameters were kept fixed throughout the refinement at the values reported for prismatic fluoro-edenite by Gianfagna and Oberti (2001), because of strong correlations with site occupancies. Restraints on bond distances were imposed as follow: T-O x 8 =1.635(25) Å, O-O x 12 = 2.67(4) Å, M(1)-O x 6 = 2.06(2) Å, M(2)-O x 6 = 2.08(3) Å, M(3)-O x 6 = 2.05(2) Å, M(4)-O x 8 = 2.51(20) Å, with a very low weight kept equal to 2 during the refinement, except for sample 4 for which it was required to use a statistical weight of 10 (due to presence of as much as 30% of minor phases in the mixture). Attempts to model the presence of preferred orientation, by means of the generalised spherical harmonics description of Von Dreele (1997), produced a very marginal reduction of the agreement indices as a results of a J texture indices close to 1 (Table 5). Experimental and calculated patterns with the relative differences are shown in Figure 7. Convergences were reached with the agreement factors reported in Table 5; fractional coordinates and isotropic displacement parameters are instead reported in Table 6, cell parameters in table 7, selected bond distances in Table 8. Notably, the structural data here reported for sample 2 are original and substantially in agreement with those previously reported by Gianfagna et al. (2007). Finally, it must be cited that the site scattering and bond distances observed for sample 4 have to be considered less reliable than those of the other samples, because of the presence of 30% of feldspars within the analyzed powder.

Table 5 – Experimental details of the X-ray diffraction data collection and miscellaneous data of the refinement. Statistical descriptor as defined by Young (1993).

Sample 1	
Instrument	Siemens D5005
X-ray tube	CuKα at 40 kV and 40 mA
Incident beam optic	Multilayer X-ray mirrors
Sample mount	Rotating capillary (30 rpm)
Soller slits	2 (2.3° divergence)
Divergence and antidivergence slits	1 mm
Detector	Solid state Si(Li) SolX
2θ range (°)	5-155
Step size (°)	0.02
Counting time (s)	30
R_p (%); R_{wp} (%); R_F (%)	5.37; 6.27; 4.61
Reduced $\chi2$	1.35
Restraints contribution to $\chi2$	185.8
Refined parameters	88
Peak-cut-off (%)	0.5
J	1.005
GV, GW	-5(6), 22(1)
LY	24.3(8)
S/L=H/L	0.0230(7)
Amphibole; albite (wt%)	87.3(1); 12.7(2)

Table 5 – continue

Sample 2*	
Instrument	Siemens D5005
X-ray tube	CuKα at 40 kV and 40 mA
Incident beam optic	Multilayer X-ray mirrors
Sample mount	Rotating capillary (30 rpm)
Soller slits	2 (2.3° divergence)
Divergence and antidivergence slits	1 mm
Detector	Solid state Si(Li) SolX
2θ range (°)	3-120
Step size (°)	0.02
Counting time (s)	30
R_p (%); R_{wp} (%); R_F (%)	5.17; 6.86; 3.93
Reduced $\chi 2$	1.21
Restraints contribution to $\chi 2$	76.1
Refined parameters	92
Peak-cut-off (%)	0.06
J	1.005
GV, GW	18(4), 6.9(7)
LY	18.4(7)
S/L=H/L	0.0231(6)
Amphibole; albite (wt%)	89.0(1); 10.0(4)

*: Starting structure of Gianfagna et al. (2007)

Table 5 - continue

Sample 3

Instrument	Siemens D8 Advance
X-ray tube	CuKα at 40 kV and 40 mA
Incident beam optic	Multilayer X-ray mirrors
Sample mount	Rotating capillary (60 rpm)
Soller slits	2 (2.3° divergence + radial)
Divergence and antidivergence slits	0.6 mm
Detector	Position Sensitive Detector (PSD) VÅNTEC-1 opening window 6° 2θ.
2θ range (°)	5-140
Step size (°)	0.02
Counting time (s)	10
R_p (%); R_{wp} (%); R_F (%)	1.02; 1.42; 1.76
Reduced $\chi 2$	4.62
Restraints contribution to $\chi 2$	115.4
Refined parameters	93
Peak-cut-off (%)	0.1
J	1.004
GV, GW	-6(2), 28.9(5)
LY	20.8(3)
S/L=H/L	0.0241(3)
Amphibole; albite; sanidine (wt%)	90.44(2); 5.43(6); 4.13 (7)

Table 5 – continue

Sample 4	
Instrument	Siemens D8 Advance
X-ray tube	CuKα at 40 kV and 40 mA
Incident beam optic	Multilayer X-ray mirrors
Sample mount	Rotating capillary (60 rpm)
Soller slits	2 (2.3° divergence + radial)
Divergence and antidivergence slits	0.6 mm
Detector	Position Sensitive Detector (PSD) VÅNTEC-1 opening window 6° 2θ.
2θ range (°)	5-140
Step size (°)	0.02
Counting time (s)	10
R_p (%); R_{wp} (%); R_F (%)	1.62; 2.17; 1.76
Reduced $\chi 2$	4.62
Restraints contribution to $\chi 2$	690.5
Refined parameters	86
Peak-cut-off (%)	0.2
J	1.008
GV, GW	-46(8), 56(2)
LY	30.0(8)
S/L=H/L	0.0255(7)
Amphibole; albite; sanidine (wt%)	70.7(1); 17.1(1); 12.2(1)

Table 6 - Fractional coordinates and isotropic thermal parameters (not refined) for the four amphibole fibrous samples from Biancavilla

Sample1 Site	*x*	*y*	*z*	U_{iso} (Å^2)
O(1)	0.1105(8)	0.0865(5)	0.2174(17)	0.01
O(2)	0.1180(10)	0.1703(6)	0.7250(21)	0.01
O(3)	0.1014(12)	0	0.7090(20)	0.01
O(4)	0.3681(12)	0.2477(4)	0.7997(24)	0.01
O(5)	0.3459(12)	0.1328(5)	0.0976(17)	0.01
O(6)	0.3442(12)	0.1139(5)	0.5987(17)	0.01
O(7)	0.3451(16)	0	0.2745(31)	0.01
T(1)	0.2772(6)	0.08347(29)	0.2926(11)	0.005
T(2)	0.2917(4)	0.16898(29)	0.8050(12)	0.005
M(1)	0	0.0884(53)	0.5	0.006
M(2)	0	0.1770(4)	0	0.006
M(3)	0	0	0	0.006
M(4)	0	0.27571(35)	0.5	0.011
A	0	0.5	0	0.025

Table 6 – continue.

Sample 2 Site	*x*	*y*	*z*	U_{iso} (Å^2)
O(1)	0.1109(10)	0.0850(6)	0.2225(21)	0.01
O(2)	0.1186(12)	0.1722(7)	0.7215(25)	0.01
O(3)	0.1048(13)	0	0.7092(25)	0.01
O(4)	0.3661(14)	0.2486(5)	0.7914(29)	0.01
O(5)	0.3475(15)	0.1342(6)	0.0990(22)	0.01
O(6)	0.3443(14)	0.1162(6)	0.5968(22)	0.01
O(7)	0.3431(18)	0	0.289(4)	0.01
T(1)	0.2794(7)	0.08388(35)	0.2957(15)	0.005
T(2)	0.2916(8)	0.17076(35)	0.8052(15)	0.005
M(1)	0	0.0882(5)	0.5	0.006
M(2)	0	0.1768(5)	0	0.006
M(3)	0	0	0	0.006
M(4)	0	0.2762(4)	0.5	0.011
A	0	0.5	0	0.020
A(*m*)	0.082(14)	0.5	0.079(22)	0.030

Table 6 - continue

Sample 3 Site	*x*	*y*	*z*	U_{iso} ($Å^2$)
O(1)	0.1121(5)	0.08488(21)	0.2196(8)	0.01
O(2)	0.1168(5)	0.17076(23)	0.7279(8)	0.01
O(3)	0.1016(4)	0	0.7136(10)	0.01
O(4)	0.3614(5)	0.24898(18)	0.7982(11)	0.01
O(5)	0.3492(6)	0.13333(19)	0.1006(9)	0.01
O(6)	0.3434(5)	0.11831(20)	0.5983(10)	0.01
O(7)	0.3454(6)	0	0.2830(13)	0.01
T(1)	0.28044(25)	0.08421(11)	0.2971(5)	0.005
T(2)	0.28837(28)	0.17102(10)	0.8057(5)	0.005
M(1)	0	0.08670(16)	0.5	0.006
M(2)	0	0.17833(15)	0	0.006
M(3)	0	0	0	0.006
M(4)	0	0.27751(13)	0.5	0.011
A	0	0.5	0	0.020
A(*m*)	0.0443(29)	0.5	0.131(8)	0.030

Table 6 - continue.

Sample 4 Site	*x*	*y*	*z*	U_{iso} (Å^2)
O(1)	0.1100(7)	0.0857(4)	0.2205 (14)	0.01
O(2)	0.1142(8)	0.1733 (4)	0.7190(17)	0.01
O(3)	0.1048(9)	0	0.7177(16)	0.01
O(4)	0.3614(10)	0.24980(34)	0.8014(19)	0.01
O(5)	0.3497(10)	0.1327(4)	0.0931(14)	0.01
O(6)	0.3427(10)	0.1195(4)	0.5938(14)	0.01
O(7)	0.3462(12)	0	0.2874(24)	0.01
T(1)	0.2780(5)	0.08468(22)	0.2939(9)	0.005
T(2)	0.2906(6)	0.17007(23)	0.8080(9)	0.005
M(1)	0	0.08645(35)	0.5	0.006
M(2)	0	0.17903(29)	0	0.006
M(3)	0	0	0	0.006
M(4)	0	0.27827(31)	0.5	0.011
A	0	0.5	0	0.025

Table 7 - Unit-cell parameters obtained from the four amphibole fibrous samples from Biancavilla. For comparison, the data obtained from single-crystal analysis (Gianfagna and Oberti, 2001) are reported.

	***a* (Å)**	***b* (Å)**	***c* (Å)**	***β*(°)**	***V* (Å^3)**
1	9.8056(4)	18.0105(7)	5.2725(2)	104.406(3)	901.86(6)
2	9.8112(3)	18.0162(6)	5.2774(2)	104.624(2)	902.61(5)
3	9.8272(1)	17.9899(2)	5.2756(1)	104.596(1)	902.57(2)
4	9.7935(3)	17.9728(5)	5.2746(1)	104.403(2)	899.23(5)
F-edenite 2001	9.846(4)	18.00(9)	5.277(2)	104.77(2)	904.8(5)

Table 8 - Selected bond-distances (Å) for the four amphibole fibrous samples from Biancavilla. For comparison, the data obtained from single-crystal analysis on prismatic fluoro-edenite (Gianfagna and Oberti, 2001) are reported.

Sample	**1**	**2**	**3**	**4**	**F-edenite 2001**	**Sample**	**1**	**2**	**3**	**4**	**F-edenite 2001**
T(1)-O(1)	1.585(8)	1.600(10)	1.601(4)	1.594(7)	1.624(1)	**T(2)-O(4)**	1.607(8)	1.592(9)	1.581(4)	1.596(6)	1.589(1)
T(1)-O(7)	1.656(7)	1.639(8)	1.653(3)	1.666(5)	1.635(1)	**T(2)-O(2)**	1.650(8)	1.643(10)	1.632(4)	1.675(7)	1.621(1)
T(1)-O(5)	1.626(8)	1.642(10)	1.633(4)	1.651(7)	1.645(1)	**T(2)-O(6)**	1.646(8)	1.653(10)	1.639(4)	1.628(6)	1.670(1)
T(1)-O(6)	1.676(8)	1.661(11)	1.670(5)	1.672(5)	1.643(2)	**T(2)-O(5)**	1.637(9)	1.646(11)	1.664(5)	1.617(8)	1.655(5)
<T(1)-O>	1.636	1.636	1.639	1.646	1.637	**<T(2)-O>**	1.635	1.634	1.629	1.629	1.634
M(1)-O(3) x 2	2.047(7)	2.057(9)	2.033(3)	2.049(6)	2.059(1)	**M(2)-O(4) x 2**	1.987(10)	2.003(12)	1.992(5)	1.967(8)	2.003(1)
M(1)-O(1) x 2	2.049(8)	2.034(10)	2.055(4)	2.030(7)	2.056(1)	**M(2)-O(2) x 2**	2.071(9)	2.094(11)	2.056(4)	2.070(8)	2.080(1)
M(1)-O(2) x 2	2.059(9)	2.079(11)	2.087(5)	2.092(7)	2.062(1)	**M(2)-O(1) x 2**	2.127(9)	2.158(11)	2.177(4)	2.168(8)	2.152(1)
<M(1)-O>	2.051	2.057	2.058	2.057	2.059	**<M2-O>**	2.062	2.085	2.075	2.068	2.078
M(3)-O(3) x 2	2.025(9)	2.052(11)	2.010(4)	1.995(8)	2.029(2)	**M(4)-O(4) x 2**	2.316(12)	2.305(14)	2.374(5)	2.387(9)	2.336(1)
M(3)-O(1) x 4	2.073(8)	2.064(10)	2.060(4)	2.067(8)	2.055(1)	**M(4)-O(2) x 2**	2.381(11)	2.355(14)	2.399(5)	2.346(9)	2.419(1)
						M(4)-O(6) x 2	2.637(11)	2.597(13)	2.560(4)	2.525(9)	2.550(2)
<M(3)-O>	2.058	2.060	2.043	2.043	2.046	**M(4)-O(5) x 2**	2.811(11)	2.779(14)	2.763(5)	2.786(9)	2.743(2)
<A-O>	3.03	3.06	3.05	3.05	2.926	**<M4-O>**	2.536	2.509	2.524	2.511	2.512
<A(*m*)-O>	–	3.02	2.87	–	2.863						

Sample 1

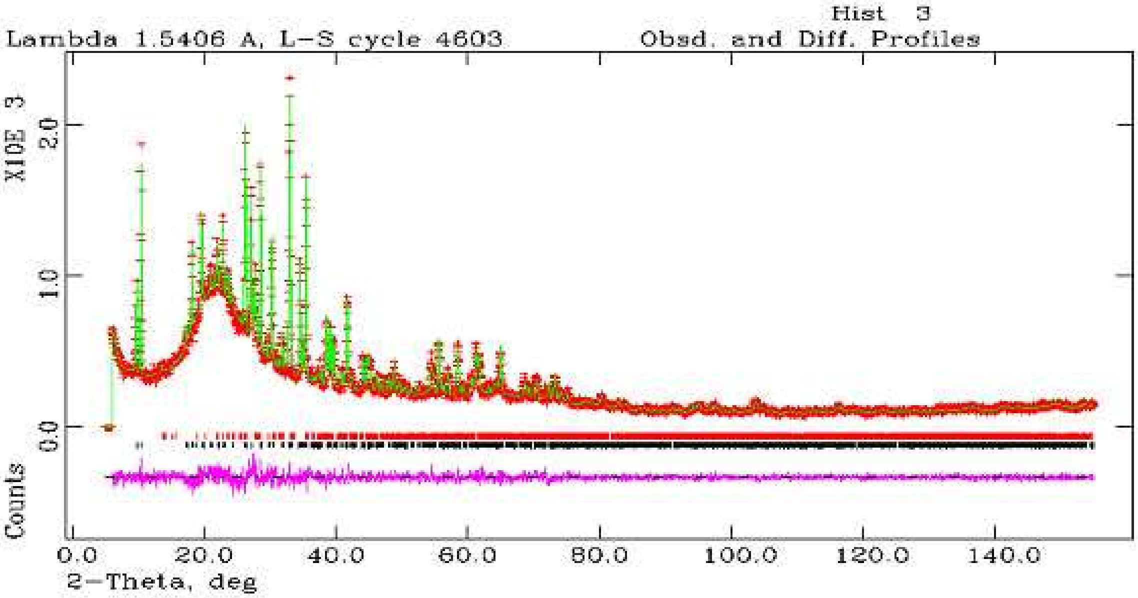

Sample 2

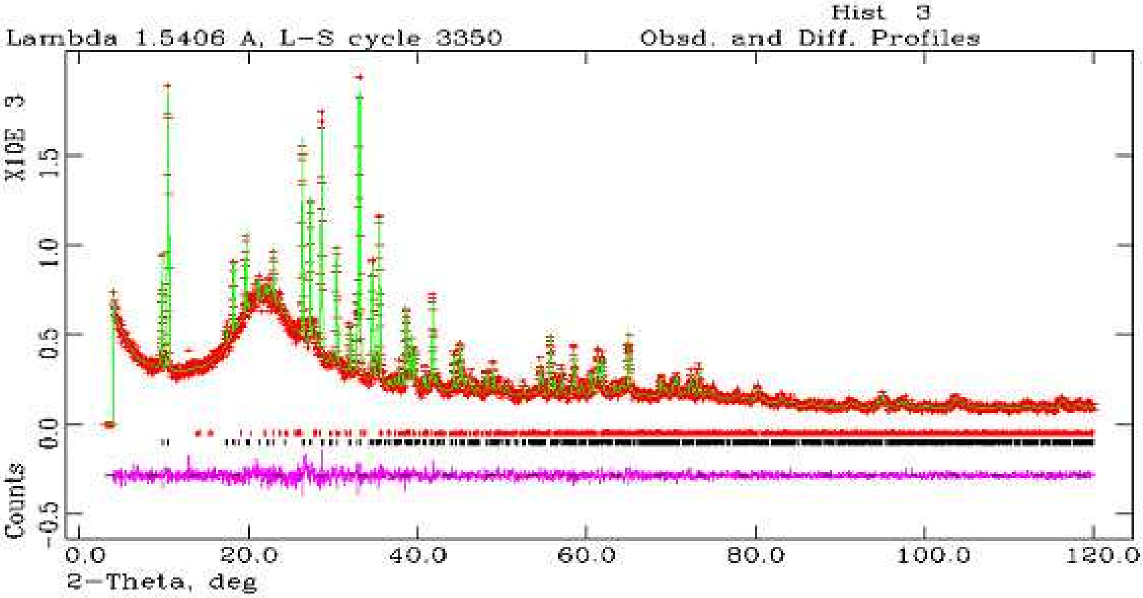

Sample 3

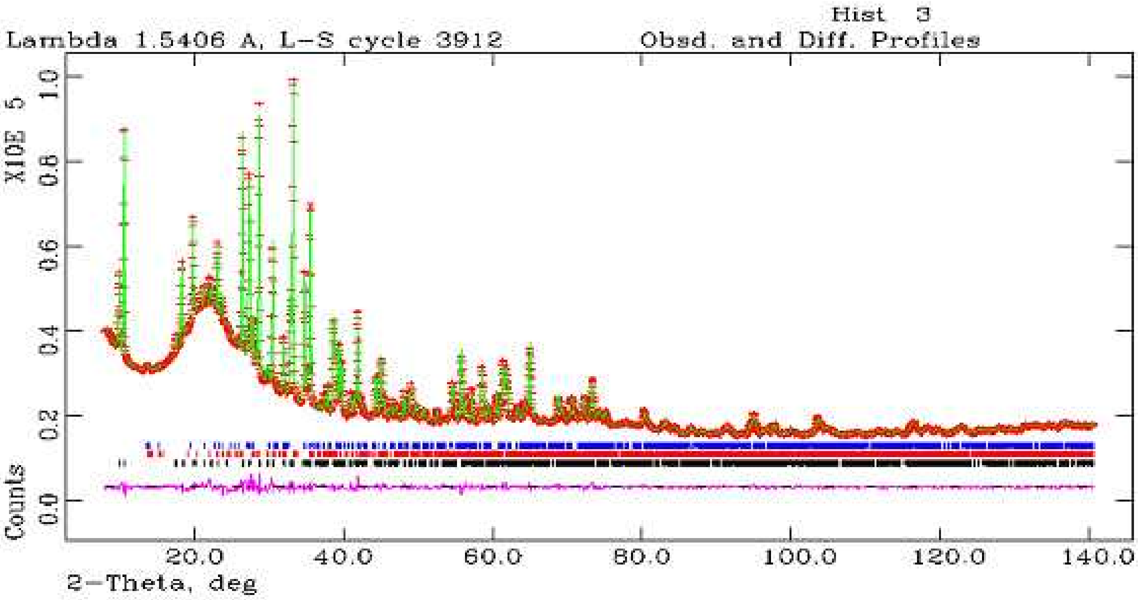

Sample 4

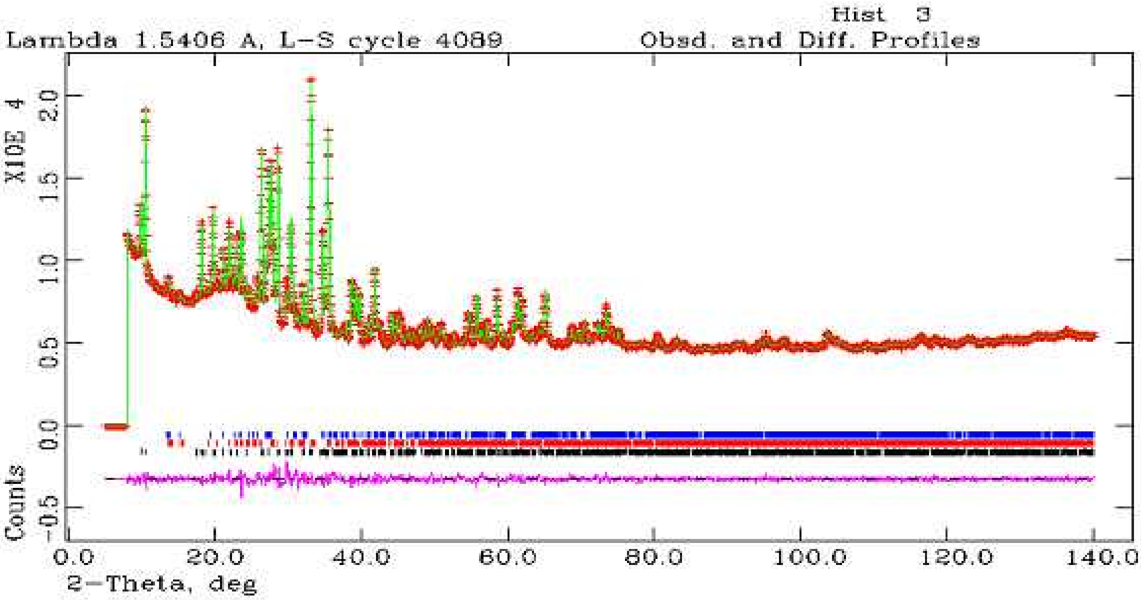

Figure 7 - Experimental (dots) and calculated (continuous line) Rietveld plots for the four amphibole fibrous samples from Biancavilla. The difference profile is shown at the bottom of the figure. Vertical markers refer to the position of the calculated Bragg reflections for amphibole (in black), albite (in red) and sanidine (in blue).

RESULTS AND DISCUSSION

The average chemical analysis and crystal-chemical formulas of the amphiboles fibers from Biancavilla are respectively reported in Tables 1 and 2. Within each sample the various fibers show different chemical compositions, and an edenite-winchite compositional trend was highlighted (Fig. 8, a-d). Moreover, all samples show nearly parallel compositional trends, and are spaced because of their tremolite component. In fact, sample 2 shows the highest tremolite content (roughly quantified as ca. 40% on the basis of its average chemical formula), sample 4 shows an intermediate tremolite content (ca. 30%) and samples 1 and 3 show the lowest tremolite content (ca. 25%). However, samples 1 and 3 are different because of their edenite content (ca. 45 and 55%, respectively). Samples 1 and 4 show winchite content similar each other (ca. 30%) and different from samples 2 and 3 (ca. 20%). Finally, sample 3 is the closest in composition to the prismatic fluoro-edenite studied by Gianfagna & Oberti (2001) and shows the most restricted compositional range. Notably, sample 2 shows a parallel trend with respect to the previous study, with a higher tremolite component. The observed compositional difference is related to the different analytical SEM-EDS method here adopted, which takes into account a significant error factor correction not previously considered. For all samples, small-to-medium amounts of iron (3.6 - 6.0% FeO_{tot}) were detected by chemical analysis. Moreover, the iron content and its oxidation state are not easily related to the compositional trends, since samples 2 and 3, in spite of their similar winchite content (ca. 30%), show the highest and the lowest iron content, respectively, and very different oxidation state. In addition, samples 1 and 4 show similar iron content, but very different oxidation state (Table 1).

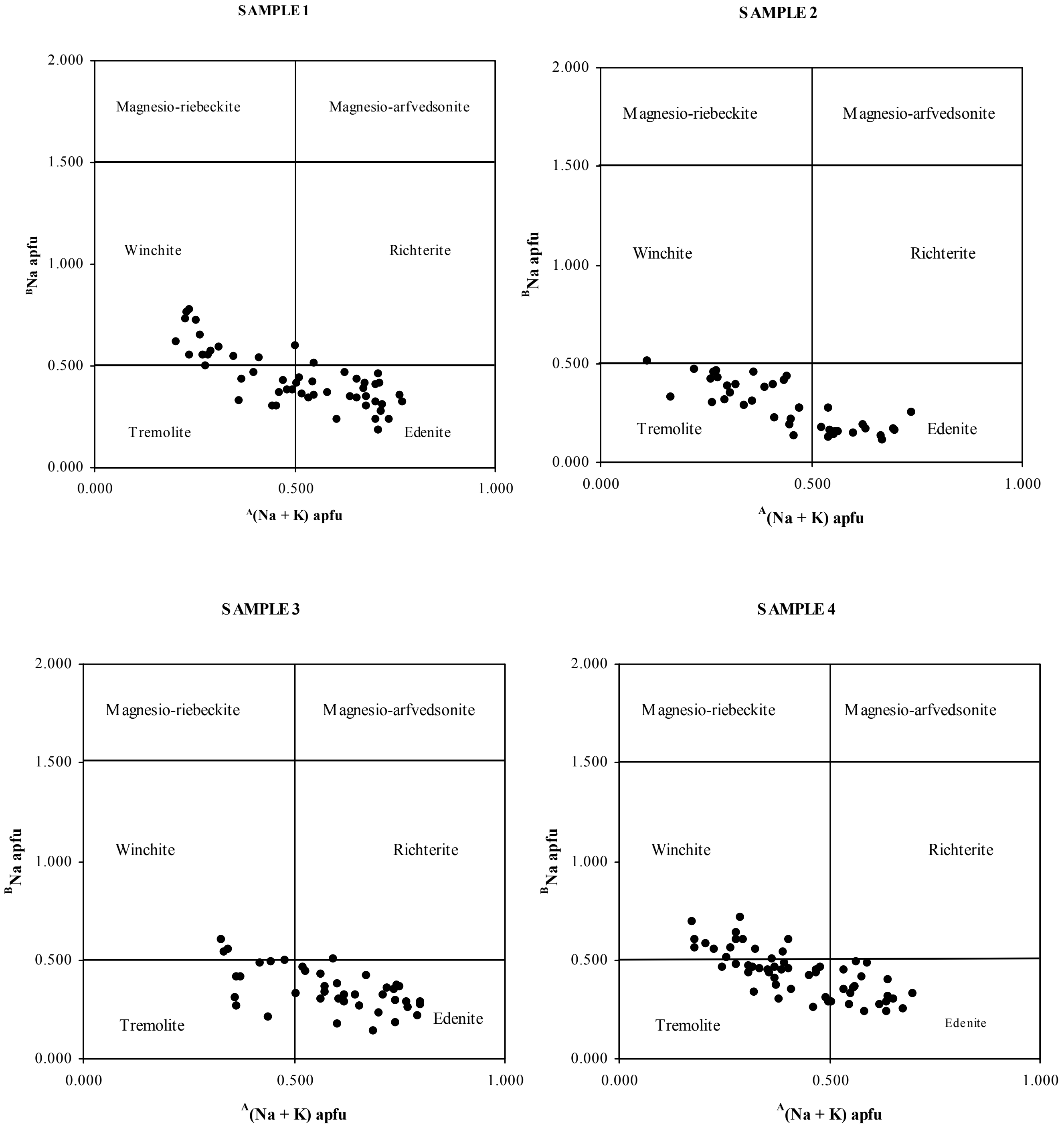

Figure 8 - Composition of the single fibers obtained from the four fibrous amphibole samples from Biancavilla, plotted in the graph $^{A}(Na+K)/^{B}Na$ (Leake et al., 1997).

The Fe^{3+}/Fe_{tot} ratios were quantified by analysis of the Mössbauer absorption spectra, which are typical of paramagnetic materials and are composed of two contributions. The first one is due to Fe^{2+} components with δ_0 of 1.1 mm/s and a quadrupole splitting centred around Δ_0 of 1.9 and 2.6 mm/s (both in the Lorentzian and in the QSD fits respectively, as showed in Figs. 2 and 3). The second contribution is due to Fe^{3+} components, with δ_0 of 0.38 mm/s and a quadrupole splitting distribution which is sharp at Δ_0 of 0.7 mm/s and very broad between 1.1 and 1.5 mm/s. The Fe^{3+}/Fe_{tot} ratio was quantified from spectral areal measurement ($Fe^{3+}{}_{raw}$) and corrected by applying the correction factor of Dyar et al. (1993). The final, corrected Fe^{3+}/Fe_{tot} ratios ($Fe^{3+}{}_{corr}$) were 54% and 67% Fe_{tot} for samples 1 and 2, respectively, and 92% and 94% Fe_{tot} for samples 3 and 4, respectively (Table 4). In agreement with the specific literature, Fe^{2+} was primarily assigned to an irresolvable combinations of M(1) + M(3) (Δ_0 of 2.6 mm/s) and M(2) + M(4) (Δ_0 of to 1.9 mm/s) and this is in agreement with the cation site-partition based on XRPD data (Table 9). In all cases (except sample 3 in which the two components were not refined) the amount of Fe^{2+} assigned to [M(2)+M(4)] is almost twice than that assigned to [M(1)+M(3)]. The two Fe^{3+} components are more difficult to explain. On the basis of reference data, Fe^{3+} should be ordered to M(2), as observed for sodic amphiboles (Ernst & Wai, 1970), strontian potassic-richterite (Sokolova et al. 2000), ferrian winchite (Sokolova et al., 2001), winchite-richterite (Gunter et al., 2003), fluoro-edenite (Gianfagna et al., 2007) and fibrous tremolite (Ballirano et al., 2008). Accordingly, we assign most of the Fe^{3+} to M(2) site. The additional, broad component observed in our spectra at 1.1-1.5 mm/s, which represents a large quadrupole splitting distribution, could derive from crystal size distribution or isolated magnetic states for Fe^{3+}, as suggested by Gunter et al. (2003). Alternatively, as commonly observed in complex silicates (Andreozzi et al., 2004; Andreozzi et al., 2008), this broad component could be related to minor Fe^{3+} disordered over different octahedra (as for sample 4, see Table 9) or even to local disorder of the other cations around Fe^{3+} (as for sample 2, see Table 9).

Table 9 - Site scattering (s.s.) values for the four fibrous amphiboles exerimentally obtained from the structural refinement (left) and calculated from site occupancy (right). Possible site-occupancy (central) is the result of combining chemical and Rietveld refinement data.

1			
	s.s. from refinement	Possible site-occupancy	s.s. from site-occupancy
A	4.6(2)	$K_{0.10}Na_{0.37}$	6.0
A*(m)*	–	–	–
Sum *A* sites	**4.6(2)**		**6.0**
M(4)	37.6(4)	$Ca_{1.29}Na_{0.48}Mn^{2+}_{0.07}Fe^{2+}_{0.16}$	37.0
Sum *B* sites	**37.6(4)**		**37.0**
M(1)	25.0(3)	$Mg_{1.90}Fe^{2+}_{0.10}$	25.3
M(2)	28.0(3)	$Mg_{1.61}Fe^{2+}_{0.04}Fe^{3+}_{0.35}$	29.5
M(3)	11.8(2)	$Mg_{1.00}$	12.0
Sum *C* sites	**64.8(5)**		**66.8**

2			
	s.s. from refinement	Possible site-occupancy	s.s. from site-occupancy
A	2.9(8)	$K_{0.09}$	1.7
A*(m)*	3.3(8)	$Na_{0.31}$	3.4
Sum *A* sites	**6.2(11)**		**5.1**
M(4)	37.3(4)	$Ca_{1.56}Na_{0.32}Mn^{2+}_{0.05}Fe^{2+}_{0.07}$	37.8
Sum *B* sites	**37.3(4)**		**37.8**
M(1)	25.3(4)	$Mg_{1.92}Fe^{2+}_{0.08}$	25.1
M(2)	30.6(4)	$Mg_{1.44}Fe^{2+}_{0.08}Fe^{3+}_{0.48}$	31.8
M(3)	12.2(3)	$Mg_{0.99}Fe^{2+}_{0.01}$	12.1
Sum *C* sites	**68.1(6)**		**69.0**

Table 9 - continue.

	3		
	s.s. from refinement	Possible site-occupancy	s.s. from site-occupancy
A	3.3(3)	$K_{0.10}$	1.9
A*(m)*	4.4(3)	$Na_{0.47}$	5.2
Sum *A* sites	**7.7(4)**		**7.1**
M(4)	34.1(1)	$Ca_{1.39}Na_{0.37}Mn^{2+}_{0.06}Mg_{0.18}$	35.5
Sum *B* sites	**34.1(1)**		**35.5**
M(1)	25.3(1)	$Mg_{1.87}Fe^{3+}_{0.12}$	25.6
M(2)	27.7(1)	$Mg_{1.70}Fe^{2+}_{0.03}Fe^{3+}_{0.27}$	28.2
M(3)	11.8(1)	$Mg_{1.00}$	12.0
Sum *C* sites	**64.8(2)**		**65.8**

	4		
	s.s. from refinement	Possible site-occupancy	s.s. from site-occupancy
A	6.8(2)	$K_{0.10}Na_{0.31}$	5.3
A*(m)*	–	–	–
Sum *A* sites	**6.8(2)**		**5.3**
M(4)	30.8(3)	$Ca_{1.30}Na_{0.45}Mn^{2+}_{0.05}Mg_{0.20}$	34.6
Sum *B* sites	**30.8(3)**		**34.6**
M(1)	24.1(2)	$Mg_{1.96}Fe^{3+}_{0.04}$	24.6
M(2)	30.3(2)	$Mg_{1.48}Fe^{2+}_{0.04}Fe^{3+}_{0.48}$	31.3
M(3)	12.7(2)	$Mg_{0.96}Fe^{3+}_{0.04}$	12.6
Sum *C* sites	**67.1(5)**		**68.5**

Structural data and site scattering (s.s.) values are reported in Tables 7, 8 and 9. Sample 4 shows the smallest *a* and *b* cell-parameters, and this is consistent with its highest Fe^{3+} content in C sites. In the fibrous samples the *c* cell-parameter is directly related to tetrahedrally-coordinated Al content. (Table 2). The main difference with respect to the prismatic fluoro-edenite is the general reduction of some of the cell parameters: in particular, *a* (9.794-9.827 Å for the fibrous samples and 9.846 Å for the prismatic sample), β (104.40°-104.62° for the fibers and 104.77° for the prismatic F-edenite) and, consequently, cell-volume (900-902 $Å^3$ for the fibers and 904 $Å^3$ the prismatic F-edenite). The reduction of the *a* parameter is consistent with the smaller A-site occupancy, and the reduction of β angle is consistent with the smaller Ca-content (Table 2). Within all samples, the refined <T-O> and <M-O> distances may be considered statistically equal (within their uncertainties). However, sample 2 shows the largest <M-O> value (2.067 Å compared with 2.057-2.060 Å of the other samples), in agreement with its highest Fe^{2+} content. For each sample, calculated site scattering (corresponding to the sum of electrons per formula unit) was derived from chemical data integrated by Mössbauer analysis. Possible site occupancy was obtained by combining integrated chemical data with Rietveld refinement results (Table 9). A good agreement is observed between the s.s. refined and those calculated from the possible site occupancy (Table 9). The largest differences, observed for C sites, are smaller then 3% relative.

Samples 2 and 4 show refined s.s. values at C sites higher than samples 1 and 3. This is due to the larger amount of heavier atoms as iron. In particular, since the refined s.s. at M(1) and M(3) sites are not significantly different within all samples, the observed increase of s.s. at C sites is mainly due to the presence of both Fe^{2+} and Fe^{3+} at M(2) site, and marginally to the presence of either Fe^{2+} (samples 1 and 2) or Fe^{3+} (samples 3 and 4) at M(1) site. Moreover, all fibrous samples show a s.s. value at C-sites higher than the prismatic fluoro-edenite, as a consequence of their highest (Fe^{2+} + Fe^{3+}) content. For all samples but number 1, the <M(4)-O> distances are randomly distributed (within their uncertainties) around the value of prismatic fluoro-edenite. For sample 1, the largest distance is consistent with the highest Na content at M(4) site. The refined s.s. values of M(4) site are in good agreement with those calculated, the largest difference being smaller than 3% relative for all samples but number 4. This latter shows a difference of 10% relative due to the abundant accessory phases. Samples 1 and 2 show s.s. values very close to that of prismatic F-edenite (37.18) and larger than those of the samples 3 and 4. Notably, for samples 1 and 2 the high value of s.s. is not justified by a high Ca content, but by the Fe^{2+} content (Table 9). In fact, the site partition for this samples allowed to decipher the combination of irresolvable $^{M(2)+M(4)}Fe^{2+}$ observed by Mössbauer spectroscopy, and to reveal that Fe^{2+} is equally distributed or preferentially ordered at M(4). Finally, all samples show statistically equal <A-O> and <A(m)-O> distances. The s.s. of fibrous samples are significantly lower than that of the prismatic fluoro-edenite, and this is related to the lowest content of ^{A}Na in the fibers.

BIANCAVILLA AMPHIBOLES: IMPLICATION FOR ASBESTOS CLASSIFICATION

In this study amphibole fibers from Biancavilla with evidented environmental and medical relevance were characterizated, but is spite of this, open questions remained about the fiber classification.

The mineral fibers showed a composition spanning from fluoro-edenite [$NaCa_2Mg_5Si_7AlO_{22}F_2$] to winchite [$\square NaCaMg_4(Al,Fe^{3+})Si_8O_{22}(OH)_2$], with different tremolite [$\square Ca_2(Mg,Fe^{2+})_5Si_8O_{22}(OH)_2$] component.The chemical variability recorded from the analysis of single fibers is extremely wide: as for example, according to Leake et al. (1997) classification, sample 2 would have more than 50% of its fibers plotting in the tremolite field, samples 1 and 3 would have more than 50% of their fibers plotting in the edenite field, and sample 4 would have almost the same amount of fibers plotting into the fields of tremolite and winchite. Consequently, the large compositional variation observed in every sample makes their classification very difficult and the definition of mineral species names almost impossible. It must be noticed, in addition, that in spite of their dangerousness, morphologies and composition, the fibers from Biancavilla are not regulated as "asbestos". In fact, within the amphibole fibers before mentioned, the regulatory agencies classify as "asbestos" the fibrous tremolite, but would not classify the whole mineral series, because of the large presence of edenite and winchite. A very similar case has been already reported by Gunter et al. (2003) for the amphibole fibers from Libby, Montana (USA). In both localities, the presence of amphibole fibers in the altered volcanic products, mined for commercial purposes, was recognized as the cause of the anomalously high incidence of malignant mesothelioma in the miners and/or local inhabitants. Also in that case, both a classification and a regulatory problem were evidenced, because fibers were recognized to be a solid solution series with dominantly compositions from winchite to richterite.

6

CHEMICAL AND STRUCTURAL CHARACTERIZATION OF A SAMPLE OF FIBROUS AMPHIBOLE FROM LIBBY (MONTANA, USA)

INTRODUCTION

Besides the "Biancavilla case study", a well-known case of not regulated amphibole fiber occurence is represented by that of Libby, Montana (USA). In fact, in the Libby town an elevated incidence of lung cancer and mesothelioma cases (Mc. Donald et al 1986, 2001) were found in the local miners and millers. Wylie and Verkouteren (2000) and Gunter et al. (2001, 2003) have carefully examined the mineralogy of the area around the Libby town, and they found fibrous amphiboles of composition dominantly ranging from winchite to richterite in the vermiculite mine near Libby. The environmental survey related the diseases to the fibrous amphiboles present in the vermiculite mine, which operated from 1923 to 1990 (Gunter et al., 2003). The vermiculite, after mined and enriched, it was expanded by rapid heating to form the Zonolite, a commercial product which was widely used in many consumer products such as fireproofing materials, absorbents, industrial fillers, and many more. The mine was located in the Rainy Creek complex, a Cretaceous age alkaline-ultramafic igneous body, essentially consisting of biotitite core, surrounded by a ring dike of biotite pyroxenite, which is in turn surrounded by a magnetite pyroxenite (Gunter et al., 2003). The biotite in the biotite pyroxenite was altered to vermiculite by low-temperature weathering, and the pyroxenes were altered to amphiboles under higher-temperature hydrotermal process (Boettcher, 1966). The amphiboles present with both fibrous and prismatic morphology in the alterated areas, can reach concentrations from 50 to 75% (Pardee and Larsen, 1928) and are intimately associated with other phases such as talc, titanium, pyrite, limonite, calcite, K-feldspar, quartz and albite. This chapter deals with a deepened crystal-chemical characterization of a sample of fibrous richterite, coming from the vermiculite mine. The crystal chemical characterization was carried out through chemical analysis in Electron Microprobe (EMP) and Inductively Coupled Plasma-Mass Spectrometry (ICP-MS), X-Ray Powder Diffraction (XRPD) and ^{57}Fe Mössbauer and Fourier Trasform Infrared (FT-IR) spectroscopies.

ANALYTHICAL METHODS

Scanning Electron Microscopy (SEM), Electron MicroProbe Analysis (EMPA) and Inductively Coupled Plasma-Mass Spectrometry (ICP-MS)

SEM was performed using a Philips XL30 equipped with EDAX system for EDS microanalysis. Images were obtained from a fragment of the hand specimen mounted on a sample stub and carbon coated. Analytical conditions were: 15 kV accelerating voltage, 10 mm working distance and tilt angle 0°. Electron micrographs showing the fibrous morphology at different magnifications are reported in Figure 1. The chemical composition was determined using a Camera SX-50 electron microprobe equipped with five wavelenght-dispersive spectrometers using the following conditions: excitation voltage 15 kV, speciment current 15nA, beam diameter 5 μm, 20 s counting time (peak), 10 s counting time (background). The following standards were used: wollastonite (Si Kα, Ca Kα), rutile (Ti Kα), corundum (Al Kα), magnetite (Fe Kα), metallic Mn (Mn Kα), periclase (Mg Kα), ortoclase (K Kα), jadeite (Na Kα), metallic Cr (Cr Kα) fuorophlogopite (F Kα) and sylvite (Cl Kα). Table 1 shows the average chemical composition and crystal-chemical formula normalized on the basis of 24 (O+F+Cl). Cations are reporded in atoms per formula unit (apfu) and were assigned, following Hawthorne (1981), to the four A, B, C and T group sites, filled according to the order recommended by Leake et al. (1997). Table 1 also shows the results of the ICP-MS analyses used as a reference of bulk chemical composition.

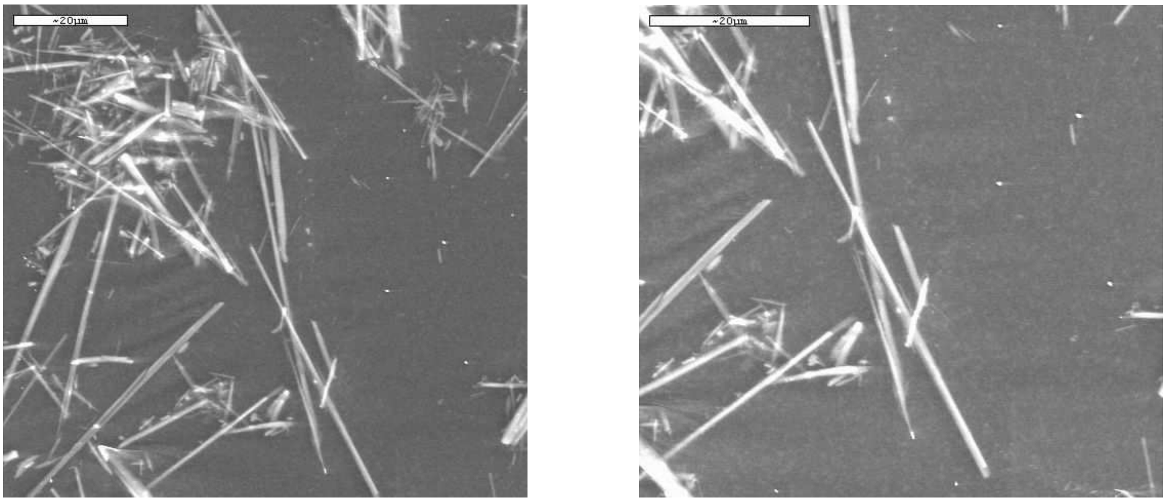

Figure 1 - SEM images of fibrous richterite from Libby.

Table 1 - Average chemical composition obtained by Electronic Microprobe (23 analytical points), ICP bulk-analysis and mean crystal-chemical formula of the fibrous richterite from Libby.

Oxides	EMPA	ICP	Sites	*apfu*
SiO_2	57.53(37)		Si	7.967
TiO_2	0.08(4)	0.29	^{IV}Al	0.033
Al_2O_3	0.25(10)	1.00	$\sum T$	8.000
Cr_2O_3	0.15(8)	0.38		
MgO	21.75(64)	19.80	^{VI}Al	0.007
CaO	7.16(70)	5.70	Ti	0.008
MnO	0.15(5)	0.09	Cr	0.017
FeO_{tot}	4.00(104)	4.90	Fe^{3+}	0.301
Na_2O	4.84(45)	4.70	Mg	4.490
K_2O	1.55(26)	2.40	Fe^{2+}	0.162
F	1.88(27)		Mn	0.020
Cl	0.01(1)		$\sum C$	5.005
H_2O*	1.26			
			Ca	1.063
	100.61		Na	0.937
F,Cl=O	0.79		$\sum B$	2.000
Total	99.82			
			Na	0.362
**Fe_2O_3	2.89		K	0.273
**FeO	1.40		$\sum A$	0.635
			OH	1.165
			F	0.822
			Cl	0.002
			$\sum O_3$	1.989

Note: *estimated from stoichiometry. **measured by ^{57}Fe Mössbauer spectroscopy

Infrared spectroscopy in a Fourier transform (FT-IR)

FT-IR data were collected on a Nicolet MAGNA 760 over the range 4000-400 cm^{-1}: 32 scans at a nominal resolution of 4 cm^{-1} were averaged. The instrument was equipped with a KBr beamsplitter and a TGS detector. The powdered samples were mixed in a 2:100 ratio with 200 mg of KBr in order to obtain transparent pellets. Measurements were done in air at room temperature. The spectrum (Fig. 2) was fitted using the PEAKFIT program (Jandel Corporation); the background was modeled using a linear function and, the peaks using symmetrical Gaussian line-shapes. Constraints were not used. Table 2 lists the values of the calculated frequencies, widths (FWHM) and intensities of each absorption peak.

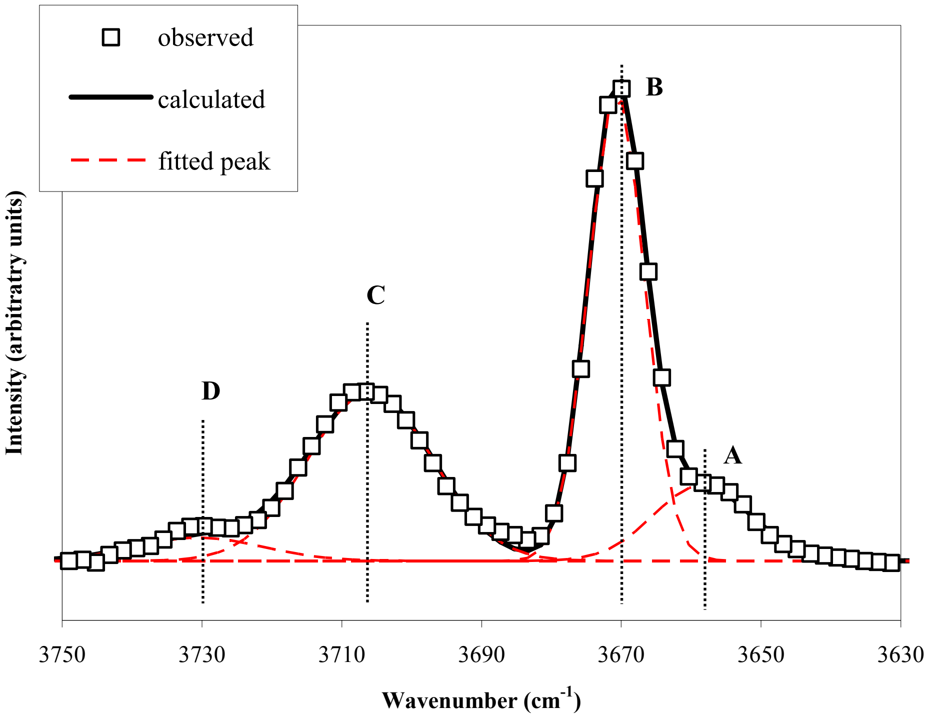

Figure 2 - FT-IR spectrum in the OH stretching region of fibrous richterite from Libby.

Table 2 - Fitted and calculated FT-IR data of fibrous richterite from Libby.

Band	Position (cm^{-1})	Width (cm^{-1})	Intensity (%)
A	3658	16	9
B	3671	9	30
C	3706	21	54
D	3731	22	7

Note: The intensity of the bands were calculated using the correction factor of Hawthorne et al. (1997).

^{57}Fe Mössbauer Spectroscopy

The amphibole fibers were gently ground in an agate mortar with acetone and mixed with a powdered acrylic resin to avoid (or reduce) preferred orientations. About 100 mg of sample were availalble, so that the absorber was within the limits for the thin absorber thickness described by Long et al. (1983). Data were collected at room temperature, using a conventional spectrometer system operated in constant acceleration mode, with a ^{57}Co source of nominal strength of 50 mCi in rhodium matrix, and recorded in a multichannel analyzer using 512 channels for the velocity range -4 to 4 mm/s. After velocity calibration against a spectrum of high-purity α-iron foil (25 μm thick), the raw data were folded to 256 channels. The spectrum was fitted using Recoil 1.04 fitting program (Lagarec and Rancourt 1988). A first cycle of refinement was performed by fitting pure Lorentzian line-shapes (Fig. 3, Table 3) but the Lorentian line-shapes showed wide line-widths ($\Gamma = 1.22$ mm/s). Therefore, a second cycle of refinement was carried out by fitting quadrupole-splitting distributions (QSD), following the approach of Gunter et al., 2003 and Gianfagna et al., 2007. A number of fitting models with unconstrained parameters [isomer shift(δ_0), coupling parameter (δ_1), center of Gaussian component(Δ_0), Gaussian width (σ_Δ), and absorption area(A)] were tried in order to obtain the best fit. A model based on two sites ($1Fe^{2+}$ + $1Fe^{3+}$) each with two components was finally chosen. The increasing of the number of Gaussian components did not change the resulting distribution resulting significantly. The uncertainties have been calculated using the covariance matrix and errors were estimated no less than ±3% for both Fe^{2+} and Fe^{3+} absorption areas (Fig. 4, Table 4).

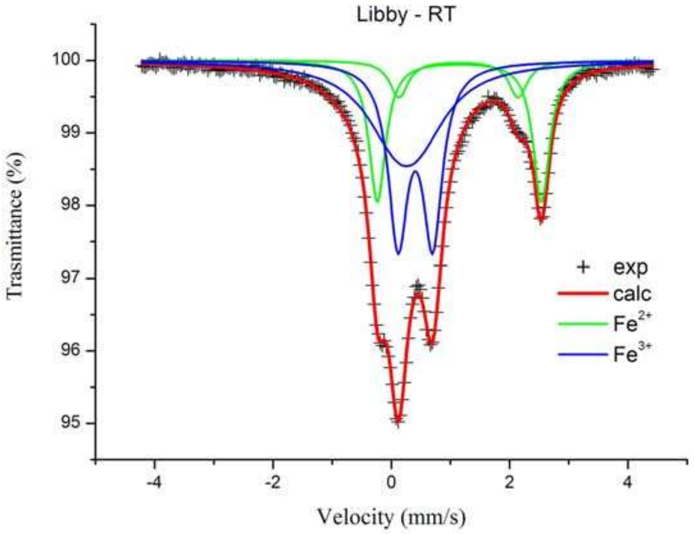

Figure 3 - Room temperature ^{57}Fe Mössbauer spectrum of Mössbauer fibrous richterite from Libby. Fitting by lorentzian line-shapes.

Table 3 – Room temperature Mössbauer parameters of fibrous richterite from Libby. Lorentzian fitting model.

δ	ΔE_Q	Γ	Assignment	Area	χ^2
1.14	2.01	0.40	Fe^{2+}	7	1.12
1.15	2.77	0.34	Fe^{2+}	24	
0.41	0.59	0.40	Fe^{3+}	34	
0.26	0.36	1.26	Fe^{3+}	35	

Note: *δ = centre shift (with respect to α iron); ΔE_Q = quadrupole splitting; Γ = full width half maximum.*

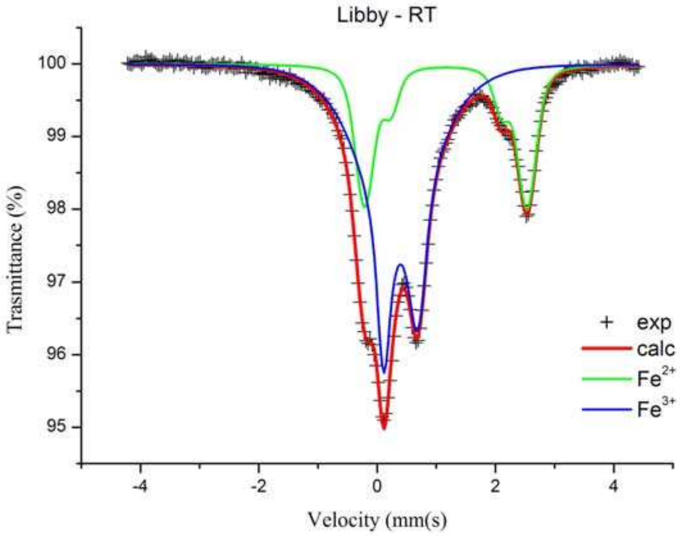

Figure 4 - Room temperature ^{57}Fe Mössbauer spectrum of fibrous richterite from Libby. Fitting by QSD.

Table 4 - ^{57}Fe Mössbauer hyperfine parameters at *RT* for fibrous richterite from Libby. QSD fitting model.

χ^2	Fe^{2+}				Fe^{3+}				Fe^{3+}_{raw}	Fe^{3+}_{corr}
	Δ_0 (mm/s)	σ_Δ (mm/s)	δ_0 (mm/s)	Area (%)	Δ_0 (mm/s)	σ_Δ (mm/s)	δ_0 (mm/s)	Area (%)	(% Fe_{tot})	(% Fe_{tot})
1,31	1,89 2,74	0,17 0,22	1,18 1,18	20,6 79,4	0,00* 0,58	1,30 0,14	0,33 0,33	70,1 29,9	69	65

Notes: Fitting approach: Quadrupole Splitting Distributions (QSD). Isomer shift (δ_0) with respect to α-iron; δ_1 always lower than 0.05; γ = 0.194 mm/s; h_+/h_- = 1. Symbols according to Rancourt and Ping (1991). The Fe^{3+}_{raw} is obtained from the area of absorption peaks assigned to Fe^{3+}. The Fe^{3+}_{corr} is obtained from the raw value by applying the correction factor C = 1.22 (Dyar et al. 1993). Estimated uncertainties are about 0.02 mm/s for hyperfine parameters, and no less than 3% for absorption areas.

*: kept fixed throghout the refinement.

X-ray Powder Diffraction

Powder diffraction data have been collected on a fully automated parallel-beam Bruker AXS D8Advance diffractometer, operating in trasmission mode, equipped with a Position Sensitive Detector (PSD) VÅNTEC-1. Fibers were ground under ethanol in an agate mortar and subsequently charged in a 0.7 mm diameter borosilicate glass capillary. Preliminary evaluation of the diffraction pattern indicated the presence of small amounts of titanite included in the refinement. Rietveld refinement was carried out by the GSAS crystallographic suite of programs (Larson and Von Dreele 1985) using the EXPGUI grafical user interface (Toby 2001). The background was fitted with a 28-terms Chebyshev polynomial of the first kind to model the amorphous contribution arising from the capillary. Peak-shape was fitted with the TCH pseudo-Voight function (Thompson et. al 1987) modified for asymmetry (Finger et. al 1994). Refined variables were GW (angle-independent) Gaussian parameter, LX (1/cosθ dependent) Lorenzian parameters, and S/L and H/L asymmetry parameters (constrained to be equal in magnitude). Refinement of two independent scale-factors for amphibole and titanite allowed a quantitative analysis of the mixture. Starting structural data were those of Gunter et al. (2003) for the amphibole and those of Huges et al. (1997) for the titanite. Cell parameters were refined for titanite, whereas fractional coordinates for all atoms and site scattering for M(1), M(2), M(3), M(4) and A were also refined for the fibers. Attempts to independently refine the position of the A(2) and A(*m*) sites failed because of the correlation with the adiacent A site. Therefore a single site A (special position 0, 0.5, 0) was considered during the refinement. The isotropic displacement parameters were kept fixed throughout the refinement to the values refined for prismatic winchite (Gunter et al., 2003) because of the strong correlations with the site occupancies. The geometry of the system was partly restrained under the following conditions: T-O x 8 =1.630(25) Å, O-O x 12 = 2.65(7) Å, M(1)-O x 6 = 2.07(2) Å, M(2)-O x 6 = 2.08(2) Å, M(3)-O x 6 = 2.07(2) Å, M(4)-O x 8 = 2.56(25) Å. The weight associated with those observations was progressly reduced to a very low value of 5 at the last stages of the refinement. Attempts to model the presence of preferred orientation by means of the generalized spherical harmonics descriptions of Von Dreele (1997) produced a small improvement of the fit as a result of a J texture index of 1.047. Convergences were reached with the agreement factors reported in Table 5; fractional coordinates and isotropic displacement parameters are instead reported in Table 6, selected bond distances in Table 7, cell parameters and site scattering (s.s.) values in Table 8. The experimental and calculated patterns with the relative differences are shown in Figure 5.

Table 5 - Experimental details of the X-ray diffraction data collection and miscellaneous data of the refinement for the fibrous richterite from Libby. Statistical descripotor ad defined by Young (1993).

Instrument	Siemens D8 Advance
X-ray tube	CuKα at 40 kV and 40 mA
Incident beam optic	Multilayer X-ray mirrors
Sample mount	Rotating capillary (60 rpm)
Soller slits	2 (2.3° divergence + radial)
Divergence and antidivergence slits	0.6 mm
Detector	Position Sensitive Detector (PSD) VÅNTEC-1 opening window 6° 2θ.
2θ range (°)	5-140
Step size (°)	0.02
Counting time (s)	10
R_p (%); R_{wp} (%); R_F^2 (%)	2.97; 3.88; 11.65
Reduced $\chi 2$	1.81
Restraints contribution to $\chi 2$	124.7
Refined parameters	85
Peak-cut-off (%)	0.2
J	1.047
GW; LX	24.8(10); 7.4(2)
S/L=H/L	0.0239*
Anfibolo; Titanite (% in peso)	98.7(3); 1.3(3)

Note: * Kept fixed throghout the last stages of the refinement.

Table 6 - Fractional coordinates and isotropic displacement parameters (not refined) for fibrous richterite from Libby.

Site	*x*	*y*	*z*	U_{iso} (Å^2)
O(1)	0.1100(8)	0.0860(4)	0.2194(14)	0.012
O(2)	0.1188(10)	0.1702(4)	0.7264(16)	0.012
O(3)	0.1051(11)	0	0.7120(18)	0.012
O(4)	0.3638(12)	0.2482(4)	0.8045(18)	0.012
O(5)	0.3450(11)	0.1301(4)	0.0901(15)	0.012
O(6)	0.3423(11)	0.1173(4)	0.5914(14)	0.012
O(7)	0.3319(14)	0	0.2851(22)	0.012
T(1)	0.2740(6)	0.08514(21)	0.2939(7)	0.005
T(2)	0.2887(6)	0.17049(22)	0.8051(8)	0.005
M(1)	0	0.08861(34)	0.5	0.005
M(2)	0	0.17939(30)	0	0.005
M(3)	0	0	0	0.005
M(4)	0	0.27734(32)	0.5	0.017
A	0	0.5	0	0.025
H	0.214*	0*	0.775*	0.050*

Note: * Kept fixed throghout the refinement.

Table 7 - Selected bond distances (Å) for the fibrous richterite from Libby. Reference data of Gunter et al. (G2003) from single-crystal refinement are also reported for comparison.

	Libby	G2003		G2003	Prismatic
T(1)-O(1)	1.569(7)	1.608(2)	T(2)-O(4)	1.582(7)	1.585(2)
T(1)-O(7)	1.638(5)	1.635(1)	T(2)-O(2)	1.626(8)	1.614(2)
T(1)-O(5)	1.636(7)	1.632(2)	T(2)-O(6)	1.662(7)	1.677(2)
T(1)-O(6)	1.652(7)	1.628(2)	T(2)-O(5)	1.637(8)	1.665(2)
<T(1)-O>	1.624	1.626	<T(2)-O>	1.627	1.635
M(1)-O(3) x 2	2.071(7)	2.088(2)	M(2)-O(4) x 2	1.969(10)	1.978(2)
M(1)-O(1) x 2	2.042(7)	2.065(2)	M(2)-O(2) x 2	2.080(9)	2.079(2)
M(1)-O(2) x 2	2.063(8)	2.051(2)	M(2)-O(1) x 2	2.171(8)	2.186(2)
<M(1)-O>	2.059	2.068	<M(2)-O>	2.073	2.081
M(3)-O(3) x 2	2.042(8)	2.045(2)	M(4)-O(4) x 2	2.382(9)	2.370(2)
M(3)-O(1) x 4	2.070(7)	2.075(2)	M(4)-O(2) x 2	2.412(9)	2.427(2)
<M(3)-O>	2.061	2.065	M(4)-O(6) x 2	2.572(9)	2.573(2)
			M(4)-O(5) x 2	2.854(10)	2.863(2)
<A-O>	2.891		<M(4)-O>	2.555	2.558

Table 8 - Unit-cell parameters and site scttering values (in electrons per formula unit) for the fibrous richterite for Libby experimentally obtained from the structure refinement (left) and calculated from possible site partition (right). Possible site partition is the result of combining chemical and Rietveld refinement data.

	Refinement	Possible site partition	Chemical data
a (Å)	9.8778(3)		
b (Å)	17.9703(4)		
c (Å)	5.2750(1)		
β (°)	104.358(1)		
V (Å^3)	907,11(4)		
A	8.91(15)		9.81
A site sum	**8.91(15)**	$Na_{0.36}$; $K_{0.27}$	**9.81**
M(4)	30.76(28)		
B site sum	**30.76(28)**	$Ca_{1.06}$; $Na_{0.94}$	**31.54**
M(1)	23.40(24)	$Mg_{1.92}$; $Fe^{2+}_{0.08}$	25.12
M(2)	29.23(26)	$Mg_{1.61}$; $Fe^{3+}_{0.30}$; $Fe^{2+}_{0.04}$; $Cr_{0.02}$; $Ti_{0.01}$; $Al_{0.01;}$ $Mn_{0.02}$	29.48
M(3)	11.86 (17)	$Mg_{0.96}$; $Fe^{2+}_{0.04}$	12.56
C sites sum	**64.49(39)**		**67.16**

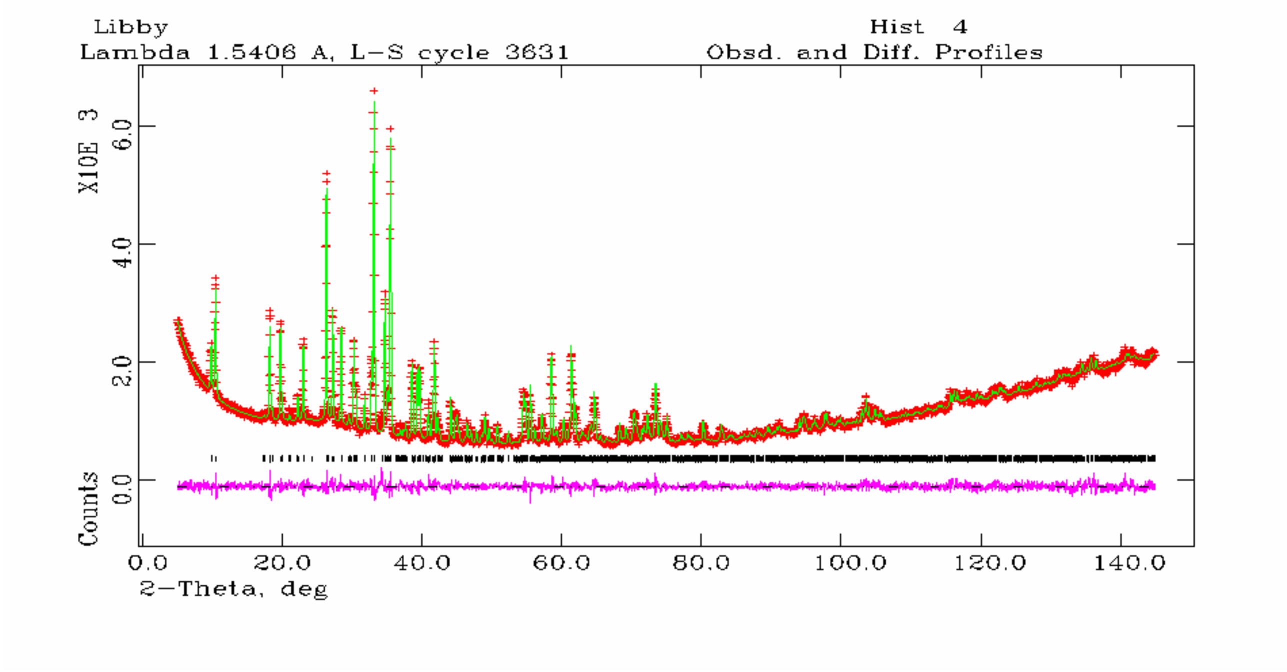

Figure 5 - Experimental (dots) and calculated (continous line) Rietveld plots for the fibrous richterite from Libby. The difference profile is shown at the bottom of the figure. Vertical markers refer to the position of the calculated Bragg reflections for amphibole (in black) and titanite (in red).

RESULTS AND DISCUSSION

The comparison between bulk (ICP-MS) and punctual (EMP) analyses (Table 1) shows differences between Al_2O_3, K_2O and TiO_2 far larger then their standar deviations. However they are related to the presence of K-feldspar and titanium in the hand-sample as previously revealed by the result of the XRPD experiments. EMP analysis reveals a substantial chemical homogeneity of the fibers and a richterite composition, with an average crystal chemical formula very close to that intermediate between ideal winchite and ideal richterite [$^{A}A_{0.5}{}^{B}NaCa^{C}Mg_{4.5}M^{3+}{}_{0.5}{}^{T}Si8O_{22}(OH)_2$, where M^{3+}= Fe^{3+} and/or Al]. Figure 6 shows the composition of the single fibers in the Leake's classification graph [^{A}(Na + K) vs ^{B}Na] (Leake et al., 1997).

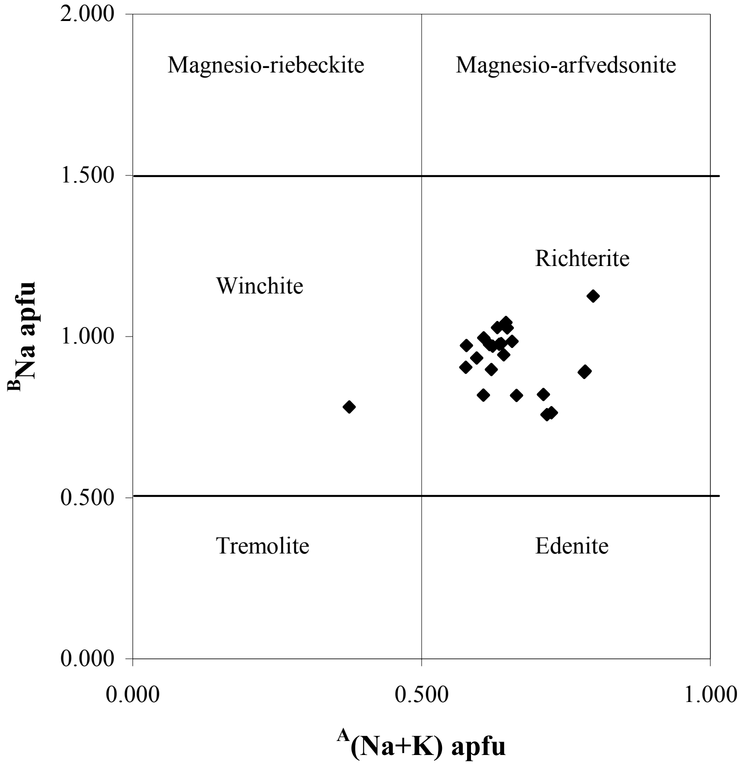

Figure 6 - Composition of the single fibers of the fibrous richterite from Libby in the Leake's classification graph (Leake et al., 1997).

The Mössbauer spectrum is typical of a paramagnetic material and is composed of two contributions. The first one is due to Fe^{2+} components with δ_0 of 1.1 mm/s (both in the Lorentzian and in the QSD fits respectly showed in Fig. 3 and Fig. 4) and a quadruple splitting centred around Δ_0 of 2.0 and 2.8 mm/s in both fits. The second contribution, due to Fe^{3+}, is composed of two components with δ_0 of 0.30 mm/s and a quadrupole splitting distribution, which is sharp at 0.41 mm/s, and very broad (Γ of 1.22) at 0.58 mm/s. In the QSD analysis for the Fe^{3+} contribution were also refined two components with Δ_0 0.0 mm/s, which is sharp and very broad with Δ_0 0.58 mm/s (see σ_Δ in table 4). The Fe^{3+} ratio is 69% of Fe_{tot} (Table 4) from spectral areal measurement (Fe^{3+}raw), and 65% when adjusting for the recoil-free fraction, as suggested by Dyar et al. (1993). Notably, the Fe^{3+} ratio obtained by QSD analysis is closely comparable with that retrieved by Lorentzian site analysis (Table 3). According with the approch previously followed in this work for the other amphibole samples and with Gunter et al. (2003), Fe^{2+} was assigned to a not resolvable combinations of [M(1) + M(3)] (Δ_0 of 2.76 mm/s) and [M(2) + M(4)] (Δ_0 of 2.0 mm/s). In both cases (lorentzian and QSD analysis) the amount of Fe^{2+} assigned to [M(1)+M(3)] is about 80% of total Fe^{2+}. The presence of Fe^{2+} at M(1) + M(3) is also confirmed by the FT-IR spectrum (Fig. 2). In fact, execpt for the typical absorbtion band at 3670 cm^{-1} assigned to the vibration of the O-H dipole bonded to three ^{VI}Mg cations, a well developped band is observed at 3656 cm^{-1} attributed to $^{M(1)+M(3)}Fe^{2+}$ environment according to results of Skogby and Rossman (1991) and Hawthorne and Della Ventura (2007). The $^{M(1)+M(3)}Fe^{2+}$ occupancy calculated using the FT-IR data of Table 2 and following Burns and Strens (1966) are in very good agreement with that obtained combining Mössbauer and EMP data (respectively $^{M(1)+M(3)}Fe^{2+}$ = 0.09 apfu and 0.12 apfu). Fe^{3+} was only assigned at M(2) according to the absence in FT-IR spectrum of absorbtion bands at Δ= -50 cm^{-1} from the tremolite reference band (Raudsepp et al., 1987), indicating the presence of $^{M(1)+M(3)}Fe^{3+}$. The measured cell parameters showed lower *b* and *c* parameters and β angle with respect to the prismatic winchite (Gunter et al., 2003). The reduction of *b* and *c* parameters and β value observed for the fibrous sample are mainly related to the highest fluorine content at O(3) (0.82 apfu for the fibrous richterite compared to 0.37 apfu for the prismatic winchite) and a lowest $^{M(4)}Ca$ content (0.94 apfu for the fibrous richterite compared to 1.12 apfu for the prismatic winchite), respectively. The observed <T-O> distance for the fibrous richterite (1.626 Å) is comparable to that of the prismatic winchite (1.630 Å); in particular, the equal <T(1)-O> distances (Table 7) are in agreement with the same tetrahedrally-coordinated Al content. The presence of tetrahedrally-coordinated Al content is also confirmed by FT-IR investigation, since the presence in the FT-IR spectrum of the absorption band at 3707 cm^{-1} (Fig. 2) indicating both the presence of $^{T(1)}Al$ and $^{O(3)}F$ (Hawthorne and Della Ventura, 2007). The observed values for the <M(1)-O> <M(2)-O> and <M(3)-O> distances (Table 7) are in close agreement with those calculated (2.067, 2.079 and 2.063 Å, respectively) using the equations of Hawthorne et al. (2007). Calculated total site scattering (corresponding to the sum of electrons per formula unit) was derived from chemical data integrated by Mössbauer analysis. Possible site occupancy was obtained by combining integrated chemical data with Rietveld refinement results (Table 8). In spite of Mössbauer and FT-IR data, the structural refinement suggests the presence at M(1) and M(3) of only Mg. Moreover, for C sites, the agreement between s.s. refined and those calculated from the possible site occupancy is quite satisfactory, with the largest difference being ca. 4% relative (Table 8). The slightly increase in <M(4)-O> distance observed for the fibrous amphibole with respect to the prismatic winchite is in accord with the presence of an highest $^{M(4)}$Na content. The observed <A-O> distance for fibrous richterite is comparable to that observed for the prismatic winchite. The difference between refined s.s. and those calculated from chemical data for the A site reachs ca. 9% relative (Table 8). This significant discrepancy could be due to the simplified model used for the A site (a single site centered at 0; 0.5; 0), which does not properly take into account the possible presence of electron density at A(*m*) and/or A(2) sites.

LIBBY AMPHIBOLES: IMPLICATION FOR ASBESTOS CLASSIFICATION

The fibrous amphiboles occuring in the vermiculite deposit near Libby, since the high rates of respiratory diseases found in the miners of the now-closed vermiculite mine, represent an environmental and health problem for the local citizens. In this study a richterite composition was observed for the mineral fibers, in accord with previous studies (Gunter et al. 2003; Meeker et al., 2003 and Sanchez 2008) showing, for the majority of the fibrous amphiboles from Libby, a winchite and/or richterite composition. Notably, neither winchite or richterite fibers are regulated as asbestos. As previously mentioned (see chapter 5) the amphibole fibers from Biancavilla represent a very similar case, being not regulated as "asbestos" in spite of their dangerousness and morphologies and composition. Therefore, both the cases allow to highlight the important role that the mineralogical investigations play on the redefinition of the not regulated materials. In Biancavilla and Libby each sample is made of fibers forming solid solution series, with an average composition residing at the boundary between two or three mineral species. Consequently, to define each sample with an unique name would not take into account of the wide compositional range of the sample. This issue, in terms of legal perspective, makes necessary to regulate all the end members occurring in the whole mineral series.

7

INVESTIGATION OF FIBROUS AMPHIBOLES BY X-RAY PHOTOELECTRON SPECTROSCOPY

INTRODUCTION

The toxicity of asbestos, as well known, is related to both morfology (Stanton, 1981) and chemical factors (Fubini 1993, 1996; Gilmour et al. 1997). Among the chemical factors, the surface chemical properties are the most important in determining the hazardous effects of the fibers. In fact, it is at the surface of the fibers that the interaction with the biological environment occur. The reactive sites at the surface include poorly coordinated (due to vacancies and edges) surface atoms and exposed ions which may coordinate molecules and play a primary role in the catalitic reactions, such as transition metal ions (Fubini 1993). The surface of asbestos has basic character and therefore can strongly react with acidic molecules such as CO_2, benzoic acid, fluorine, and it is capable of forming hydrogen bonds with adsorbing species (Fubini 1993). The hydrogen bonding capability makes the asbestos stronly hydrophilic and they easily react with cell membranes (Fubini 1993). In addition, biomolecular components of the cell membranes have many sites which can form hydrogen bonding, and as a result interaction of mineral fibers and cell membranes leads to membranolysis (Fubini 1993). Asbestos fibers can adsorb on their surface, both in air and after inhalation, toxic substances and become more hazardous. However, they can also be coated by non-toxic substances such as phospholipids and surfactants present in the air, that prevent the dangerous surface reactions by covering the active sites (Fubini 1993). As mentioned above, the presence of transition metal ions on the surface is one of the factors of surface reactivity of the fibers. Many autors agree in attributing to them the strong catalyzation of HO° free radicals by parteciping in Fenton chemistry (Kane et al. 1996; Fubini and Otero Aréan 1999; Kamp and Weitzman, 1999; Robledo and Mossman, 1999). In particular, the attention has been focused on the Fe exposed on the fiber surface and its relevant role in the Reactive Oxigen Species (ROS) production (Gazzano et al. 2005; Favero-Longo et al. 2005). These evidences make the investigation of the surface of the fibers necessary to better define the possible mechanism induced in the interaction between the fibers and biological system. In this work some of the various amphibole fibers, previously characterized in term of crystal-chemistry, have been analyzed by X-ray photoelectron spectroscopy (XPS). The study was focused on the determination of the surface composition and its Fe^{3+}/Fe_{tot} ratio. The specimens that will be discussed include: the UICC crocidolite, the richterite from Libby sample 1 from Biancavilla, Ala di Stura and San Mango tremolites.

EXPERIMENTAL METHOD

Measurement by XPS and sample preparation

The studied samples were mechanically polished in ethanol and immediately transferred to the X-ray spectrometer. The XPS measurements were performed using a PHI 5700 photoelectron spectrometer (Physical Electronics, Eden Prairie, USA) equipped with a hemispherical analyzer. The instrument was operated in the minimum-area mode with an aperture diameter of 0.4 mm using an Al K source at 350 W. The γ angle, defined as the angle between the X-ray source and the analyzer, was 54.7°. The acceptance angle was ±7°. The residual pressure in the chamber was 10^{-8} Pa. The high-resolution spectra of Fe 2p were recorded with the pass energy of 23.5 eV, with a dwell time of 100 ms and at an energy step of 0.05 eV.

Spectral processing

Collected spectra were analysed using Casa XPS software (Fairley, 1999-2003). All spectra were calibrated against the C1s peak with a fixed value of 285.0 eV. After calibration, the background was substracted using a Shirley-type backrground to remove most of the extrinsic loss structure (Norgren et al., 1994). The total surface composition of the amphibole fibers was obtained by integrating the intensities of the detailed spectra of the various elements and then correcting for the photoionization cross sections, σ, and the analyzer transmission function, as reported in Piras (2002). To determine oxidation state of the Fe, the high-resolution Fe $2p_{3/2}$ was resolved by using two different approaches. The first-one, hereafter referred to as approach I, is based on the calculated multiplets of Gupta and Sen (Gupta and Sen, 1974, 1975). They calculated the multiplet structure expected for core p levels of the free Fe^{2+} and Fe^{3+} ions, taking account of electrostatic and spin-orbit interactions and using the Hartree-Fock approximation for free ion. To analyze the oxidation state of Fe in amphibole fibers, reference spectrum of powder Fe_3O_4 was acquired and studied. This is necessary because of the numerous multiplet splitting which occur for each oxidation state of iron. The second approach, hereafter referred to as approach II, is based on the data recorded from pure iron oxides and oxy-hydroxides (Olla et al., 2006). Notably, for Ala di Stura tremolite because of the low resolution of the Fe $2p_{3/2}$ peak due to the small amount of Fe in the sample, it was not possible to resolve the peak in its components. The XPS high resolution spectra of Fe $2p_{3/2}$ and curve fit for all sample based on the approaches I and II are reported in Figure 1 and 2, respectively.

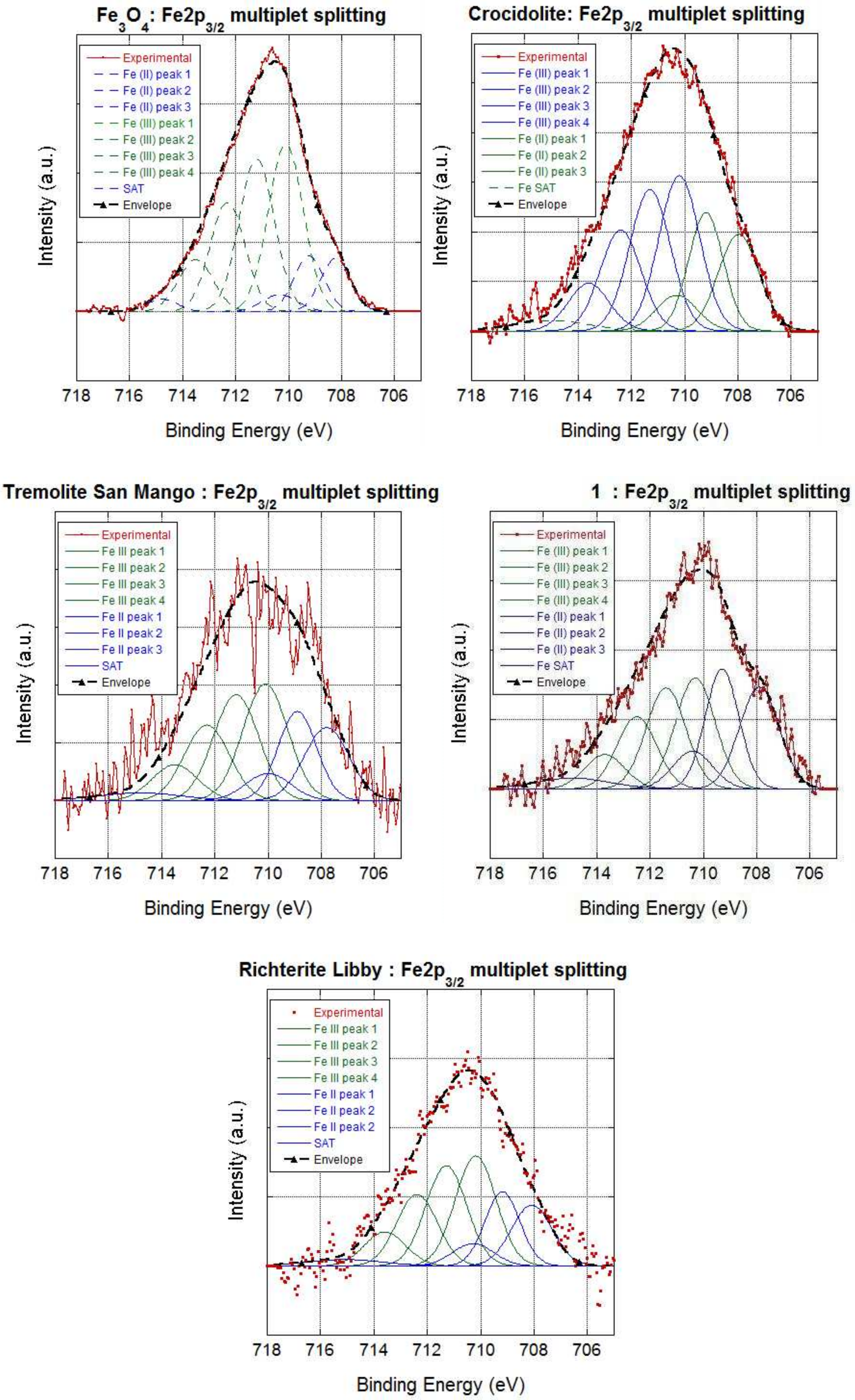

Figure 1 - Shirley background subtracted Fe $2p_{3/2}$ spectra and curve fit for all studied sample. Fit based on the approach I.

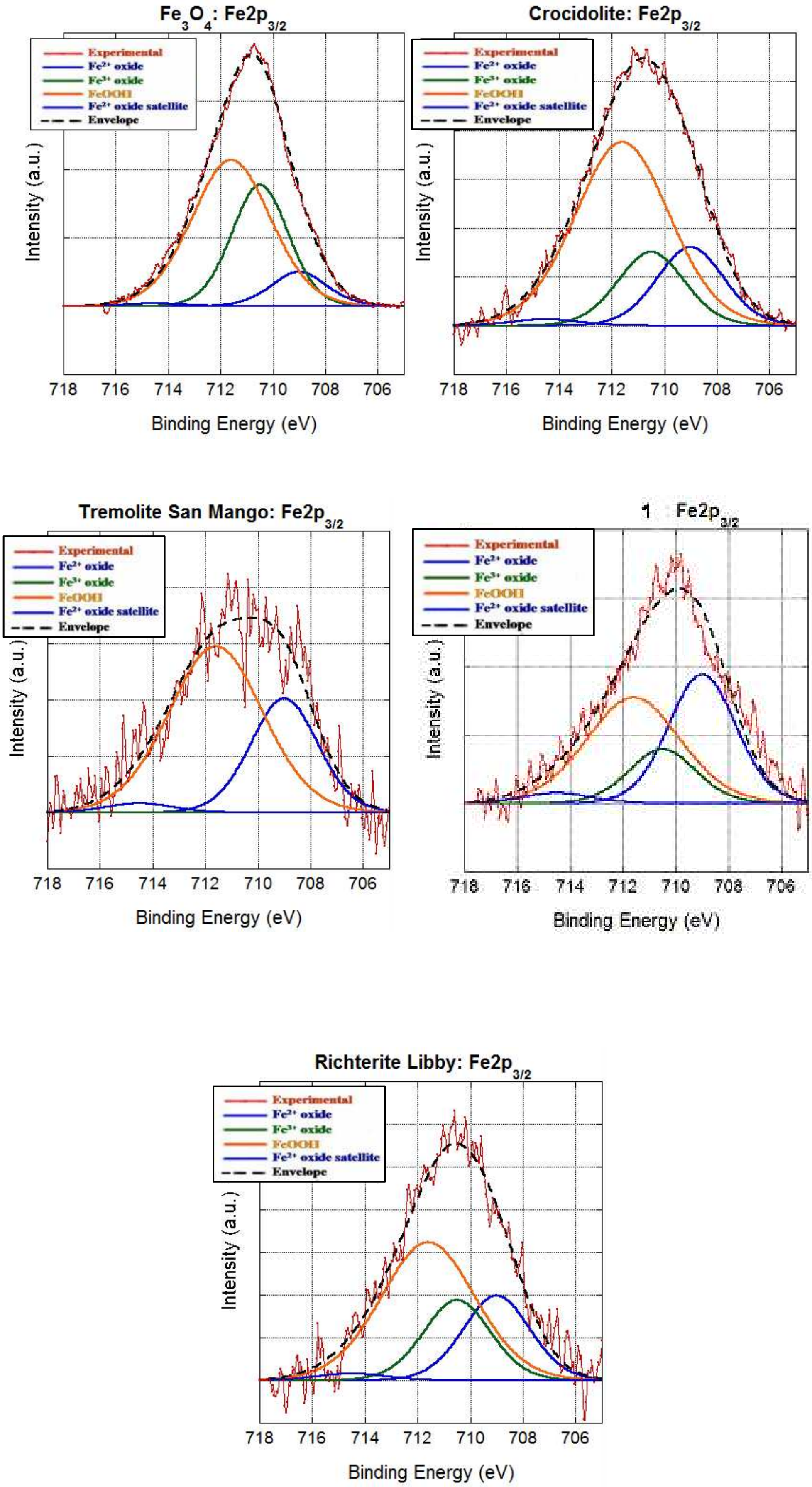

Figure 2 – Shirley background subtracted Fe 2p$_{3/2}$ spectra and curve fit for all studied sample. Fit based on the approach II.

RESULTS

The surface composition of the studied fiberous amphiboles is reported in Table 1. The major elements detected were oxigen, silicon, iron and magnesium. For the UICC crocidolite, richterite from Libby and sample 1 from Biancavilla a small amount of Na was also detected; Ca and Al were present only in sample 1 from Biancavilla and tremolite San Mango. For the richterite from Libby and sample 1 from Biancavilla flourine was also detected. The surface composition of the fibers did not show significantly differences with respect to their bulk composition.

Table 1 - XPS-determined composition of the studied amphibole fibers.

	Fe at%	**O at%**	**Si at%**	**Na at%**	**Mg at%**	**Al at%**	**Ca at%**	**F at%**
UICC Crocidolite	5.2	64.5	23.2	3.3	3.8	-	-	-
Richterite	1.0	57.8	24.3	4.0	11.3	-	-	1.6
Sample 1	1.1	65.4	22.3	0.3	6.9	0.9	1.1	2.2
Tremolite San Mango	0.6	57.7	21.2	-	15.4	0.8	4.3	-
Tremolite Ala Stura	0.5	61.3	25.1	-	13.1	-	-	-

Table 2 shows the multiplet peak parameters used on the basis of the approach I to fit the high-spin Fe^{2+} and Fe^{3+} components in the Fe_3O_4 spectrum (Fe reference spectrum). The calculated Fe^{3+}/Fe_{tot} ratio was found to be 0.80, which is far from the ratio of 0.67 obtained on the bulk by Mössbauer spectroscopy. When applying the curve-fit model obtained from Fe reference spectrum (Table 2) to the Fe $2p_{3/2}$ spectrum of the amphibole fibers the only changes made to optimize the fit were to vary the heights of the peaks and to rigidly shift of the whole curve along the binding energy scale. The relative position and heights of the subpeaks were kept constant. The Fe^{3+}/Fe_{tot} ratios obtained for the amphibole fibers are shown in Table 3.

Table 2 - Multiplet peak parameters used to fit the high-spin Fe^{2+} and Fe^{3+} compounds in the Fe_3O_4 (reference Fe spectrum).

Peak	FWHM (eV)	Area	Binding Energy (eV)
Fe^{3+} peak 1	1.8 ± 0.1	Unconstrained	710.1 ± 0.1
Fe^{3+} peak 2	1.8 ± 0.1	Area Peak 1* 0.95	Binding energy peak 1 + 1.1
Fe^{3+} peak 3	1.8 ± 0.1	Area Peak 1* 0.75	Binding energy peak 2 + 1.1
Fe^{3+} peak 4	1.8 ± 0.1	Area Peak* 0.31	Binding energy peak 2 + 1.1
Fe^{2+} peak 1	1.8 ± 0.1	Unconstrained	708.0 ± 0.2
Fe^{2+} peak 2	1.53 (picco 1*0.85)	Area Peak 1*1.04	Binding energy peak 1 + 1.1
Fe^{2+} peak 3	1.8 ± 0.1	Area Peak 1*0.37	Binding energy peak 2 + 1.2
Fe^{2+} peak 4 (Fe Satellite)	3.3 ± 0.1	Area Peak 1* 2.0	Binding energy peak 1 + 7.0

Table 3 - Calculated Fe oxidation state by using the Gupta and Sen (1974, 1975) multiplets.

Sample	Fe^{3+}/Fe_{tot}
UICC Crocidolite	0.61
Richterite Libby	0.67
Sample 1	0.55
Tremolite San Mango	0.63

The fit parameters obtained from the fit of the Fe $2p_{3/2}$ spectrum of Fe_3O_4 (Fig. 2) by using the approach II are shown in Table 4. The Fe $2p_{3/2}$ spectrum shows four contributions at 709.0, 710.5, 711.6 and 714.5 eV. The signals at 709.0 and 710.5 eV are assigned to Fe^{2+}- and Fe^{3+}-oxide, respectively. The signal at 711.6 eV is assigned to iron hydroxide (FeOOH). The signal at 714.5 eV is assigned to the shake-up satellites of Fe^{2+}. These assignments are in agreement with those in the literature (McIntyre et al., 1977; Mathieu and Landolt, 1986; Grosvenor et al., 2004; Rossi et al., 2006). The calculated Fe^{3+}/Fe_{tot} ratio obtained for the Fe_3O_4 using the approach II was found to be 0.89. The Fe^{3+}/Fe_{tot} ratios obtained by applying the curve-fit model (Table 4) to the amphibole fibers are reported in Table 5.

Table 4 - Curve fit parameters obtained by using the approach II.

Component	FWHM (eV)	% Gaussian[a]	Binding Energy (eV)
Fe^{2+} oxide	3.0 ± 0.1	55	709 ± 0.1
Fe^{3+} oxide	3.0 ± 0.1	55	710.5 ± 0.1
FeOOH	4.1 ± 0.1 [Fe^{2+} * 1.75]	55	711.6 ±0.1
Fe^{2+} oxide satellite	3.0 ± 0.1	55	714.5 ± 0.1 [BE Fe^{2+}+5.5]

Note: [a] values kept fixed.

Table 5 – Fe^{3+}/Fe_{tot} ratios obtained for the amphibole fibers by using the approach II

Sample	Fe^{3+}/Fe_{tot}
UICC Crocidolite	0.80
Richterite Libby	0.75
Sample 1	0.59
Tremolite San Mango	0.65

DISCUSSION

The Fe^{3+}/Fe_{tot} ratios calculated for all studied sample by using the approach I and approach II are reported in Table 6. Except for sample1 from Biancavilla and tremolite San Mango, the two approaches lead to Fe^{3+}/Fe_{tot} ratios statistically different. The highest Fe^{3+}/Fe_{tot} ratios found on basis of both approaches for Fe_3O_4 (0.80 and 0.89, respectively) with respect to the theoretical value (0.67) indicate the presence of excess Fe^{3+} on the surface with respect to the bulk. In particular, during the fit a subpeak of oxigen at 531.5 eV was recognized in the Fe_3O_4 spectrum, wich is typical of the oxigen bonded to the Fe^{3+} in the hydroxy-group FeOOH (Olla et al., 2006). The approach II allowed this FeOOH contribution to be better defined (Fig. 2). On the contrary, this is quite impossible when using the Gupta and Sen (1974, 1975) model because of the numerous multiplets which occur for each oxidation state of iron. The Fe^{3+}/Fe_{tot} ratio of Fe_3O_4 was then re-calculated on the basis of approach II excluding the contribution of the signal at 711.6 eV, which is known to be related to Fe^{3+} in the hydroxy-group FeOOH (Olla,et al. 2006), and the ratio 0.68 was obtained, in very good agreement with the bulk ratio of 0.67 measured by Mössbauer spectroscopy. For this reason the results obtained by using the approach II are considered more accurate .

The amphibole samples showed the presence of a large variety of surface vs bulk oxidation state relationships (Table 7). In fact, the highest difference between surface and bulk Fe^{3+}/Fe_{tot} ratios is displayed by the San Mango tremolite (which is 10 times oxidized on the suface), whereas the lowest difference was observed for sample 1 from Biancavilla (which is almost unoxidized on the surface). In addition, for all fibrous amphiboles a significant amount (from 70 to 100%) of the Fe^{3+} present at the surface was revealed to be Fe^{3+} in FeOOH hydroxide (Table 8).

Table 6 - Fe^{3+}/Fe_{tot} ratios calculated by using the approach I and the approach II.

Sample	I approach	II approach
Fe_3O_4	0.80	0.89
UICC Crocidolite	0.61	0.80
Richterite Libby	0.67	0.75
1	0.55	0.59
Tremolite San Mango	0.63	0.65

Table 7 - Fe^{3+}/Fe_{tot} ratios obtained on the bulk by Mössbauer spectroscopy and on the surface by using the approach II.

Sample	Bulk	Surface
UICC Crocidolite	0.65	0.80
Richterite Libby	0.65	0.75
1	0.54	0.59
Tremolite San Mango	0.06	0.65

Table 8 - Fe^{2+}-oxide/Fe_{tot}, Fe^{3+}-oxide/Fe_{tot} and Fe^{3+}- hydroxide/Fe_{tot} (FeOOH) ratios on the surface of the studied amphibole fibers.

Sample	Fe^{2+}-oxide	Fe^{3+}-oxide	FeOOH
UICC Crocidolite	0.20	0.18	0.62
Richterite Libby	0.25	0.22	0.53
1	0.41	0.16	0.43
Tremolite San Mango	0.35	0	0.65

8

STUDY OF THE REACTIVITY OF THE FIBROUS AMPHIBOLES BY ELECTRON PARAMAGNETIC RESONANCE (EPR) SPECTROSCOPY

INTRODUCTION

In this chapter, the redox properties (monoelectronic transfers) of some mineral fibres previously characterized in terms of crystal-chemistry will be addressed. The surface reducing-properties of the fibres were first studied in the presence of oxygen, at 37 ° C, in an aqueous medium buffered at pH 7.4, focalising on the formation of the hydroxyl radical HO°, a very reactive electrophilic oxidizing species.

HO° Radical formation from Hydrogen Peroxide (H_2O_2)

It is already well established that if Fe^{2+} ions are added to a solution of hydrogen peroxide, hydroxyl radicals are produced according to the Fenton reaction:

$$(1) \qquad Fe^{2+} + H_2O_2 \rightarrow Fe^{3+} + HO° + HO^-$$

Fe^{3+} ions themselves can also react with hydrogen peroxide, which in this case acts as a reducing agent, giving a superoxide radical anion ($O_2^{°-}$) through the following reaction:

$$(2) \qquad Fe^{3+} + H_2O_2 \rightarrow Fe^{2+} + 2H^+ + O_2^{°-}$$

A second molecule of hydrogen peroxide can then react with the radical $O_2^{°-}$ according to the Haber-Weiss reaction, producing again HO° radicals:

(3) $$H_2O_2 + O_2^{\circ -} \rightarrow O_2 + HO^{\circ} + HO^{-}$$

The rate constant of this reaction is virtually zero in aqueous solution, but it increases noticeably in the presence of opportune catalysts, such as iron salts (Halliwell et al., 1986).

Superoxide radical anions can also react themselves reducing Fe^{3+} ions, according to the following reaction:

(4) $$O_2^{\circ -} + Fe^{3+} \rightarrow Fe^{2+} + O_2$$

Fe^{2+} ions formed in reaction (2) and (4), can then react again with H_2O_2, producing more hydroxyl radical according to the previously mentioned Fenton reaction (1).

Summarising, in the presence of iron ions in solution (both Fe^{2+} and Fe^{3+}), the Fenton and Haber-Weiss reactions allow the reduction of hydrogen peroxide, promoting the production of HO° radical.

Stability of HO° radicals in the presence of Solid material

Besides the reactions in the liquid phase, attention must also due to the presence of the solid.

The studied solids are potential electron donors which can react with HO° radicals according to the following reaction:

(5) $$HO^{\circ} + e^{-} \rightarrow HO^{-}$$

In the case where the reactivity of solids is considered weak because of the low amount of available donor sites at the surface, it is however likely that the very strong oxidizing power of the radical HO° may be able to extract electrons from the solid.

Under these conditions, the concentration of electrons can be very high so that the reaction (5) becomes predominant.

Spin Traps

The EPR spectroscopy allows the characterization of radicals and the measurement of their absolute concentration. The half-life of the HO° radical, however, is around 10^{-9} seconds, which is too short a period to allow its analysis and quantification (Zalma, 1988). In order to solve this problem, one usually employs spin traps, i.e., chemical species forming a radical with the HO° having a sensibly longer half-life and thus allowing their indirect analysis. The most common spin traps are nitrons, no radical molecules, which react with any X° radical forming a radical, more stable and easily characterized by EPR; among known nitrons, the 5-5 Dimethyl-1-Pyrroline-N -Oxyde (DMPO) is one of the most widely used. DMPO reacts with the HO° radical through the following reaction:

(6)

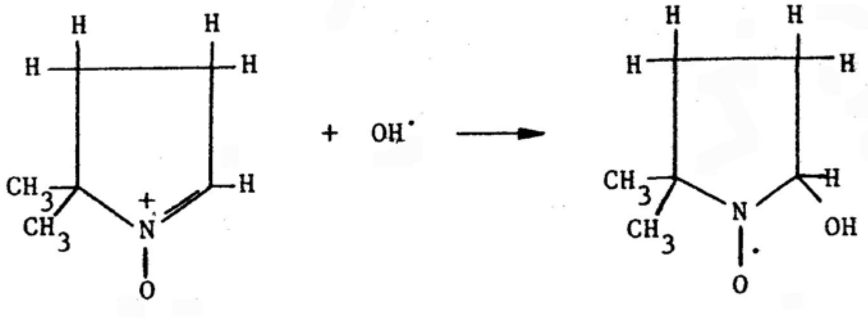

or, simplifying:

$$\mathrm{DMPO} + \mathrm{HO}^\circ \rightarrow (\mathrm{DMPO,HO})^\circ$$

The stability of this radical adduct (DMPO, HO)° is a function of the initial concentration of reactive species (Zalma, 1988). This author estimated the half-life time of this radical adduct in about 45 minutes under conditions analogous to those used in this work.

ANALYTICAL METHOD

Experimental process

The experiments were performed in a reactor consisting of a tube inserted in a glass vessel (Figure 1) kept at constant temperature by a water flow at 37°C. The thermostated reactor was placed on a swinging table in order to ensure the continuous agitation of reagents. The reaction takes place in an aerobic medium and protected from light.

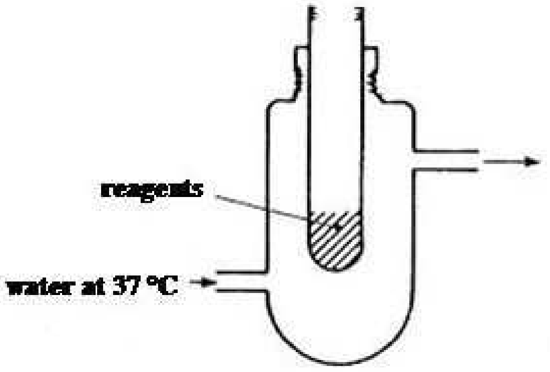

Figure 1 - Scheme of the reactor in which the experiments were performed.

All solutions were prepared in a phosphate buffer (pH = 7.4, 0.5 mol/L) obtained starting from disodium hydrogen phosphate (Na_2HPO_4, Sigma, 99% in purity) and sodium dihydrogen phosphate (Na_2HPO_4, Sigma, 99% in purity). The solid sample (25 mg) was introduced in the reactor together with 0.5 ml of sodium phosphate buffer solution at pH = 7.4 (0.5 mol/L), 1ml of aqueous solution of DMPO (10^{-1} mol/L) and 0.5 mL of H_2O_2 (0.6%/vol). The DMPO solution was obtained from commercial DMPO (Aldrich, 97% in purity) previously purified on activated carbon (Prolabo). The hydrogen peroxide solution was prepared from 2ml of commercial hydrogen peroxide (30% in volume) to which 18 mL of phosphate buffer were added; then 4mL of this solution were diluted to 20 mL by the addition of other 16 mL of buffer in order to obtain a final concentration of H_2O_2 of

0.6%. All studied samples were ground in an agate mortar for 1 minute; it is worth remembering that the effectiveness of the grounding is not perfectly reproducible, since it depends on the operator, on the morphology and amount of starting solid. Five minutes and 30 seconds after the introduction of H_2O_2 in the reactor, part of the suspension was sampled using a syringe with a needle of internal diameter of about 2mm, and filtered on a cellulose acetate filter with a porosity of 0.22 μm. The solution was put in a flat cell of quartz and used for analysis EPR. In order to improve the quality of the results, duplicate tests were performed for all samples. Reference tests, obtained using only the buffer solution, the DMPO the hydrogen peroxide solution and no solid inside, were also prepared and analysed under the same experimental conditions. These controls permit to verify the quality of reactants. Seven samples were studied: the fibrous amphiboles 1 and 4 from Biancavilla, the fibrous richterite from Libby Montana and four samples of fibrous tremolite named Ala di Stura, San Mango, Castelluccio and Mt. Rufeno. As reference samples, a sample of UICC (Union Internationale contre le Cancer, Johannesburg, South Africa) crocidolite and a sample of calcite (Iceland spar) were also tested.

Determination of the formed HO° radical by EPR

All the EPR spectra (Fig. 2) were obtained at room temperature using a Brucker ESP-300E spectrometer. Analytical conditions were: magnetic field 3440 G, frequency field 9.65 GHz, power 10 mW, frequency modulation 100 KHz, modulation amplitude 3.24 G and a gain of $5 * 10^4$, acquisition time 84.92 ms. Figure 1 shows a EPR spectrum of the radical adduct (DMPO, HO)°. The signal is composed of 4 lines with coupling constant (a_N et a_H) of 14.9 G (Jansen et Liu Ping, 1973).

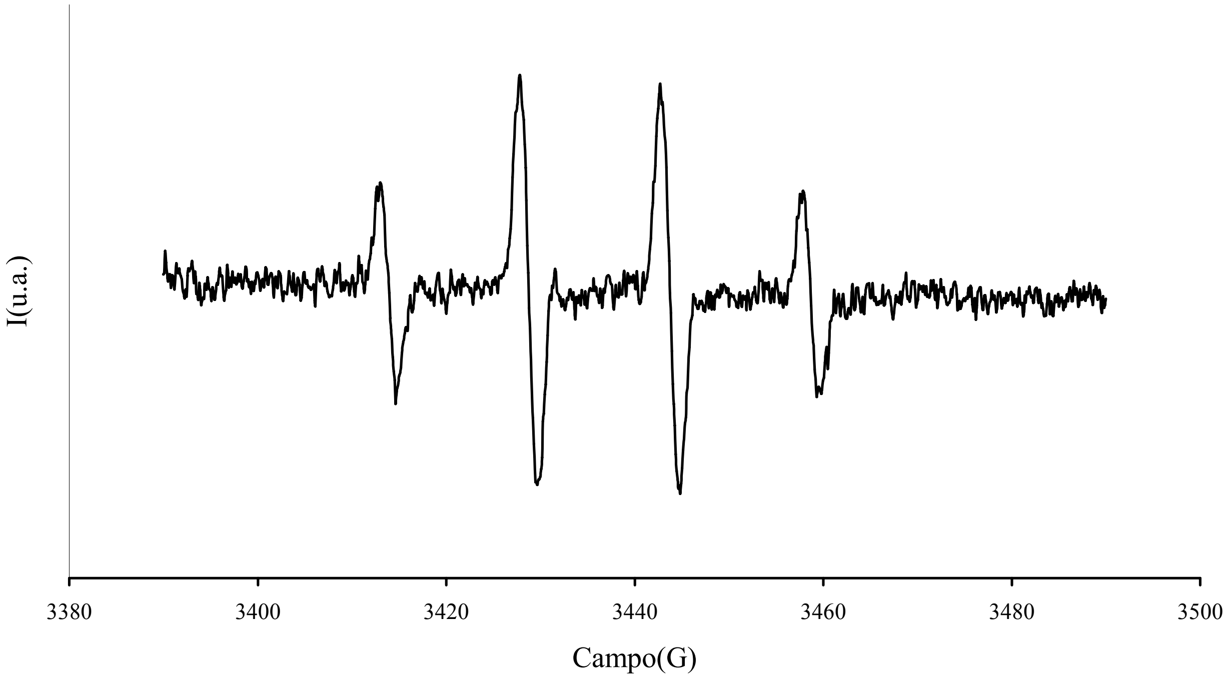

Figure 2 - EPR spectrum of the radical adduct (DMPO, HO)°. The intensity scale in arbitrary unit.

For all the samples and for the reference samples the height of the strongest peak was measured for each spectrum. From this height, the intensity was derived using the following equation:

$$I = \frac{(Ht * 10^6)}{(5 * 10^4 * 1500)}$$

where I is the intensity (arbitrary unit, a.u.), Ht is the height of the measured peak, $5 * 10^4$ is the value of gain and the other two factors are instrumental conversion factors. From the intensity values measured for the spectra obtained after 5 and 30 minutes from the beginning of the reaction, a single average value of intensity was calculated. This value was subtracted from the average intensity calculated for the controls in order to obtain the real values of intensity (Ir). Knowing that 1 u.a. corresponds to $2.3*10^{15}$ spins/L, the concentration of radicals in solution for the various samples tested was finally calculated using the following equation:

$[HO°] = 2.3 * 10^{15} * Ir$

RESULTS

The results are summarised in Table 1 and in Figure 2.

Table 1 - EPR spectral intensity (a.u.) and radical concentration (spins/L), and their respective standard deviations for the tested samples.

Sample	**I(r)**	**σ**	**[HO°]*10^{16}**	**σ*10^{15}**
Libby Montana	27.99	1.11	6.44	2.55
1	10.14	2.01	2.33	4.63
4	11.95	2.71	2.75	6.24
Ala di Stura	15.14	1.21	3.48	2.79
Castelluccio	5.19	2.90	1.19	6.68
San Mango	20.42	2.08	4.70	4.78
Mt. Rufeno	11.85	1.53	2.73	3.52
UICC Crocidolite	65.46	3.40	15.10	7.82
Calcite	2.81	0.13	0.65	2.91

From the histogram of Figure 3, the most evident result is that the concentration of radicals is by far the highest for the UICC crocidolite sample, whereas it is virtually zero for the calcite reference. Among the remaining tested samples, richterite from Libby Montana produces the highest amount radicals, whereas tremolite Castelluccio is the least active one. San Mango is the most reactive among the tested tremolites. Finally, sample 1 and 4 from Biancavilla do not show significant differences each other. Notably, except for sample 1 and 4 the concentration of HO° radicals produced by the fibrous amphiboles is related to their FeO_{tot} content (Figure 4), in accord with the Fenton and Haber-Weiss reactions. The scatter observed for sample 1 and 4 could be attribute to the grounding operation not perfectly reproducible, since it depends, as previously mentioned, on the operator, on the morphology and amount of starting solid.

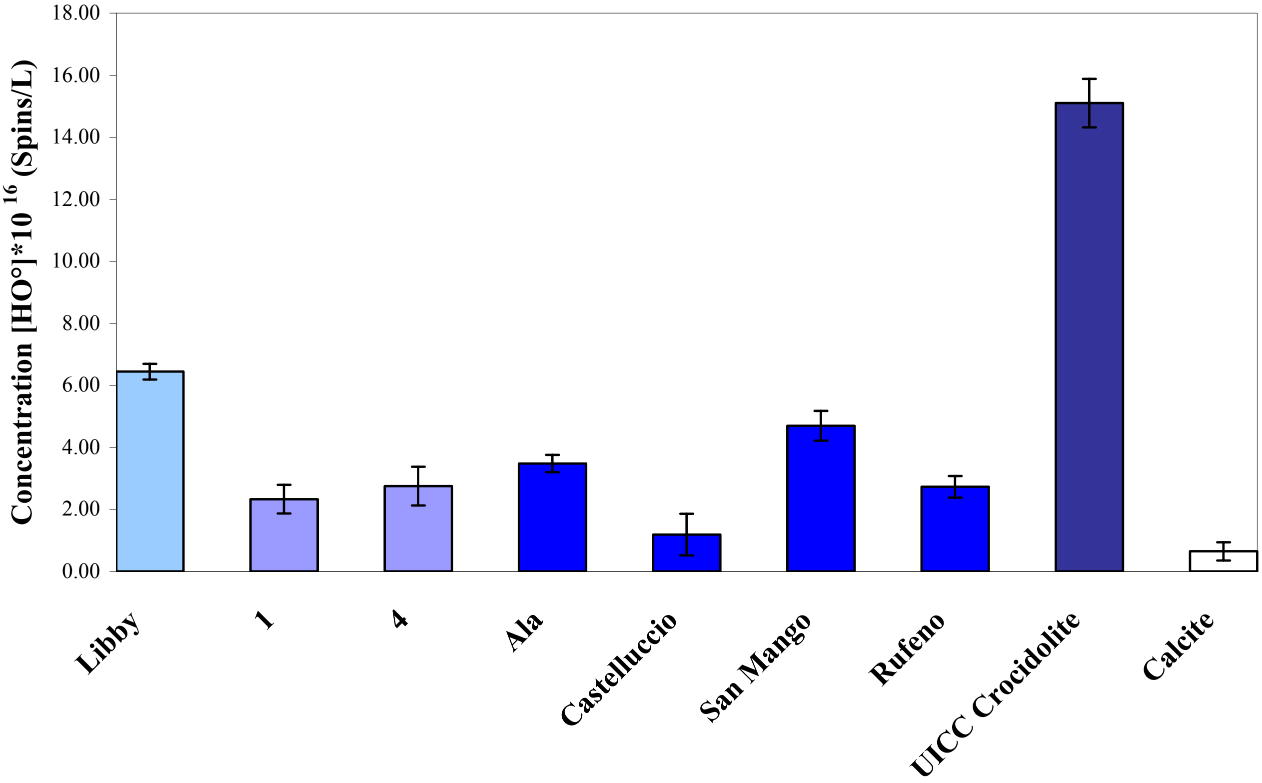

Figure 3 - Concentration of radical calculated for the tested samples.

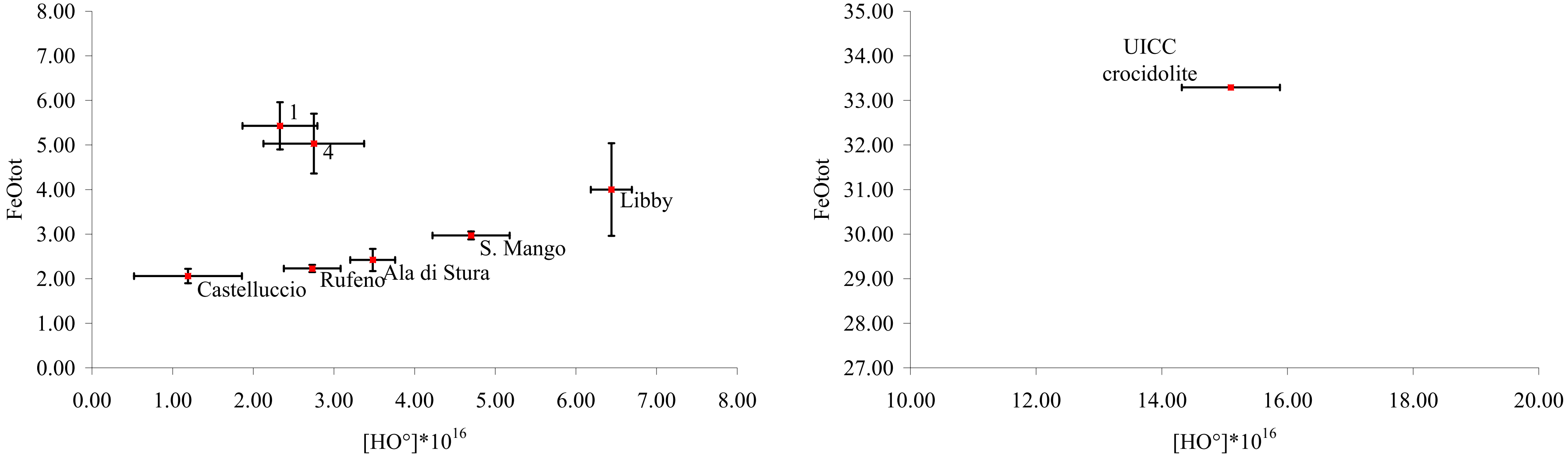

Figure 4 - [HO°] concentration produced by the tested fibrous amphiboles in relationship with their FeO$_{tot}$ content.

Note: the FeO$_{tot}$ content of the UICC crocidolite was mesaured by ICP-MS analysis.

9

STUDY OF THE LIPID PEROXIDATION IN PRESENCE OF HYDROGEN PEROXIDE ON VARIOUS FIBROUS AMPHIBOLES

INTRODUCTION

The lipid peroxidation (oxidative degradation of lipids) is a chemical reaction of degradation of cell membranes, consisting largely of long chain of polyunsaturated fatty acids linked to one polar end. This reaction causes irreversible damage leading to the destruction of the cell membrane. The mechanism (chemical and biochemical) of lipid peroxidation is very complex and proceeds through several radical chain reactions, involving the participation of free radicals, oxygen, metal cation, as well as a number of protective factors and antioxidants. (Kappus, 1991). The lipid molecules are made up of aliphatic and hydrophobic paraffin regions and a hydrophilic polar head. In the phospholipids, the most common lipids present in animal cell membranes, the hydrophobic part consists of two chains of fatty acids linked to a glycerol molecule, which is in turn connected to a phosphoric group, and ultimately linked to a hydrophilic base (Fig. 1). The most common fatty acids that are found in the hydrophobic part are linoleic acid, oleic acid, arachidonic and linolenic acid. This latter last acid was used in the peroxidation tests presented in this work.

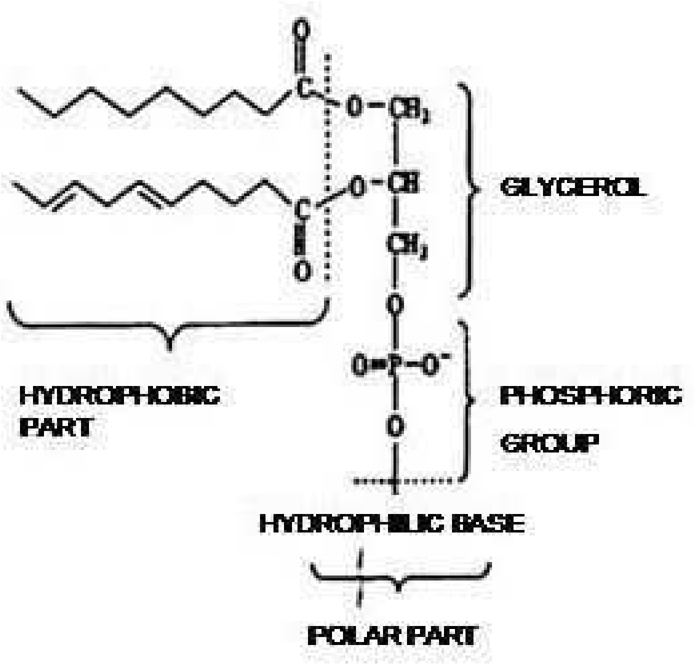

Figure 1 - General structure of a phospholipid.

Linolenic Peroxidation mechanism

As already mentioned, among the available polyunsaturated fatty acids, linolenic acid, of chemical formula:

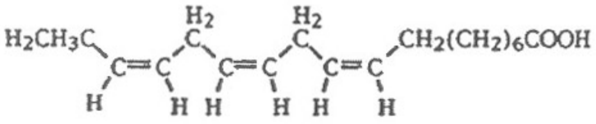

$$H_2CH_3C{-}CH{=}CH{-}CH_2{-}CH{=}CH{-}CH_2{-}CH{=}CH{-}CH_2(CH_2)_6COOH$$

is taken as the model molecule for the peroxidation tests. This molecule presents two methylene groups ($-CH_2-$), localised between two unsaturated bonds ($C=C$). The carbon-hydrogen bound of these groups is very sensible to an oxidative process.

The mechanism of radical lipid peroxidation implies three distinct steps: initiation, propagation and termination (Fig. 2).

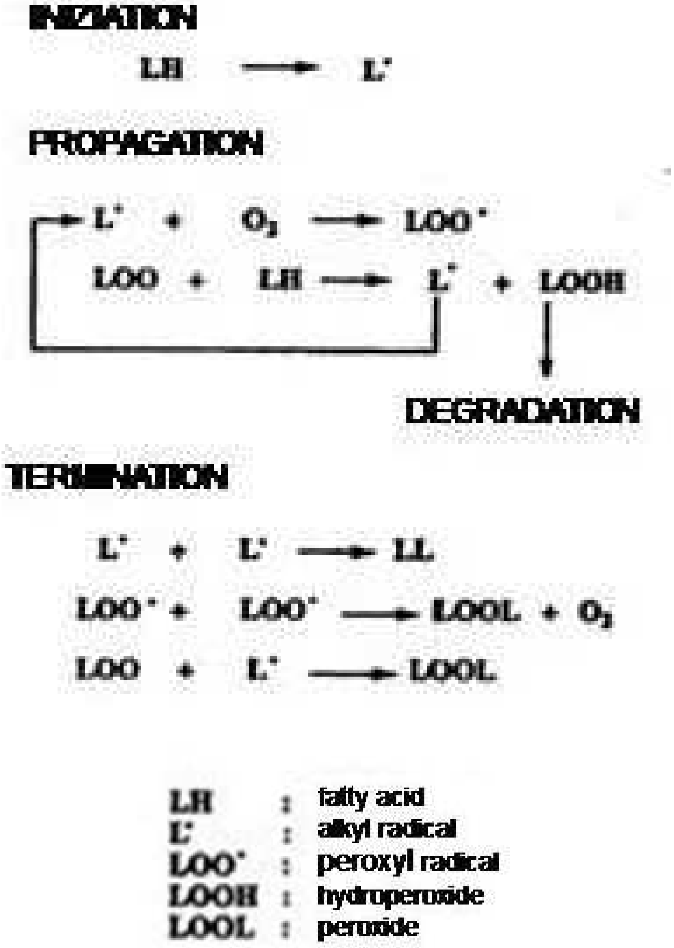

Figure 2 - General mechanism of lipid peroxidation (Fournier et al., 1995)

The number of degradation products is very high (Halliwell and Gutteridge, 1986). Fournier et al. (1995) summarised all the degradation routes and all the possible reaction products of linolenic acid in the presence of molecular oxygen, as shown in the scheme presented in Figure 3.

The process is activated by ROS which are able to rip a hydrogen atom from a methylene group of the fatty acid (LH) conducting to the formation of alkyl radicals (L°). The radical HO° is often mentioned as a starter of the initiation step, even though some authors suggested the superoxo and/or peroxo species, and the oxo-metals, such as Fe(IV)=O and Fe(V)=O, as other possible starters (Minotti and Aust, 1989; Fournier et al., 1995). During the propagation stage a series of oxidation reactions of the radical L°, obtained during the initiation phase, occurs with the consequent formation of peroxyl radicals (LOO °) in the presence of molecular oxygen. These radicals are able to react themselves in the presence of new molecules LH, forming the hydroperoxide (LOOH) and new L° radicals feeding a new round of propagation.

The radical entities (LOO° and L°) react between them, conducting to the formation of no radical products (termination step). However the hydroperoxides are highly unstable and degrade quickly in different ways from the propagation step. The number of degradation products is very high (Halliwell and Gutteridge, 1986). From the linolenic peroxidation, around forty breakdown products can be formed (Fournier et al.,1995). These last autors summarised all the degradation routes and all the possible reaction products of linolenic acid in the presence of molecular oxygen, as shown in the scheme presented in Figure 3. In the case where ROS are present in solution, malonaldehyde (MDA), hydroperoxides, and conjugated dienes and trienes are formed; in the presence of metallic cations such as Fe^{2+} monoaldehydes (MONO) and conjugated diolefins are rather produced (Fig. 3).

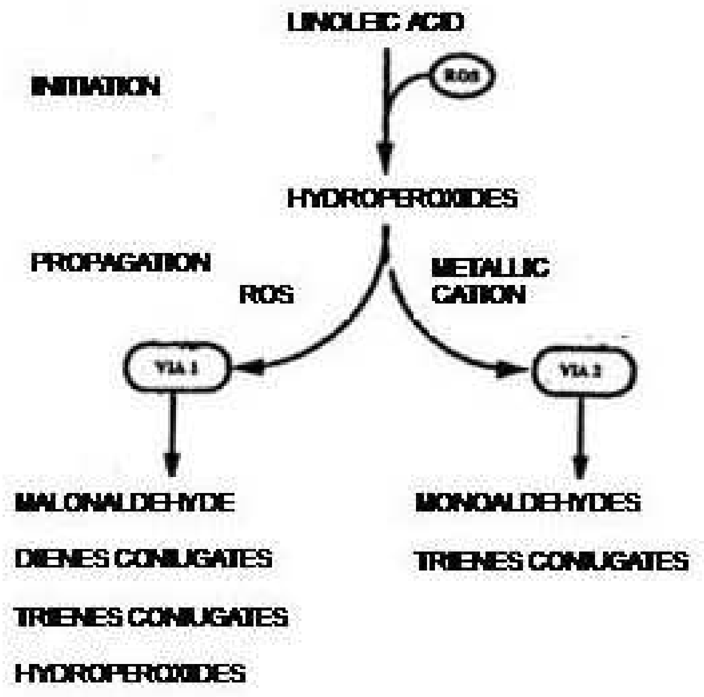

Figure 3 - Linolenic degradation scheme (from Fournier et al., 1995).

Principle of detection of some degradation products

In this study, we have chosen to detect two products of degradation typical of both degradation (Fig. 3): malonaldehyde (MDA) and monoaldehydes (MONO). These products are the most frequently studied ones both in *in vivo* and *in vitro* tests. During the linolenic acid peroxidation, some products of degradation typical of both degradation ways were identified (Fig. 3): malonaldehyde (MDA) and monoaldehydes (MONO). These products are the most frequently studied ones both in *in vivo* and *in vitro* tests. The research interest of both these products (MDA and MONO) are related to several observations:

- the MDA is usually considered as an indicator of toxicity, as well as the first evidence of peroxidation ;
- the selectivity of the materials in the degradation of linolenic acid (Fig. 3) provides information on the reactivity of ROS and/or heavy metal cations with strong reducing power ;
- a single operating procedure allows the determination of the production of both MDA and MONO.

The determination of the amounts of MDA and MONO involves a condensation reaction with thiobarbituric acid (TBA) in an aerobic aqueous medium (Ottolenghi, 1959; Gavino et al., 1981). In acidic solutions, at 100°C, MDA and TBA react as follows:

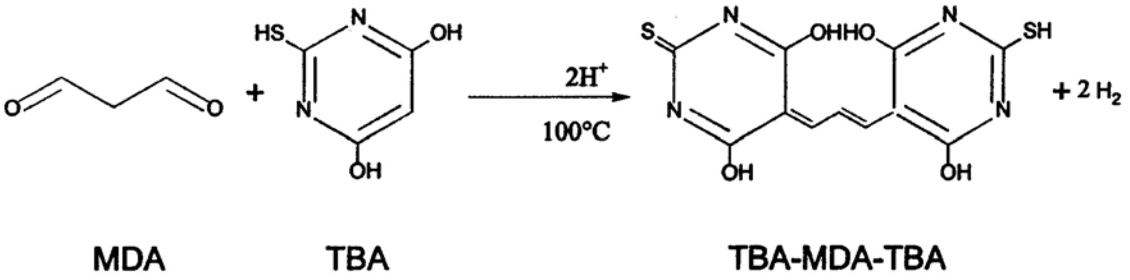

The condensation product (TBA-MDA-TBA) is a pink chromophore. Under the same conditions, the reaction between MONO and TBA goes as follows:

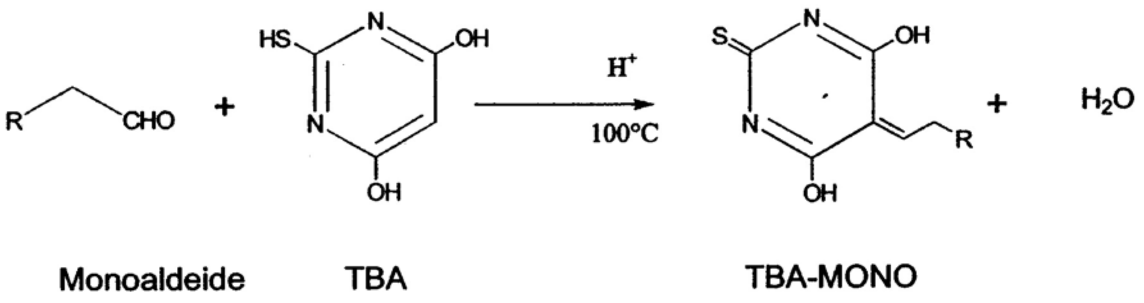

The condensation product (TBA-MONO) is a yellow or yellow-orange (depending on the nature of monoaldehyde) chromophore. These chromophores are easily extracted from the aqueous solution by an organic solvant and analyzed by UV-visible spectroscopy. The absorption spectra have typical absorption bands at different wavelengths: 535 nm for the MDA, 500 nm for polyunsaturated monoaldehydes carrying many functional saturated groups (-COOH,-OH, ...), and 450 nm for saturated monoaldehydes.

EXPERIMENTAL PROCESS

Tests of lipid peroxidation in the presence of hydrogen peroxide were performed on various fibrous amphiboles to identify and distinguish their reactivity, following the degradation of linolenic acid in conditions similar to those found in pulmonary alveoli. During the linolenic acid peroxidation, two products of degradation typical of both degradation ways were identified (Fig. 3): malonaldehyde (MDA) and monoaldehydes (MONO). These products are the most frequently studied ones both in *in vivo* and *in vitro* tests. The research interest of both these products (MDA and MONO) are related to several observations:

- the MDA is usually considered as an indicator of toxicity, as well as the first evidence of peroxidation;

- the selectivity of the materials in the degradation of linolenic acid (Fig. 3) provides information on the reactivity of ROS and/or heavy metal cations with strong reducing power;
- a single operating procedure allows the determination of the production of both MDA and MONO.

The determination of the amounts of MDA and MONO involves a condensation reaction with thiobarbituric acid (TBA) in an aerobic aqueous medium (Ottolenghi, 1959; Gavino et al., 1981). In acidic solutions, at 100°C, MDA and TBA react as follows:

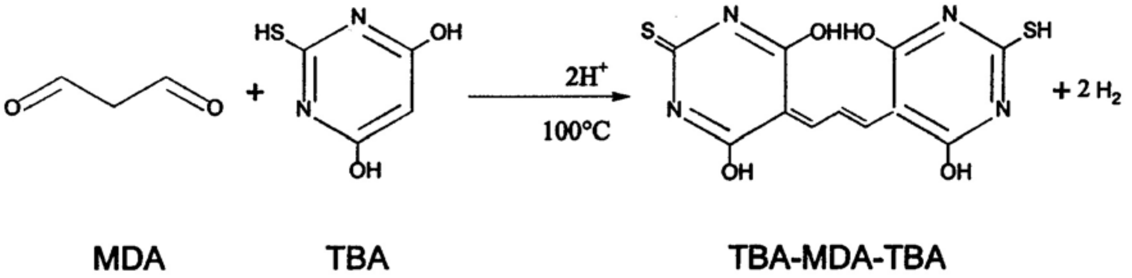

The condensation product (TBA-MDA-TBA) is a pink chromophore. Under the same conditions, the reaction between MONO and TBA goes as follows:

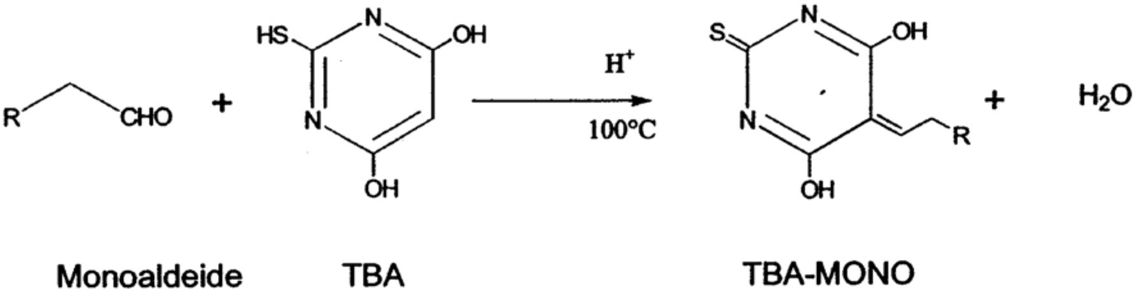

The condensation product (TBA-MONO) is a yellow or yellow-orange (depending on the nature of monoaldehyde) chromophore. These chromophores are easily extracted from the aqueous solution by an organic solvant and analyzed by UV-visible spectroscopy. The absorption spectra have typical absorption bands at different wavelengths: 535 nm for the MDA, 500 nm for polyunsaturated monoaldehydes carrying many functional saturated groups (-COOH,-OH, ...), and 450 nm for saturated monoaldehydes.

All tests were carried out in a reactor (Diagram 1 in the chapter on EPR) at 37°C, in aerobic conditions and protected from light. The following fibrous amphiboles were tested: the richterite from Libby Montana, three tremolites (Ala di Stura, San Mango and Mt. Rufeno) and the UICC crocidolite; pure calcite (Iceland spar variety) was also studied as a reference compound. Unfortunately it was not possible to analyze some of the samples previously characterised by EPR spectroscopy because of little amount of available material. All suspensions were prepared in a phosphate buffer (pH 7.4, 0.5 M). The solids (25 mg per sample) were ground in an agate mortar for 1 minute prior to introduction in a reactor with 0.5 ml of aqueous H_2O_2 (0.3 % vol.) and 0.5 ml of a linolenic acid solution (2 mM) at pH 7.4. The solution of the fatty acid was prepared with purified linolenic acid (Sigma, 99% in purity) in order to remove traces of hydroperoxides (Bolland and Koch, 1945). The reactor has been placed on a swinging table in order ensure the homogeneity of the suspension. Controls (without solid) were performed in the same experimental conditions. After 18 hours, 100 μL solution of BHT (butylated hydroxytoluene, Sigma, 99.5% in purity) were added to the suspension in order to stop the reaction of the fatty acid oxidation; indeed the BHT inhibits the lipid peroxidation, breaking the radical chains and converting the free radicals into stable products. For this purpose, 2mL of a second solution containing 0.375% w/v of TBA (Sigma, 98% in purity) and 15% w/v. of TCA (trichloroacetic acid, Merck, 99.5% in purity) in HCl 0.25 M (Gavino et al., 1981) were added to the reaction vessel. After this addition, the solution was incubated for 15 minutes in a water bath at 100 ° C. After cooling down to room temperature, 3 mL of 1-butanol (Merck, 99.5% in purity) were added, and the solution, poured into special tubes, was centrifuged for 10 minutes (8000 rpm) in order to allow the extraction of yellow and pink chromophores from the aqueous phase. The solution was then placed in a quartz cuve and analyzed by a double-beam UV-visible spectrometer (Jasco, V-550). The maxima of the absorption bands are located at $\lambda = 535$ nm for the MDA and $\lambda = 500$ and 450 nm for MONO. The reference cuve was filled with pure 1-butanol.

RESULTS

The results (Table 1 and Fig. 5), expressed in absorbance, represent the average value derived from duplicate sample tests; this value was reduced by the value of the reference sample (obtained under the same conditions) corresponding to the auto-oxidation of linolenic acid.

Table 1 - Final values of absorbance and their standard deviations (σ) for the MDA and MONO for the various tested samples.

MDA (535 nm)	Absorbance	σ
Calcite	0.01	0.01
Libby	0.55	0.04
Ala di Stura	0.43	0.02
San Mango	0.33	0.02
Mt. Rufeno	0.46	0.03
UICC Crocidolite	1.10	0.02

MONO (450 nm)	Absorbance	σ
Calcite	0.00	0.00
Libby	0.38	0.04
Ala di Stura	0.38	0.03
San Mango	0.25	0.01
Mt. Rufeno	0.77	0.05
UICC Crocidolite	0.61	0.01

MONO (500 nm)	Absorbance	σ
Calcite	0.00	0.00
Libby	0.42	0.06
Ala di Stura	0.32	0.03
San Mango	0.25	0.02
Mt. Rufeno	0.43	0.03
UICC Crocidolite	0.54	0.04

MDA (534 nm)

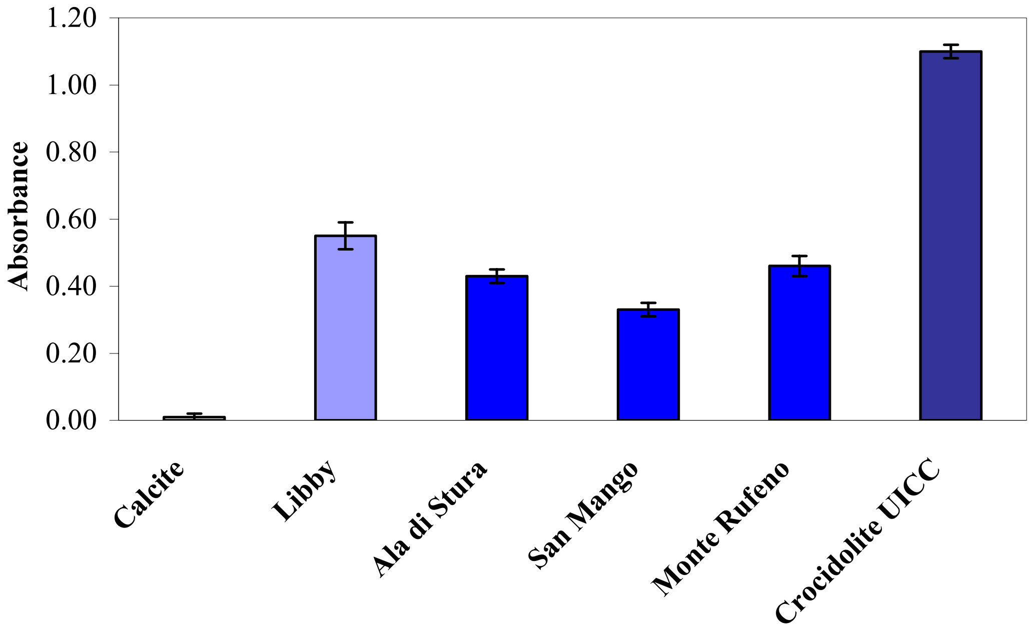

MONO (450 nm)

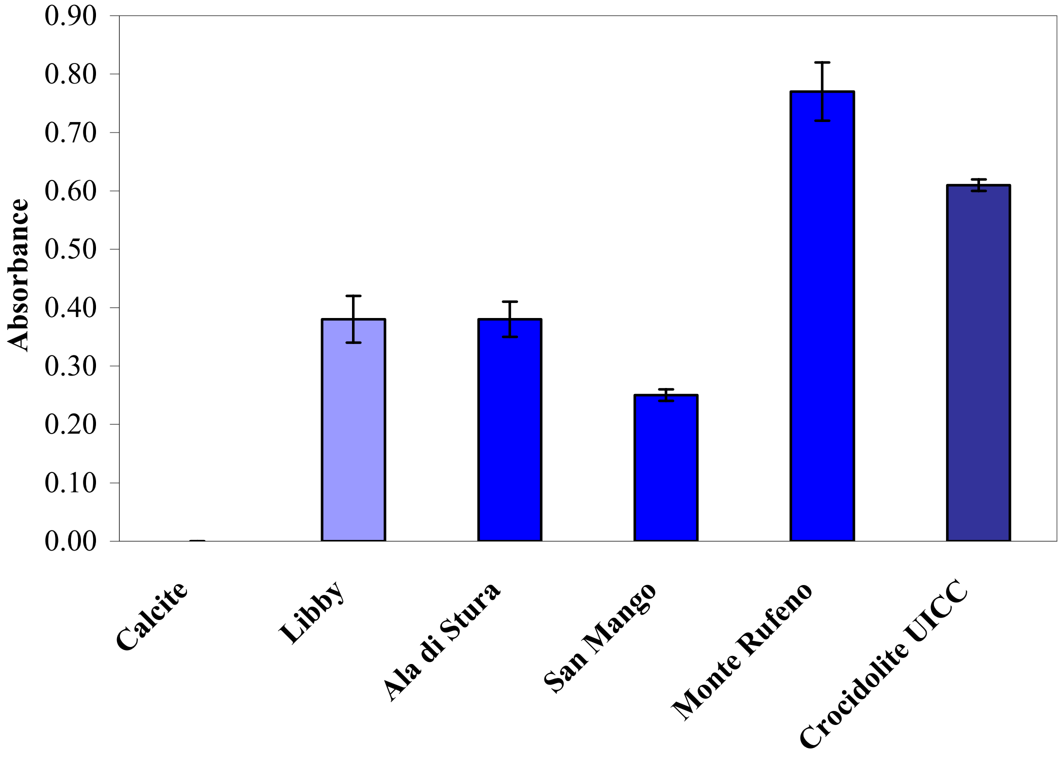

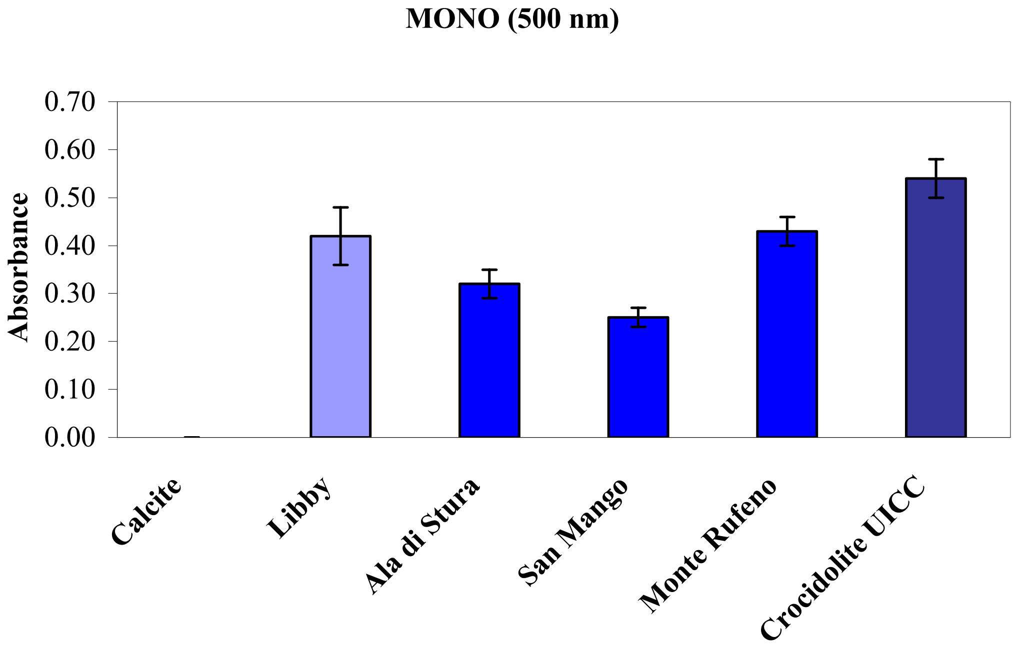

Figure 4 - Formation of MDA and MONO (absorbance per mL) for the various tested samples.

As expected in the case of the reference calcite sample, no significant amounts of malonaldehyde and monoaldehydes are formed. Conversely, the presence of MDA and MONO in the organic phase for all the other samples indicates that they are active in the peroxidation of linolenic acid. In particular, the crocidolite sample is the most active one, producing the greatest amount of degradation products. The only exception concerns the amount of MONO measured by the absorption band at 450 nm, for which a slightly lower amount is measured in the case of crocidolite than in the case of Mt. Rufeno tremolite. The richterite from Libby Montana is, after crocidolite, the highest producer of MDA. The tremolites are classified in the same order of reactivity (Mt. Rufeno> Ala di Stura> San Mango) whatever is the molecule or the analyzed band. In addition, the tremolites were the least reactive samples in the production of MDA, but not in the production of MONO. Indeed for the MONO measured at 450 nm, tremolite Rufeno is the most active sample, whereas tremolite Ala di Stura is comparable to the richterite from Libby; finally for the MONO measured at 500 nm, the similar production was measured for richterite and Rufeno tremolite. The results here obtained did not allow to establish a relationship among the tested samples between their FeO_{tot} content and amount of products of degradation detected.

10

GENERAL DISCUSSION AND CONCLUSIONS

Cytotoxicity of San Mango, Ala di Stura and Castelluccio tremolites on A549 lung cells (carcinomic human alveolar epithelial cells) has been shown to be comparable each other and significantly higher then cytotoxicity of Rufeno tremolite (Fig. 1). The role of free radicals in inducing cell mortality is well recognized in scientific literature. However the results of the tests on the HO° radicals production (see chapter 7, section results) showed a different order of reactivity of such tremolites, not correlable with the observed cytotoxicity. Notably, in this study only the HO° radicals have been determined, but among the different ROS, other very electrophilic oxygen species [iron oxo entities as Fe(IV)=O, Fe(VI)-O, and many more], not radical and as reactive as the HO° radical, are also able to attack a great variety of target molecules as DNA (Nejjari et al., 1993). So it is possible that these last entities (iron oxo species) intervene in the cytotoxicity, which could explain this no correlation between cytoxicity and chemical reactivity of these solids.

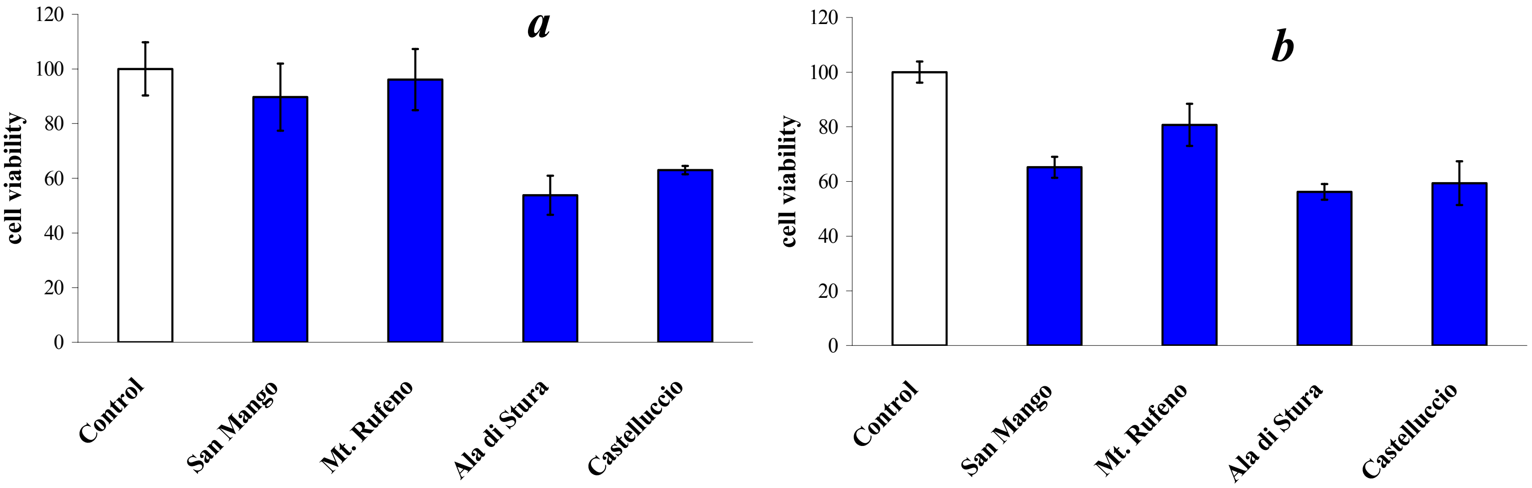

Figure 1 – Viability of A549 cells measured with the MTT assay following exposure to the tremolite fibers after 24 (a) and 48 h (b). The values are reported as percentage with respect to the untreated control considered as 100 % of cell viability.

On the contrary, the cytotoxicity on MeT-5A cells (human mesothelial cell line) of Rufeno tremolite did not show differences with that of the other tremolites, excluding Ala di Stura tremolite, which shows the highest cell mortality (Fig. 2). It must be noted that the reponse of the Met-5A cells to the fiber exposure can be different from the A549 cells, being the former more sensitive. Moreover, Rufeno tremolite revealed the highest activity in the production of both malonaldehyde and monoaldehydes (see chapter 8, section results). The production of malonaldehyde is considered an indicator of toxicity and among all the monoaldehydes some could play a primary role in the cell mortality. In the case of Ala di Stura tremolite, its cytotoxicity on MeT-5A cells cannot be explained from only its chemical reactivity in the production of the HO° radical , MDA and monoaldehydes (activity lower thant that of Rufeno tremolite). As previously mentioned, this observation allows to think of a possible formation of other ROS (for example metal oxo species), in quantity maybe superior to that of Rufeno tremolite, which could be implicated in the cellular death.

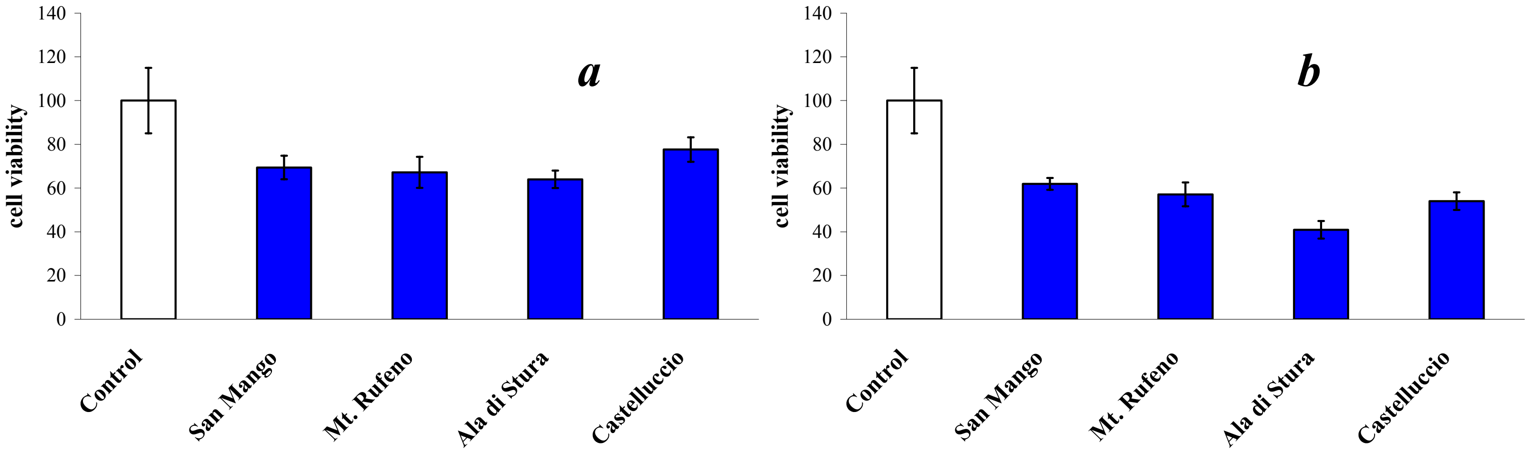

Figure 2 – Viability of MeT-5A cells measured with the MTT assay following exposure to the tremolite fibers after 24 (a) and 48 h (b). The values are reported as percentage with respect to the untreated control considered as 100 % of cell viability.

In addition, a certain delay of cell mortality was observed for San Mango and Rufeno tremolites (Fig 1). XPS investigation on San Mango tremolite revealed the most part of iron at the surface as oxidized (Fe^{3+}/Fe_{tot} ratio of 0.65). It is well know that the Fe^{3+} to determine a strong release of ROS must be previously reduced to Fe^{2+} via iron-catalyzed Haber-Weiss cycle (Fubini and Otero Arean, 1999). This is consistent with the delay of cell mortality observed for San Mango tremolite.

Preliminary results of toxicological tests on the fibrous amphiboles from Biancavilla (samples 1, 3 and 4) did not show large differences of cell mortality for both the A549 and MeT-5A cells among the various samples (Fig. 3 and 4).

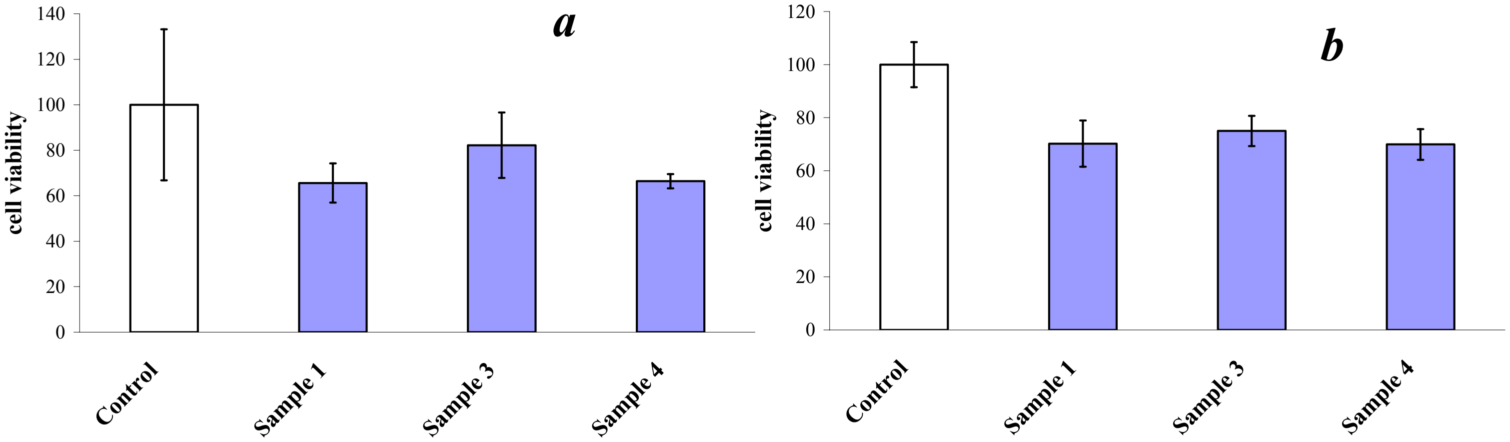

Figure 3 – Viability of A549 cells measured with the MTT assay following exposure to the fibers from Biancavilla after 24 (a) and 48 h (b). The values are reported as percentage with respect to the untreated control considered as 100 % of cell viability.

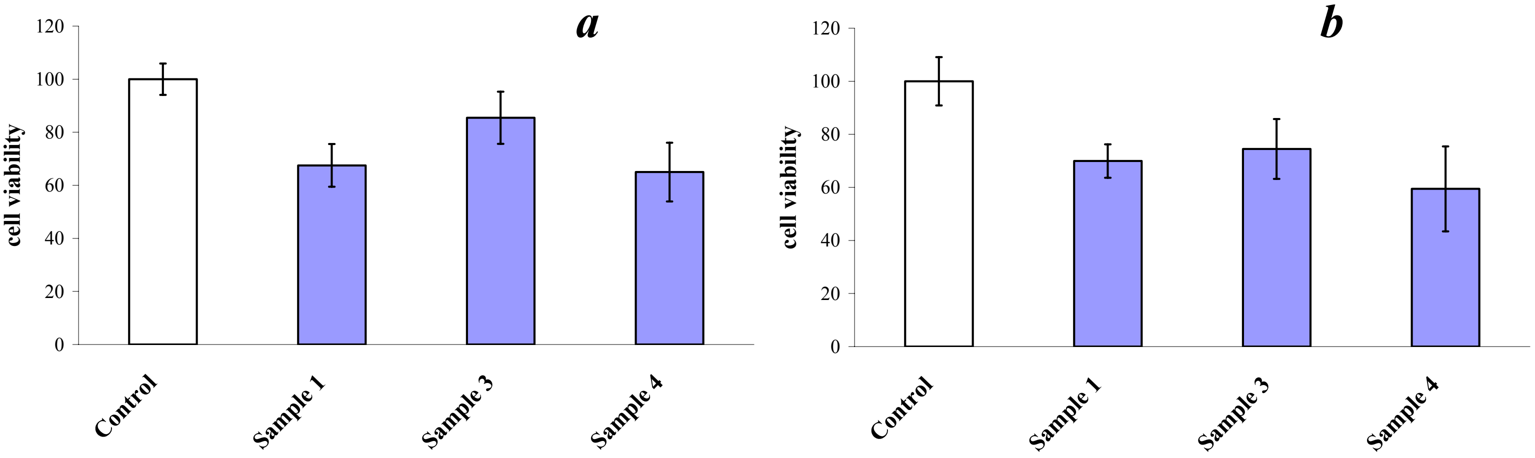

Figure 4 – Viability of MeT-5A cells measured with the MTT assay following exposure to the fibers from Biancavilla after 24 (a) and 48 h (b). The values are reported as percentage with respect to the untreated control considered as 100 % of cell viability.

This is consistent with the results obtained for sample 1 and 4 on the formation of HO° radicals (see chapter 7, section results). A certain delay of cell mortality was observed for the samples 3 and 4, which are the samples with the highest Fe^{3+}/Fe_{tot} ratios (0.92 and 0.94, respectively). As mentioned before, this is consistent with the Fe-catalyzed Haber-Weiss cycle in which the Fe^{3+} must be previously reduced to Fe^{2+} in order to produce ROS (Fubini and Otero Arean 1999).

According to these very challenging findings, the cytotoxic pathway following the fibers/cell interaction seems to be strictly dependent on the fiber crystal-chemical features as well as on surface chemistry. Therefore, a full characterization (morphology, crystal structure, crystal chemistry, Fe^{3+}/Fe_{tot} ratio, cation site partitioning, surface compostion) of different fibrous amphiboles coupled with both analysis of reactivity and citotoxicity tests is necessary to understand the chemical processes in the interaction between fiber and biological environment.

This complete interdisciplinary study represents an important goal in individuating the specific methodological approach to correlate the deepened and detailed characterization of mineral fibers (in this case amphiboles) and their biological and toxicological reactivity. Even though the carcirogenicity of these materials is generally well known, the exact molecular-chemical phenomenon implied in the interaction fiber/cell is yet to understand. Therefore, through the present study it was possible:

1) to attribute a consistent role to the total iron content, and its oxidation state, in the analyzed fibers;
2) to verify the importance of the fibrous morphology, independently to the chemistry nature of the fiber;
3) to highlight different reactivity types subordinately to the specific test adopted.

Further studies are in progress at the moment such as the citotoxicity tests on the UICC crocidolite and the richterite from Libby; the measurement of the oxidative stress and the inhibition of antioxidative defenses induced in the cells by the fibers using the release of lactate dehydrogenase (LDH) enzyme and the reduction of the pentose phosphate pathway, respectively (Gazzano et al. 2007); the characterization of the fiber surface chemistry of all tested samples. In addition the EPR study of the oxidative very strong electrophilic species not radical by using of the formate anion as target molecule in the presence of DMPO (Nejjari et al., 1993) will be necessary for a better understanding of the role of these ROS in the mechanisms of the cell mortality.

REFERENCES

Abbate, E., Bortolotti, V., Principi, G. (1980) Appennine ophiolites: a peculiar ocean crust. Ofioliti, Special Issue on Tethyian ophiolites, Western area, 59-96.

Addison, J. and McConnel, E.E. (2005) A review of carinogenicity studies of asbestos and non-asbestos tremolite and other amphiboles. International Symposium on the Health Hazard Evaluation of Fibrous Particles associated with Taconite and the adjacent Duluth Complex.

Agard, P., Goffé, B., Touret, L.R. And Vidal, O. (2000) Retrograde mineral and fluid evolution in high pressure metapelites (Schistes Lustrés Unit, Western Alps). Contrib. Mineral. Petrol., 140, 296-315.

Amodio-Morelli, L., Bonardi, G., Colonna, V., Dietrich, D., Giunta, G., Ippolito, F., Liguori, V., Lorenzoni, S., Paglionico, A., Perrone, V., Piccarretta, G., Russo, M., Scandone, P., Zanetti - Lorenzoni, E. e Zuppetta, A. (1976) L' Arco Calabro- peloritano nell'orogene appenninico-magrebide . Mem. Soc. Geol. Ital. 17, pp 1-60.

Andreozzi, G.B., Bosi, F., Longo, M. (2008) Linking Mössbauer and structural parameters in elbaite-schorl-dravite tourmalines. Am. Mineral., 93, 658-666.

Andreozzi, G.B., Lucchesi, S., Graziani, G., Russo, U. (2004) Site distribution of Fe^{2+} and Fe^{3+} in axinite mineral group: the new crystal-chemical formula. Am. Mineral., 89, 1763-1771.

Astolfi, A., Belluso, E., Ferraris, G., Fubini, B., Giamello, E., and Volante, M. (1991) Asbestiform minerals associated with chrysotile from Western Alps (Piedmont-Italy): Chemical characteristics and possible related toxicity. In R.C Brown, J.A. Hoskins, and N.F. Johnson, Eds., Mechanisms in Fiber Carcinogenesis, 223, p. 269–283. NATO ASI Series A: Life Sciences, Plenum Press, New York.

Ballirano, P., Andreozzi, G.B., Belardi, G. (2008) Crystal chemical and structural characterization of fibrous tremolite from Susa Valley, Italy, with comments on potential harmful effects on human health. Am. Mineral., 93, 1349-1355.

Bignon, L., Brochard, P., and Pairon, L.C. (1996) Mesothelioma: causes and fiber-related mechanism. In J. Aisner, M.C. Perry, and M.R. Green, Eds., Comprehensive textbook of thoracic oncology, p. 735–756. Lippincott, Williams, and Wilkins, Baltimore.

Boettcher, A. L. (1967) The Rainy Creek Alkaline-Ultramafic Complex near Libby, Montana. I : Ultramafic rocks and Fenite. J. Geol 75, 526-553.

Boettcher, A. L. (1966) The Rainy Creek Alkaline-Ultramafic Complex near Libby, Montana: PhD thesis, Pennsylvania State Univ.

Bolland, J.L. and Koch, H.P. (1945) The primary thermal oxidation products of ethyl linoleate. J. Chem. Soc., 445–447.

Bruni, B.M, Pacella, A., Mazziotti-Tagliani, S., Gianfagna, A., Paoletti, L. (2006) Nature and extent of the exposure to fibrous amphiboles in Biancavilla. Sc. Total Environment, 370, 9-16.

Branca, S., Coltelli, M., & Groppelli, G., (2004) Geological evolution of Mount Etna, in Mt. Etna Volcano Laboratory AGU (Geophysical Monograph Series Volume), 43, pp. 49-63.

Buonasorte, G., Cataldi, R., Ceccarelli, A., Costantini, A., D' Offizi ,S., Lazzarotto, A., Ridolfi, A., Baldi, P., Barelli. A., Bertini, G., Bertrami, R., Calamai, A., Cameli, G., Corsi, R., Dacquino, C., Fiordelisi, A., Ghezzo, A., Lovari, F. (1988) Ricerca ed esplorazione nell'area geotermica di Torre Alfina (Lazio-Umbria). Boll. Soc. Geol. Ital., 107, 265-337.

Burns, R.G. and Greaves C. (1971) Correlations of infrared and Mössbauer site population measurements of actinolites. American Mineralogist, 56, 2010-2033.

Burns, R.G and Strens, R. G. J. (1966) Infrared Study of the Hydroxyl Bands in Clinoamphiboles. Science, 153, 890-892.

Burragato, F., Comba, P., Baiocchi, V., Palladino, D.M., Simei, S., Gianfagna, A., Paoletti, L., Pasetto, R. (2005) Geo-volcanological, mineralogical and environmental aspects of quarry materials related to pleural neoplasm in the area of Biancavilla, Mount Etna (Eastern Sicily, Italy). Environ. Geology., 47 (6), 855-868.

Burragato, F., Mastacchi, R., Papacchini, L., Rossigni, F., Sperduto, B. (2004) Mapping of risk due to particulates of natural origin containing fibrous tremolite: the case of Seluci di Lauria (Basilicata, Italy). Modelling, computer assisted simulation and mapping of natural phenomena for hazard assessment. Geophisycal Research Abstract, 6, 2004.

Burragato, F., Ballirano, P., Fiori, S., Papacchini, L., Sonno, M. (2001) Segnalazione di tremolite asbestiforme nel Lazio. Il Cercapietre Notiziario del Gruppo Mineralogico Romano, 1-2, 33-35.

Cardile, V., Renis, M., Scifo, C., Lombardo, L., Gulino, R., Mancari, B., Panico, A.M. (2004) Behaviour of new asbestos amphibole fluoro-edenite in different lung cell systems. Int. J. Bioch. Cell Biol., 36, 849-860.

Castelli D., Rolfo F. & Rossetti P. (1995) Petrology of ore-bearing rodingite veins from the Balangero asbestos mine (Western Alps). In: B. Lombardo (Ed). Studies on metamorphic rocks and minerals in the western Alps. A Volume in Memory of Ugo Pognante, Boll. Museo Reg. Sc. Nat., (Torino, Italy), 13, 153-189.

Cello G., Lentini F., Tortorici L. (1990) La struttura del settore calabro-lucano e suo significato nel quadro dell'evoluzione tettonica del sistema a thrust sudappenninico. Studi Geologici Camerti, vol. spec., 27-34.

Comba, P., Gianfagna, A., Paoletti, L. (2003) The pleural mesothelioma cases in Biancavilla are related to the new fluoro-edenite fibrous amphibole. Arch. Environ. Health, 58, 229-232.

Compagnoni R., Sandrone R. & Zucchetti S. (1980) Some remarks on the asbestos occurrences in the Western Alps with special reference to the chrysotile asbestos deposit of Balangero (Valle di Lanzo, Piemonte, Italy). Fourth Conference on Asbestos, Torino, 20-30 May 1980, Preprint, I, 49-71.

Constantopoulos, S.H., Saratzis, N.A., Kontogiannis, D., Karantanas, A., Goudevenos, J.A., and Katsiotis, P. (1987) Tremolite whitewashing and pleural calcifications. Chest, 92, 709–712.

Dal Piaz , G.V. (1974) - Le métamorphisme de haute pressione et basse température dans l' évolution structurale du bassin ophiolitique alpino-appenninique. Bull. Soc. Miner. Pétrog., 54 (2/3), 399-424.

Davis, J.M.G., Addison, J., McIntosh, C., Miller, B.G., Niven, K. (1991) Variations in thecarcinogeneticy of tremolite dust samples of differing morphology. Ann. N. Y. Acad. Sci. 643, 473-490.

Di Paola, M., Mastrantonio, M., Carboni, M., Belli, S., Grignoli, M., Comba, P. e Nesti, M (1996) - La mortalità per tumore maligno della pleura in Italia negli anni 1988-1992. Rapporti ISTISAN, 40, 30 pp.

Drake, A.A., Jr. (1986) Geologic map of the Fairfax quadrangle, Fairfax County, Virginia: U.S., Geological Survey, Reston, Virginia.

Drake, A.A., Jr. and Morgan, B.A. (1981) The Piney Branch Complex-a metamorphosed fragment of the central Appalachian ophiolite in northern Virginia. American Journal of Science, 281, p. 484–508.

Duncan, A. M. (1976) Pyroclastic flow deposits in the Adrano area of Mount Etna,
Sicily. Geological Magazine, 113(4), 357-363.

Dyar, M.D., Mackwell, S.M., McGuire, A.V., Cross, L.R., and Robertson J.D. (1993) Crystal chemistry of Fe^{3+} and H^{+} in mantle kaersutite: Implications for mantle metasomatism. American Mineralogist, 78, 968-979.

Ernst, W.G. and Wai C.N. (1970) Mössbauer, infrared, X-ray and optical study of cation ordering and dehydrogenation in natural and heat-treated sodic amphiboles. American Mineralogist, 55, 1226-1258.

Evans, B.W. and Yang, H. (1998) Fe-Mg order-disorder in tremolite-actinolite-ferro-actinolite at ambient and high temperature. American Mineralogist, 83, 458-475.

Fairley N. (1999-2003) CasaXPS Version 2.2.19.

Favero-Longo SE, Castelli D, Salvadori O, Belluso E, Piervittori R (2005) Pedogenetic action of the lichens Lecidea atrobrunnea, Rhizocarpon geographicum gr. and Sporastatia testudinea on serpentinized ultramafic rocks in an alpine environment. Int Biodeterior Biodegrad 56, 17–27.

Finger, L.W., Cox, D.E., and Jephcoat, A.P. (1994) A correction for powder diffraction peak asymmetry due to axial divergence. Journal of Applied Crystallography, 27, 892-900.

Fournier, J., Copin, E., Dzwigaj, S., Couchane, S., and Guignard, J. (1995) Peroxydation lipique en présence de composés inorganiques. Relation avec les mécanisme de stress oxydant. C.R. Soc. Biol., 189, 1-15.

Fubini B. (1993) The possible role of surface chemistry in the toxicity of inhaled fibers. In D.B. Wahreit Ed., Fiber Toxicology, 11, 229-257. Academic Press, San Diego.

Fubini, B. (1996) Physico-chemical and cell free assays to evaluate the potential carcinogenicity of fibres., In A.B. Kane, P. Boffetta, R. Saracci, and J. Wilbourn Eds., Mechanisms of Fibre Carcinogenesis, IARC Scientific Publication 140, International Agency for Research on Cancer, Lyon.

Fubini, B.; Fenoglio, I.; Elias, Z.; Poirot, O. (2001) On the variability of the biological responses to silicas: effect of origin, crystallinity and state of the surface on the generation of reactive oxygen species and consequent morphological transformations in cells. J.Environ. Pathol. Toxicol. Oncol. 20, 87–100.

Fubini, B. and Otero Aréan C. (1999) Chemical aspects of the toxicity of invale mineral dusts. Chemical Society Reviews, 28, 373-381.

Gavino, V.C., Miller, J.S., Ikharebha, S.O., Milo, G.E., and Crwell, D.G. (1981) Effect of plyunsaturated fatty acids and autoxidation on lipid peroxidation in tissue culture. J. lipid. Res., 22, 763-769.

Gazzano, E., Turci, F., Riganti, C., Tomatis, M., Fubini, B., Bosia, A., and Ghigo, D. (2007) La tremolite nelle alpi occidentali: test cellulari con prospettive tossicologiche. Workshop “Anfiboli fibrosi: nuove problematiche relative al rischio ambientale e sanitario". Roma, 27-28 April 2007, Abstracts, 73-74.

Gazzano E, Riganti C, TomatisM, et al. (2005) Potential toxicity of nonregulated asbestiform minerals: balangeroite from the western Alps. Part 3: depletion of antioxidant defenses. J. Toxicol Environ Health 2005;68:41–9.

Gianfagna, A., And Oberti, R. (2001) Fluoro-edenite from Biancavilla (Catania, Sicily, Italy): crystal chemistry of a new amphibole end-member. Am. Mineral., 83, 1486–1493.

Gianfagna, A., Ballirano, P., Bellatreccia, F., Bruni, B.M., Paoletti, L., and Oberti, R. (2003) Characterization of amphibole fibers linked to mesothelioma in the area of Biancavilla, Eastern Sicily, Italy. Mineralogical Magazine, 67, 1221-1229.

Gianfagna, A., Andreozzi, G.B., Ballirano, P., Mazziotti-Tagliani, S., and Bruni, B.M. (2007) Structural and chemical contrasts between prismatic and fibrous fluoro-edenite from Biancavilla, Sicily, Italy. Canadian Mineralogist, 45, 249-262.

Gilmour P.S., Brown D.M., Beswik P.H., Macnee W., Rahman I., and Donaldson K. (1997) Free radical activity of industrial fibers : role of iron in oxidative stress and activation of transcription factors. Environmental Health Perspectives, 105 Suppl. 5, 1313-1317.

Goldstein J.I., Newbury D.E., Echlin P., Joy D.C., Fiori C.E. and Lifshin E. (1981) Scanning Electron Microscopy and X-Ray Microanalysis. A Text for Biologists, Materials Scientists, and Geologists. Ed. Plenum Press, pp. 673.

Gottschalk, M., Andrut, M., and Melzer, S. (1999) The determination of the cummingtonite content of synthetic tremolite. European Journal of Mineralogy, 11, 967–982.

Grosvenor AP., Kobe BA., Biesinger MC., McIntyre NS. (2004) Investigation of multiplet splitting of Fe 2p XPS spectra and bonding in iron compounds. Surf. Interface Anal., 1564-1574.

Gualtieri, A. F. (2000) Accuracy of XRPD QPA using the combined Rietveld-RIR method. Journal of Applied Crystallography, 33, 267-278.

Gunter, M.E., Brown, B.M., Bandli, B.R., and Dyar, M.D. (2001) Amphibole asbestos, vermiculite mining and Libby, Montana: What's in a name? (abstract #3455): Eleventh Annual V.M., Goldschmidt Conference, Hot Springs, Virginia.

Gunter, M.E., Dyar, M.D., Twamley, B., Foit, F.F. Jr., and Cornelius, C. (2003) Composition, $Fe^{3+}/\Sigma Fe$, and crystal structure of non-asbestiform and asbestiform amphiboles from Libby, Montana, U.S.A. American Mineralogist, 88, 1970-1978.

Gupta R.P., Sen S.K. (1974) Calculation of multiple structure of core *p*-vacancy levels. Phys. Rev., B 1, 10, 71-77.

Gupta R.P, Sen S.K. (1975) Calculation of multiple structure of core *p*-vacancy levels II. Phys. Rev., B, 12, 15-19.

Halliwell, B. and Gutteridge, J.M.C. (1986) Oxygen free radicals and iron in relation to biology and medicine: some problems and concepts. Arch. Biochem. Biophys., 246, 501–514.

Hawthorne, F.C. and Della Ventura (2007) Short range order in amphiboles. In: Amphiboles 2007, 67 , 173-222.

Hawthorne, F.C., Oberti, R. On the classification of amphiboles. Can. Mineral. 44, 1-21.

Hawthorne, F.C., Oberti, R., Della Ventura, G. and Mottana, A. (2007) Amphiboles: Crystal Chemistry, Occurence ahd Healt Issues. Reviews in Mineralogy and Geochemistry, 67.

Hawthorne, F.C. (1983) The crystal chemistry of the amphiboles. Can. Mineral. 21, 173-480.

Hawthorne, F.C. (1981) Crystal chemistry of the amphiboles. In D.R. Veblen Ed., Amphiboles and other hydrous pyriboles Mineralogy. Reviews in Mineralogy 9A, Mineralogical Society of America, 1-102.

Hospon , C. A., (1964) The crystalline rocks of Howard an Montgomery Counties. In the geology of Howard and Montgomery Counties: Baltimore, Md., Maryland. Geol. Survey, 27- 215.

Hughes, J. M., Bloodaxe, E .S., Hanchar, J. M., Foord, E. E. (1997) Incorporation of rare earth elements in titanite: Stabilization of the A2/a dimorph by creation of antiphase boundaries. Am. Min., 82, 512-516.

Jansen E.G. et Ping Liu J.I. (1973). J. Magnetic Resonance, 9, 510.

Kamp, D.W. and Weitzman, S.A. (1999) The molecular basis of asbestos induced lung injury. Thorax, 54, 638-652.

Kane, A.B., Boffetta, P., and Wilbourn, J.D. (1996) Mechanisms of Fibre Carcinogenesis. IARC Scientific Publication 140; IARC: Lyon, France, 1996.

Kappus, H., (1991) Lipid peroxidation: mechanism, anlysis, enzymology and biological relevance. In "Oxidative stress", Sies H., (Eds), Academic Press, 273-310.

Kieffer, G. (1979a) Les depots detritiques et pyroclastiques du versant oriental de l'Etna. Atti Acc. Gioenia Sci. Nat. (Catania), 2, pp. 3–32.

Kieffer, G. (1979b) Une ultime phase d'activité explosive de la Valle del Bove (Etna) vieille de 5000±130 ans et ses enseignements sur l'histoire récente du grand volcan sicilien. C.R. Acad. Sci. Paris 277D, pp. 2321–2324.

Lagarec, K. and Rancourt, D.G. (1998) RECOIL. Mössbauer spectral analysis software for Windows, version 1.0. Department of Physics, University of Ottawa, Canada.

Langer, A.M., Nolan, R.P., Costantopoulos, S. H. and Moutsopoulos, H. M. (1987) Association of Metsovo lung and pleural mesothelioma with exposure to tremolite-containing whitewash. Lancet, 25, 965-967.

Lanzafame, G., Spadea, P., Tortorici, L. (1979) Mesozoic ophiolites of northern Calabria and Lucanian appennine (southern Italy). Ofioliti, 4 (2), 173-182.

Larson, A.C. and Von Dreele, R.B. (1985) General Structure Analysis System (GSAS). Los Alamos National Laboratory Report LAUR 86-748.

Laskin, A., Cowin, J.P., Iedema. M.J. (2006) Analysis of individual environmental particles using modern methods of electron microscopy and X-ray microanalysis. Journal of Electron Spectroscopy and Related Phenomena, 150, 260–274.

Leake, B.E., Woolley, A.R., Arps, C.E.S., Birch, W.D., Gilbert, M.C., Grice, J.D., Hawthorne, F.C., Kato, A., Kisch, H.J., Krivovichev, V.G., Linthout, K., Laird, J., Mandarino, J.A., Maresch, V.W., Nickel, E.H., Rock, N.M.S., Schumacher, J.C., Smith, D.C., Stephenson, N.N., Ungaretti, L., Withtaker, E.J.W., and Youzhi, G. (1997) Nomenclature of amphiboles: report of the subcommittee on amphiboles of the International Mineralogical Association, Commission on New Minerals and Mineral Names. American Mineralogist, 82, 1019–1037.

Leake, B.E., Woolley, A.R., Birch, Burke , E.A.J., Ferraris, G., Grice, J.D., Hawthorne, F.C., Kisch, H.J., Krivovichev, Schumacher, J.C., Stephenson, Withtaker, E.J.W. (2003) Nomenclature of amphiboles: additions and revisions to the International Mineralogical Associatio's amphibole nomenclature. Can Min., 41, 1355–1370.

Long, G.J., Cranshaw, T.E., and Longworth, G. (1983) The ideal Mössbauer effect absorber thickness. Mössbauer Effect Reference Data Journal, 6, 42-49.

Martuzzi, M., Comba, P., De Santis, M., Lavarone, I., Di Paola, M., Mastrantonio, M., and Pirastu, R. (1999) Asbestos-related lung cancer mortality in Piedmont, Italy. American Journal of Industrial Medicine, 33, 565–570.

Mastrantonio, M., Belli, S., Binazzi, A., Carboni, M., Comba, P., Fusco, P., Grignoli, M., Lavarone, I., Martuzzi, M., Nesti, M., Trinea, S., and Uccelli, R. (2002) La mortalità per tumore maligno della pleura nei comuni italiani (1988–1997). Rapporti ISTISAN 02/12, 27 p. (in Italian).

Mathieu HJ, Landolt D. (1986) Investigation of thin oxide films thermally grown in situ on Fe-24Cr and Fe-24Cr-11Mo by Auger electron spectroscopy and x-ray photoelectron spectroscopy. Corros. Sci. 26: 547-559.

Mazziotti-Tagliani, S. (2007) Mineralogical, genetic and environmental aspects of the fluorite-rich amphiboles from Biancavilla (Mt Etna, Sicily, Italy). Plinius, 33, 169-174.

Mazzoli, S. (1998) The Liguride units of southern Lucania (Italy): structural evolution and exhumation of high-pressure metamorphic rocks. Rend. Fis. Acc. Lincei s. 9, v. 9:271-291

McDonald, J.C., McDonald, A.D., Armstrong, B. and Sébastien (1986) Cohort study of mortality of vermiculite miners exposed to tremolite. British Journal of Industrial Medicine, 43, 436–444.

McDonald, J.C., Harris, J., and Armstrong, B (2001) Cohort mortality study of vermiculite miners exposed to fibrous tremolite: an update (abstract): Inhaled Particles, Robinson College, Cambridge, United Kingdom, September 2–6.

McIntyre N.S., Zetaruk D.G. (1977) X-ray photoelectron spectroscopic studies of iron oxides. Anal. Chem., 49, 1521-1529.

Meeker, G.P., Bern, A.M., Brownfield, I.K., Lowers, H.A., Sutley, S.J., Hoefen, T.M., Vance, J.S. (2003) The composition and morphology of amphiboles from the Rainy Creek Complex, near Libby, Montana. Am. Mineral., 88, 1955-1969.

Meneghinello, E., Alberti, A., Cruciani, G. (1999) Order-disorder process in the tetrahedral sites of albite. Am. Min., 84, 1144-1151.

Minotti, G., and Aust, S.D. (1989) The role of iron oxygene radical mediated lipid peroxidation. Chem. Biol. Interaction, 71, 1-19.

Monaco, C. (1993) Le Unità Liguridi nel confine calabro-lucano (Appennino meridionale): revisione dei dati esistenti, nuovi dati ed interpretazione. Boll. Soc. Geol. It., 112, 751-769.

Morgan, B.A. (1977) The Baltimore Complex, Maryland, Pennsylvania, and Virginia. In Coleman, R.G., and Irwin, W.P., eds., North American ophiolites: Oregon Dept. Geology and Mineral Industries Bull. 95, 41-49.

Nejjari, A., Fournier, J., Pezerat, H., and Leanderson, P. (1993) Mineral fibres: correlation between oxidising surface activity and DNA base hydroxylation. Occup. Environ. Med., 50, 501-504.

Norgren B.S., Somers M.A.J., de Wit J.H.W. (1994) Application of tougaard background subtraction to XPS spectra of passivated Fe-17 Cr. Surf. Interface Anal., 21, 378-381.

Oberti, R., Hawthorne F.C., Ungaretti, L., Cannillo, E. (1995) $^{[6]}$Al disorder in amphibole from mantle peridotite. Can. Min., 33, 867-878.

Oberti, R.,Caballero, J.M., Ottolini, L., Lopez-Andres, S., Herreros, V. (2000) Sodic-ferripedrizite, a new monoclinic amphibole bridging the magnesium-iron-manganese-lithium and sodium calcium group. Am. Min, 85, 578-585.

Oberti, R.,Camara, F., Ottolini, L., Caballero, J.M. (2003) Lithium in amphiboles: detection, quantification and incorporation mechenisms in the composizional space bridging sodic and ^{B}Li amphiboles. Eur. J. Mineral., 15, 309-319.

Oberti, R.,Camara, F., Caballero, J.M. (2004) Ferri-ottoliniite and ferriwhittakerite, two new end members of the new Group 5 for monoclinic amphiboles. Am. Min, 88, 888-893.

Ogniben, L. (1969) Schema introduttivo alla geologia del confine Calabro-lucano. Mem. Soc. Geol. It., 8, 453-763.

Ogniben, L. (1973) Schema geologico della Calabria in base ai dati odierni. Geol. Romana, 12, 243-585.

Olla, M., Navarra, G., Bernhard Elsener, B., and Rossi, A. (2006) Nondestructive in-depth composition profile of oxy-hydroxide nanolayers on iron surfaces from ARXPS measurement. Surf. Interface Anal., 38, 964-974.

Ottolenghi, A. (1959) Interaction of ascorbic acid and mitochondrial lipids. Arch Biochem Biophys 79, 355.

Paoletti, L., Batisti, D., Bruno, C., Di Paola, M., Gianfagna, A., Mastrantonio, M., Nesti, M., Comba, P. (2000) Unusually high incidence of malignant pleural mesothelioma in a town of the eastern Sicily: an epidemiological and environmental study. Arch. Environ. Health, 55(6), 392-398.

Pasetto, R., Bruni, B.M., Bruno, C., D'Antona, C., De Nardo, P., Di Maria, G., Di Stefano, R., Fiorentini, C., Gianfagna, A., Marconi, A., Paoletti, L., Putzu, M.G., Soffritti, M. e Comba, P. (2004) Problematiche sanitarie della fibra anfibolica di Biancavilla. Aspetti epidemiologici, clinici e sperimentali. Not. Ist. Super. Sanità, 17, 8-12.

Piccardo G.B., Müntener O., Zanetti A., Romairone A., Bruzzone S., Poggi E., SpagnoloG. (2004) The Lanzo south peridotite: melt/peridotite interaction in the mantle lithosphere of the jurassic ligurian Tethys. Ofioliti, 29, 63-74.

Piolatto, G. (1996) Valori di riferimento e valori limite per l'amianto. In C. Aprea, G. Sciarra, M.L.

Piolatto, G., Negri, E., La Vecchia, C., Pira, E., Decarli, A., and Peto, J. (1990) An update of cancer mortality among crysotile asbestos miners in Balangero, Northern Italy. British Journal of Industrial Medicine, 47, 810–814.Fiorentino, and C. Minoia, Eds., I valori di riferimento e i valori limite nella prevenzione ambientale e occupazionale, p. 153–161. Morgan Edizioni Tecniche, Milano (in Italian).

Piluso E., Cirrincione R., Morten L. (2000) Ophiolites of the Calabrian Peloritan Arc and their relationship with the cristalline basament (Catena Costiera and Sila Piccola, Calabria, Southern Italy). Ofioliti, 25 (2), 117-140.

Piras F.M. (2002) Ph. D Thesis. In situ Attenuated Total Reflection Tribometry: A new approach for the chemical analysis of tribological films, ETH, Zurich.

Pognante U., Rösli U. & Toscani L. (1985) Petrology of ultramafic and mafic rocks from the Lanzo peridotite body (Western Alps). Lithos, 18, 201-214.

Pognante U. (1991) Petrological constraints on the eclogite and blueschist-facies metamorphism and P-T-t path in the Western Alps. J. Metam. Geol., 9, 5-17.

Pugnaloni, A., Lucarini, G., Giantomassi, F., Lombardo, L., Capella, S., Belluso, E., Zizzi A., Panico, A.M., Biagini, G., Cardile, V. (2007) In vitro study of biofunctional indicators after exposure to asbestos-like fluoro-edenite fibres. Cell. Mol. Biol., 53, 965-80.

Punturo R. et al. (2002) Le Cave storiche della "Pietra Verde" di Gimigliano e Monte Reventino (Calabria): studio petrografico e geochimico. Bollettino della Società Gioenia di Scienze Naturali, 37, 37-59.

Rancourt, D.G. and Ping, J.Y. (1991) Voigt-based methods for arbitrary-shape static hyperfine parameter distributions in Mössbauer spectroscopy. Nuclear Instruments and Methods in Physics Research, B58, 85-97.

Reinecke, T. (1995) Ultrahigh and highpressure metamorphic rocks of the Zermatt- Saas zone, western Alps: Records of burial and exhumation paths. In: W. Schreyer, F. Rummel, B. Stiickhert, (Eds.) High-Pressure Metamorphism in Nature and Experiment. Abstr. Vol. Int. COB. Bochumer Geol. u. Geotech. Arb. 44, 152-157.

Rittmann, A. (1973) Structure and evolution of Mount Etna. Philosophical Transaction of the Royal Society of London, 274, 5-16.

Ro, C., Osan, J., Szaloki, I., de Hoog, J., Worobiec, A., and Van Grieken, R. (2003) A Monte Carlo program for quantitative electron-induced X-ray analysis of individual particles. Anal. Chem., 75, 851-859.

Robledo, R. and Mossman, R. (1999) Cellular and molecular mechanisms of asbestos-induced fibrosis. Journal of Cellular Physiology, 180, 158-166.

Romano, R. (1979) The evolution of the Etnean Volcanism. Pubbl. N. 235 del Progetto Finalizzato Geodinamica (C.N.R.), 103-117, Napoli.

Romano R. (1982) Succession of the volcanic activity in the Etnean area. Mem. Soc. Geol. It., 23, 27-48.

Romano, R. and Sturiale, C. (1981) Geologia del versante sud-orientale Etneo, F270 IV. Bollettino della Società Geologica Italiana, 100, 15-40.

Ross, M., Nolan, R.P. (2003) History of asbestos discovery and use and asbestos-related disease in context with the occurrence of asbestos within ophiolite complexes. Geological Society of America. Special paper 373.

Rossi A., Puddu G., Elsener B. (2006) EFC Series Publication. Woodhead Publishing Limited, 38.

Sanchez, M. S, Gunter, M. E. and Dyar M. D. (2008) Characterization of historical amphibole samples from the former vermiculite mine near Libby, Montana, U.S.A. European Journal of Mineralogy, 20, 6, p. 1043-1053.

Scandone, P. (1975) Triassic seaway and the Jurassic Tethys in the Central Mediterranean area. Nature, 256, 117.

Scott V.D., Love G. and Reed S.J.B. (1995) Quantitative electron probe microanalysis. 2nd ed., XIV, 311 S., New York (Ellis Horwood).

Small J.A. (2002) The analysis of particles at low accelerating voltages (≤ 10 kV) with Energy Dispersive X-Ray Spectroscopy (EDS). Journal of Research of the National Institute of Standards and Technoloy, 107 (6), 555-566.

Stanton, M.F., Layard, M., Tegeris, A., Miller, E., May, M., Morgan, E., and Smith, A. (1981) Relation of particle dimension to carcinogenicity in amphibole asbestoses and other fibrous minerals. Journal of the National Cancer Institute, 67, 965–975.

Soffritti, M., Minardi, F., Bua, L., Degli Esposti, D., Belpoggi, F. (2004) First experimental evidence of peritoneal and pleural mesotheliomas induced by fluro-edenite fibres in Etnean volcanic material from Biancavilla (Sicily, Italy). Eur. J. Oncol., 9, 169-175.

Sokolova, E.V., Kabalov, Y.K., McCammon, C., Schneider, J., and Konev, A.A. (2000) Cation partitioninig in an unusual strontian potassicrichterite from Siberia: Rietveld structure refinement and Mössbauer spectroscopy. Mineralogical Magazine, 64, 19-23.

Sokolova, E.V., Hawthorne, F.C., McCammon, C., and Schneider, J. (2001) Ferrian winchite from the Ilmen Mountains, Southern Urals, Russia and some problems with the current scheme of nomenclature. Canadian Mineralogist, 39, 171-177

Spadea, P. (1976) I carbonati delle rocce metacalcaree della Formazione del Frido della Lucania. Ofioliti, 1, 431-465.

Spadea, P. (1982) Continental crust rocks associated whit ophiolites in Lucanian Appennine (Southern Italy). Ofioliti, 2 (3), 501-522.

Skogby, H., and Rossman, G.R. (1991) The intensity of amphibole OH bands in the Infrared absorption spectrum. Physics and Chemistry of Minerals, 18, 64-68.

Thompson, P., Cox, D.E., and Hastings, J.B. (1987) - Rietveld refinement of Debye-Scherrer synchrotron X-ray data from Al_2O_3. Journal of Applied Crystallography, 20, 79-83.

Toby, B.H. (2001) EXPGUI, a graphical user interface for GSAS. Journal of Applied Crystallography, 34, 210-213.

Turci, F., Gazzano, E., Tomatis, M., Riganti, C., Ghigo, D., and Fubini, B. (2007) La tremolite nelle alpi occidentali: un'analisi chimico-fisica con prospettive tossicologiche. Workshop "Anfiboli fibrosi: nuove problematiche relative al rischio ambientale e sanitario". Roma, 27-28 April 2007, Abstracts, 68-72. (in Italian).

U.S. National Research Council (1985) Asbestiform fibres: Non-occupational health risks 352 p. National Academy Press, Washington.

Vai, G.B. (1992) Il segmento Calabro-Peloritano dell'orogene Ercinico. Disaggregazione palinspastica. Boll. Soc. Geol. It., 111, 109-129.

Van Oss, C.J., Naim, J.O., Costanzo, P.M., Gieise, R.F. Jr., Wu, W., Sorlung, A.F. (1999) Clays and clay Minerals, 47 (6), 697-707.

Verkouteren, J.R. and Wylie, A.G. (2000) The tremolite-actinolite-ferro-actinolite series: systematic relationship among cell parameters, composition, optical properties, and habit, and evidence of discontinuities. American Mineralogist, 85, 1239-1254.

Vezzani, L. (1968a) Rapporti tra ofioliti e formazioni sedimentarie nell'area compresa tra Viaggianello, Francavilla sul Sinni, Terranova di Pollino e San Lorenzo Bellizzi. Atti Acc. Gioienia Sci. Nat. Catania, 6 (20), 189-222.

Vezzani, L. (1969) La Formazione del Frido (Neocomiano-aptiano) tra il Pollino ed il Sinni Lucania). Geol. Romana, 8, 129-176.

Von Dreele, R.B. (1997) Quantitative texture analysis by Rietveld refinement. Journal of Applied Crystallography, 30, 517-525.

Wilye, A. and Verkouteren, J. (2000) Amphibole asbestos from Libby, Montana: aspects of nomenclature. American Mineralogist, 85, 1540-1542.

Yang, H. and Evans, B.W. (1996) X-ray structure refinements of tremolite at 140 and 295 K: Crystal chemistry and petrologic implications. American Mineralogist, 81, 1117-1125.

Young, R.A. (1993) Introduction to the Rietveld method,. In R.A. Young, Ed., The Rietveld method, 1-38, Oxford Science, Oxford.

Zalma, R. (1988) Contribution à l’etude de la réactivité de surface des fibres minerales. Relations possibles avec leurs propriétés cancérogènes. Thèse de doctorat d’état. Université Pierre et Marie Curie Paris VI.

Abstract:

This work concerns the physico-chemical and structural characterisation of mineral fibres (asbestos) and the comprehension of the chemical and molecular mechanisms which are responsible of the development of human pathologies specific to their inhalation. In particular, in this work we performed a crystallochemical and surface reactivity study of floro-edenite, a natural amphibole of volcanic origin recently discovered in Biancavilla (Sicily, Italy). The properties of this mineral were compared to those of other natural mineral fibres, such as tremolite and chrysotile, also present in ophiolitic formations of the Italian peninsula.

This work consists of several different parts, which are proof of its multidisciplinary and applied character. In the first part, we studied the mineralogical, chemical and morphological analysis of previously purified natural fibres of fluoro-edenite. The main goal of this part was to determine precisely the crystallographic structure and the composition of this material.

This information has been of fundamental importance in the second part of this study, which concerned the toxicochemical properties and the surface reactivity of this mineral. In order to underline the possible pathogenic effect of the inhalation of these fibres, these properties were compared to those of other mineral fibres, such as tremolite and chrysotile, the toxicological properties of which are already known.

The second part of this study was finally validated by parallel in vitro and in vivo tests of these materials, in collaboration with a biomedical research group.

Résumé :

Ce travail de thèse concerne la caractérisation physico-chimique et structurale de fibres minérales (asbeste) et la compréhension de mécanismes chimiques et moléculaires qui peuvent amorcer des pathologies spécifiques relatives à leur inhalation. En particulier, dans ce travail on s'est concentrés sur l'étude cristallochimique et de réactivité de surface de la fluoro-édénite, une amphibole naturelle d'origine volcanique découverte récemment à Biancavilla (Sicile), en comparaison avec d'autres fibres minérales, comme les trémolites et le chrysotile, aussi présents dans les formations ophiolitiques de la péninsule italienne.

Ce travail comprend différentes étapes qui témoignent de son caractère pluridisciplinaire et appliqué. Dans la première partie, nous avons effectué l'étude minéralogique, chimique et morphologique des fibres naturelles de fluoro-édénite préalablement purifiées. Le but de cette partie du travail a été de déterminer précisément la structure cristallographique et la composition de ce matériau.

Ces informations ont été fondamentales pour la deuxième partie de cette étude, qui a concerné l'étude des propriétés toxicochimiques et la réactivité de surface de ce minéral. Ces propriétés ont été étudiées en parallèle avec celles d'autres fibres minérales dont les propriétés toxicologiques sont connues, tels que les trémolites et les chrysotiles, pour pouvoir enfin mettre en évidence des possibles des effets pathogènes potentiels déclenchés par leur inhalation.

Cette deuxième partie de l'étude a été enfin validée à travers des tests in vitro et in vivo de la toxicité de ces matériaux, en collaboration avec une équipe de médecins et biologistes.